VIRGINIA POLYTECHNIC INSTITUTE
AND STATE UNIVERSITY

The Charles E. Via, Jr. Department
of Civil and Environmental Engineering
Blacksburg, VA 24061

Structural Engineering and Materials

THE EFFECT OF POWDER ACTUATED FASTENERS ON THE SEISMIC PERFORMANCE OF PROTECTED ZONES IN STEEL MOMENT FRAMES

by
Matthew R. Eatherton, Ph.D., S.E.
Assistant Professor

Bradley W. Toellner
Graduate Research Assistant

Charles E. Watkins
Graduate Research Assistant

Ebrahim Abbas
Graduate Research Assistant

Report No. CE/VPI-ST-13/05

July 2013

EXECUTIVE SUMMARY

Special moment resisting frames (SMRF) depend on large inelastic strains in the beam-to-column connections to dissipate seismic energy and protect buildings from collapse. The ANSI / AISC 341-10 Seismic Provisions for Structural Steel Buildings define the ends of the beams in a SMRF as protected zones at the locations where large inelastic strains are expected. In the protected zone, AISC 341-10 prohibits any decking attachments that penetrate the beam flange and any welded, bolted, screwed, or shot-in attachments for other purposes. However, these restrictions are based primarily on a lack of data showing that such fasteners will not cause premature low cycle fatigue fracture in the moment connection.

A series of full-scale beam-to-column moment connection tests were conducted to evaluate the effects of powder actuated fasteners (PAF) applied in the protected zone on the seismic behavior of steel moment connections. The primary objective of the testing program was to determine if beam-to-column connections with deck attachments using PAF's satisfy the SMRF qualification criteria of AISC 341-10. The test matrix consisted of twelve full-scale specimens with varying parameters to represent both common and extreme conditions. Variations in fasteners included control specimens with no fasteners, PAF at 12 in. spacing representing typical deck attachment, puddle welds at 12 in. spacing, and PAF in a dense grid over the protected zone with 1in. spacing to any edge. The powder actuated fasteners were Hilti X-ENP-19L15 type fasteners and were selected because they were some of the larger fasteners used for attachment to structural steel members. Both W24x62 and W36x150 beams were tested with flange thicknesses of 0.59 in. and 0.94 in. respectively. The test matrix included reduced beam section (RBS) connections and non-RBS connections that are considered representative of the range of currently prequalified moment connection types.

The experimental configuration consisted of one-sided (exterior) moment connections. The column was twelve feet tall to approximately simulate the distance between inflection points of two adjacent stories. The beam specimens were connected to the column using extended end plate connections to allow the reuse of the column section for all tests. A displacement protocol in accordance with the AISC 341-10 Chapter K SMRF qualification criteria was applied using an

actuator connected to the cantilever end of the beam specimen at a distance of 17 ft from the centerline of the column. Additional cycles were performed at 4.7% story drift.

All twelve specimens passed the SMRF qualification requirements by maintaining 80% of the specimen nominal plastic moment strength through the first cycle of 4% story drift. Furthermore, in comparing results from specimens with and without PAF, there was negligible difference in the cyclic envelope, energy dissipation, and strength degradation prior to fracture. The general progression of limit states included yielding at the extreme fibers, spread of plasticity through the depth of the section, and local buckles formed at story drifts of 3% or larger. Ductile tears initiated during the 4% or 4.7% story drift cycles at the flange tips (common in the W24 RBS specimens), on the flange surface at the inside of a local buckle (common in the W36 RFS specimens), at the junction of the stiffener and the flange (in the W36 specimens), and at the PAF.

Fracture that caused significant loss of strength in specimens with PAF generally occurred during a similar cycle or during an earlier cycle than specimens with no fasteners, although it is noted that all fractures occurred at the 4.7% story drift level after qualification was complete. Because the difference was not sizable and the data set relatively small, it was not possible to quantitatively evaluate the difference in a statistically significant manner. Since all of the specimens including three specimens with a grid of PAF satisfied the qualification criteria, it is expected that SMRF beams in configurations such as the ones tested in this study, with PAF applied in the protected zone with 1 in. spacing to edges or welds, would satisfy SMRF qualification criteria and thus be expected to produce ductile SMRF seismic performance.

ACKNOWLEDGEMENTS

This material is based on work supported by the Hilti, Inc. and the American Institute of Steel Construction. In-kind funding was provided by Banker Steel and Applied Bolting Technology.

Valuable assistance in the preparation and conducting of tests was provided by Karim Laknejadi, Ngan Dinh, and Stuart Salmon as well as our lab technicians Dennis Huffman and Brett Farmer.

TABLE OF CONTENTS

Contents

CHAPTER 1 INTRODUCTION

1.1 Motivation and Background

Special moment resisting frames (SMRF) depend on large inelastic strains in the beam-to-column connections to dissipate seismic energy and protect buildings from collapse. The ANSI / AISC 341-10 Seismic Provisions for Structural Steel Buildings (AISC 2010a) define the ends of the beams in a SMRF as protected zones at the locations where large inelastic strains are expected. In this region AISC 341 (AISC 2010a) prohibits any decking attachments that penetrate the beam flange and any welded, bolted, screwed, or shot-in attachments for other purposes. Figure 1.1 shows examples of the extents of the protected zone for two types of moment connections.

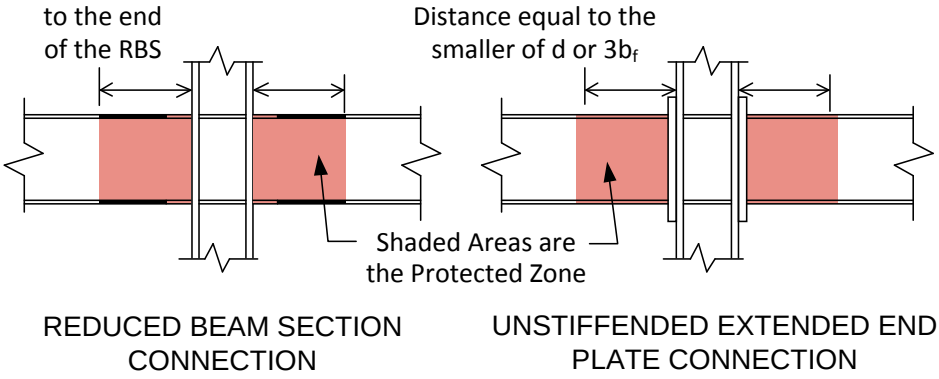

Figure 1.1 – Examples of Protected Zone for Two Moment Connection Types

The restriction on attachments in the protected zone of moment frames is based on test specimens that had welded shear studs and composite slabs conducted as part of the FEMA/SAC project. Two potential concerns were identified. One beam-to-column connection specimen with welded shear studs in the protected zone experienced fracture of the flange initiating at the shear stud (Ricles et al. 2002). It was concluded that the fracture of the beam flange was a direct result of the reduced notch toughness of the base metal caused by shear stud welding. Other beam-to-column tests using composite slabs and welded shear studs through the protected zone demonstrated that composite action in the connection region changes the strain distribution in the beam and causes increased strain demands in the beam bottom flange (Leon et al. 1998, Hajjar et al. 1998, Tremblay et al. 1997). Larger strain demands in the critical bottom flange where the majority of fractures were observed after the Northridge earthquake, the rapid change from

composite section to steel beam connection, and the one test with flange fracture initiating at the stud led to the conclusion that it would be a prudent precaution to exclude shear studs from the protected zone.

However, the test specimen that experienced fracture at the shear stud was one out of a number of tests on beam-to-column connections with composite slabs and welded shear studs in the protected zone and none of the other specimens experienced a fracture originating at the shear stud (e.g. Uang et al. 2000, Leon et al. 1998, Hajjar et al. 1998, Chen and Chao 2001, and Cifjan et al. 2000). A picture of one of these specimens is included in Figure 1.2. Furthermore, the effects of welded shear studs on the base metal properties, degree of composite action, beam flange strain demands, ductility, and inelastic rotation capacity of the beam is significantly different than the effects due to other types of fasteners such as PAF's. The exclusion of other types of fasteners in the protected zone is primarily due to a lack of data demonstrating the acceptability of connections including them.

Figure 1.2 - Picture of Beam-to-Column Connection Test with Welded Shear Studs and Composite Floor Slab After Testing (Picture from Uang et al. 2000).

The restriction on fasteners in the protected zone creates issues in construction due to the inability to connect steel deck to the beam using connections other than arc spot puddle welds, and difficulty in communicating and enforcing the requirements. Figure 1.3 shows examples of some unauthorized attachments made to the beam in the protected zone. Other common conditions that have been identified are the attachment of steel deck to the beam top flange, attachment of cold-formed steel wall track to the underside of the beam, and attachments for mechanical / electrical nonstructural systems.

Figure 1.3 - Examples of Unapproved Attachments in the Protected Zone. Photos (a) and (b) Courtesy of Thomas Murray, Photo (c) from Hamburger et al. (2009).

Powder actuated fasteners (PAF) are a common method for attaching steel deck to the top flange of steel beams, as well as a common means for attaching nonstructural elements such as cold-formed steel tracks, mechanical, electrical, and plumbing elements to the structure. The fastener (example shown in Figure 1.4) is driven into the steel plies using a powder actuated fastening tool. The effect of PAF's on fracture of steel coupons subjected to monotonic tension has been studied by Beck and Engelhardt (2002). It was determined that coupons with PAF's had higher tensile strength than coupons with drilled holes. Moreover, a typical coupon specimen with PAF was shown to reach a strain of 17% before fracture. Although less than a specimen with no holes, this corresponds to approximately 70% more ductility than a similar specimen with drilled holes. The increased strength and ductility of steel coupons with PAF's as compared to drilled holes might be attributed to increased strength in the surrounding base metal caused during the fastener application or to residual compressive stresses in the material surrounding the hole. Studies have also been conducted to investigate the fatigue performance of steel with PAF's (e.g. Niessner and Seeger 1999). However, the behavior of steel with PAF's subjected to cycles of large inelastic strains, such as those experienced in the protected zones, has not been experimentally investigated.

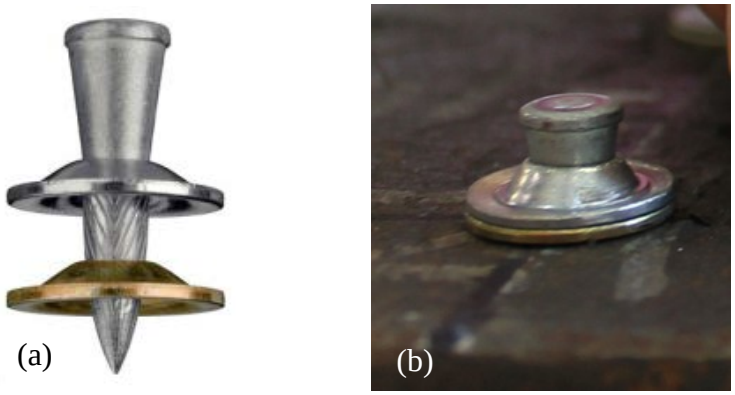

Figure 1.4 – Hilti X-ENP Powder Actuated Fastener Before (a) and After (b) Installation

A recent Japanese study investigated the Vickers hardness surrounding PAF and welded shear studs to determine the extent of base metal affected by each (Lee et al. 2012). At the surface, the base metal as far as 6 mm (0.236 in.) away from the edge of the PAF was found to have an affected Vickers hardness. The effected zone extended as deep as the fastener penetrated. The total diameter of effected base metal was approximately 15 mm (0.591 in.) for the particular type of fastener investigated. The extent of the heat affected zone (HAZ) around a welded shear stud weld was estimated based on Vickers hardness to be 3 mm (0.236 in.) away from the weld and extends to a depth less than 6 mm (0.236 in.). The hardness of the HAZ was found to be characteristic of the weld metal. The total diameter of effected base metal near the surface around a welded shear studs was found to be 20 mm (0.787 in.).

1.2 Approach

A series of full-scale beam-to-column moment connection tests were conducted to evaluate the effects of powder actuated fasteners applied in the protected zone on the seismic behavior of steel moment connections. The primary objective of the testing program was to determine if beam-to-column connections with deck attachments using PAF's satisfy the SMRF qualification criteria of AISC 341-10 (AISC 2010a).

The test matrix consisted of twelve full-scale specimens with varying parameters to represent both common and extreme conditions. Variations in fasteners included control specimens with no fasteners, PAF at 12 in. spacing representing typical deck attachment, puddle welds at 12 in. spacing, and PAF in a dense grid over the protected zone with 1in. spacing to any edge. Both W24x62 and W36x150 beams were tested with flange thicknesses of 0.59 in. and 0.94 in. respectively. Reduced beam section (RBS) connections and non-RBS connections were considered representative of the range of currently prequalified moment connection types. The instrumentation plan was designed to capture global performance of the test setup, local deformations of the protected zone, and strain variations across the flanges in the protected zone. The strain variations measured across the flanges give information about the effect of PAFs on strain distribution.

1.3 Organization of This Report

This report describes relevant background, details of the full-scale testing program, results from the tests, analysis of the fracture surfaces, and summary of the findings. The report is organized into the following chapters:

- Chapter 1 describes the motivation for investigating the effect of PAF on the seismic behavior of moment connections and some of the background on the subject. It also summarizes what is included in this document.

- Chapter 2 discusses the full-scale moment connection testing program including the goals of the testing, the test matrix, dimensions and details of the test setup and specimens, the instrumentation plan, and material testing.

- Chapter 3 discusses the performance of each tested specimen. The load-deformation response is presented and the progression of limit states is discussed. For specimens experiencing significant fracture, the fracture surface is analyzed.

- Chapter 4 uses data from the set of instrumentation to decompose the imposed story drift into components for verifying adequacy of the test setup behavior, validating instrumentation accuracy, and assessing demands on the protected zone.

- Chapter 5 synthesizes the results from all specimens to evaluate the effect of powder actuated fasteners and puddle welds on the cyclic behavior of moment connections. Comparisons are made for the fracture potential, moment capacity, hysteretic shape, strength degradation, energy dissipation, and strain distribution for specimens with and without fasteners.

- Chapter 7 includes a summary of the work and conclusions reached in this study. These include overall observations of test performance.

- Appendices provide additional information about the test setup, procedure for decomposing the story drift into components, story drift decomposition plots for each specimen, and strain distribution information.

CHAPTER 2 EXPERIMENTAL TESTING PROGRAM

2.1 Test Configuration

The test setup is shown in Figure 2.1. The configuration uses a W14x257 vertical column, approximately 12 ft tall, that is restrained against lateral translation at the top and bottom. The beam specimens attach to the column with a bolted end plate connection to allow the same column to be used for every test. Additional details on geometry and sizes of reaction frames is given in Appendix A, Toellner (2013) and Watkins (2013). Pictures of the test setup are shown in Figure 2.2 and Figure 2.3. Load was applied with an MTS model 201.70 actuator with force capacity of 215 kips in tension and 330 kips in compression and stroke equal to 20 in.

The geometry of the test setup is intended to simulate an exterior column subassemblage of a moment frame undergoing rotation due to story drift. The 17 ft distance from the column centerline to the actuator represents the distance from the column centerline to the beam inflection point in a 34 ft long bay assuming an idealized moment diagram. Similarly, the column height of 12 ft represents the distance between column inflection points on adjacent floors assuming an idealized moment distribution and implying a building with 12 ft floor heights.

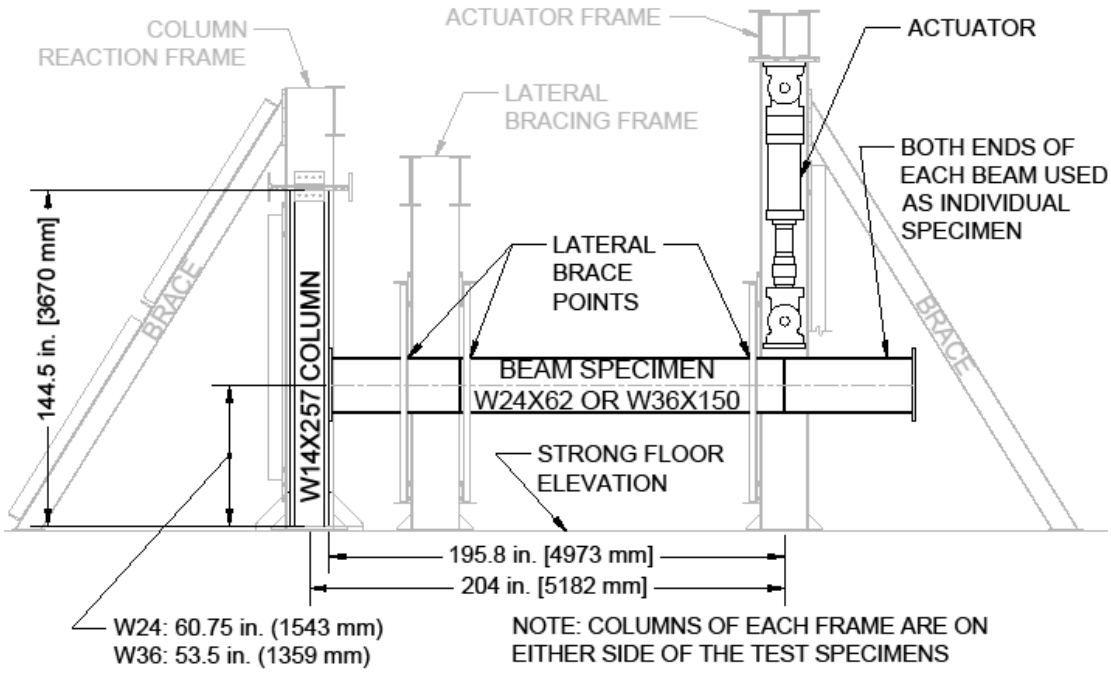

Figure 2.1 - Full-scale Test Configuration

Figure 2.2 – Picture of the Test Setup from an Angle

Figure 2.3 - Picture of the Test Setup from the Side

Each specimen was subjected to the same displacement history as specified by the qualification protocol in AISC 341-10 (AISC 2010a). The target actuator displacements were determined by multiplying the target story drifts by the distance between the actuator and the column centerline, 17ft (5182 mm). Beyond the qualification amplitude of 4% story drift, additional cycles were performed at amplitude of 4.7% story drift which corresponds to the maximum stroke of the actuator. The displacement history is given in Table 2.1 and shown in Figure 2.4. The displacement rate for all tests was 2.4 in/min.

Table 2.1 – Displacement Protocol Based on AISC 341-10

AISC 341-10 Story Drift (rad)	Percent Story Drift (%)	Number of Cycles	Actuator Displacement (in)
0.0038	0.38	6	0.765
0.0050	0.50	6	1.02
0.0075	0.75	6	1.53
0.0100	1.00	4	2.04
0.0150	1.50	2	3.06
0.0200	2.00	2	4.08
0.0300	3.00	2	6.12
0.0400	4.00	2	8.16
0.0466	4.66	Varies	9.50

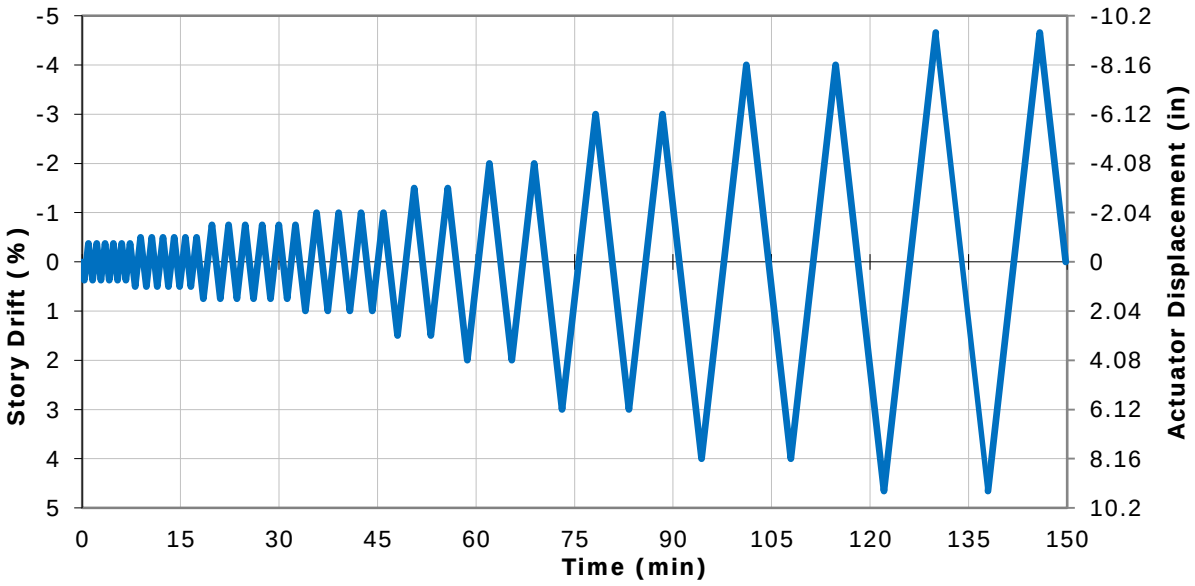

Figure 2.4 - Displacement Protocol

The SMRF qualification criteria in AISC 341-10 chapter K specifies that a specimen must undergo one complete cycle at 4% story drift while sustaining a moment resistance at the face of the column that is at least 80% of the nominal plastic moment capacity. The nominal plastic moment capacity is computed with nominal yield stress and nominal plastic section modulus.

2.2. Test Matrix and Specimens

A total of six beams were used to make the 12 specimens. Each end of each beam was designed as an individual specimen shown in the test matrix. The beams were 21 ft long, allowing enough beam length that the inelastically deformed section from one specimen is beyond the actuator and not participating in the testing of the next specimen. The beams were flipped over (bottom to top) and turned around (front to back) from the testing of one end of the beam to the next.

Table 2.2 shows the test matrix outlining the variable of interest of each test. The first six specimens utilized W24x62 beams. Among these first six specimens, three used bolted unstiffened extended endplate connections (BUEEP) and three used reduced beam section (RBS) connections. The final six specimens were W36x150 beams. Among these six tests, three used bolted stiffened extended endplate connections (BSEEP) and three used RBS connections.

Table 2.2 - Test Matrix

Specimen Number	Beam Size	Connection Type	Fasteners in the Protected Zone	Specimen Name
1	W24x62	RBS	None	RBS24
2	W24x62	RBS	4 PAF @ 12"	RBS24-PAF12
3	W24x62	BUEEP	None	W24
4	W24x62	BUEEP	4 PAF @ 12"	W24-PAF12
5	W24x62	RBS	4 Puddle Welds @ 12"	RBS24-PW12
6	W24x62	BUEEP	Grid of PAF	W24-PAF_ARRAY
7	W36x150	RBS	None	RBS36
8	W36x150	RBS	4 Puddle Welds @ 12"	RBS36-PW12
9	W36x150	RBS	Grid of PAF	RBS36-PAF_ARRAY
10	W36x150	BSEEP	None	W36
11	W36x150	BSEEP	4 PAF @ 12"	W36-PAF12
12	W36x150	BSEEP	Grid of PAF	W36-PAF_ARRAY
12 Tests	6 W24x62 6 W36x150	6 RBS 6 BEEP		

This set of specimens will include variation in beam depth (nominal W24 to W36), flange thickness (0.59 in. to 0.94 in.), flange width (7 in. to 12 in.), and beam weight (62 lb/ft to 150 lb/ft). The flange thickness may be an important variable as the location of the PAF tip in the depth of the flange will vary and the relative magnitude of the disturbance of the strain field may vary depending on the flange thickness and width. The depth of the section will affect the inelastic strain demands as the distance from the neutral axis to the fastener will vary. The flange width and incorporation of RBS cuts will further affect inelastic strain demands at the flange tips and are thus are also key variables that were varied in this study.

The testing plan focuses on the reduced beam section and bolted extended end plate connections, but the results are expected to be applicable to other connection types. The prequalified connection types allowed in ANSI / AISC 358-10 (AISC 2010b) include the reduced beam section (RBS), bolted unstiffened extended end plate (BUEEP), bolted stiffened extended end plate (BSEEP), bolted flange plate (BFP), welded unreinforced flange-welded web (WUF-W), and Kaiser bolted bracket (KBB). The principal difference between the connection types is the method for connecting the beam flanges to the column in a way that prevents fracture while the beam undergoes large inelastic rotations. Connections with straight flange edges, identical beam sections, and similar column panel zones, would be expected to experience similar inelastic strain demands and local buckling in the beam plastic hinge region (protected zone) regardless of the

beam flange to column connection type. Therefore, the inelastic behavior of the flanges in the protected zone is expected to be similar for all six connection types with the exception of the RBS which has different flange geometry. It is assumed that the PAF's would not to be applied to the weld region of the connection, the flange plate of the BFP connection, or the bracket of the KBB connection.

Each of the six beams contained an RBS specimen on one end and a non-RBS specimen on the other, although both ends had end plates so that the same column could be reused. It is noted that while RBS specimens don't typically include endplates, they were used for these full-scale tests so that the same column could be used throughout testing. However, the use of an endplate does not significantly affect the inelastic deformations of the RBS plastic hinge which are the focus of this investigation. The end plate connections were designed in accordance with ANSI / AISC 358-10, are shown in Figure 2.5, and additional details on their design can be found in Watkins (2013). The specimen geometry is shown in Figure 2.6 and Figure 2.7 for the W24x62 and W36x150 specimens respectively.

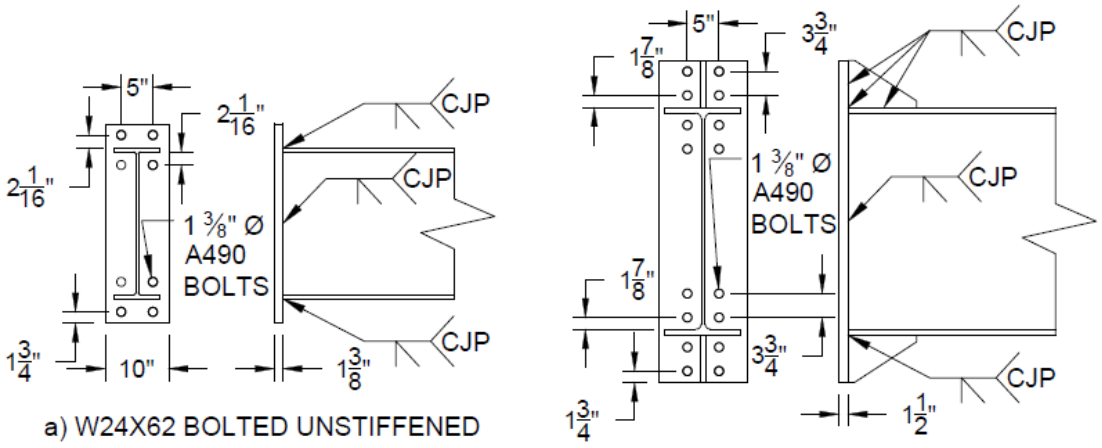

Figure 2.5 - Specimen End-Plate Connections

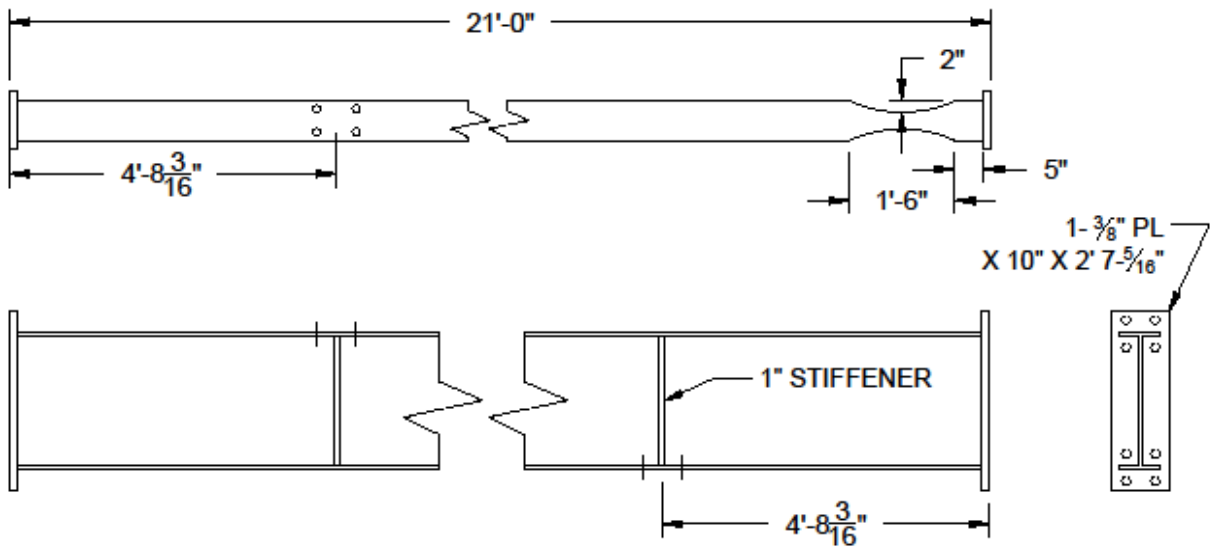

Figure 2.6- W24X62 Specimen General Dimensions

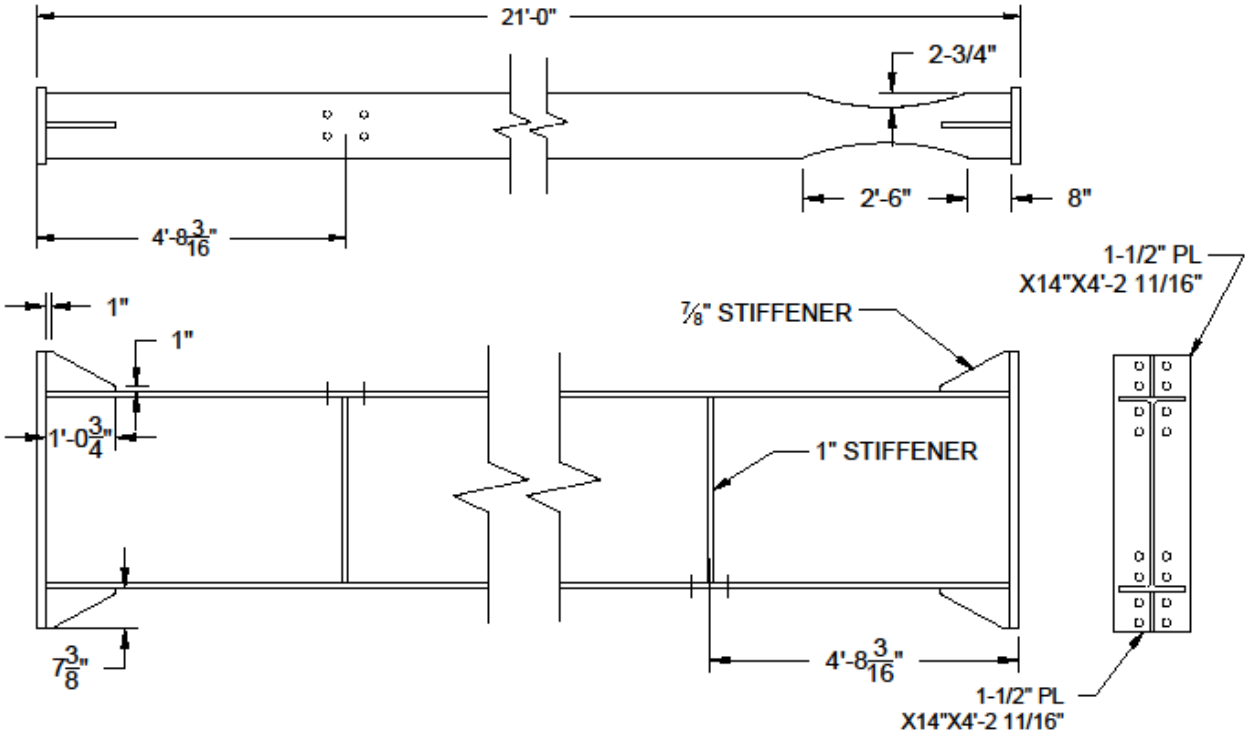

Figure 2.7 - W36x150 Specimen General Dimensions

The protected zone differed between many of the specimens because of geometric variables such as the inclusion of RBS cuts, end plate stiffeners, and the difference in beam size. Therefore, a summary of the protected zone for each type of specimen is listed in Table 2.3.

Table 2.3 - Specimen Protected Zone Limits from Column Face

Specimen Number	Specimen Name	Protected Zone Length (in)
1	RBS24	24.4
2	RBS24-PAF12	24.4
3	W24	22.5
4	W24-PAF12	22.5
5	RBS24-PW12	24.4
6	W24-PAF_ARRAY	22.5
7	RBS36	39.5
8	RBS36-PW12	39.5
9	RBS36-PAF_ARRAY	39.5
10	W36	32.2
11	W36-PAF12	32.2
12	W36-PAF_ARRAY	32.2

A similar variation of fasteners was used for both beam types as shown in Figure 2.8. For both the W24x62 and W36x150, one RBS specimen (Specimen 1 and Specimen 7) and one BUEEP specimen (Specimen 3 and Specimen 10) were treated as control tests with no PAFs or welds. Each connection type was also tested with PAFs spaced at 12 in. along the centerline of the top flange (Specimens 2, 4, and 11). This is typical for deck attachments to the top flange or partition attachments to the underside of the bottom flange. The remaining RBS specimens (Specimens 5 and 8) were tested using four puddle welds spaced at 12 in. as was done with the PAFs. Currently, puddle welds are the only type of deck attachment method allowed in the protected zone so this comparison is a baseline against currently allowed construction.

Three specimens (Specimens 6, 9, and 12) were tested using a grid of PAFs on both flanges. The grid on each flange of Specimen 6 included 14 rows of fasteners spaced at 2 in. with the first row occurring 2 in. from the surface of the endplate. Each row contained three PAFs with one occurring along the flange centerline and the others spaced 2.5 in. away from the centerline. This means the outer two fasteners in each row were centered 1 in. from the edge of the flange. Specimen 12 similarly included 14 rows of fasteners at 2 in. spacing. Each row contained five PAF at 2.5 in. spacing across the flange width. For Specimen 9, the outer rows of PAFs were arranged such that they followed the curvature of the RBS cuts and were located 1 in. from the

edge of the flange. Both Specimen 9 and Specimen 12 incorporated a grid of PAFs on one side of the web as depicted in Figure 2.8.

PAF grid tests were intended to create a worst-case scenario. While in practice PAFs wouldn't be applied in a grid, it is possible that a PAF could be used in any of the locations present in the grid. Since local buckles may occur at slightly different locations from one test to another, the PAF grid ensured that there would be a PAF near the peak of the local buckles for a particular specimen. PAFs were spaced sufficiently far apart so as to minimize their interaction with each other. The extent of the local strain concentrations were analyzed using FEM models to select the 2 in. spacing, although the results are not presented here. A single PAF grid test can represent a multitude of individual tests in which a PAF is present at any of the given locations. Combining all the PAF into a grid on one specimen however is an extreme condition that does not represent common practice in the field.

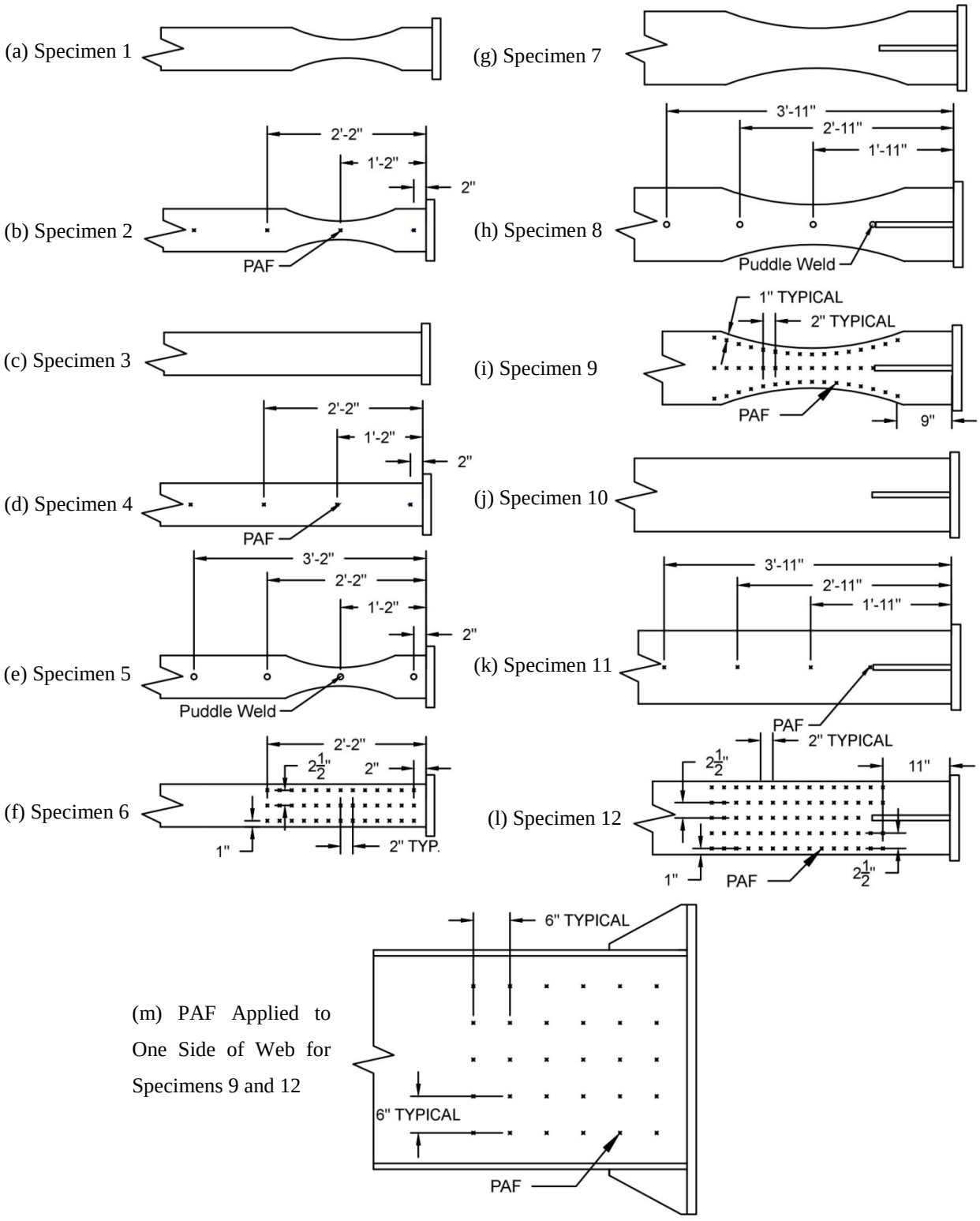

Figure 2.8 – Layout of Fasteners for the 12 Specimens

The PAFs used in this study were Hilti X-ENP-19 L15 Nails. The PAFs were driven into test specimens with a 0.27 caliber Hilti DX 76 powder-actuated tool. Three criteria were used to assess acceptable PAF application included a penetration check with a power adjustment guide where the depth must not be too deep or too shallow, as indicated by the pointer landing within the vertical range of a green bar. The second installation check was verifying the existence of a piston ring mark from the tool piston on the PAF top washer, a C-shaped ring on the washer. Lastly, the two washers needed to be in contact around the entire circumference of both washers. All three PAF application checks are shown in Figure 2.9. Virtually all of the PAF satisfied the three installation criteria, but installed PAF that did not meet all three criteria were documented in Watkins (2013).

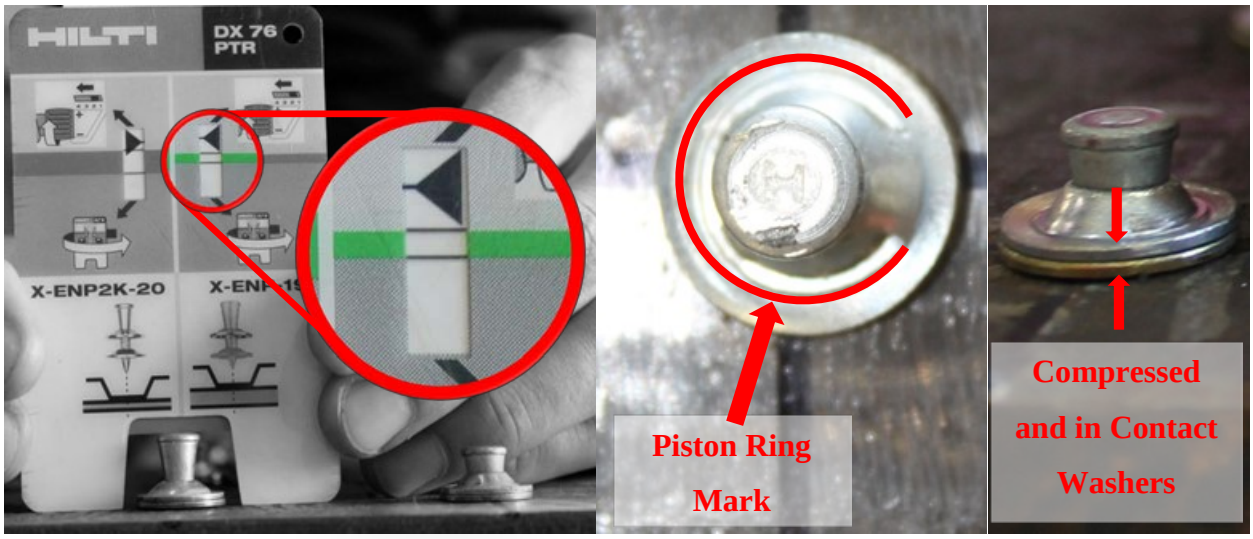

Figure 2.9 - PAF Installation Checks Including from Left to Right:
Penetration (Insufficient as Shown), Piston Mark, and Compressed Washers in Contact

For specimens with puddle welds, the welds were applied by a qualified lab technician with substantial previous experience making puddle weld deck attachments and is AWS certified for puddle welding as well as certified for GMAW and SMAW welding. The puddle welds were ¾" diameter and made through small square standard 20 gage metal decking with typical field puddle welds as shown in Figure 2.10. After welding, the extra decking metal was trimmed off using a torch such that the specimen flange surface was exposed around the weld. As shown in the test matrix (Table 2.2), two RBS specimens included puddle welds in the same pattern as two of the RBS specimens with PAF for comparison.

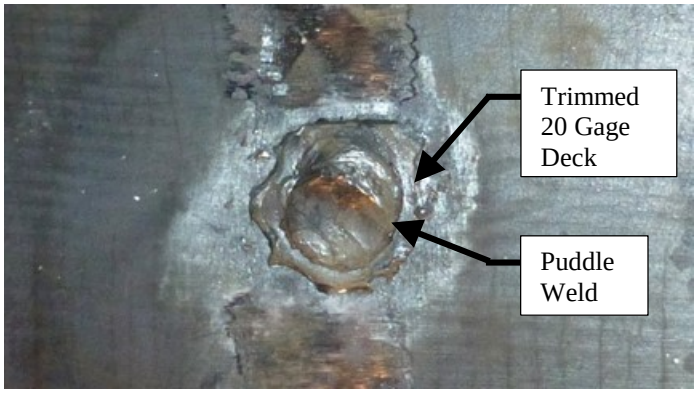

Figure 2.10 – Typical Puddle Weld

2.3 Instrumentation Plan

A program written in the National Instruments Software LabView was used for test control and data acquisition. Instrumentation was provided to record displacements and rotation in the column, deformation in the connection region, displacements in the beam, strain distributions in the beam flanges, and the force applied to the specimen. The instrumentation plan is shown in Figure 2.11. The load applied to the specimen was recorded with a load cell built into the actuator.

The loading protocol from AISC 341 (AISC 2010a) is intended to produce a particular pattern of story drift on the specimen, but this story drift inherently includes many sources of deformation outside of the plastic hinge region. Furthermore, the intended boundary conditions for the column are pinned at the top and bottom but in reality includes sources of reduced flexibility (e.g. partial rotational restraint of the column ends), and sources of increased flexibility (e.g. elastic deformations of the reaction frames). It is necessary to monitor the sources of deformation to ensure that the plastic hinge region undergoes an appropriate amount of inelastic deformation demand.

Several types of instrumentation were employed to record the contribution of different deformation mechanisms to story drift as shown in Figure 2.11. Nine LVDTs were utilized to

track motion of the column panel zone as well as movement of the beam endplate and rotation of the beam plastic hinge. A string potentiometer extended to the top of the test column to measure motion in the top of the column. A second string potentiometer (SP3 in Figure 2.11) mounted to the beam beyond the plastic hinge was used in the calculation of beam deflection due to elasticity (this sensor was included for Specimens 7-12). A final string potentiometer located under the beam/actuator connection was used for external feedback in the test control program. The test was controlled so that the string potentiometer under the beam at the actuator location (SP2 in Figure 2.11) followed the displacement protocol described previously. Additionally, three inclinometers measured the rotation of the column and beam near the connection. The procedure for decomposing the story drift into components and the resulting decompositions for each test are presented in Appendix B.

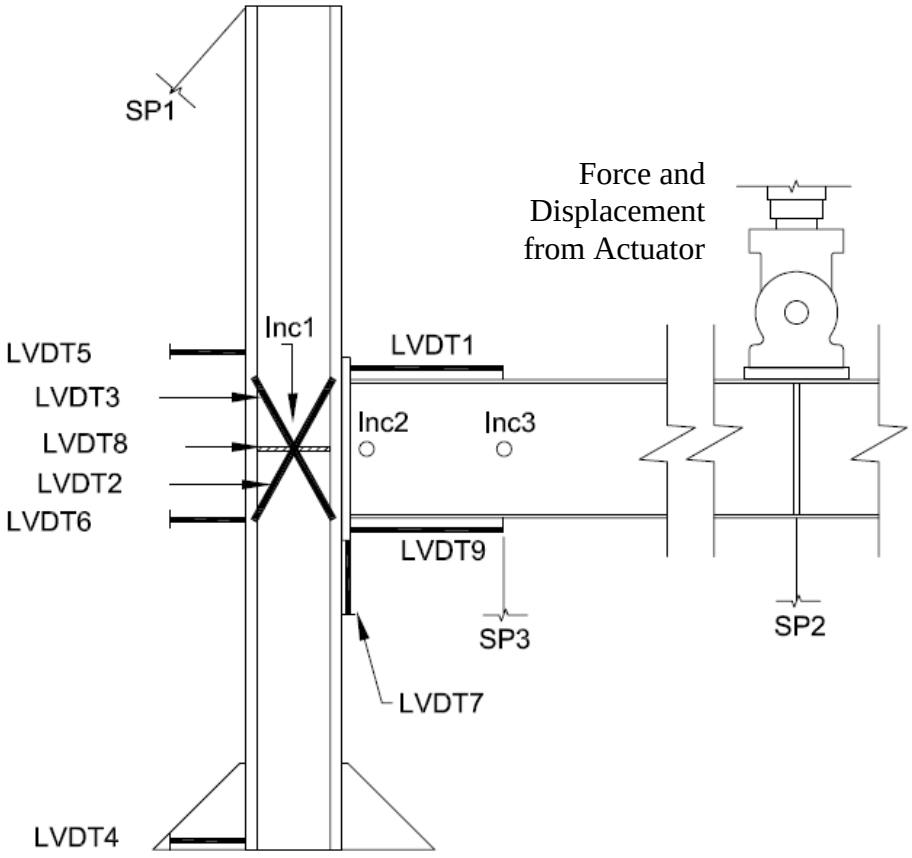

Figure 2.11 – Layout of Displacement Transducers and Load Cells (Not To Scale)

High strain rated strain gages were adhered to the top and bottom surfaces of the beam top flange in lines across the flange at the PAF locations. The strain gage locations were held constant for specimens that had puddle welds or no fasteners and are intended to provide a comparison of

strain distribution between specimens. The strain gages were Texas Measurements brand YEFLA-5-1LT gages with strain range of 10%-15% max strain. The gages were applied with Texas Measurements brand CN-Y adhesive.

Figure 2.12 and Figure 2.13 show the general placement of the strain gages for RBS and non-RBS specimens. For the W36 specimens, after finding that the effect of fasteners on the strain gradient across the flange was small, only two strain gage lines were used with the first occurring approximately 13-3/8 in. from the endplate and approximately 1/4 in. beyond the end of the endplate stiffener. The second line occurred at 23 in. from the endplate. The motivation behind these lines of strain gages is to provide "strain line" profiles at the location of the fasteners. Comparison of strain profiles between tests is conducted in a later chapter to assess strain concentrations that might occur due to the presence of PAFs or puddle welds.

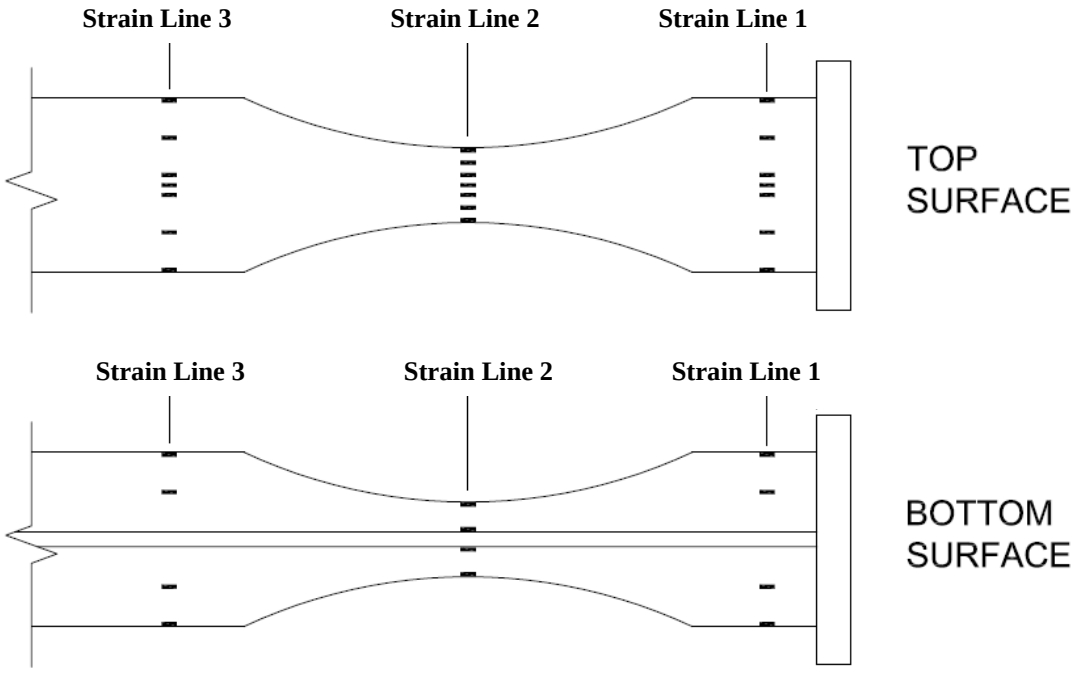

Note: For W36x150 RBS Specimens, Only Strain Line 1 and 2 Were Used

Figure 2.12 - Typical Strain Gage Layout for RBS Specimens (Top and Bottom of Top Flange)

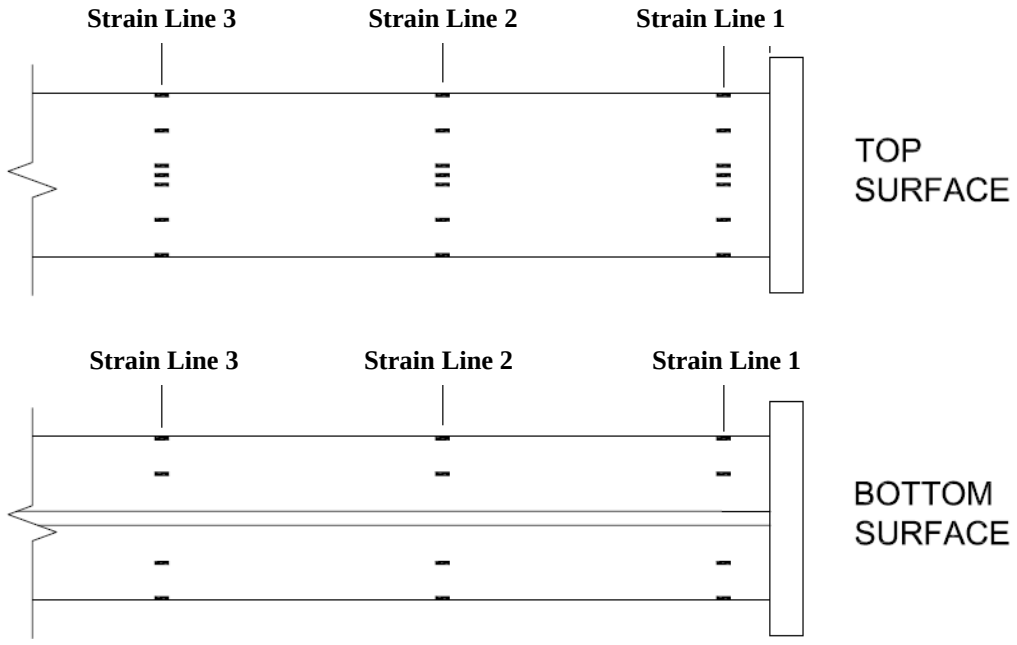

Note: For Specimens 10 and 11, Only Strain Line 1 and 2 Were Used

Figure 2.13 - Typical Strain Gage Layout for Non-RBS Specimens (Top and Bottom of Top Flange)

Additional visual data collection methods include whitewash (a lime and water mixture) painted on the beam at the protected zone to provide a visual indication of the yielding behavior of the beam. Since the full displacement protocol requires several hours of testing, timelapse videos were produced to help visualize the progression of specimen behavior. Four cameras mounted around the test setup took a fixed image every 6 seconds for the duration of the test from locations providing side, top, and angled views of the protected zone as well as a fourth wide view of the entire test setup as shown in Figure 2.14. The time stamped images also provided a visual history of the tests for any necessary correlation of significant events to corresponding data records and observations.

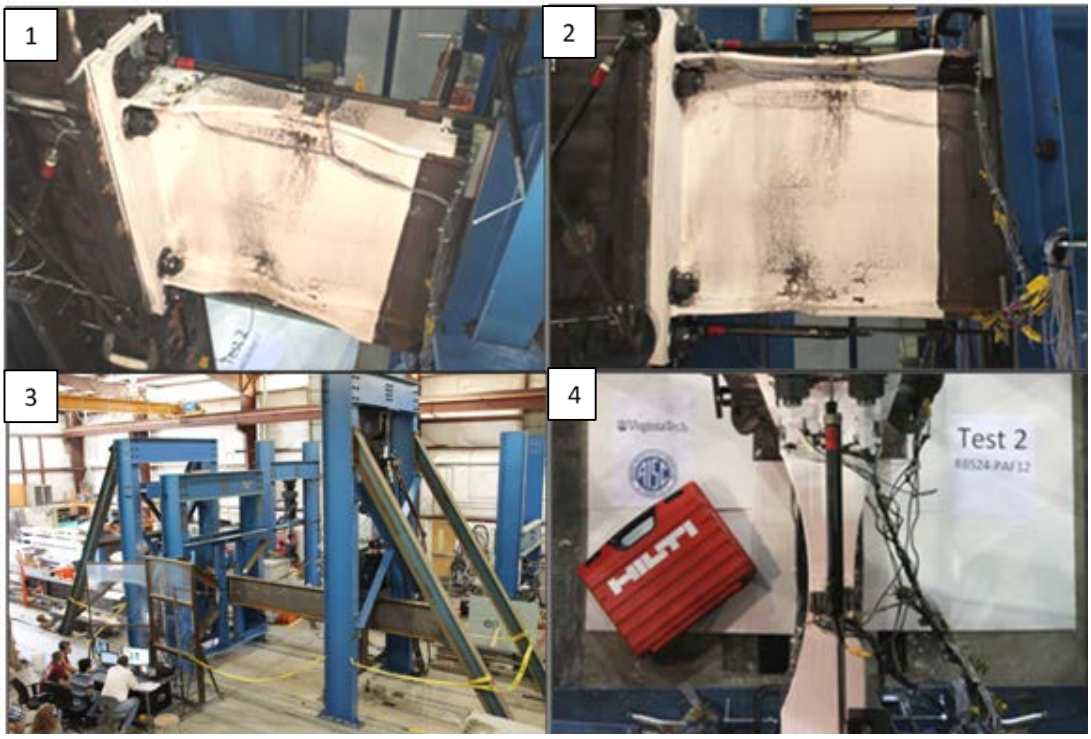

Figure 2.14 - Timelapse Camera Views: 1) Angle, 2) Side, 3) Wide, 4) Top

2.4 Tension Coupon Material Testing

All beam specimens were specified to be ASTM A992 structural steel with a minimum yield stress of 50 ksi and a minimum tensile strength of 65 ksi. The end-plate material was specified to be ASTM A572 Gr. 50 with minimum yield stress of 50 ksi and minimum tensile strength of 65 ksi.

Tension tests were performed on six coupon specimens. Three were cut from an undeformed region of the W24x62 beam specimen used for Specimens 2 and 4. The other three were cut from an undeformed region of the W36x150 specimen used for Specimens 8 and 11. All W24x62 specimens were from the same heat of steel and similarly, all W36x150 specimens were manufactured from the same heat of steel. The geometry of the coupon specimens is consistent with dimensions provided in ASTM 370-07a (ASTM 2007) for tension coupons with a total length of 18 in. and a gage length of 8 in. For all tension coupons, the specimens were cut in a longitudinal orientation from each of the top flange, bottom flange, and web according to ASTM A6/A6M-12

(ASTM 2012). Each specimen included punch marks spaced at approximately one inch along the eight inch gage length. This provides the means for measuring elongation at fracture. In addition, the average section area along the gage length prior to testing was recorded in order to calculate stress from applied force.

Recorded test data included displacement of the moving platform, applied force, and strain measured using an extensometer. Extensometer limitations only allowed direct strain readings up to 3%, at which point testing was paused and the extensometer was removed. This was done in order to prevent damage to the extensometer. Since strain hardening data beyond this point is desired, displacement recordings of the moving platform of the test machine can be used to estimate strain values after the extensometer is removed.

A specimen pseudo-length was calibrated so that the final strain is equal to the elongation measured using the punch marks. The final strain was calculated as the final extensometer strain before being removed summed with the platform displacement after the extensometer was removed divided by the specimen pseudo-length. The resulting pseudo-length of 9.5 in. was used for all tension specimens. It is noted that utilizing this pseudo-length method is approximate.

Figure 2.16 shows the stress-strain data for the three tension coupon tests cut from the W24x62 section and Figure 2.15 shows a photograph of one of the tension coupons. Solid lines represent strain data reported directly from the extensometer. Dotted lines are calculated as the platform displacement divided by the pseudo-length as described above. The single dashed line in Figure 2.17 represents extensometer data from a test in which the W36x150 top flange coupon was reloaded after previously being loaded in a test that was halted prior to reaching significant inelastic strain. The presence of a higher first yield stress during reloading is due to strain aging.

Table 2.4 shows the measured yield stress, ultimate stress, and elongations for each tension coupon. Average values for the W24x62 and W36x150 sections are also provided.

Figure 2.15: Photograph of Tension Coupon

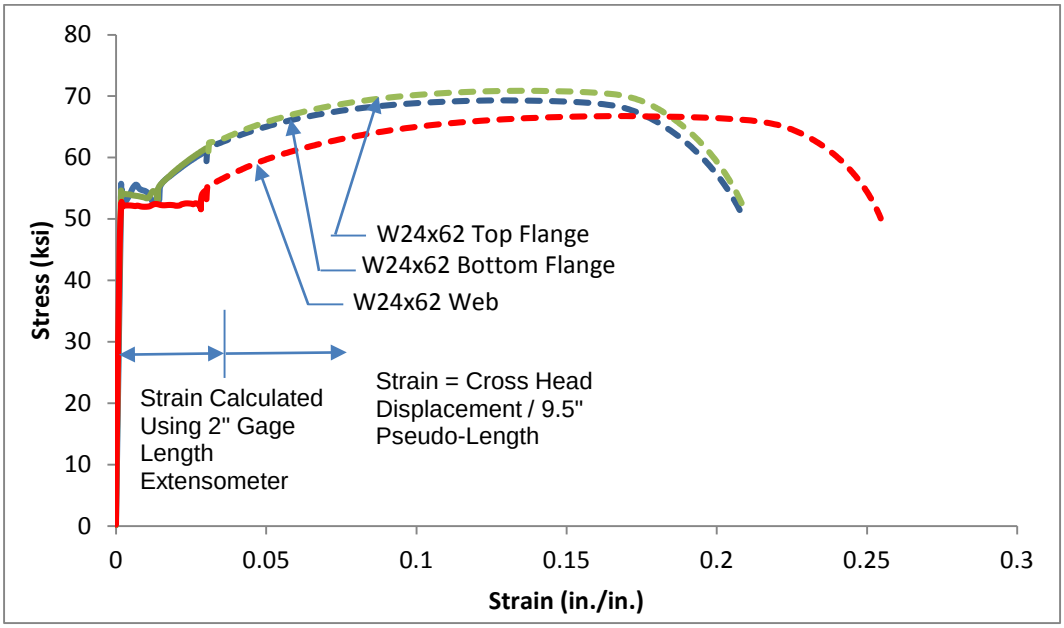

Figure 2.16: Tension Coupon Test Data for W24x62

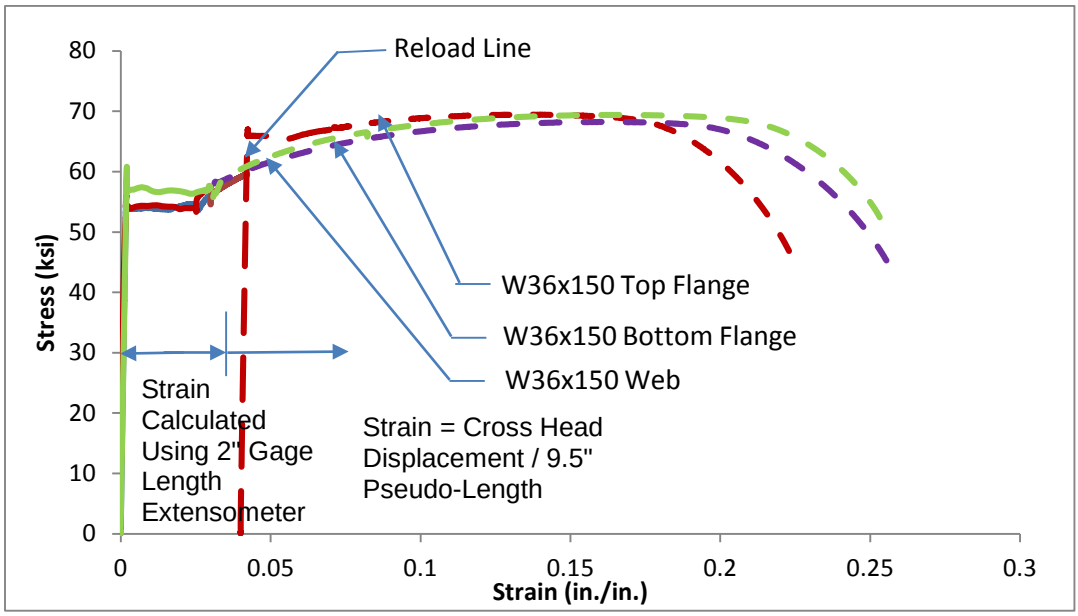

Figure 2.17: Tension Coupon Test Data for W36x150

Table 2.4 – Measured Yield Stress, Ultimate Stress, and Elongation for Tension Coupons

		Yield Stress, F_y (ksi)	Ultimate Stress, F_u (ksi)	Elongation at Fracture Using Punch Marks (%)
W24x62	Top Flange	52.6	70.9	22
	Bottom Flange	52.9	69.3	27
	Web	52.2	66.8	23
	Average	52.6	69.0	24
W36x150	Top Flange	52.8	69.5	30
	Bottom Flange	54.2	68.2	30
	Web	54.6	69.3	29
	Average	53.9	69.0	30

CHAPTER 3 TEST RESULTS

This chapter includes results for all twelve full-scale tests. The behavior of the specimens will be examined in four groups: W24x62 specimens with RBS (Specimens 1, 2, and 5), W24x62 specimens without RBS (Specimens 3, 4, and 6), W36x150 specimens with RBS (Specimens 7, 8, and 9), and W36x150 specimens without RBS (Specimens 10, 11, and 12). This chapter includes load-deformation response, description of the behavior, and analysis of the fracture surfaces. A detailed comparison between specimens is provided in Chapter 5.

Hysteretic plots presented in this report are in terms of applied moment at the face of the column and story drift. The story drift is calculated as the string potentiometer (SP2 in Figure 2.11) displacement divided by the distance between the column centerline to the actuator centerline (17.0 ft). Similarly, the applied moment at the face of the column is computed by multiplying the actuator force by the distance from the actuator to the face of the column (16.32 ft).

The SMRF qualification criteria states that the specimen must sustain a moment capacity at the face of the column that is at least 80% of the nominal plastic moment capacity during one complete cycle at 4% story drift. The nominal plastic moment capacity, M_p, is computed with nominal yield stress of F_y=50 ksi and nominal plastic section modulus, Z_x. The nominal plastic moment capacities and qualification moment capacities are given in Table 3.1. All specimens satisfied the qualification criteria for SMRF.

Table 3.1 - Beam Specimen Design Moment Capacities and Qualifying Moment Capacities

Specimen Type	Specimen Numbers	M_p (kip-ft)	0.8*M_p (kip-ft)
RBS24	1, 2, 5	410	328
W24	3, 4, 6	638	510
RBS36	7, 8, 9	1668	1335
W36	10, 11, 12	2420	1937

3.1 Behavior of W24x62 Specimens with RBS

All W24x62 specimens with RBS satisfied the qualification criteria. Furthermore, they all completed at least one full cycle of 4.7% story drift before experiencing significant moment capacity loss due to fracture. The progression of limit states was similar for all specimens in this group starting with significant yielding in the extreme fibers at the reduced section, spread of plasticity, local buckling of the flanges in association with out-of-plane buckling of the web, crack initiation typically at the flange tips on the inside face of the local buckle, and fracture propagation through an entire flange. All specimens experienced some amount of fracturing at the minimum flange section. In all cases, the fractures initiated at the edge of the flange on the inside of a local buckle and propagated toward the center of the beam flange.

Specimen 1: W24x62 with RBS and No Fasteners

Specimen 1 served as the control test for the W24x62 specimens with RBS connections. No PAFs or puddle welds were present on the specimen. Figure 3.1 shows the load-deformation behavior for Specimen 1. The specimen passed qualification, and furthermore completed two cycles of 4% story drift while maintaining a moment greater than 80% of the nominal plastic moment capacity computed with nominal yield stress. Pictures of the specimen before and after testing are shown in Figure 3.2 and Figure 3.3.

During the subsequent cycles of 4.7% story drift, cracks formed at the flange tips at the RBS location. During the second cycle at 4.7% story drift, a ductile tear propagating from the tip of the bottom flange toward the middle of the flange, as shown in Figure 3.4, caused significant loss in strength. The propagation of the tear was not sudden, but instead a gradual, ductile process. Crack initiation was noted in several other locations typically initiating on the inside surface of local buckles at the flange tips where the greatest inelastic compressive strains due to local buckling had occurred.

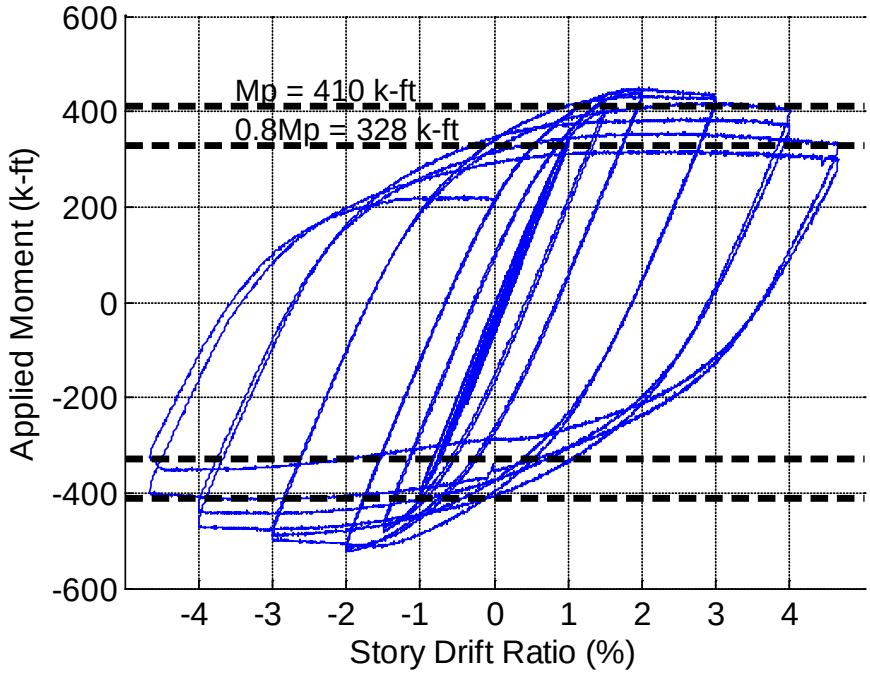

Figure 3.1 - Load-Deformation Response for Specimen 1 (W24x62 with RBS but No Fasteners)

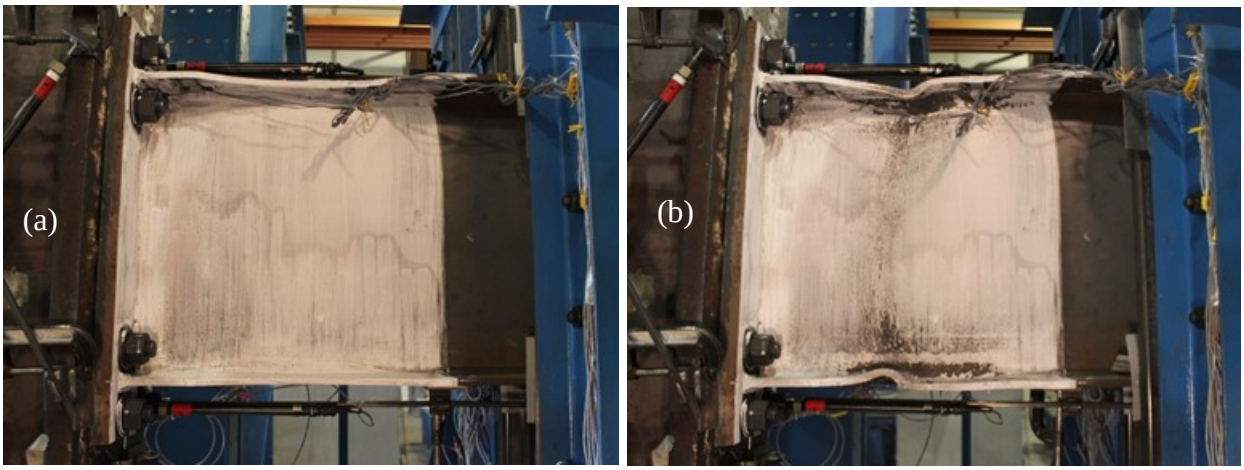

Figure 3.2 – Side View Pictures of Specimen 1 (W24x62 with RBS but No Fasteners)
at (a) Start of Test, and (b) Final Deformation

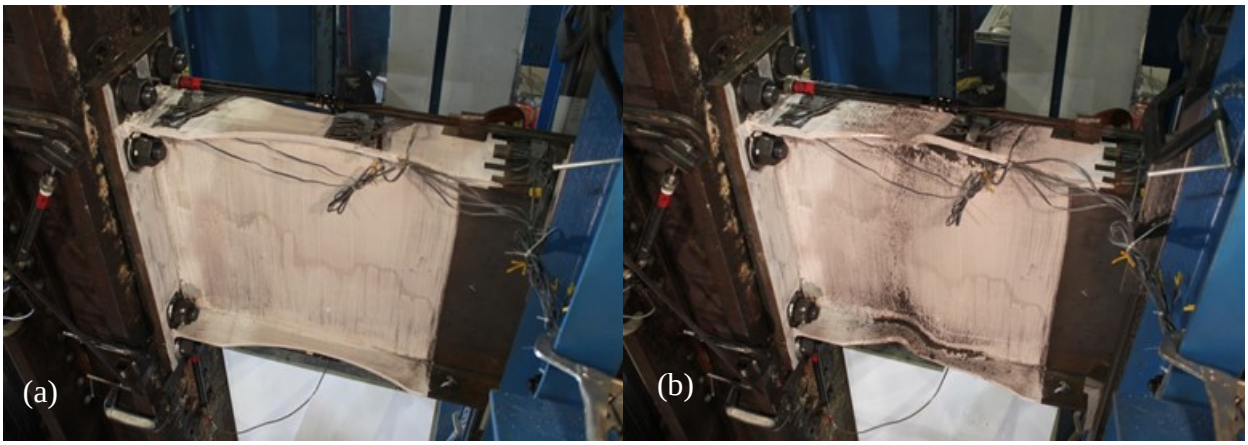

Figure 3.3 – Angled View Pictures of Specimen 1 (W24x62 with RBS but No Fasteners) at (a) Start of Test, and (b) Final Deformation

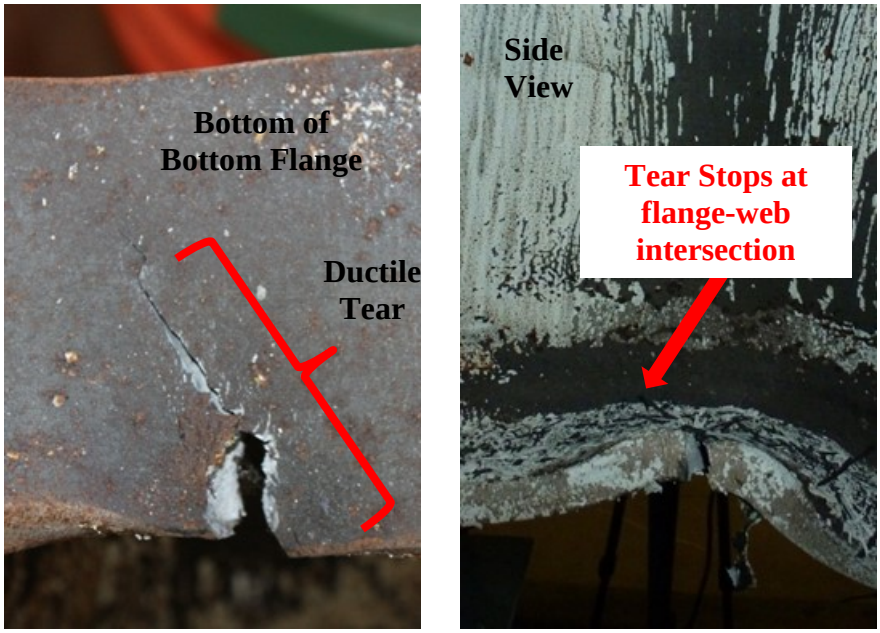

Figure 3.4 - Bottom Flange Ductile Tear in Specimen 1 (W24x62 with RBS but No Fasteners)

Crack initiation occurred at the middle of the reduced beam section at different locations of the bottom flange tip during the second cycle at 4.7% story drift. There were visible notches and internal cracking at the flange tip, and the edge of the flange exhibited multiple failure origins at both sides of the bottom flange as shown in Figure 3.5. It is expected that these cracks were associated with large compressive plastic deformation, since they are at the compression side of the flange local buckle. Also, the crack initiation at the flange tips can be related to minor surface scratches caused by cutting and handling the RBS before testing.

Although fracture initiation occurred at multiple locations at the bottom flange, fracture propagated primarily from one side leading to brittle fracture through half of the flange width and stopping at the web as shown in Figure 3.6.

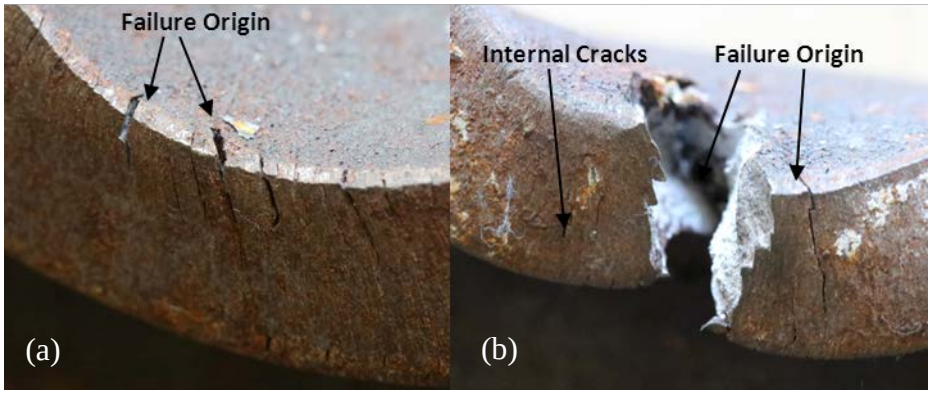

Figure 3.5 – Crack Initiation at Two Different Locations on Both Sides of the Bottom Flange. Crack and Fracture Initiation (a) and Crack Initiation at Other Side of the Flange (b)

Figure 3.6 – Flange Surface of Fracture Propagation

Specimen 2: W24x62 with RBS and PAFs at 12 in.

Specimen 2 varied from Specimen 1 in the inclusion of four PAFs spaced at 12 in. along the center of the top flange. Figure 3.7 shows the load-deformation behavior of Specimen 2 which also demonstrates that the qualification criteria was satisfied. Pictures of the specimen before testing and prior to fracture are shown in Figure 3.8 and Figure 3.9.

During the second cycle of 4.7% story drift, a brittle fracture occurred through the top flange and through approximately 6 in. of the web. The fracture occurred at the location of the second PAF which was spaced 14 in. from the endplate, in line with the minimum flange width at the RBS cuts. The fracture is shown in Figure 3.10.

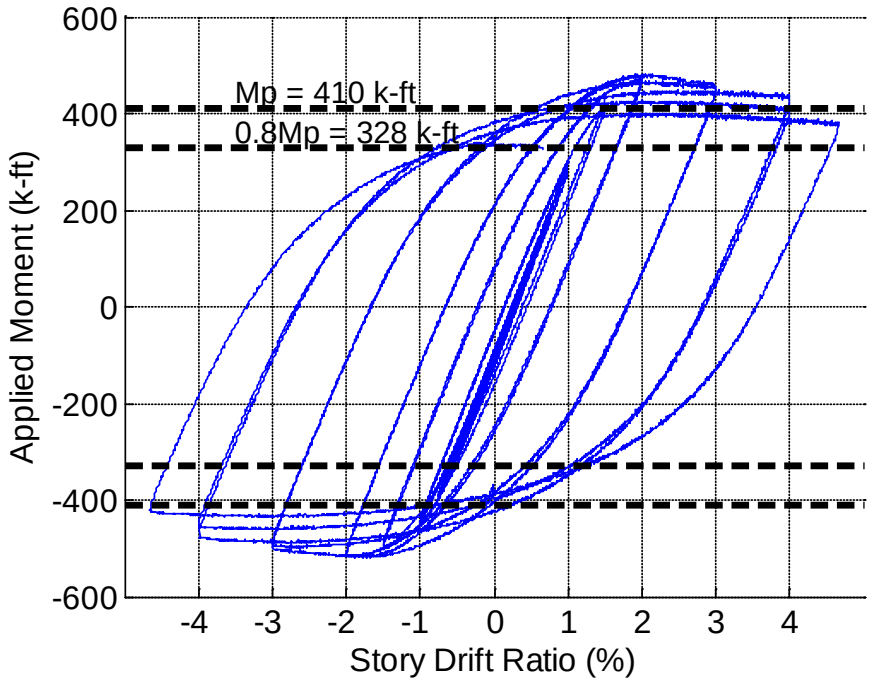

Figure 3.7 - Load Deformation Response for Specimen 2 (W24x62 with RBS and PAF at 12 in.)

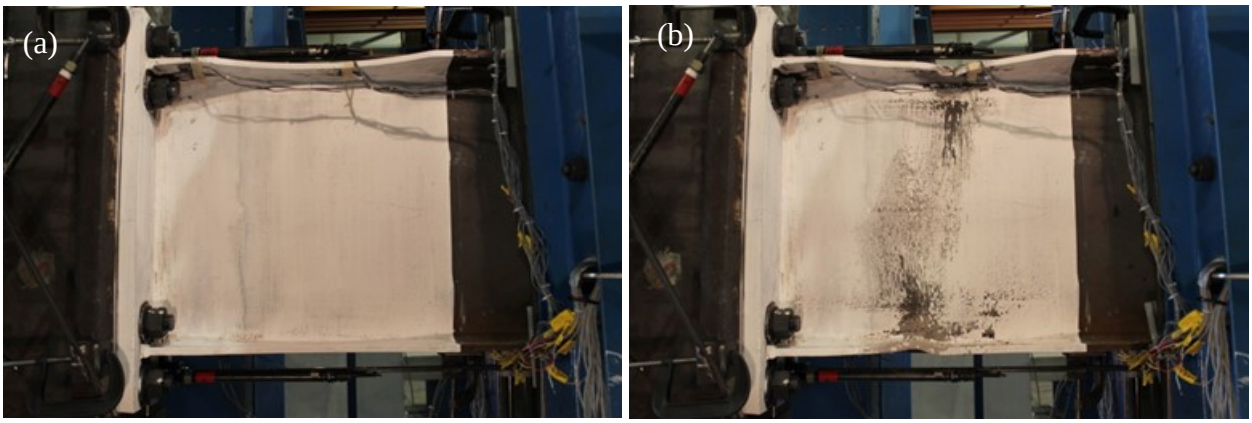

Figure 3.8 –Side View Pictures of Specimen 2 (W24x62 with RBS and PAF at 12 in.)
at (a) Start of Test, and (b) Prior to Fracture

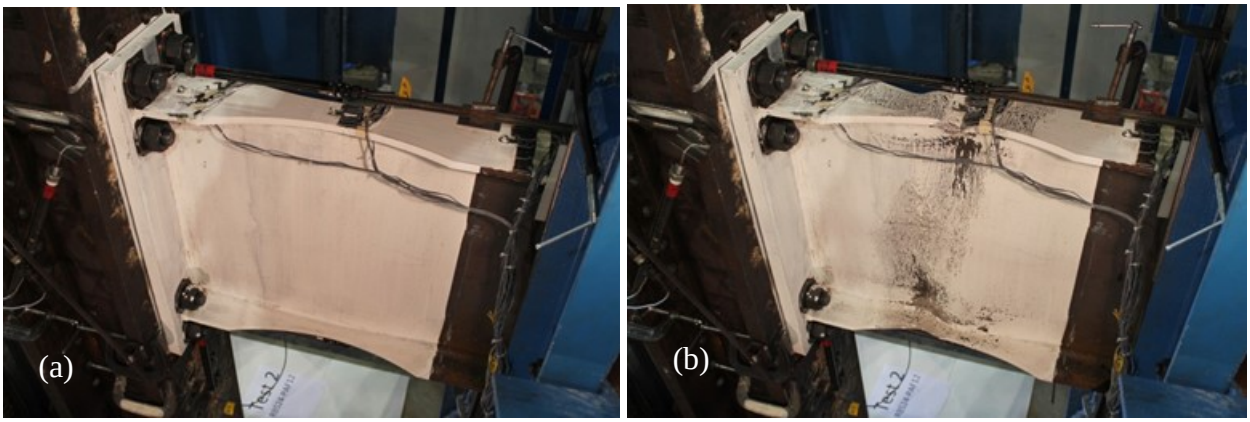

Figure 3.9 - Angled View Pictures of Specimen 2 (W24x62 with RBS and PAF at 12 in.)
at (a) Start of Test, and (b) Prior to Fracture

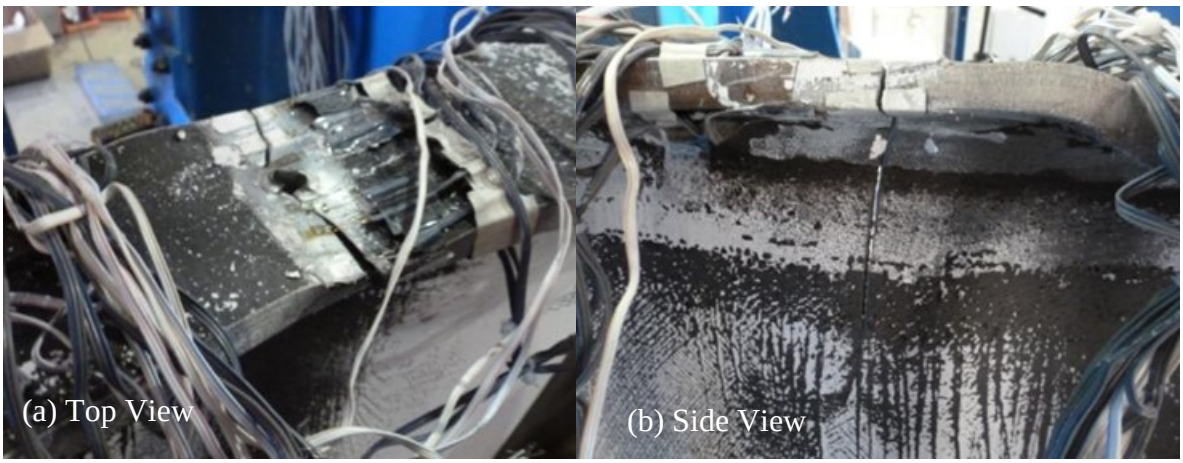

Figure 3.10 – Fracture of the Flange and Web in Specimen 2 (W24x62 with RBS and PAF at 12 in.)

The fracture surface was analyzed to determine the location of crack initiation, direction of fracture propagation and the nature of the fracture process. Crack initiation occurred at the center of the reduced beam section at one side of the flange. There were visible notches and internal cracking at the flange tip. It is expected that these defects were related to surface scratches caused by cutting and handling the RBS before testing since they were observed only at one side of the top flange. The other side of the top flange did not show signs of notches and internal defects. The edge of the flange exhibited multiple failure origins as shown in Figure 3.11. This can also be illustrated by the smooth shiny texture at the tip of the fractured flange as shown in Figure 3.12 and Figure 3.13. The smooth shiny texture is suspected to be due to the rubbing of the crack during cyclic loading combined with a slow crack growth.

Non-uniform fatigue striations with smooth shiny texture were observed to be related to the last five cycles of the fatigue crack propagation before failure. The fatigue striations are numbered in Figure 3.12 and Figure 3.14 based on their sequence. The first striation, shown in Figure 3.13, had a different texture from the next four striations associated with a ductile overload fracture mode. The increase in flange thickness at the fillet caused more rubbing during cycles with local flange buckling, leading to the visual striations as shown in Figure 3.14.

Penetration of the PAF caused plastic displacement of the base material during installation. When the crack reached the plastically deformed area around the PAF, the section ruptured. The fracture mode was brittle overload. This type of failure occurs by rapid crack propagation with less expenditure of energy than in ductile fractures and without appreciable gross plastic deformations. The brittle overload fracture showed chevron marks pointing back to the fracture origin with coarse texture which can be seen in Figure 3.14b. Also, partial shear lips were observed on the edge where the brittle overload occurred and this shows that there was some ductility.

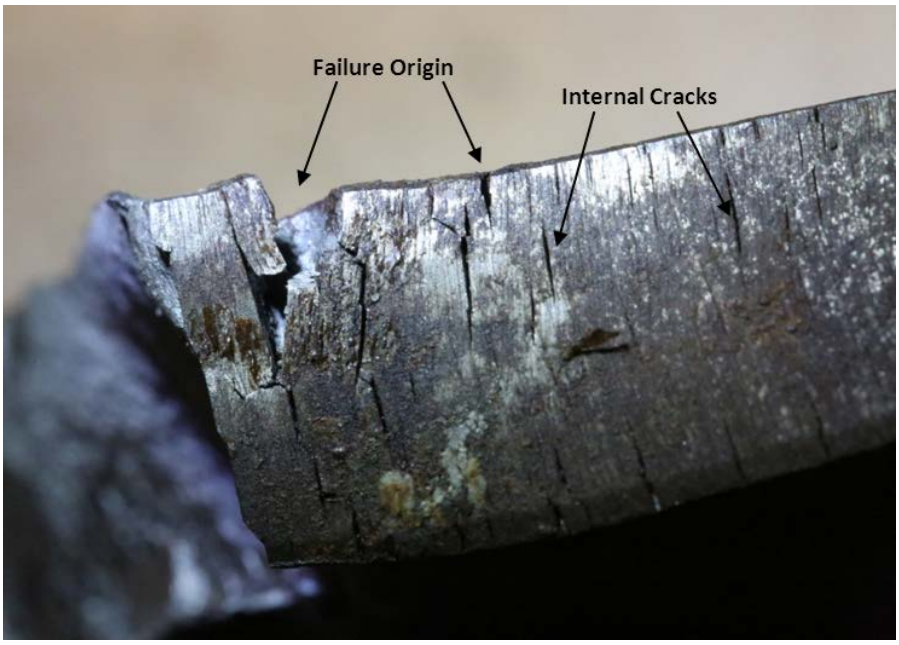

Figure 3.11 – Failure Origin in the Top and Bottom Side of the Top Flange with Some Internal Cracks, This Was Noticed Only on One Side of the Top Flange

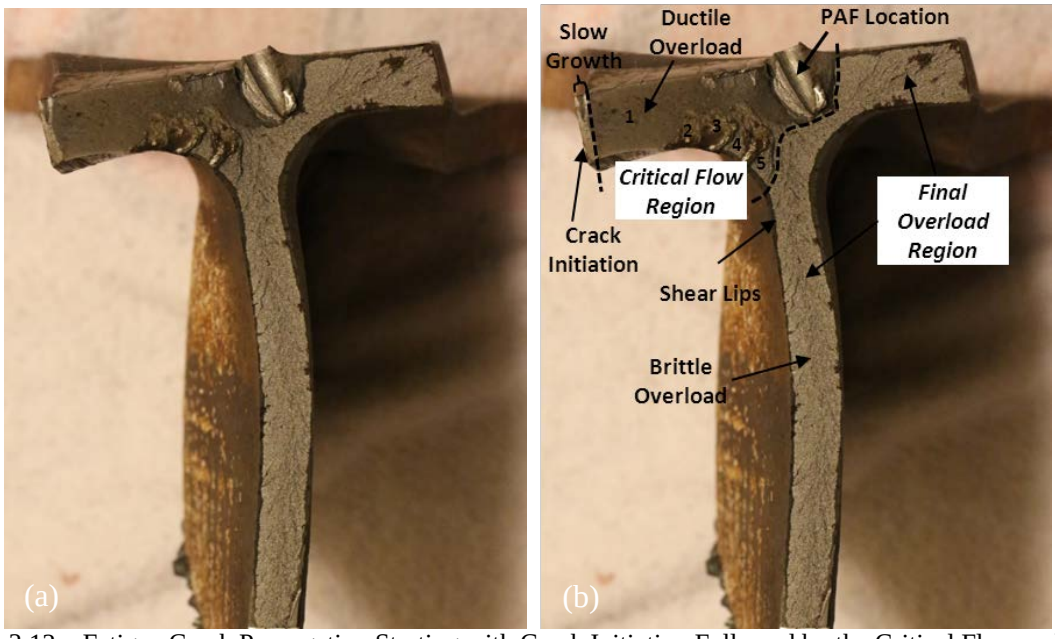

Figure 3.12 – Fatigue Crack Propagation Starting with Crack Initiation Followed by the Critical Flow and Final Overload Regions

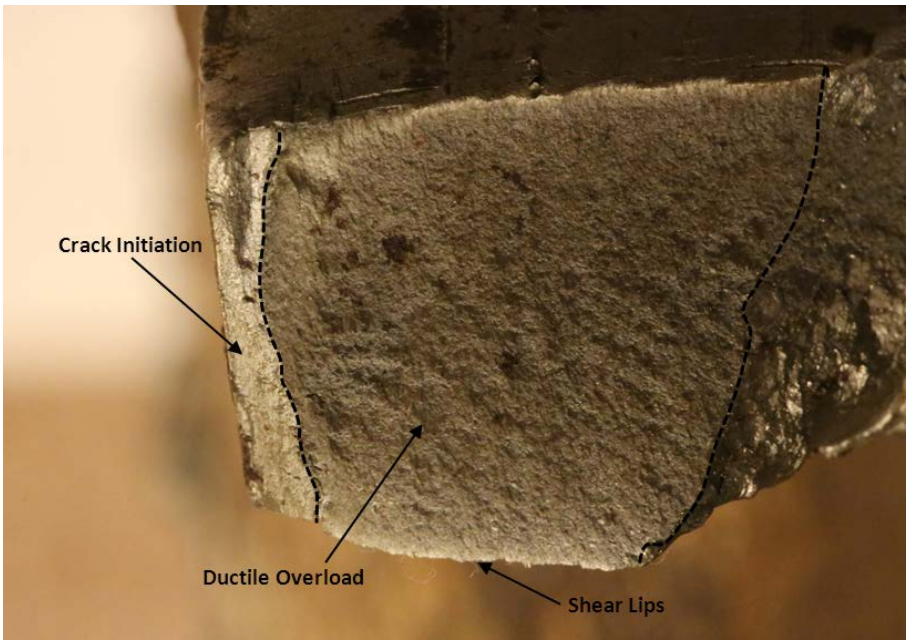

Figure 3.13 – Close-Up of Crack Initiation and Ductile Overload Location within the Critical Flow Region, Which Shows Two Different Surface Textures and the Striations

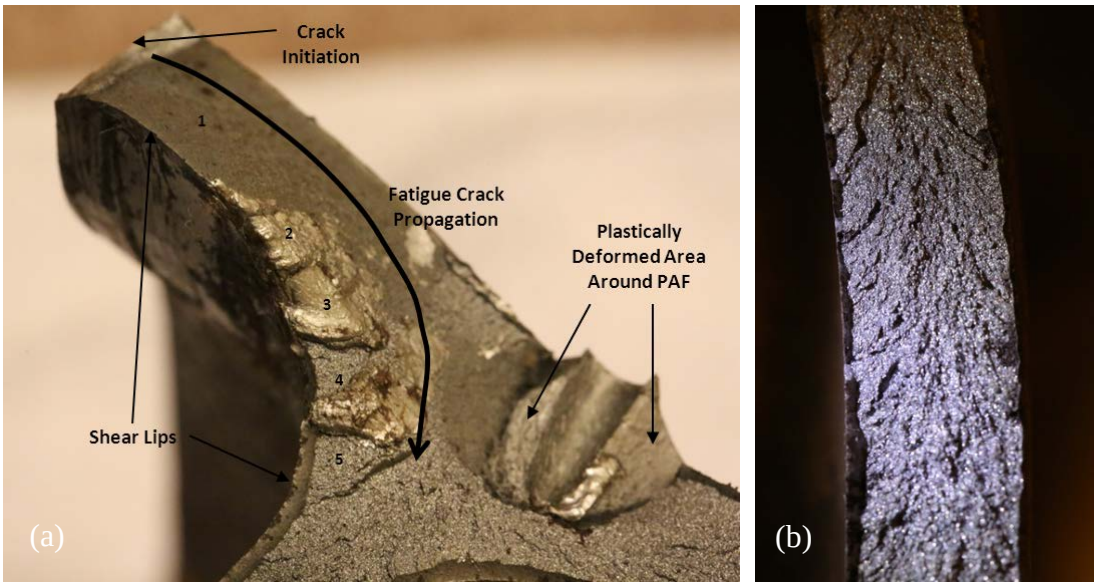

Figure 3.14 – Close-Up of Striation Locations and Fatigue Crack Propagation (a) and Chevron Markings at the Web Pointing Back to the Fracture Origin Due to the Brittle Overload Fracture Mode (b)

Specimen 5: W24x62 with RBS and Puddle Welds at 12 in.

Specimen 5 included puddle welds on the top flange at 12 in. spacing. Figure 3.15 shows the load-deformation behavior for Specimen 5. Figure 3.15 shows that the qualification criteria was satisfied. Pictures of the specimen before testing and prior to fracture are shown in Figure 3.16 and Figure 3.17.

During the third full cycle of 4.7% story drift, a brittle fracture of the bottom flange and several inches of the adjacent web occurred. The fracture occurred in the same fashion as that of Specimen 2 in which the brittle fracture occurred after the bottom flange underwent the half cycle in compression and was beginning to be pulled into tension. Apart from the fracture, cracks were observed in the flange tips at the inner surface of local buckles as occurred with Specimens 1 and 2. The fracture is shown in Figure 3.18.

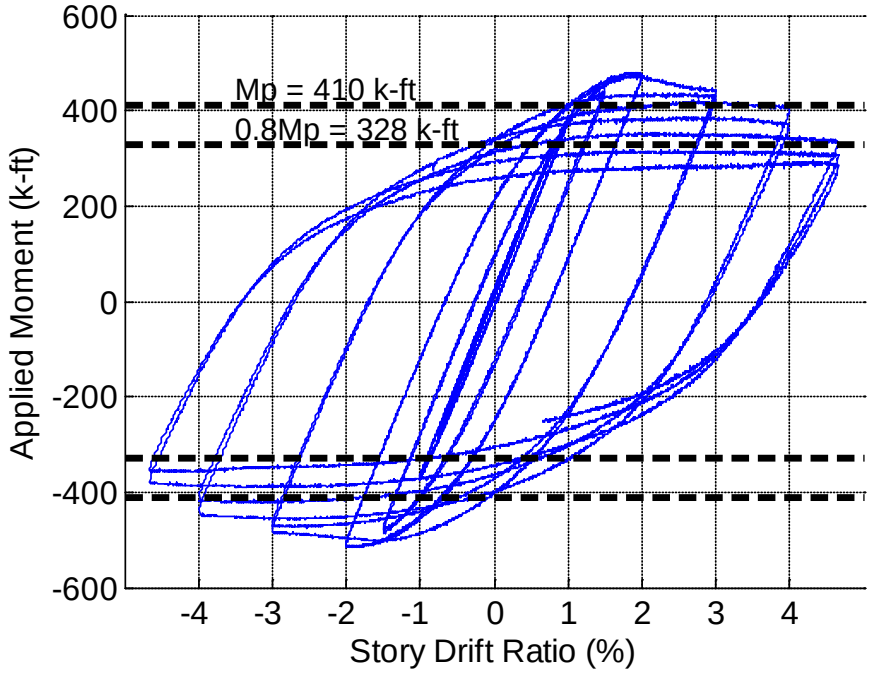

Figure 3.15 – Load-Deformation Response for Specimen 5 (W24x62 with RBS and Puddle Welds)

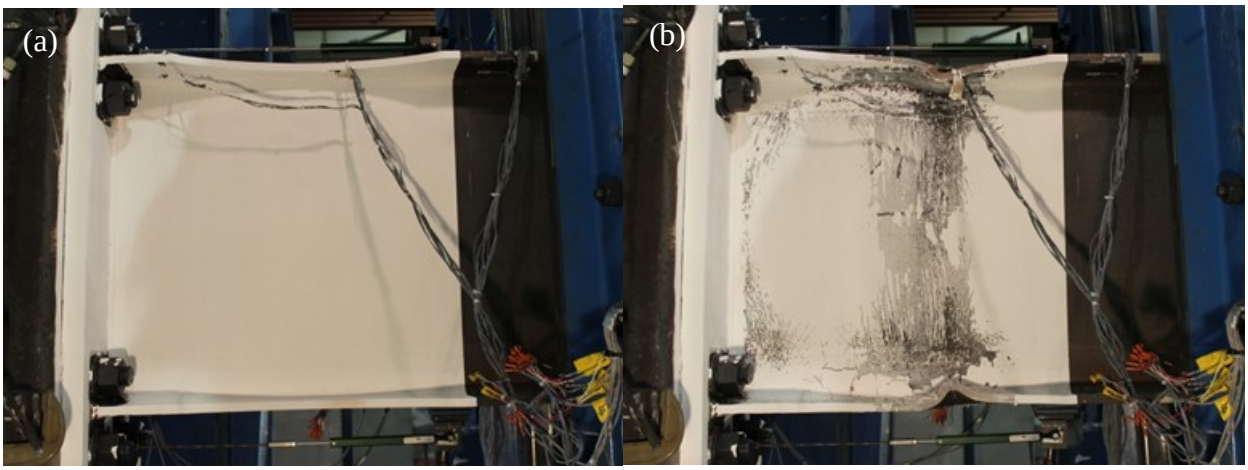

Figure 3.16 –Side View Pictures of Specimen 5 (W24x62 with RBS and Puddle Welds)
at (a) Start of Test, and (b) Prior to Fracture

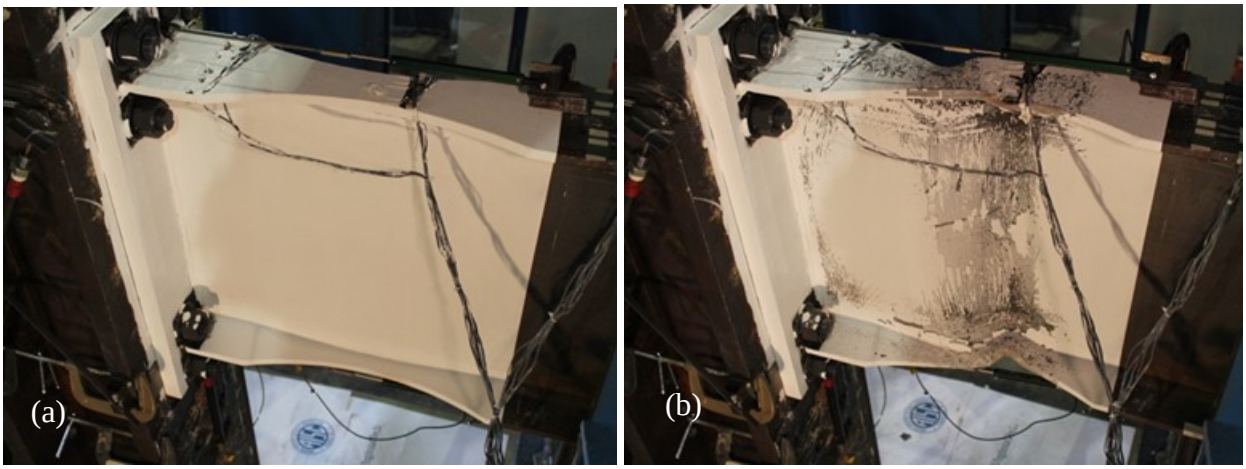

Figure 3.17 – Angled View Pictures of Specimen 5 (W24x62 with RBS and Puddle Welds)
at (a) Start of Test, and (b) Prior to Fracture

Crack initiation occurred at the center of the reduced beam section at different locations of the bottom flange away from the puddle welds during the third cycle at 4.7% story drift. There were visible notches and internal cracking at the flange tip and at the flange surface near the flange tip, and the edge of the flange exhibited multiple failure origins as shown in Figure 3.19. It is expected that these cracks were associated with the compressive plastic deformation, since they are at the compression side of the flange local buckle. Another factor for the crack initiation at the flange tips can be related to surface scratches caused by cutting and handling the RBS before testing since they were observed only at one side of the bottom flange.

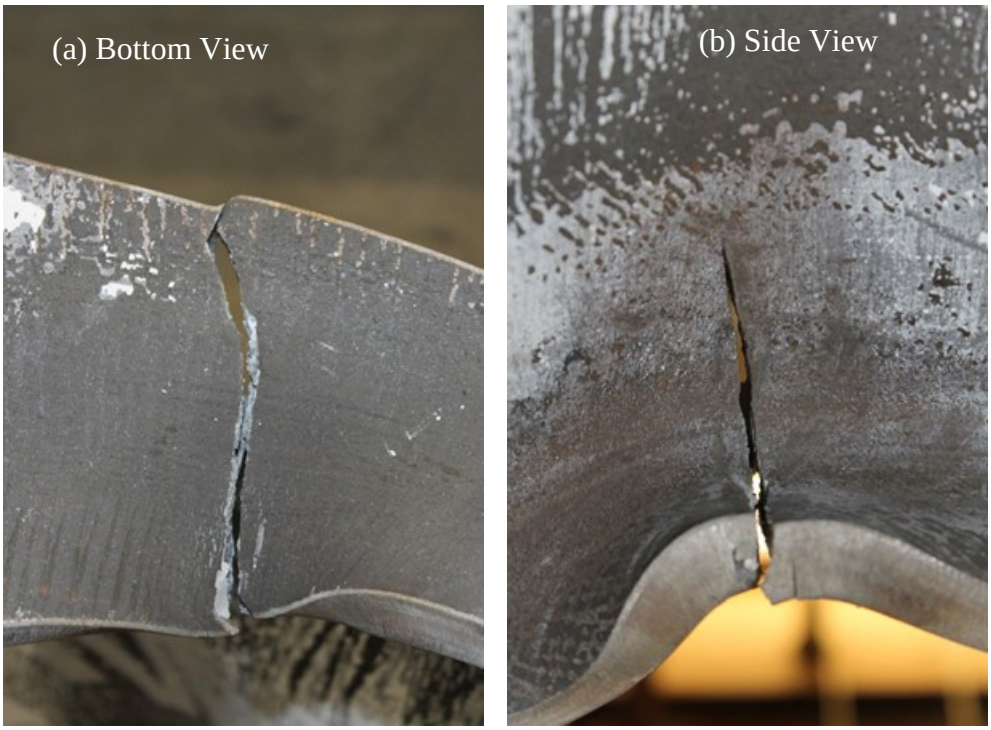

Figure 3.18 – Fracture of the Bottom Flange and Web in Specimen 5 (W24x62 with RBS and Puddle Welds)

The other side of the bottom flange did not show significant signs of external notches and crack initiation at the flange tips and did not show any sign of visible notches or internal cracking at the top flange as the other side. There were signs of smooth shiny texture at the tip of the fractured flange as shown in Figure 3.20. The smooth shiny texture is suspected to be due to the rubbing of the crack during cyclic loading combined with a slow crack growth. Non-uniform fatigue striations with smooth shiny texture were observed to be related to the last two cycles of the fatigue crack propagation before failure. The fatigue striations are numbered in Figure 3.20 and Figure 3.21 based on their sequence.

The fracture mode was brittle overload which initiated as shown in Figure 3.20 and Figure 3.21. This type of failure occurs by rapid crack propagation with less expenditure of energy than in ductile fractures and without appreciable gross plastic deformations. The brittle overload fracture showed chevron marks pointing back to the fracture origin with coarse texture which can be seen in Figure 3.20 and Figure 3.21. Also, partial shear lips were observed on the edge where the brittle overload occurred and this shows that there was some ductility.

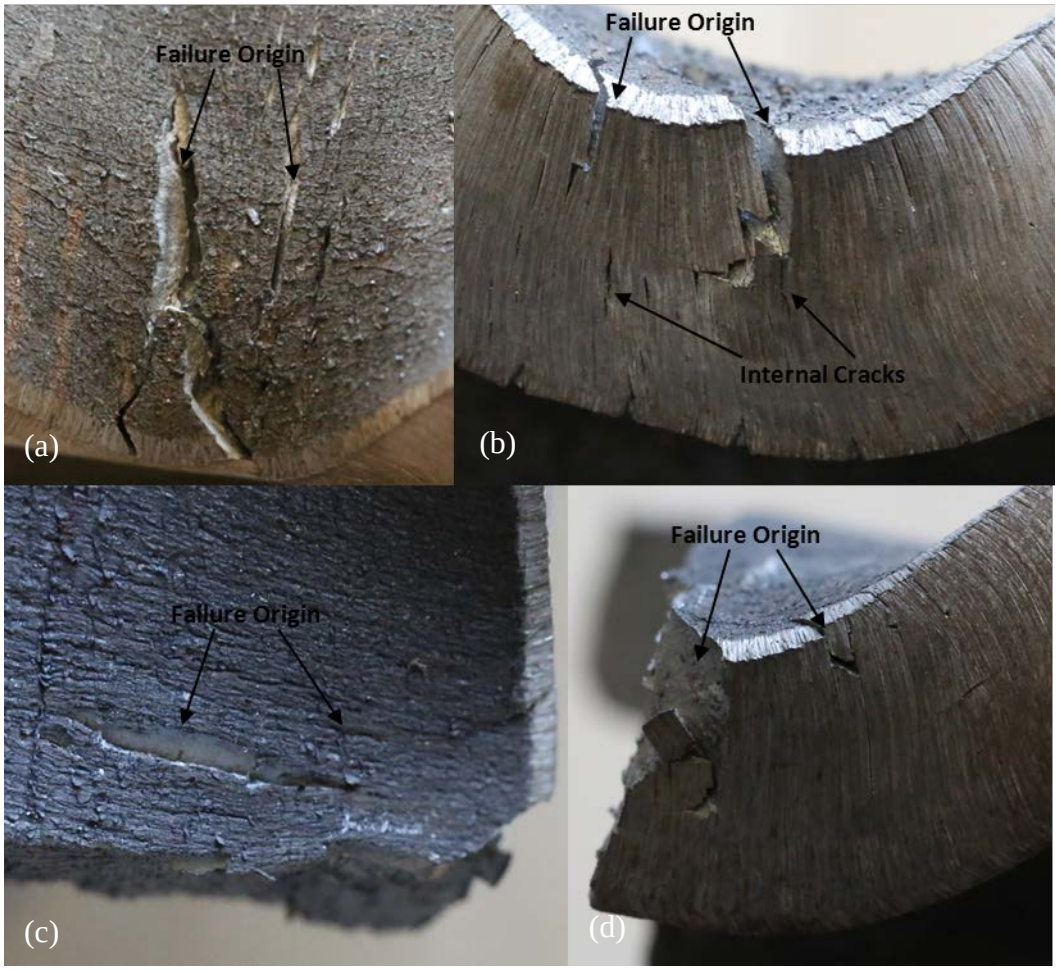

Figure 3.19 – Visible Notches and Internal Cracking at the Flange Tip and at the Flange Surface near the Flange Tip at Two Different Locations. (a) Surface View (b) and Side View of the Bottom Flange with Crack Initiation. (c) Surface View (d) and Side View of the Bottom Flange near the Fractured Area.

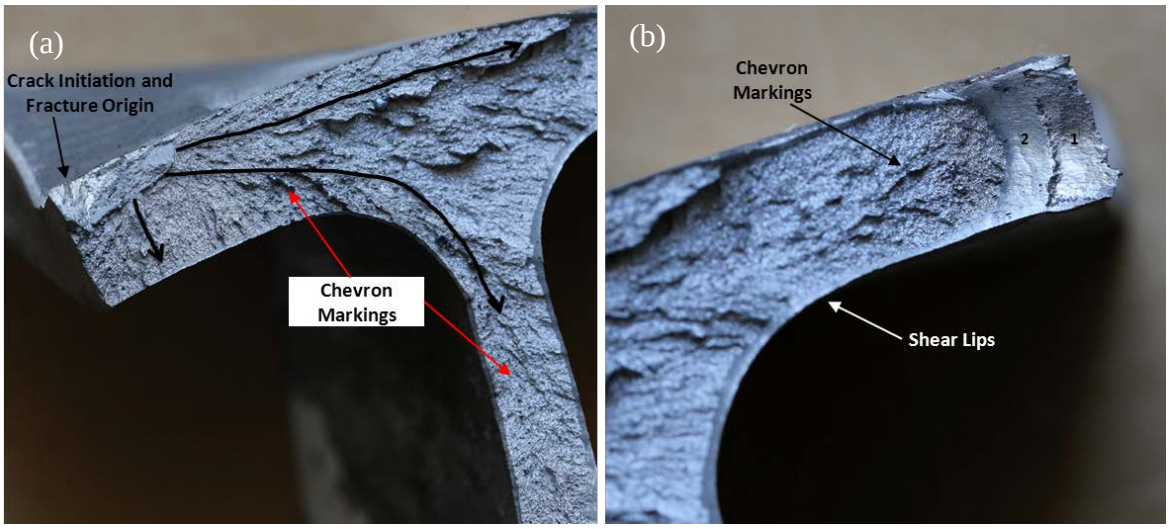

Figure 3.20 – Close-Up of Crack Initiation and Fracture Origin with Chevron Marking Pointing Back to the Fracture Origin Due to the Brittle Overload Fracture Mode (a) and Close-Up of Striation Locations at the other Side with Chevron Markings Pointing Back to the Fracture Origin (b)

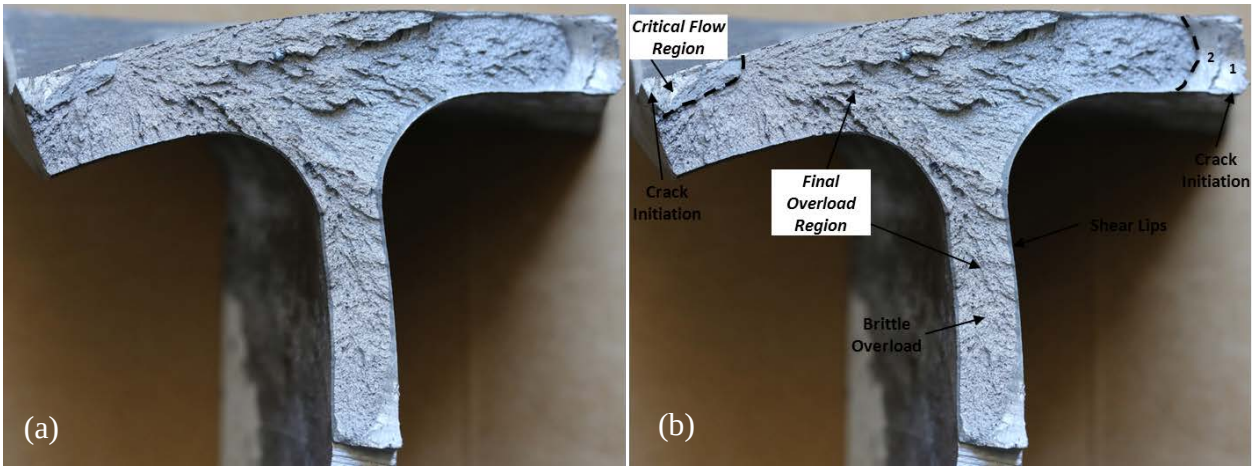

Figure 3.21 – Fatigue Crack Propagation Starting with Crack Initiation at Two Locations Followed by the Critical Flow and Final Overload Regions. Unmodified Photograph (a) and Labeled Photograph (b)

3.2 Behavior of Non-RBS W24x62 Specimens

All Non-RBS W24x62 specimens satisfied the qualification criteria. The progression of limit states was similar for all specimens in this group starting with significant yielding in the extreme fibers near the endplate connection, spread of plasticity, and local buckling of the flanges in association with out-of-plane buckling of the web. None of the specimens experienced

significant fractures even after being subjected to multiple cycles at 4.7% story drift. As discussed below, Specimen 6 with a grid of PAFs experienced minor crack initiation around several PAFs. However, the tears were propagating so slowly that they did not significantly affect the global moment-story-drift behavior.

Specimen 3: W24x62 with No RBS and No Fasteners

Specimen 3 was a control test for W24x62 specimens with no RBS. As with Specimen 1, no PAFs or puddle welds were included on Specimen 3. The specimen provided the increased moment capacity expected of a full flange section over that of the previous RBS specimens. Figure 3.22 shows the hysteresis behavior of Specimen 3. Qualification requirements were more than met with moment capacity greater than 80% of the plastic moment capacity being maintained through both cycles at 4% story drift and 4.7% story drift.

The test was halted after two cycles of 4.7% story drift. Although there was some degradation in the strength, there were no signs of fracture. Subsequent test specimens were tested up to five cycles at a story drift of 4.7%, but testing of Specimens 3 and test 4 were halted after two cycles in part because there were no observable signs of cracking or fracture. Figure 3.23 and Figure 3.24 show pictures of the initial and final conditions of Specimen 3.

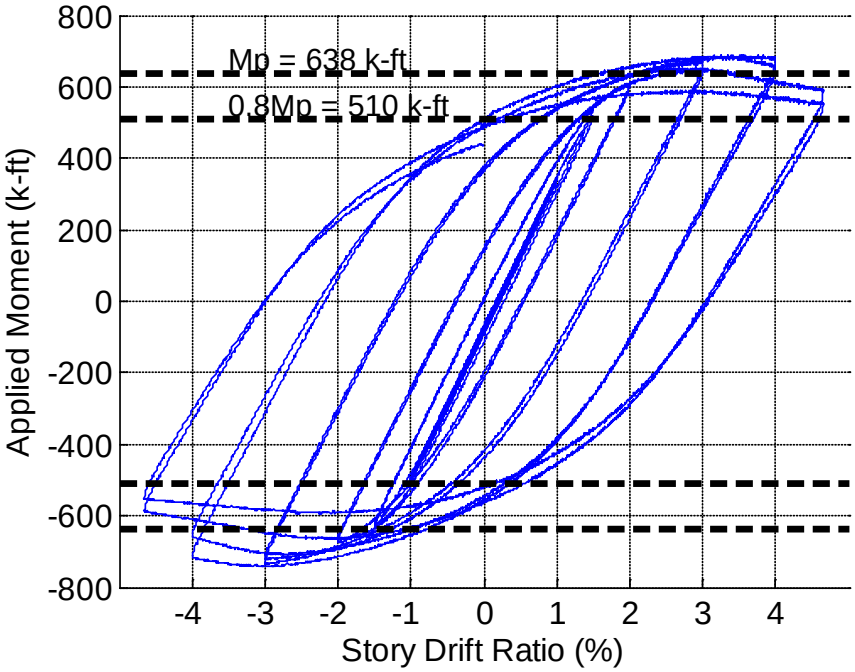

Figure 3.22 – Load-Deformation Response for Specimen 3 (W24x62 with No RBS or Fasteners)

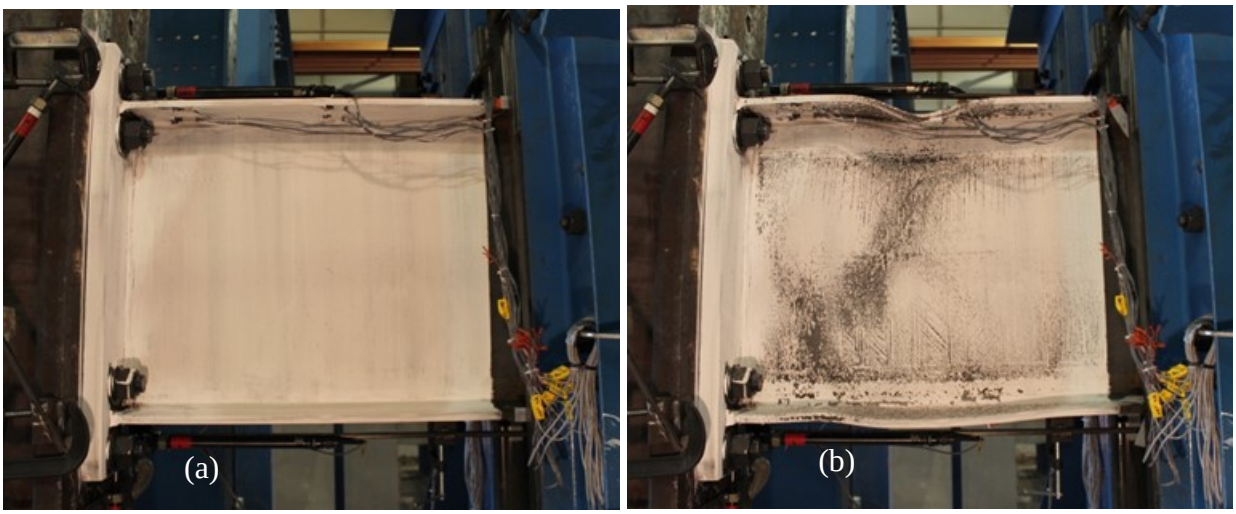

Figure 3.23 – Side View Pictures of Specimen 3 (W24x62 with No RBS or Fasteners)
at (a) Start of Test, and (b) Final Deformation

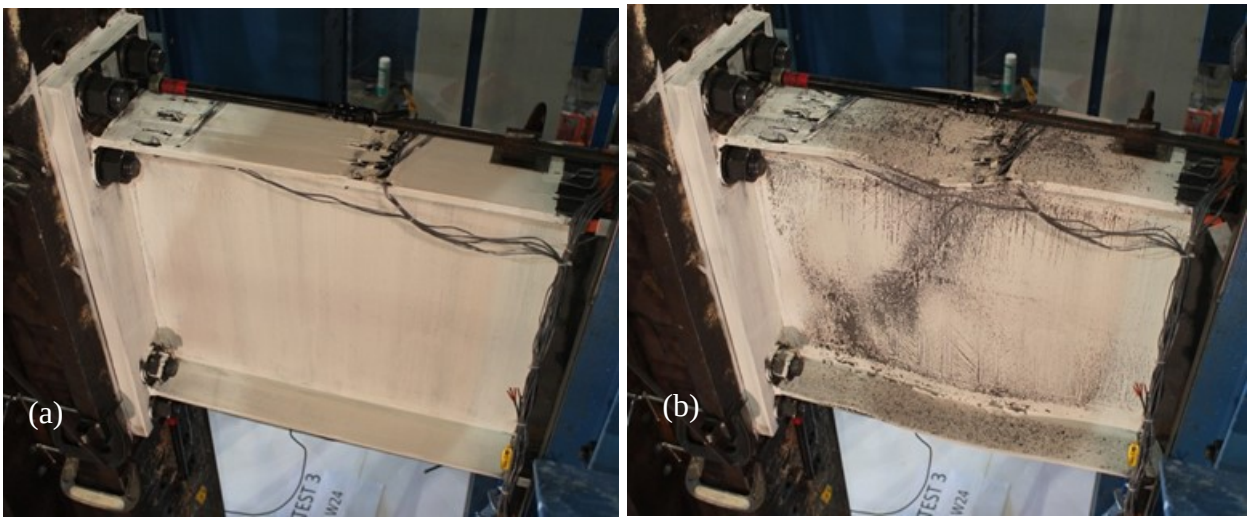

Figure 3.24 – Angled View Pictures of Specimen 3 (W24x62 with No RBS or Fasteners)
at (a) Start of Test, and (b) Final Deformation

Specimen 4: W24x62 with No RBS and PAFs at 12 in.

Specimen 4 was a W24x62 specimen with the same 12 in. spacing of PAFs used in Specimen 2. The SMRF qualification criteria were satisfied with the qualification cycle and subsequent cycling completed without any observable crack formation or tearing. The test was halted after two complete cycles at 4.7% story drift. Figure 3.25 shows the load-deformation

behavior of Specimen 4. Figure 3.26 and Figure 3.27 show pictures of the initial condition and final deformed state for Specimen 4.

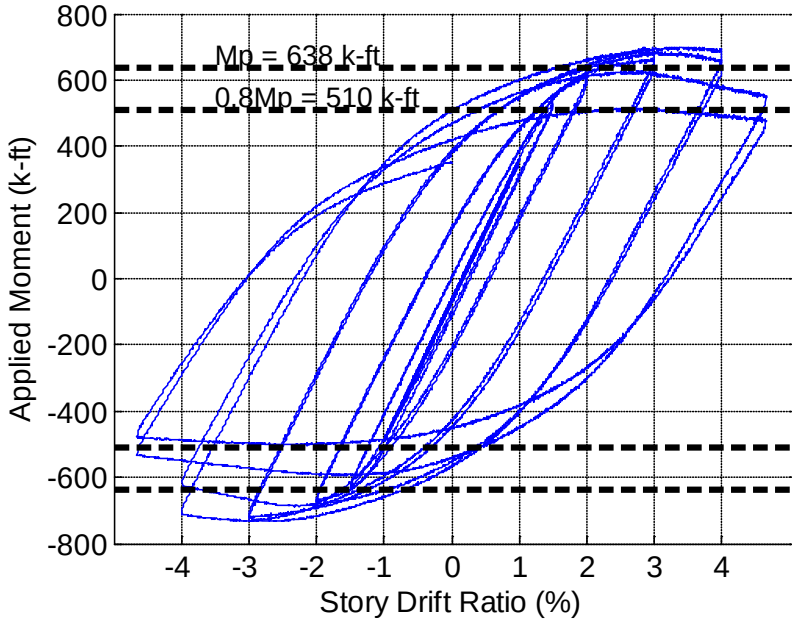

Figure 3.25 – Load-Deformation Response for Specimen 4 (W24x62 with No RBS and PAF at 12 in.)

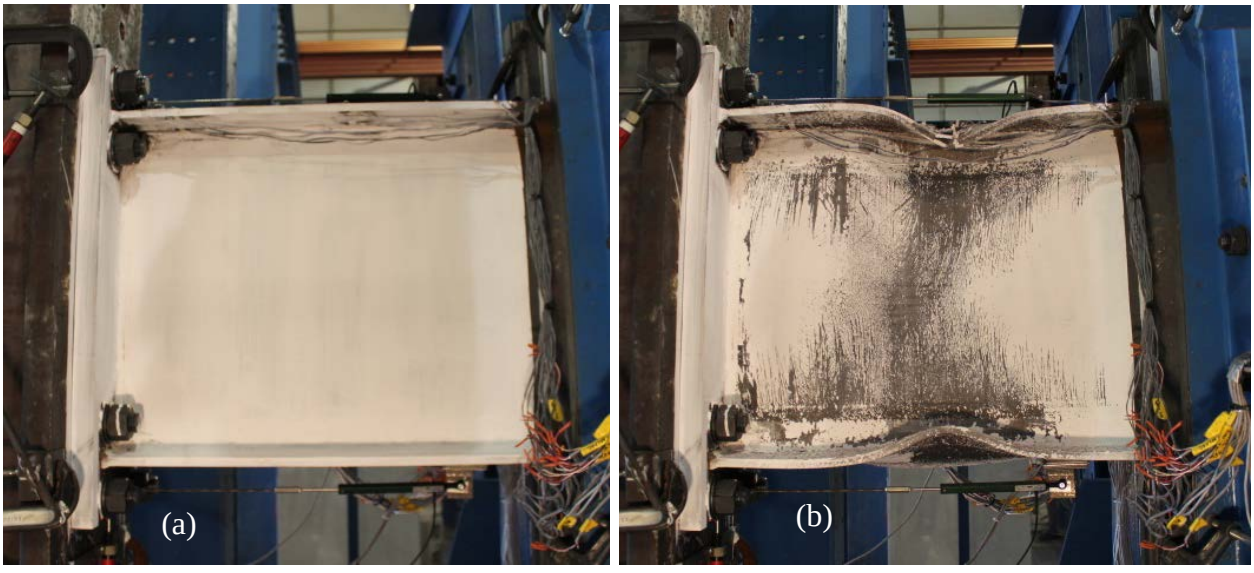

Figure 3.26 –Side View Pictures of Specimen 4 (W24x62 with No RBS and PAF at 12 in.)
at (a) Start of Test, and (b) Final Deformation

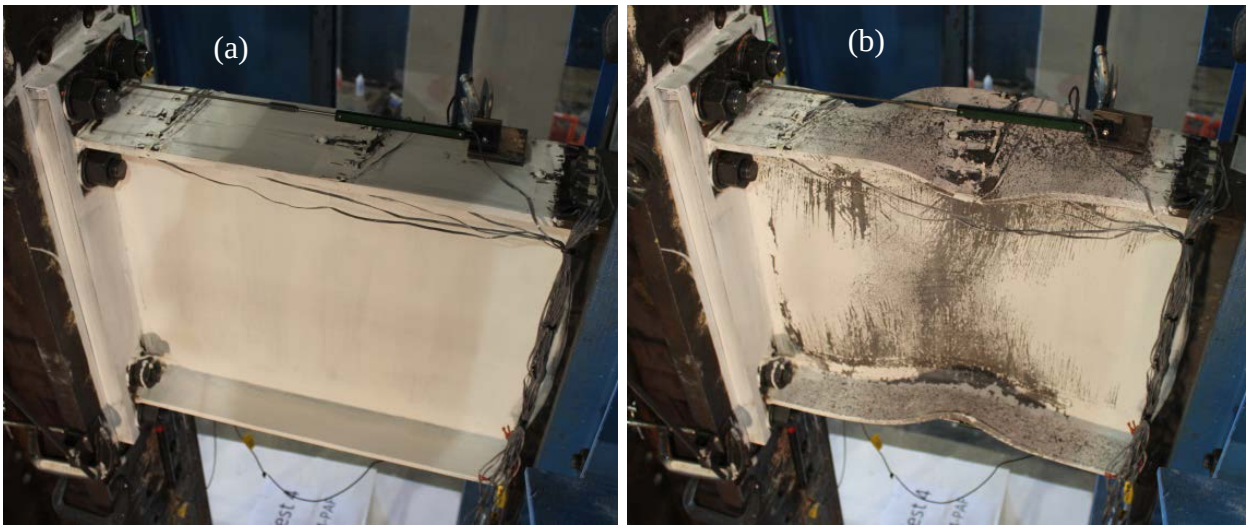

Figure 3.27 –Angled View Pictures of Specimen 4 (W24x62 with No RBS and PAF at 12 in.) at (a) Start of Test, and (b) Final Deformation

Specimen 6: W24x62 with No RBS and Grid of PAFs

Specimen 6 included an array of PAFs on both the top and bottom flange. Despite the array of fasteners, the specimen maintained sufficient plastic moment capacity to pass qualification. Furthermore, the specimen underwent both cycles at 4% story drift and an additional cycle at 4.7% story drift before the moment capacity fell below the $0.8M_p$ limit. The specimen underwent a total of five full cycles of 4.7% story drift with strength degradation associated with local buckling, but no significant loss in moment capacity associated with fracture. Pictures of the specimen before and after testing are shown in Figure 3.29 and Figure 3.30.

Minor cracking initiated at several PAFs as shown in Figure 3.31. Two of the PAFs could easily be pulled out of the flange with no resistance. Removing these fasteners revealed further evidence of small tears around the holes and signs that the holes underwent stretching and elongation during cycling (see Figure 3.31). However, compared to the fractures in the flange tips of the W24x62 RBS specimens, the fracture propagation was quite slow around the PAF. It is possible that the residual compressive stress field around the PAF slows fracture propagation, although sufficient data to support this hypothesis was not available in this testing program.

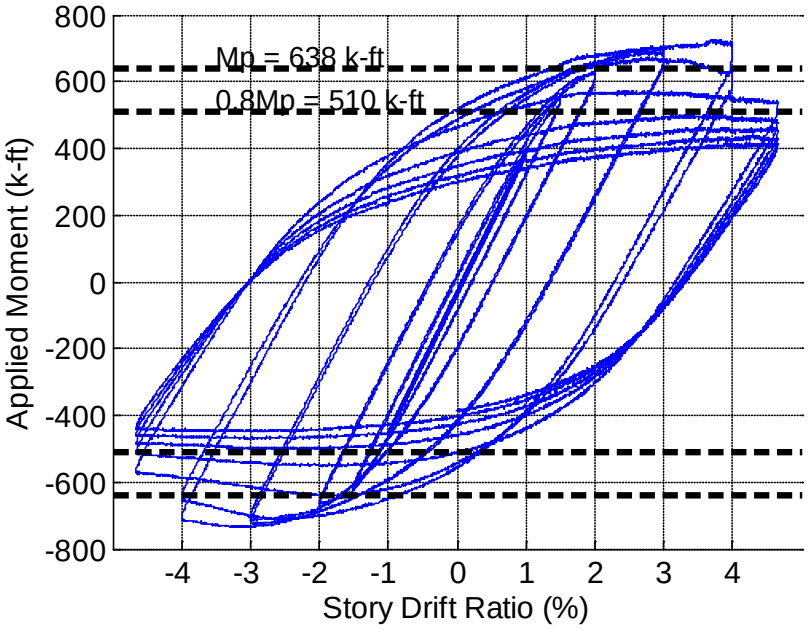

Figure 3.28 – Load-Deformation Response for Specimen 6 (W24x62 with No RBS and Grid of PAF)

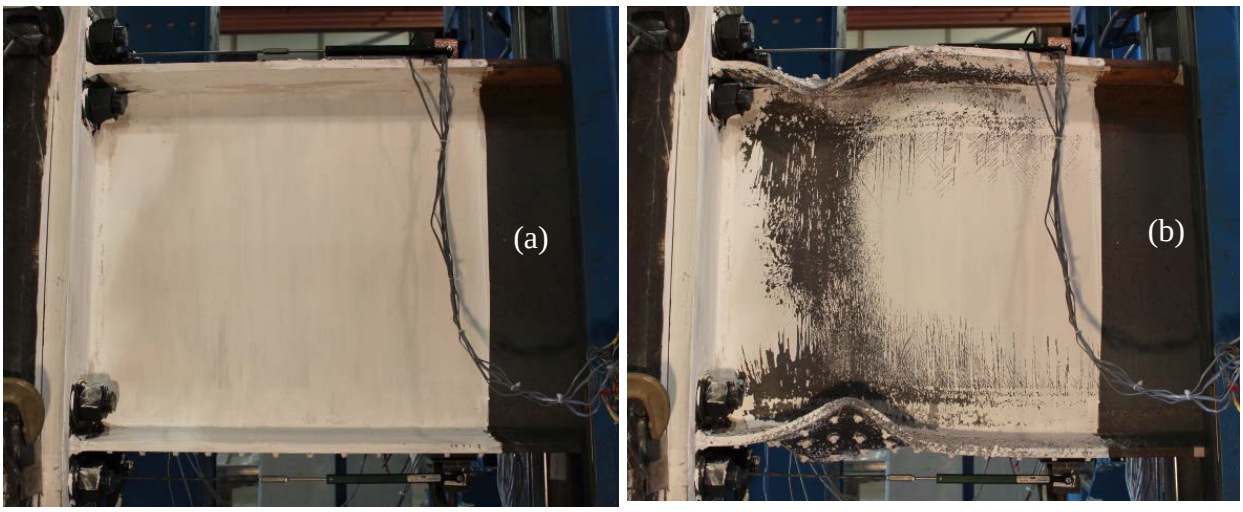

Figure 3.29 –Side View Pictures of Specimen 6 (W24x62 with No RBS and Grid of PAF)
at (a) Start of Test, and (b) Final Deformation

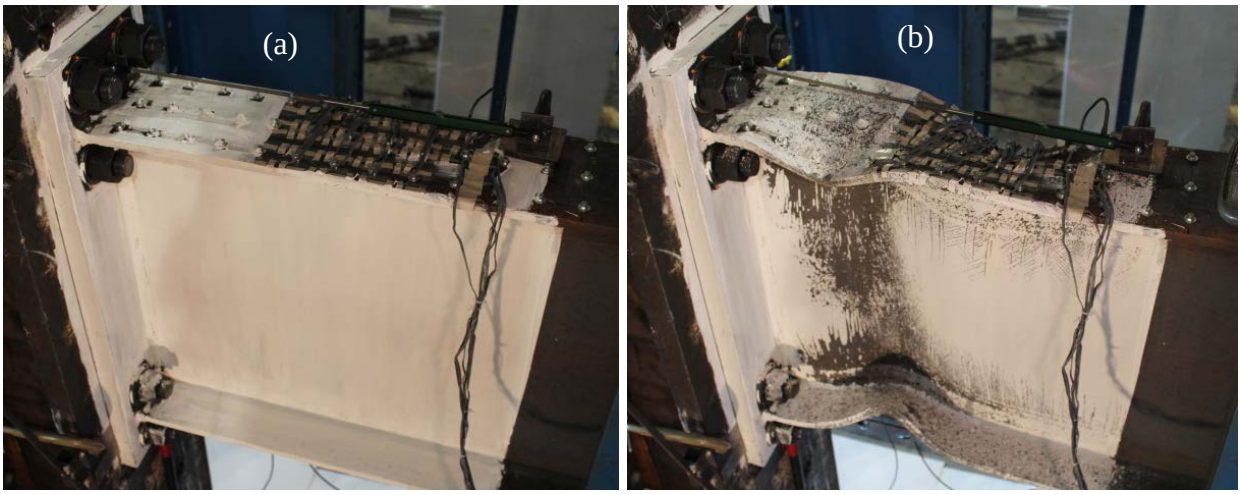

Figure 3.30 –Angled View Pictures of Specimen 6 (W24x62 with No RBS and Grid of PAF)
at (a) Start of Test, and (b) Final Deformation

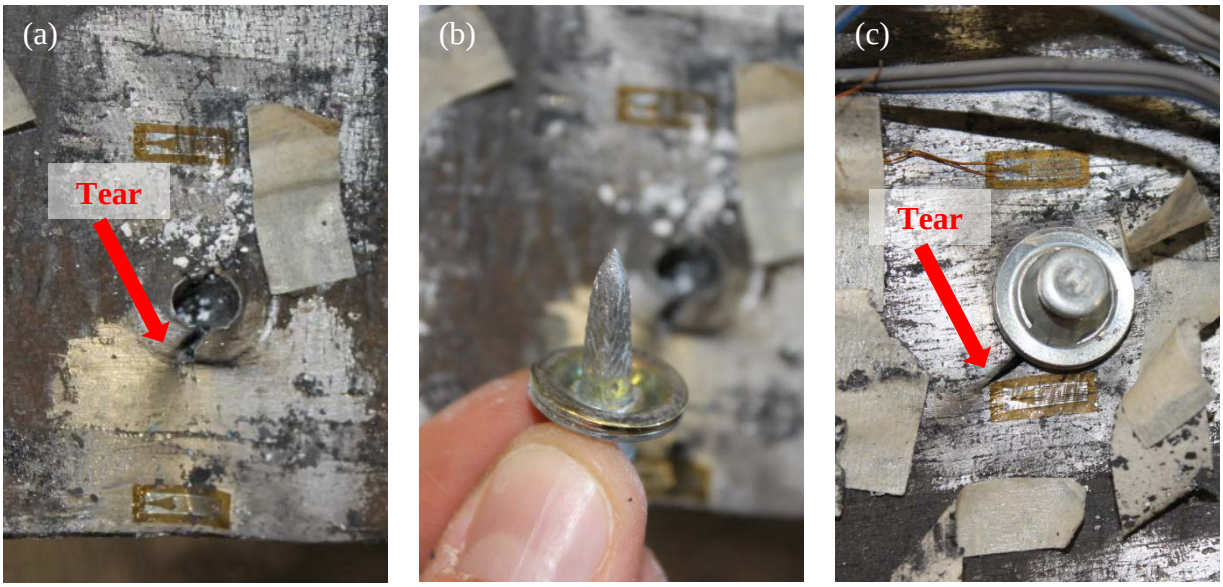

Figure 3.31 – Examples of Tearing at PAF and Loose PAF
for Specimen 6 (W24x62 with No RBS and Grid of PAF)

3.3 Behavior of W36x150 Specimens with RBS

All W36x150 specimens with RBS satisfied the SMRF qualification criteria. The progression of limit states was similar for all specimens in this group. All specimens showed significant yielding in the extreme fibers at the reduced section, followed by a spread of plasticity and local buckling of the flanges in association with out-of-plane buckling of the web. Following this, crack initiation was most prominent on the face of the flange on the inside of the local buckles in the region between the flange edges and flange centerlines. This trend differs from that of W24x62 RBS specimens in which crack initiation was most prominent at the flange edges. All specimens experienced some amount of cracking at the welded junction of the stiffener to the flanges. This tearing prompted the full bottom flange fracture of Specimen 8 as described below.

Specimen 7: W36x150 with RBS and No Fasteners

Test 7 served as the control test for the W36x150 specimens with RBS connections. No PAFs or puddle welds were present on the specimen. Figure 3.32 shows the load-deformation behavior of Specimen 7. The specimen satisfied the SMRF qualification criteria and went on to complete both 4% story drift cycles while maintaining an applied moment capacity greater than 80% of the nominal plastic moment capacity. Pictures of the specimen before and after testing are shown in Figure 3.33 and Figure 3.34.

Multiple crack initiation locations were observed in Specimen 7 at different locations. They were located at the outer surface of the top and bottom flanges at the interior curvature of the local buckle, and at the top and bottom flanges at the weld metal at the junction of the toe of the end plates stiffeners. The crack initiation locations were noticed after the completion of the 4% story drift final cycle during the 4.7% cycle. After several cycles of 4.7% story drift, tearing was observed on the outer surfaces of both the top and bottom flange on the inside surface of local buckles (see Figure 3.35). These tears propagated during the half cycle in which the flanges were pulled in tension. The propagation was ductile and continued to propagate in width and through the depth of the flange as shown in Figure 3.36a. During the fifth cycle of 4.7% story drift, the specimen experienced a complete fracture of the top flange at the location of the RBS with multiple failure origins as shown in Figure 3.37. By this point, the tearing on the underside of the bottom flange was significant as well. In addition, tearing was observed on both top and bottom flanges at the junction of the endplate stiffeners to the flanges. It is expected that these cracks were due

to the extreme compressive plastic loading, since they are at the compression buckled side of the flange due to the local flange buckling. Crack initiation was not noticed at the flange tips similar to the W24x62 RBS specimens. This can be related to polishing and smoothing the RBS edge surface since scratches and dents were observed. While the other side of the top flange surface did not show any signs of crack initiation neither on the surface or the tip of the flange.

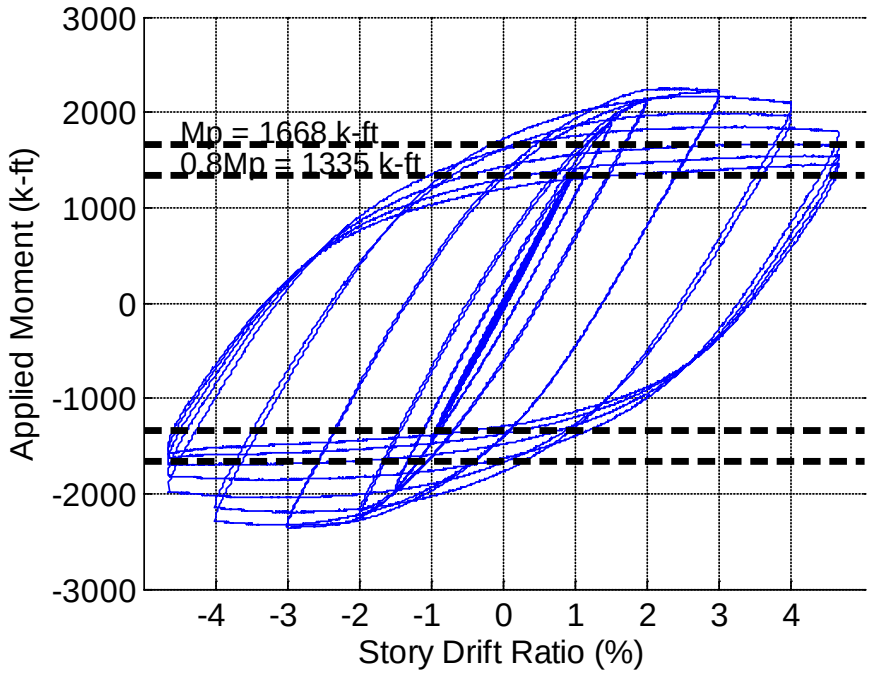

Figure 3.32 – Load-Deformation Response for Specimen 7 (W36x150 with RBS and No Fasteners)

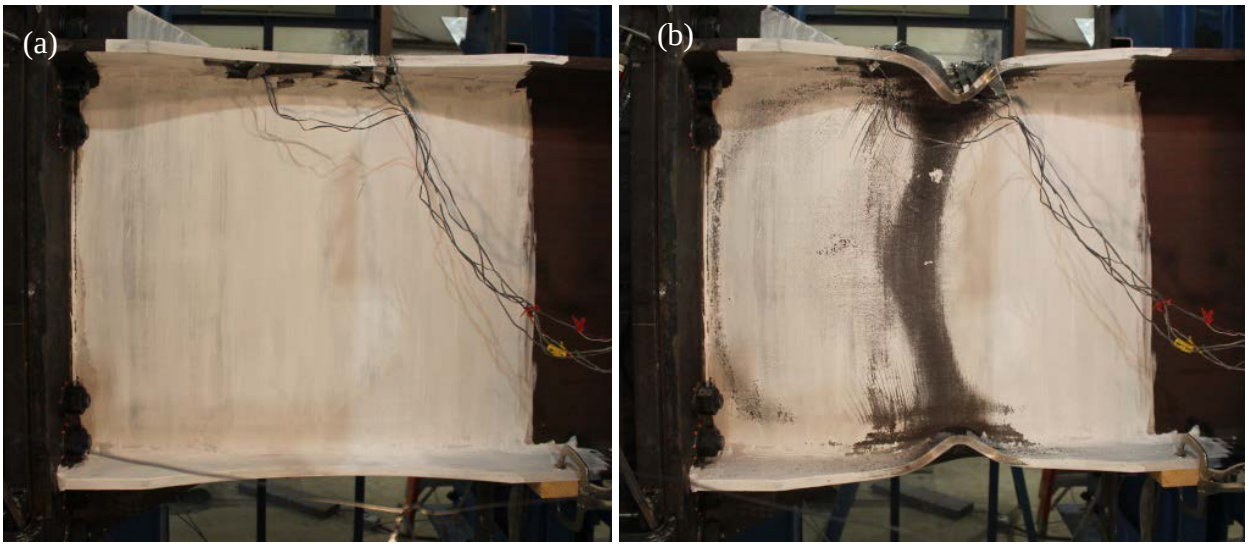

Figure 3.33 – Side View Pictures of Specimen 7 (W36x150 with RBS and No Fasteners) at (a) Start of Test, and (b) Final Deformation

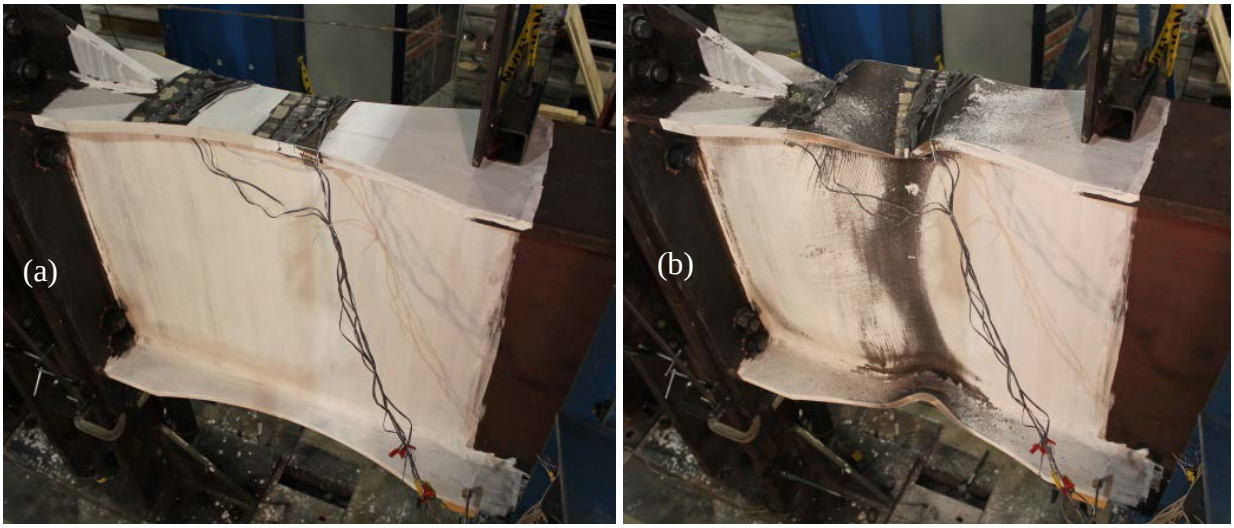

Figure 3.34 – Angled View Pictures of Specimen 7 (W36x150 with RBS and No Fasteners) at (a) Start of Test, and (b) Final Deformation

Figure 3.35 – Crack Initiation on Surface of Bottom Flange for Specimen 7 (W36x150 with RBS and No Fasteners)

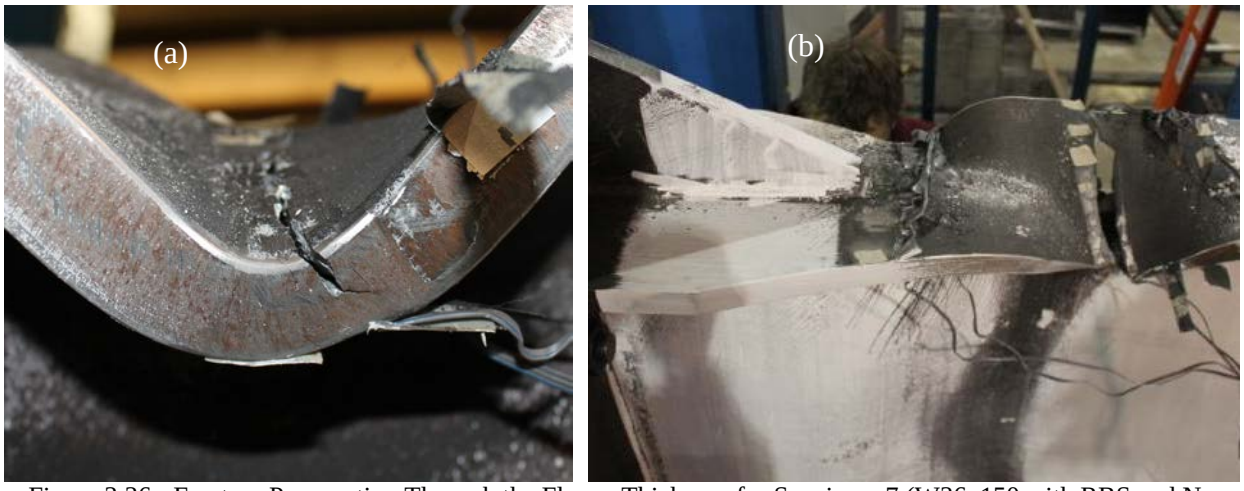

Figure 3.36 - Fracture Propagation Through the Flange Thickness for Specimen 7 (W36x150 with RBS and No Fasteners) Including (a) Partial Depth Crack, and (b) Final Fracture Through Flange

When the fracture surfaces were analyzed, the fracture mode was clearly brittle overload fracture which initiated as shown in Figure 3.38. This type of failure occurs by rapid crack propagation with less expenditure of energy than in ductile fractures and without appreciable gross plastic deformations. There were signs of bright coarse dimpled texture under the crack initiation location which can be related to brittle fracture as shown in Figure 3.38. The brittle overload fracture showed chevron marks pointing back to the fracture origin with coarse texture which can be seen in Figure 3.38. Also, shear lips were observed on the edge where the brittle overload occurred and this shows that there was significant amount of ductility.

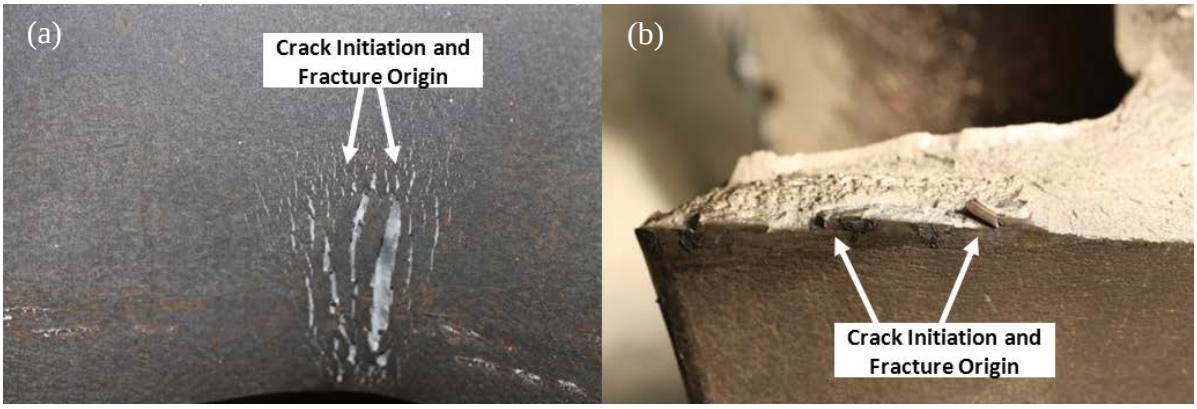

Figure 3.37 – Crack Initiation and Failure Origin in the Top Flange Surface Before Fracture Occurrence (a). After Fracture Occurrence of Crack Initiation and Fracture Origin Location (b).

Figure 3.38 – Fatigue Crack Propagation Starting with Crack Initiation Followed by the Critical Flow and Final Overload Regions

Specimen 8: W36x150 with RBS and Puddle Welds at 12 in.

Specimen 8 was a W36x150 specimen with an RBS connection and puddle welds spaced at 12 in. along the top flange in the same fashion as in Specimen 5. The load-deformation behavior from Specimen 8 is given in Figure 3.39. During 4% story drift cycling, tearing was observed at the junction between the end plate stiffener and the flange within the weld metal. However the specimen still passed qualifying requirements. Pictures of the initial configuration and final deformed shape are shown in Figure 3.40 and Figure 3.41.

Immediately following the first 4.7% cycle, the tearing at the bottom flange stiffener weld metal propagated sufficiently to cause a complete fracture of the bottom flange at the location of the stiffener toe. The location of the fracture indicates that its occurrence was unrelated to the puddle welds. It is noted that the location of the stiffener toe includes a large stress triaxiality in addition to large strain demands. Figure 3.42 shows the tearing at the top flange stiffener weld metal (Figure 3.42a) and the fracture due to tearing at the bottom flange stiffener weld metal (Figure 3.42b).

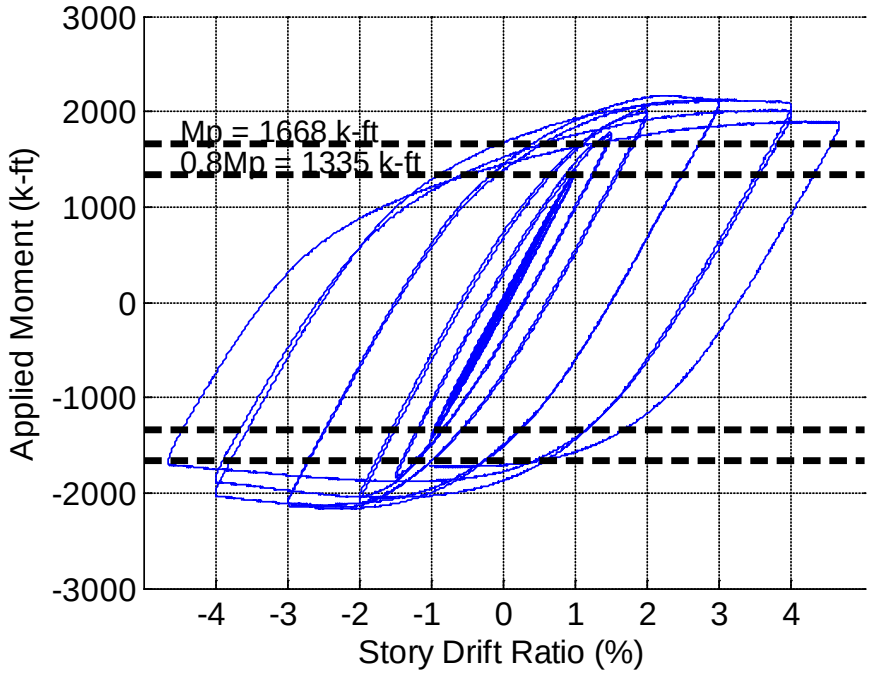

Figure 3.39 – Load-Deformation Response for Specimen 8 (W36x150 with RBS and Puddle Welds)

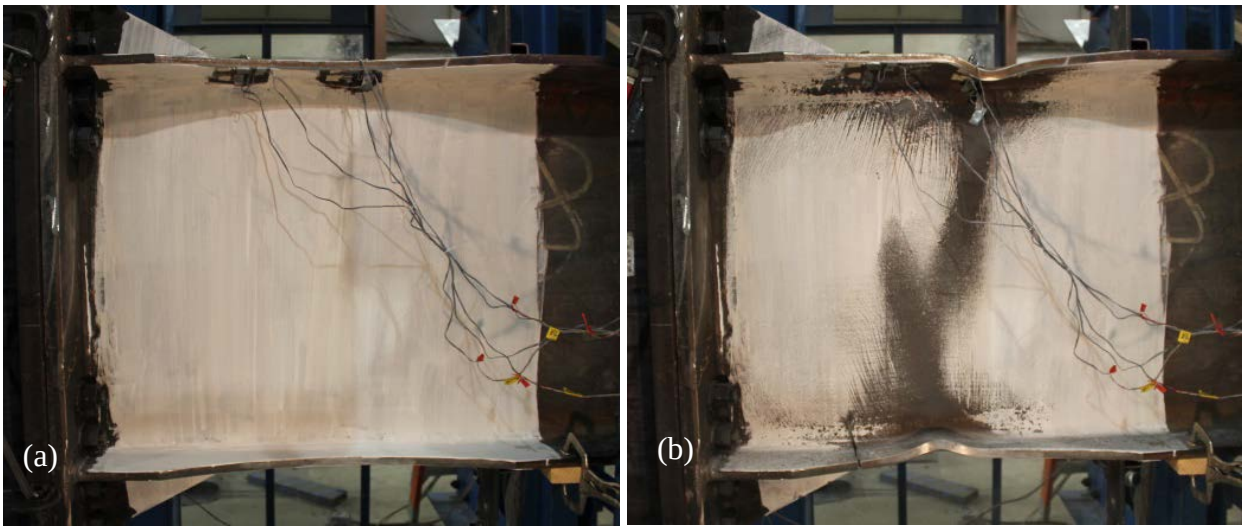

Figure 3.40 –Side View Pictures of Specimen 8 (W36x150 with RBS and Puddle Welds)
at (a) Start of Test, and (b) Final Deformation

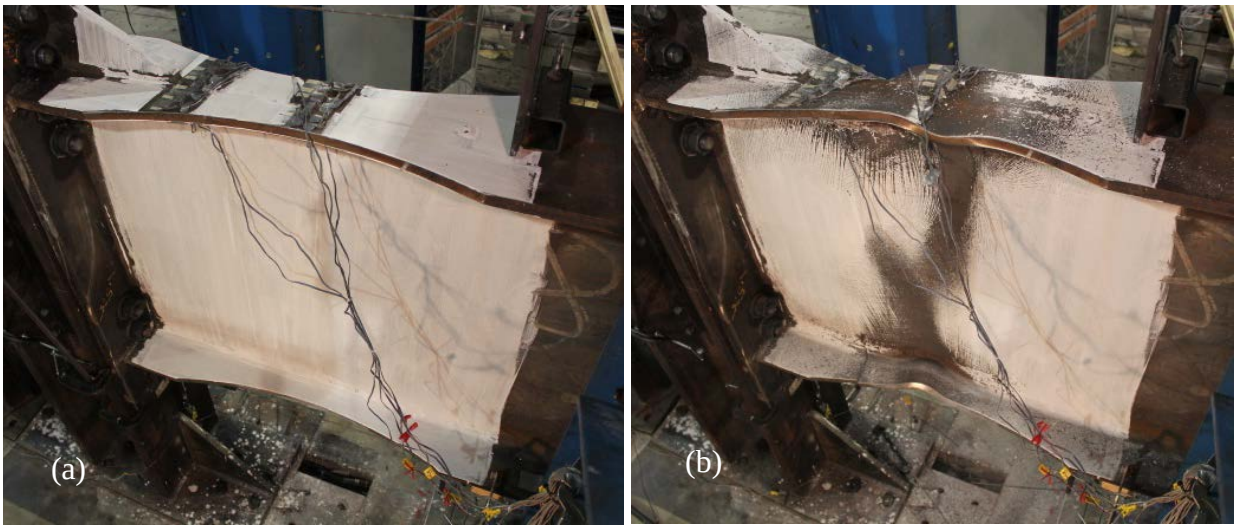

Figure 3.41 –Angled View Pictures of Specimen 8 (W36x150 with RBS and Puddle Welds)
at (a) Start of Test, and (b) Final Deformation

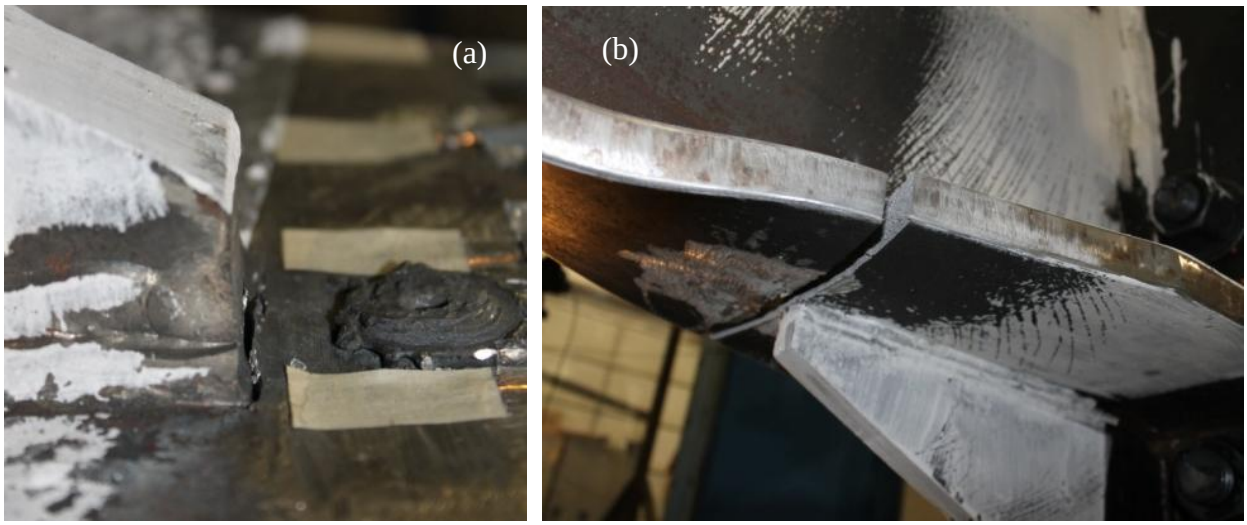

Figure 3.42 – Cracks in Specimen 8 (W36x150 with RBS and Puddle Welds) Including
(a) Initiation of Crack at Toe of Stiffener Weld to Top Flange and
(b) Complete Fracture at the Bottom Flange at the Same Location

It was found that crack initiation occurred at the top and bottom flange at the weld metal at the junction of the toe of the end plates stiffeners during the 4% story drift cycling, as shown in Figure 3.42. The location of the crack initiation is unrelated to the puddle welds, it is expected that these cracks were due to the high stress triaxiality and strain demand at the stiffener toe. Following the first cycle of 4.7% story drift the bottom flange fractured as shown in Figure 3.42. There were no signs of crack initiation noticed at other locations within the specimen.

When the fracture was opened, it was clearly noticed that the fracture mode was brittle overload fracture that initiated at the weld metal at the junction of the toe of the end plates stiffeners as shown in Figure 3.43. This type of failure occurs by rapid crack propagation with less expenditure of energy than in ductile fractures and without appreciable gross plastic deformations. The brittle overload fracture showed chevron marks pointing back to the fracture origin with coarse texture that can be seen in Figure 3.43 and Figure 3.44. Also, partial shear lips were observed on the edge where the brittle overload occurred and this shows that there was some ductility.

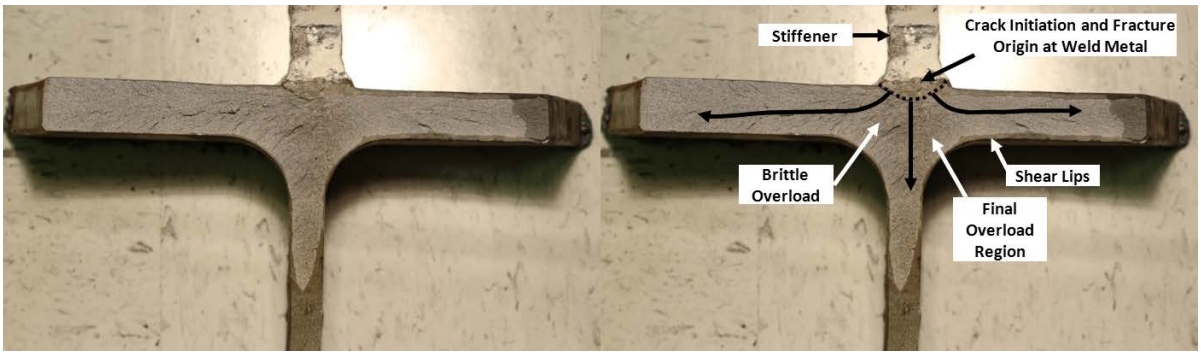

Figure 3.43 – Fatigue Crack Propagation Starting at the Weld Metal with Crack Initiation Followed by the Critical Flow and Final Overload Regions

Figure 3.44 – Close-Up of Chevron Markings at the Web and Flange Pointing Back to the Fracture Origin at the Weld Metal of the Stiffener Due to the Brittle Overload Fracture Mode

Specimen 9: W36x150 with RBS and Grid of PAFs

Specimen 9 was a W36x150 RBS specimen with a grid of PAFs. The load-deformation behavior for Specimen 9 is shown in Figure 3.45. Specimen 9 satisfied SMRF qualification requirements. Pictures of the initial configuration and deformed shape are shown in Figure 3.46 and Figure 3.47.

During the second cycle of 4% story drift, significant tearing was observed at the middle of the top flange RBS where one of the PAFs became dislodged as the hole enlarged during inelastic cycles (Figure 3.48). During the next cycle, the first cycle at 4.7% story drift, a complete fracture of the top flange occurred at this same location. The fracture passed through two PAF holes in line with the minimum flange width and well into the web (Figure 3.49).

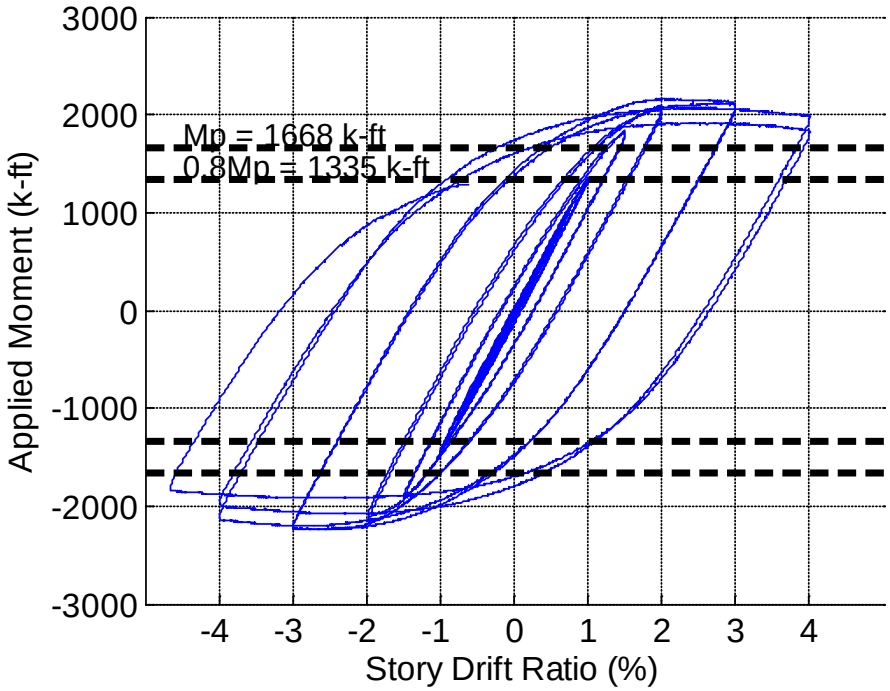

Figure 3.45 – Load-Deformation Response for Specimen 9 (W36x150 with RBS and Grid of PAF)

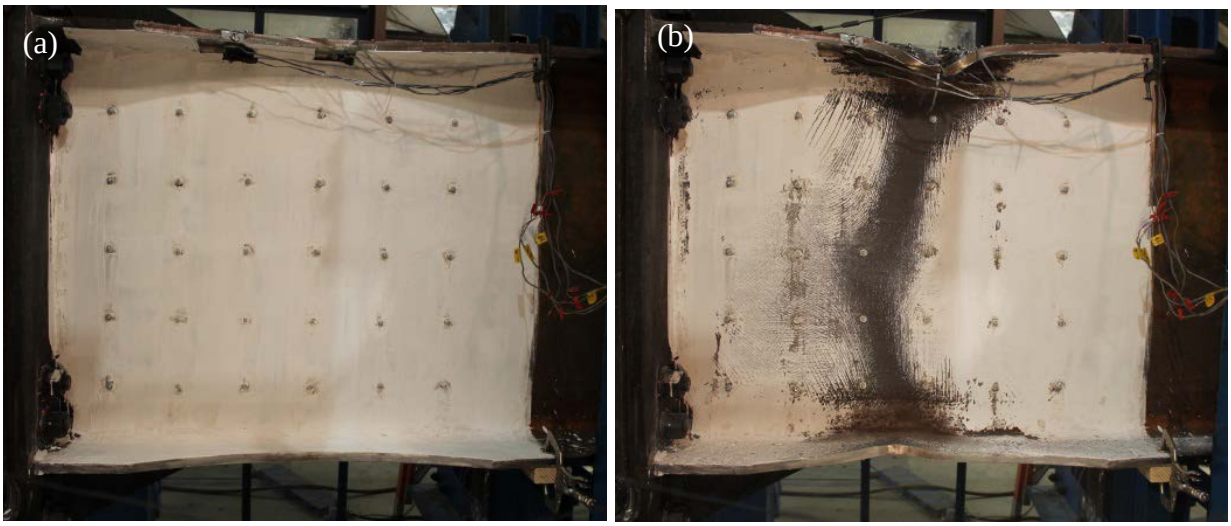

Figure 3.46 –Side View Pictures of Specimen 9 (W36x150 with RBS and Grid of PAF)
at (a) Start of Test, and (b) Final Deformation

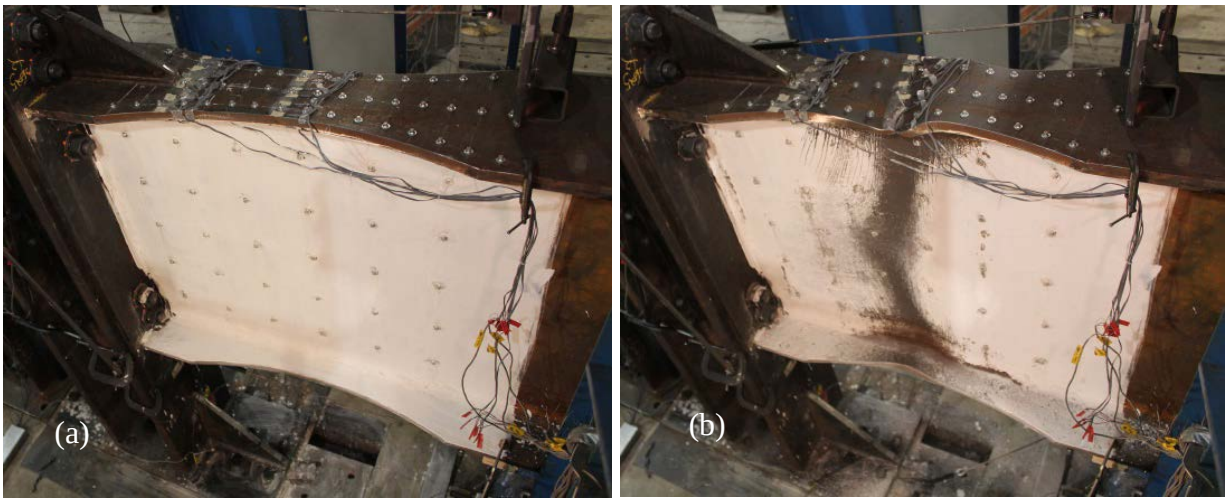

Figure 3.47 – Angled View Pictures of Specimen 9 (W36x150 with RBS and Grid of PAF)
at (a) Start of Test, and (b) Final Deformation

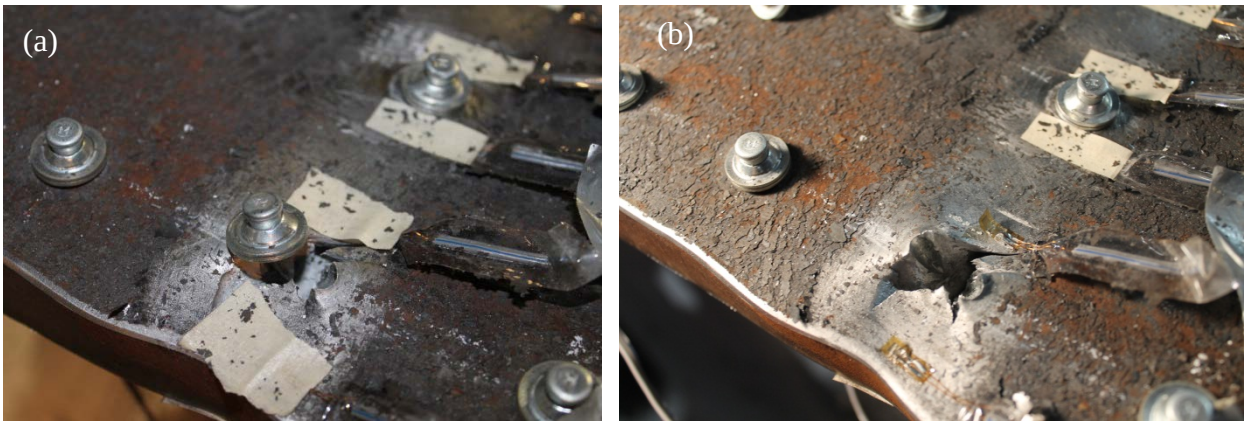

Figure 3.48 – Pictures of Tears Forming at PAF for Specimen 9 (W36x150 with RBS and Grid of PAF)

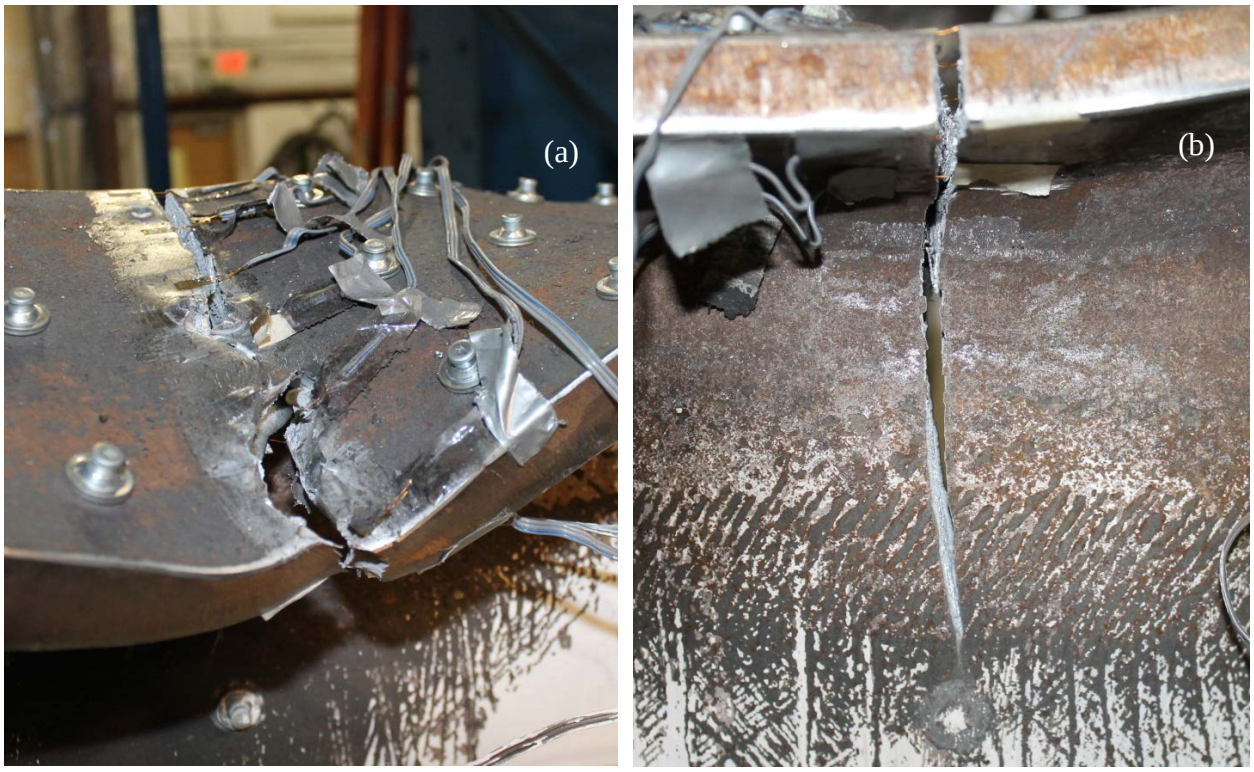

Figure 3.49 – Pictures of Final Top Flange Fracture for Specimen 9 (W36x150 with RBS and Grid of PAF)

Crack initiation occurred at the top flange at the outer PAF located at the minimum flange width during the second cycle of the 4% story drift as shown in Figure 3.48. The weld metal at the junction of the toe of the end plates stiffeners at the top and bottom flanges also showed signs

of crack initiation. During the first cycle of 4.7% story drift the PAF hole, which showed signs of crack initiation, fractured passing through a second PAF, which is located at the center of the RBS flange, and missing the third PAF located at the other side of the flange as shown in Figure 3.50.

When the fracture was opened, there were signs of smooth shiny texture around the PAF where crack initiation was noticed as shown in Figure 3.51. The smooth shiny texture is suspected to be due to the rubbing of the crack during the final cycle loading combined with a rapid crack growth. No fatigue striations with smooth shiny texture were observed which means failure occurred the next cycle or relatively shortly after the crack initiation was noticed. Followed by chevron marks pointing back to the fracture origin with coarse texture that refers to brittle overload fracture occurrence as shown in Figure 3.50. This type of failure occurs by rapid crack propagation with less expenditure of energy than in ductile fractures and without appreciable gross plastic deformations. Also, partial shear lips were observed on the edge where the brittle overload occurred and this shows that there was some ductility.

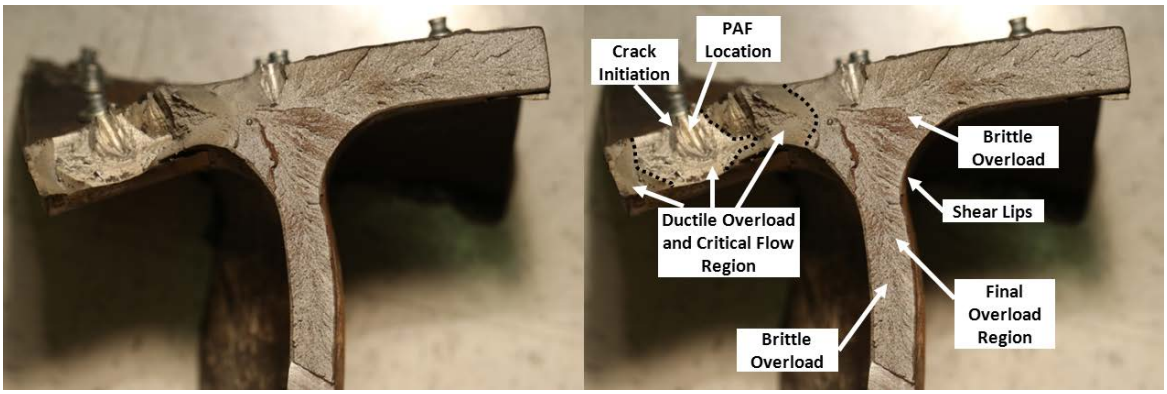

Figure 3.50 – Fatigue Crack Propagation Starting with Crack Initiation Followed by the Critical Flow and Final Overload Regions

Figure 3.51 – Close-Up of Fracture Initiation Location at Outer PAF

3.4 Behavior of Non-RBS W36 Specimens

All W36x150 specimens without RBS satisfied the SMRF qualification criteria. The progression of limit states was similar for all specimens in this group. All specimens showed significant yielding in the extreme fibers at the reduced section, followed by a spread of plasticity and local buckling of the flanges in association with out-of-plane buckling of the web. Although all specimens in the group experienced some crack initiation at the toe of the stiffener to flange junction, none of these fractures propagated very far. Specimens 10 and 11 did not experience significant loss of moment capacity associated with fracture, and Specimen 12, which included a grid of PAF, experienced significant moment strength loss only after four cycles at 4.7% story drift.

Specimen 10: W36x150 with No RBS and No Fasteners

Test 10 served as the control test for the W36x150 specimens without RBS. No PAFs or puddle welds were included in the protected zone. Qualification requirements were satisfied and testing was ended after the specimen completed five full cycles of 4.7% story drift. The hysteretic behavior, shown in Figure 3.52 experienced slight strength degradation during these large inelastic

cycles, but the degradation was associated with local buckling, not fracture propagation. Pictures of the initial configuration and deformed shape are shown in Figure 3.53 and Figure 3.54.

At the start of the 4.7% story drift cycles, tearing was observed at the endplate stiffener toe weld metal similar to the tears observed in the W36x150 specimens with RBS. However, the tears did not propagate significantly through the five cycles at 4.7% story drift.

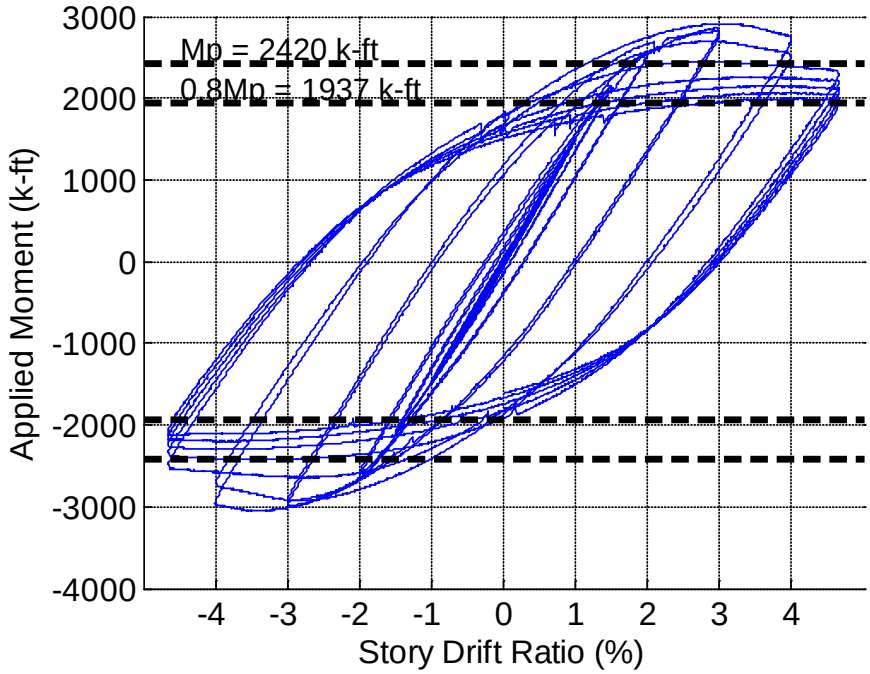

Figure 3.52 – Load-Deformation Response for Specimen 10 (W36x150 with no RBS or Fasteners)

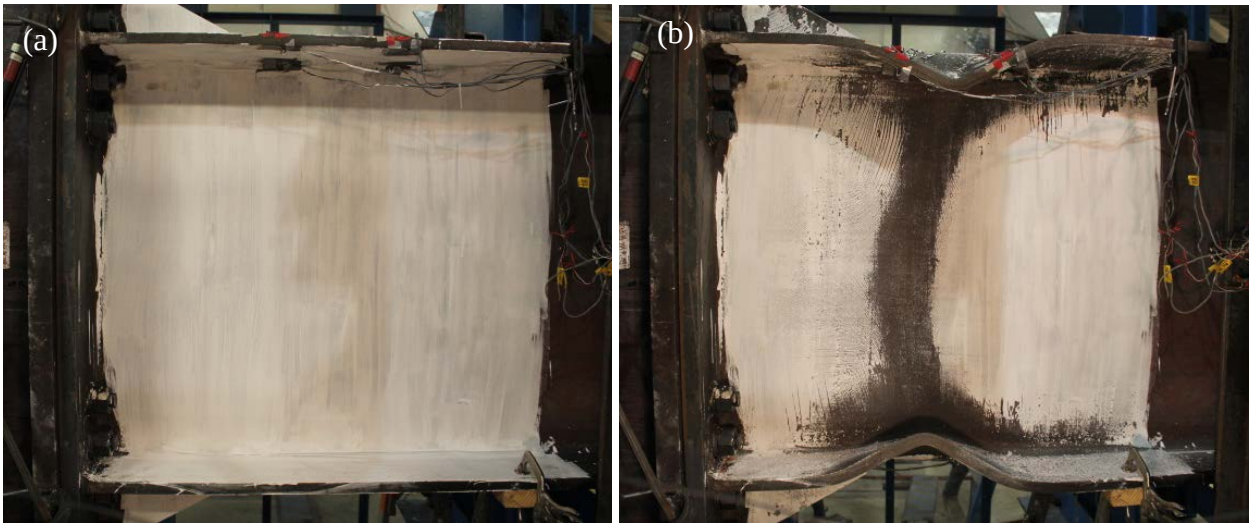

Figure 3.53 – Side View Pictures of Specimen 10 (W36x150 with no RBS or No Fasteners) at (a) Start of Test, and (b) Final Deformation

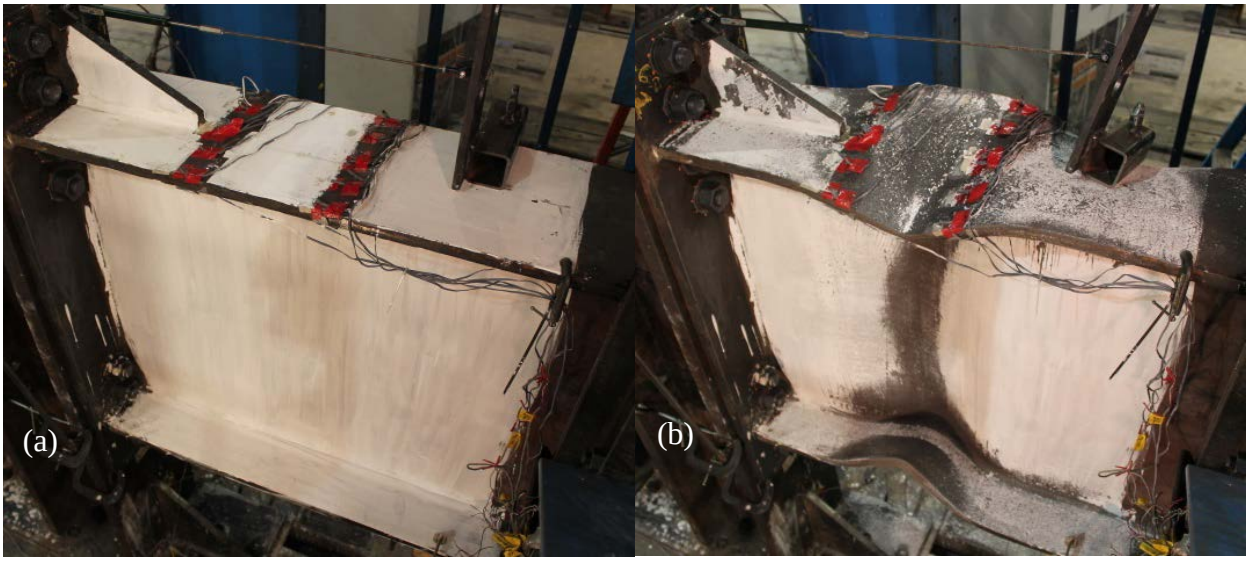

Figure 3.54 – Angled View Pictures of Specimen 10 (W36x150 with no RBS or No Fasteners) at (a) Start of Test, and (b) Final Deformation

Specimen 11: W36x150 with No RBS and PAFs at 12 in.

Specimen 11 was a W36x150 specimen without RBS and PAFs spaced at 12 in. along the top flange in the same fashion as in Specimen 4. As in the previous test, qualification requirements were met and the test was ended after five cycles of 4.7%. The load-deformation behavior is shown in Figure 3.55 and pictures of the initial configuration and final deformed shape are shown in Figure 3.56 and Figure 3.57. The same endplate stiffener weld metal tearing observations were made as in previous tests. Figure 3.58 shows the tearing at both the top and bottom endplate stiffener toe welds. The tears did not propagate significantly during the cycles at 4.7% story drift.

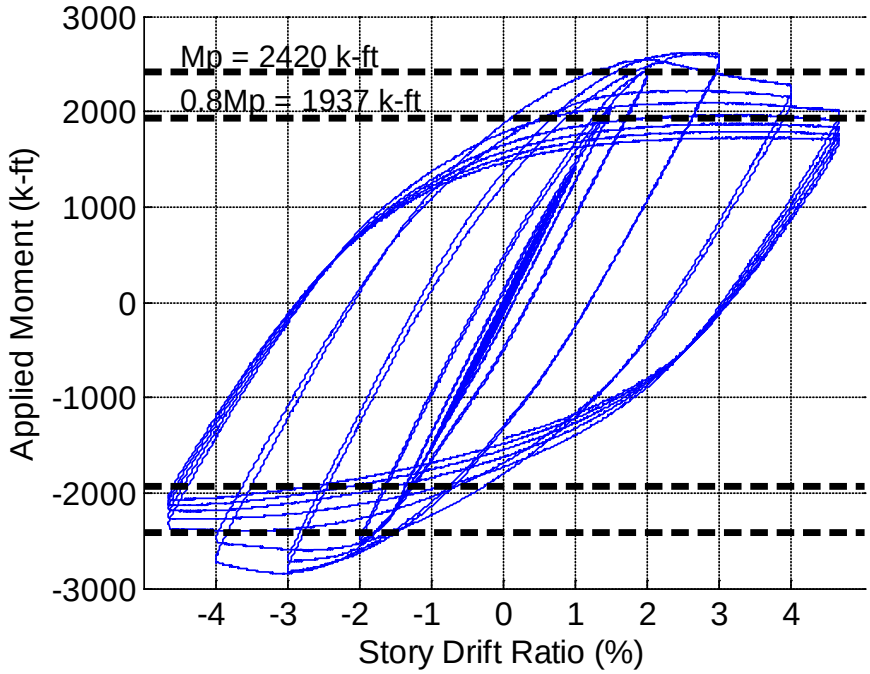

Figure 3.55 – Load-Deformation Response for Specimen 11 (W36x150 with no RBS and PAF at 12 in.)

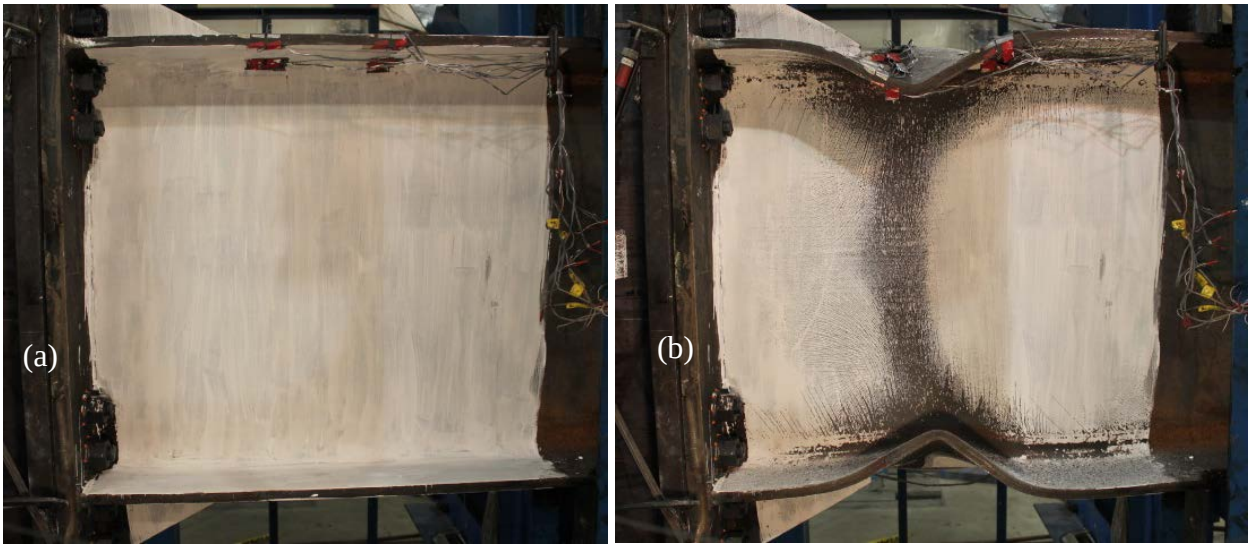

Figure 3.56 – Side View Pictures of Specimen 11 (W36x150 with no RBS and PAF at 12 in.)
at (a) Start of Test, and (b) Final Deformation

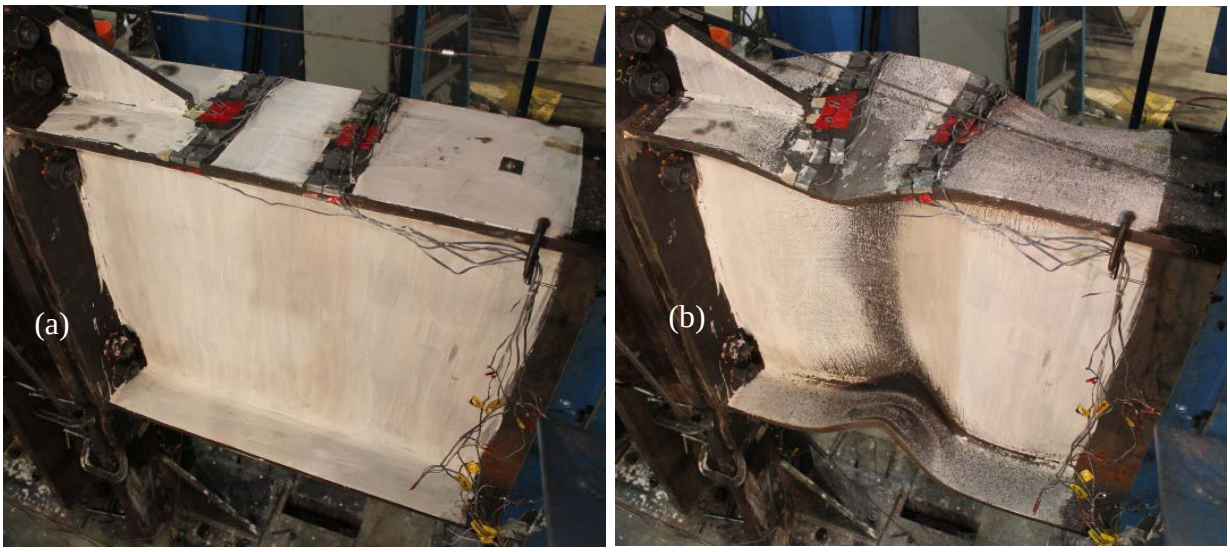

Figure 3.57 – Angled View Pictures of Specimen 11 (W36x150 with no RBS and PAF at 12 in.) at (a) Start of Test, and (b) Final Deformation

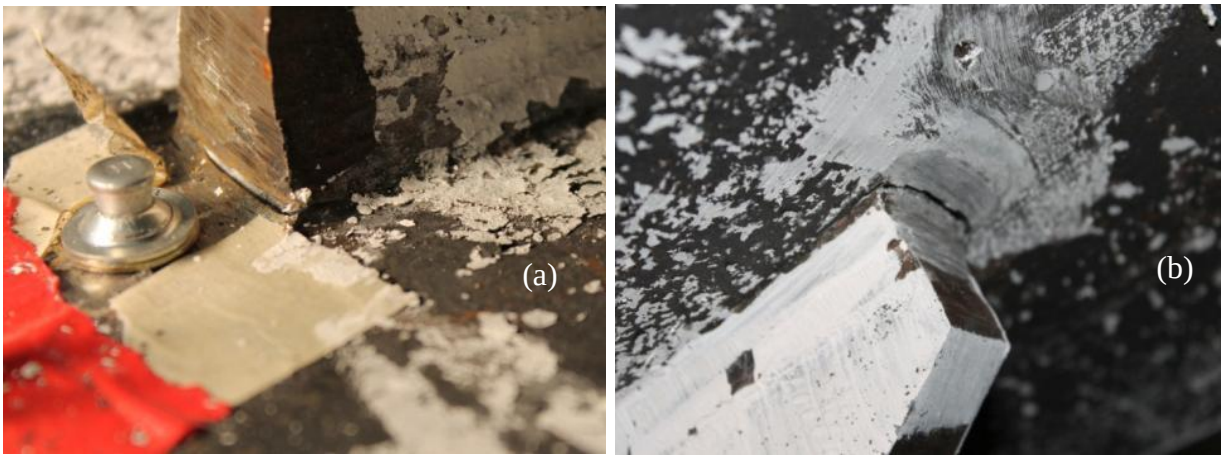

Figure 3.58 - Tearing at Junction of Stiffener to Flange at the (a) Top Flange and (b) Bottom Flange for Specimen 11 (W36x150 with no RBS and PAF at 12 in.)

Specimen 12: W36x150 with No RBS and Grid of PAFs

Specimen 12 was a W36x150 specimen with no RBS and a grid of PAFs. Qualification requirements were met and the load-deformation behavior is given in Figure 3.59. Pictures of the initial configuration and deformed shape are shown in Figure 3.60 and Figure 3.61.

An analysis of the fracture surface showed that crack initiation occurred at the bottom flange at multiple PAF. During the second cycle of 4.7% story drift, two PAFs on the underside of the bottom flange were observed to fall out of the beam as their holes began tearing and

enlarging (Figure 3.62). During the next cycle, significant tear propagation occurred, originating from a PAF hole 3.5 inches from the edge of the flange. During the extreme upward deflection of the fourth 4.7% cycle, the tear propagated to the flange edge. This was followed almost immediately by a full fracture of the bottom flange as shown in Figure 3.63. The fracture extended approximately six inches up the web intersecting one of the PAFs in the web (Figure 3.63b).

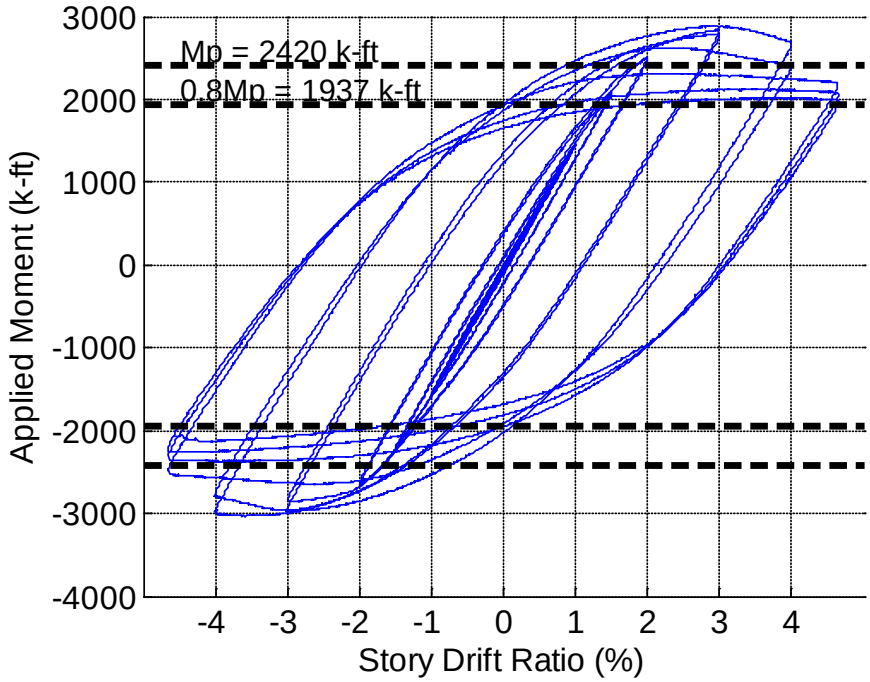

Figure 3.59 – Load-Deformation Response for Specimen 12 (W36x150 with no RBS and Grid of PAF)

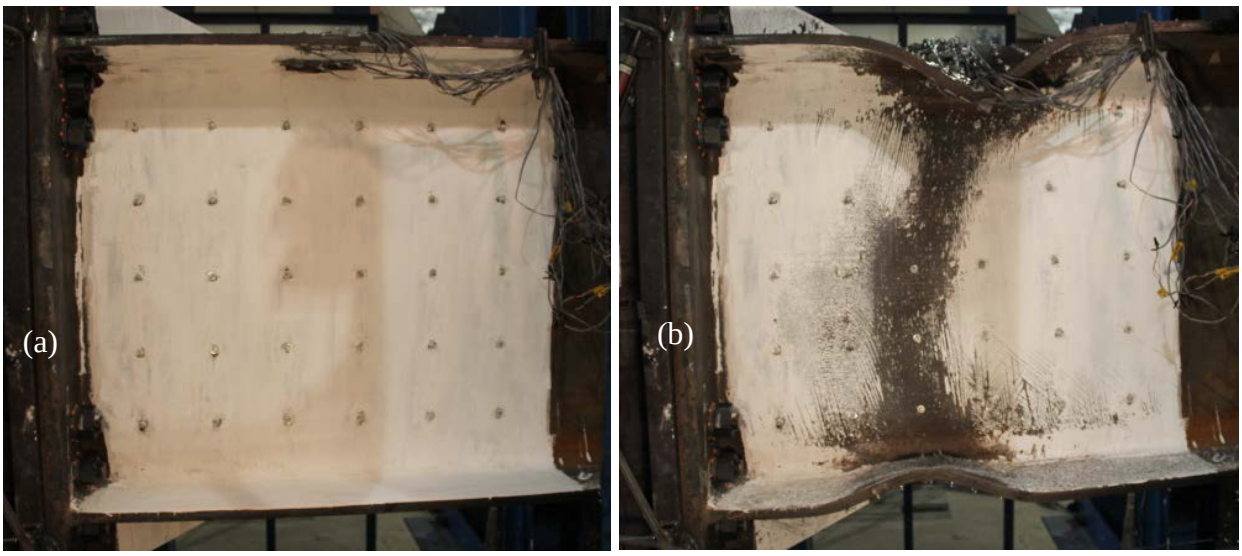

Figure 3.60 – Side View Pictures of Specimen 12 (W36x150 with no RBS and Grid of PAF) at (a) Start of Test, and (b) Final Deformation

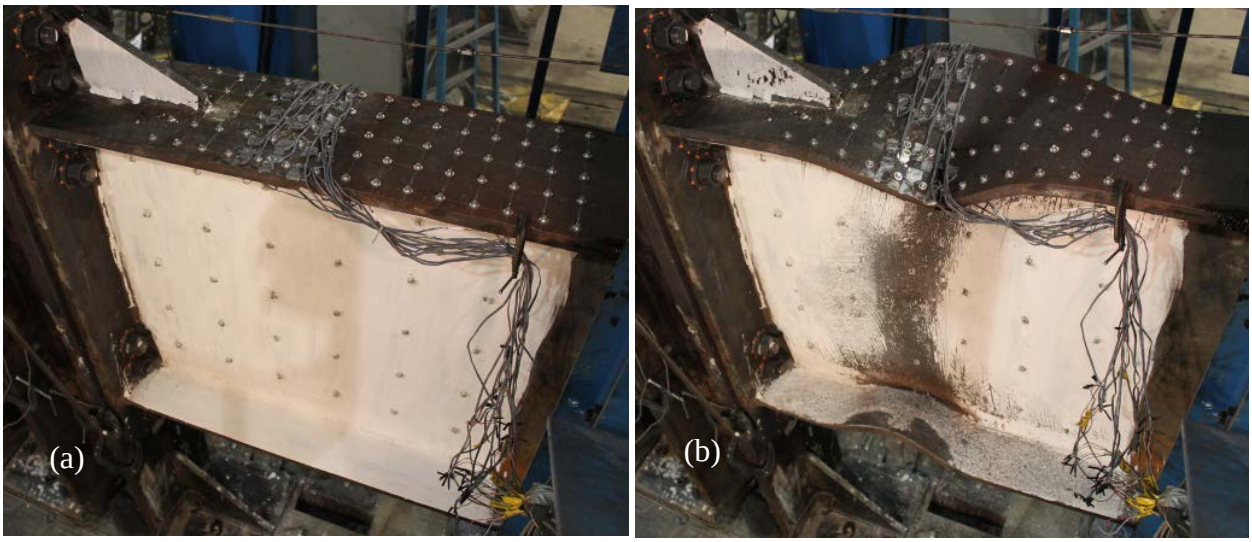

Figure 3.61 – Angled View Pictures of Specimen 12 (W36x150 with no RBS and Grid of PAF)
at (a) Start of Test, and (b) Final Deformation

Figure 3.62 – Cracks Forming on the Surface of the Bottom Flange
for Specimen 12 (W36x150 with no RBS and Grid of PAF)

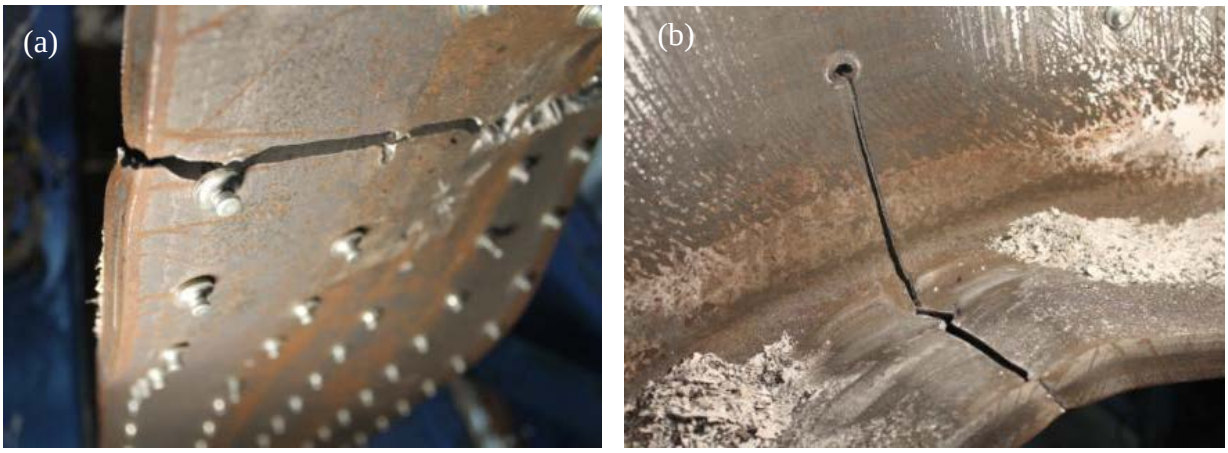

Figure 3.63 - Fracture Through the Bottom Flange as Shown From the (a) Bottom Side View and (b) Side View Showing Fracture Extension to Web PAF Hole for Specimen 12 (W36x150 with no RBS and Grid of PAF)

Two different brittle fracture textures were observed around the PAF located 3.5 inches and the first PAF from the flange edge as shown in Figure 3.64 and Figure 3.65. Both textures show signs of chevron marks pointing back to the fracture origin with coarse texture that refers to brittle overload fracture occurrence as shown in Figure 3.64, Figure 3.65, and Figure 3.66. No fatigue striations with smooth shiny texture were observed which means failure occurred the next cycle or relatively shortly after the crack initiation was noticed. This type of failure occurs by rapid crack propagation with less expenditure of energy than in ductile fractures and without appreciable gross plastic deformations. Also, shear lips were observed on the edge where the brittle overload occurred and this shows that there was significant amount of ductility.

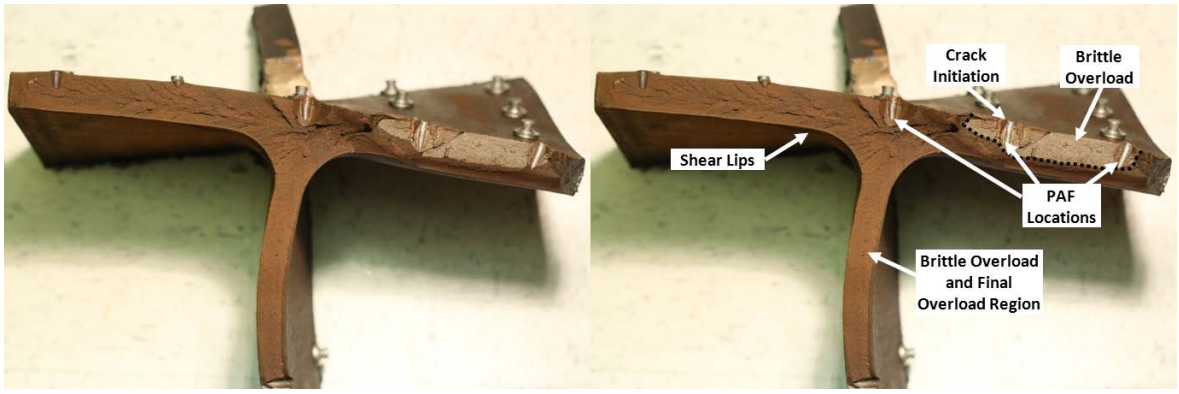

Figure 3.64 – Fatigue Crack Propagation with Initial Brittle Overload Followed by a Final Overload Region

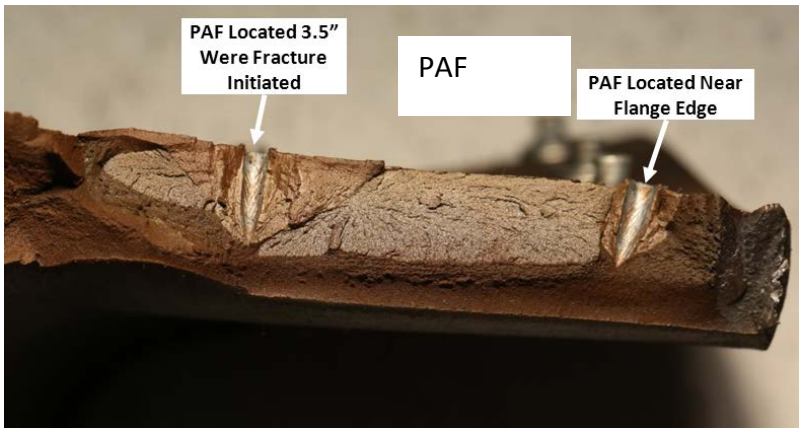

Figure 3.65 – Close-Up of Chevron Markings at the Web between PAF Located 3.5 inches and the First PAF from the Flange Edge Pointing Back to the Fracture Origin Due to the Brittle Overload Fracture Mode

Figure 3.66 – Close-Up of Chevron Markings at the Web and Flange Pointing Back to the Fracture Origin at the PAF Due to the Brittle Overload Fracture Mode

CHAPTER 4 STORY DRIFT DECOMPOSITION

It is necessary to decompose the story drift to quantify the contribution of each component of the test setup to the total system story drift. The six components of flexibility that were identified, measured, and separated include:

- Flexibility of the reaction frame
- Shear deformation of the panel zone
- Shear and flexural deformations of the column including flexural deformations in the panel zone
- Prying of the endplate connection coupled with localized deformations of the column flange and web
- Elastic flexural and shear deformation of the beam outside the plastic hinge region
- Deformation of the plastic hinge region of the beam

The equations that were used to convert recorded displacements into each story drift component are derived in Appendix B. Some components of story drift were measured using two separate but redundant measurement systems. Appendix B also contains a comparison of some of the redundant measurements, and comparisons to theoretical values used to validate the test data.

There are two primary uses intended for the decomposed story drift data including verification of the story drift due to plastic hinge deformation and producing a data set that can be used to calibrate or validate computational models. AISC 341 Commentary K2.3a (AISC 2010a) permits up to 25% of the total system story drift to occur in system components outside the plastic hinge region of the beam. Since this study assesses qualification requirements at a total story drift of 4%, plastic hinging of the beam at these cycles should account for at least 3% story drift. Another way to look at this requirement is that the qualification cycle should be one in which the plastic hinge deformations account for 3% of the story drift.

Story drift decomposition data is presented in two formats to better understand the degree of each component's contribution to the total system story drift. First, the values for each story drift component is plotted. Next, the relative contributions of each component are plotted as a

percentage of the total story drift such that their sum always totals 100%. Although representative plots are presented in this Chapter for each beam type, Appendix C includes additional story drift decomposition plots for all specimens.

4.1 Component Absolute Values

Figure 4.1 through Figure 4.4 show line plots of the absolute contribution of each story drift component for one of each of the four beam types tested. As expected, during high amplitude cycles, plastic hinge rotation is the primary contributor to story drift. Beam elasticity contributes moderately, while the other elastic components contribute a minor amount to the total story drift. It is also noted that for large amplitude cycles, each elastic component develops a plateau in its magnitude. This indicates that the elastic sources of flexibility reach limiting values of deformation associated with the plastic moment of the specimen.

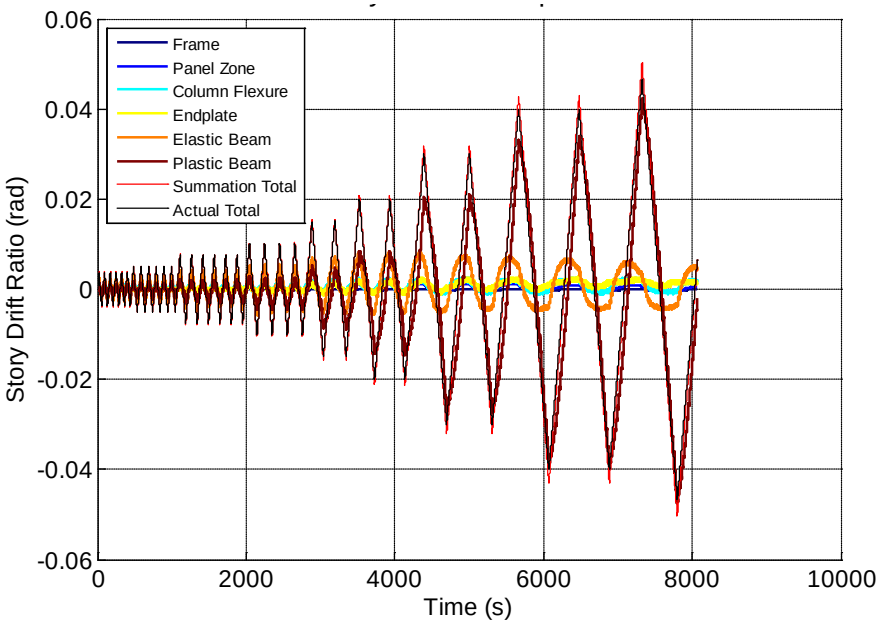

Figure 4.1 – Story Drift Decomposition for a Representative W24x62 Specimen with RBS (Specimen 2)

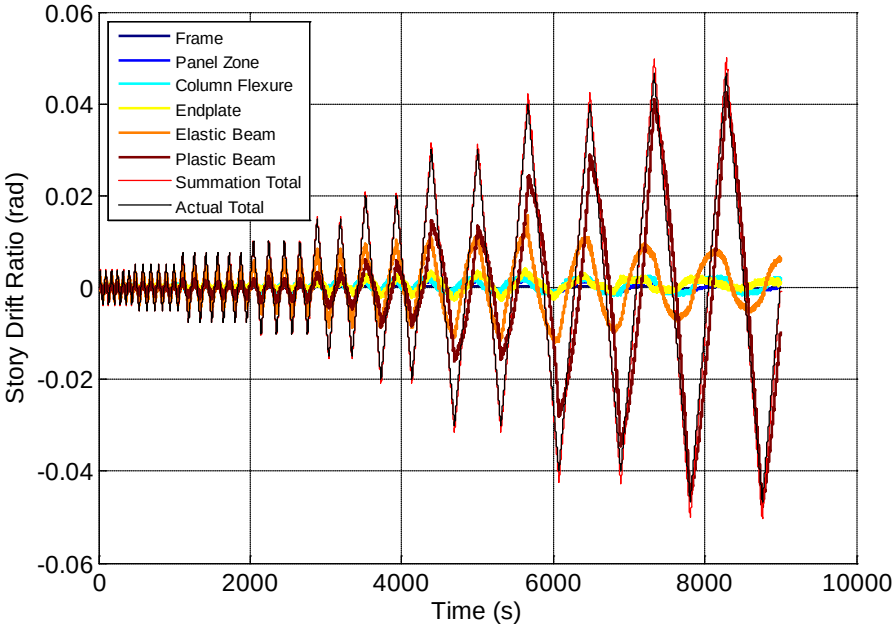

Figure 4.2 – Story Drift Decomposition for a Representative W24x62 without RBS (Specimen 4)

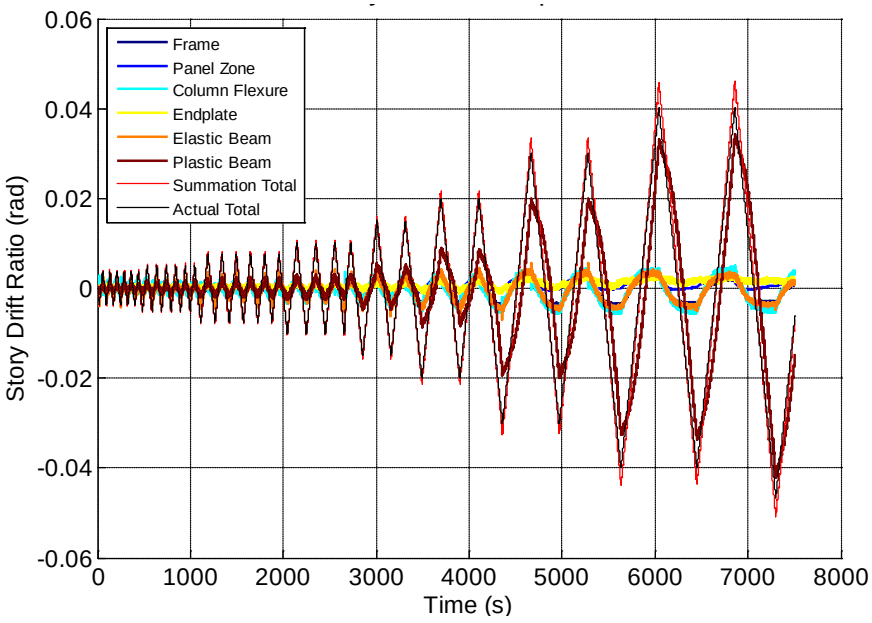

Figure 4.3 – Story Drift Decomposition for a Representative W36x150 with RBS (Specimen 9)

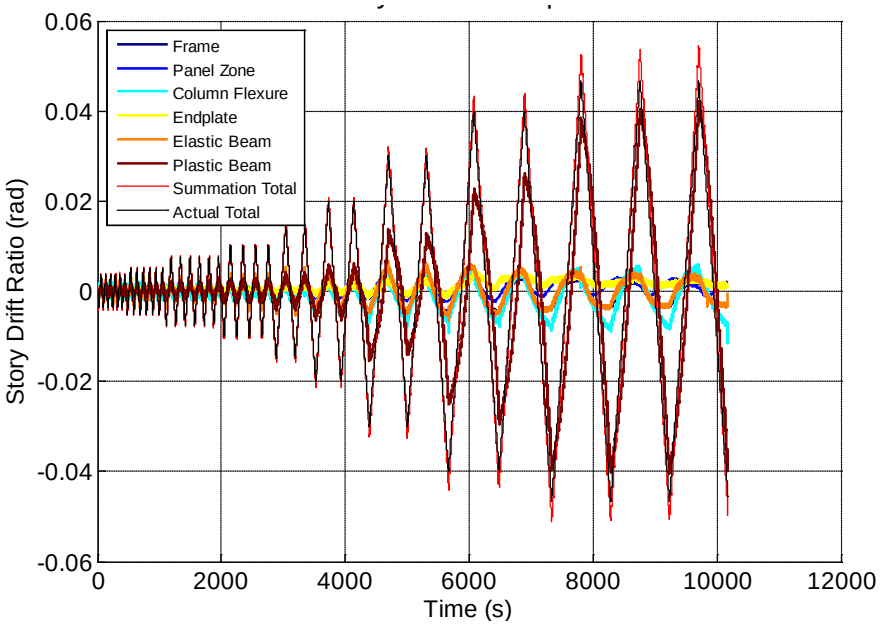

Figure 4.4 – Story Drift Decomposition for a Representative W36x150 without RBS (Specimen 12)

Observation of story drift plots from all tests supports a confidence that no plastic deformation of the test system occurred beyond the plastic hinge of the beam itself. Figure 4.5 presents story drift components over a short period of time during the qualification cycle of Specimen 2 as an example of the general behavior observed in all tests. It is observed that not all elastic components' maximum drift magnitudes occur at the same instance. The elastic system components cycle out of phase from the more prominent beam plasticity. Elastic components occur earlier in the cycle than the plastic hinge component by approximately a quarter cycle. This occurs because elastic deflections are proportional to the current load with a sign related to the current loading direction. Conversely, the story drift due to the plastic hinge maintains the same sign until the plastic deformations are fully reversed. As such, the plastic hinge story drift component is more related to and in sync with the total displacement instead of the applied force.

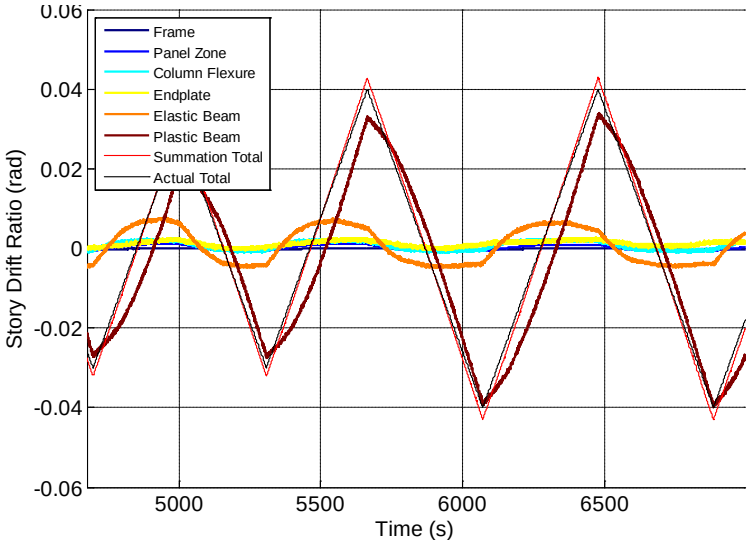

Figure 4.5 – Story Drift Decomposition for Isolated Qualification Cycle for Specimen 2

4.2 Relative Component Contributions

The relative contribution of each system component to the total story drift can also be visualized by viewing the stacked story drift components as percentages of the total. In this way, the summation of all individual story drift relative contributions always equals 100%. In order to avoid graphical shortcomings when certain contributors are of opposite signs or anomolies when the total story drift approaches zero, data is only used from the peaks of the cycles. Figure 4.6 through Figure 4.9 show representative relative component contribution plots for each of the four specimen types. The plots are labeled to indicate the first instance that the system reaches a new story drift amplitude in both the positive and negative directions. Lines between the calculated points associated with each peak is linearly interpolated. It is noted that the apparent presence of beam plasticity during early cycles when the beam is expected to be elastic is due to the fact that the instrumentation placed in the plastic hinge region will inherently record elastic deformation in that portion of the beam. While the absolute value of the elastic beam deformation in the plastic hinge region remains relatively constant through the test, the magnitude is small relative to plastic deformations for cycles of 3% story drift and larger.

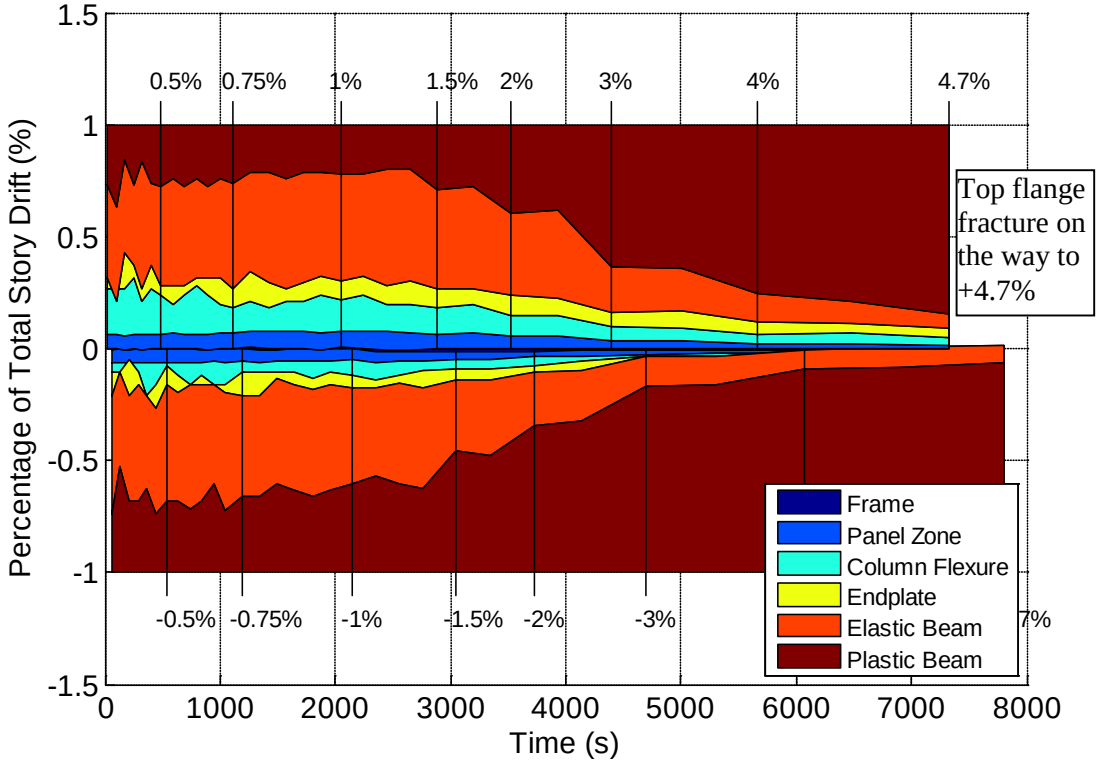

Figure 4.6 – Relative Story Drift Contributions for a Representative W24x62 with RBS (Specimen 2)

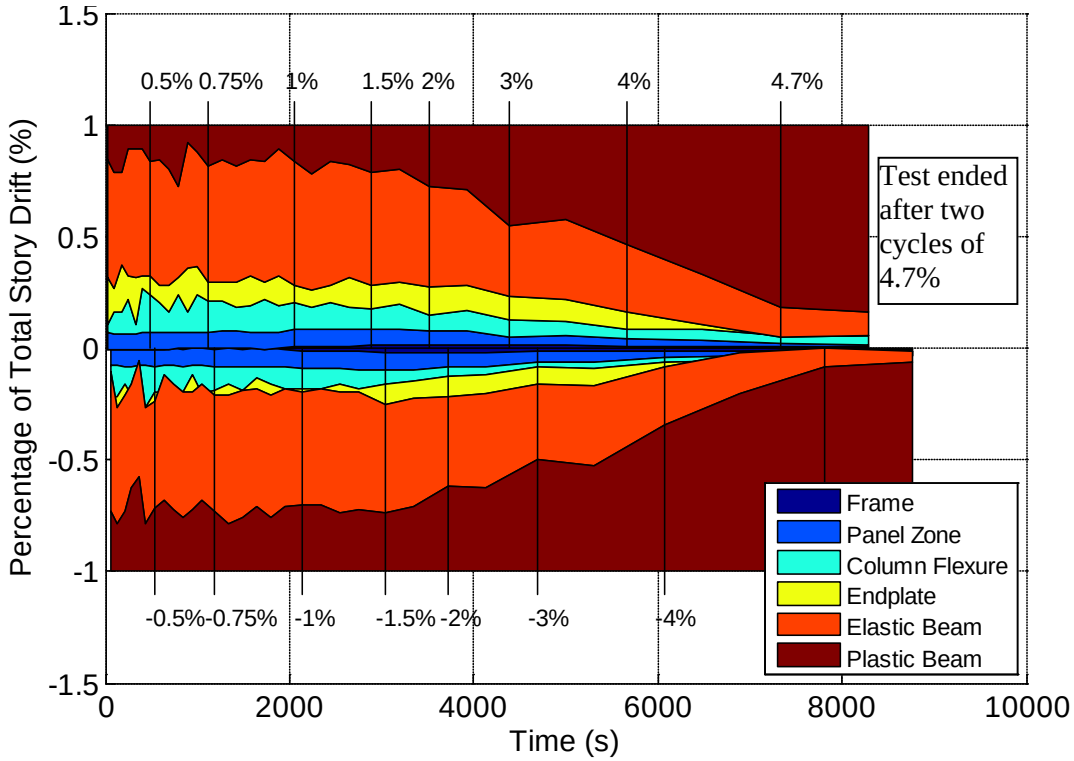

Figure 4.7 – Relative Story Drift Contributions for a Representative W24x62 without RBS (Specimen 4)

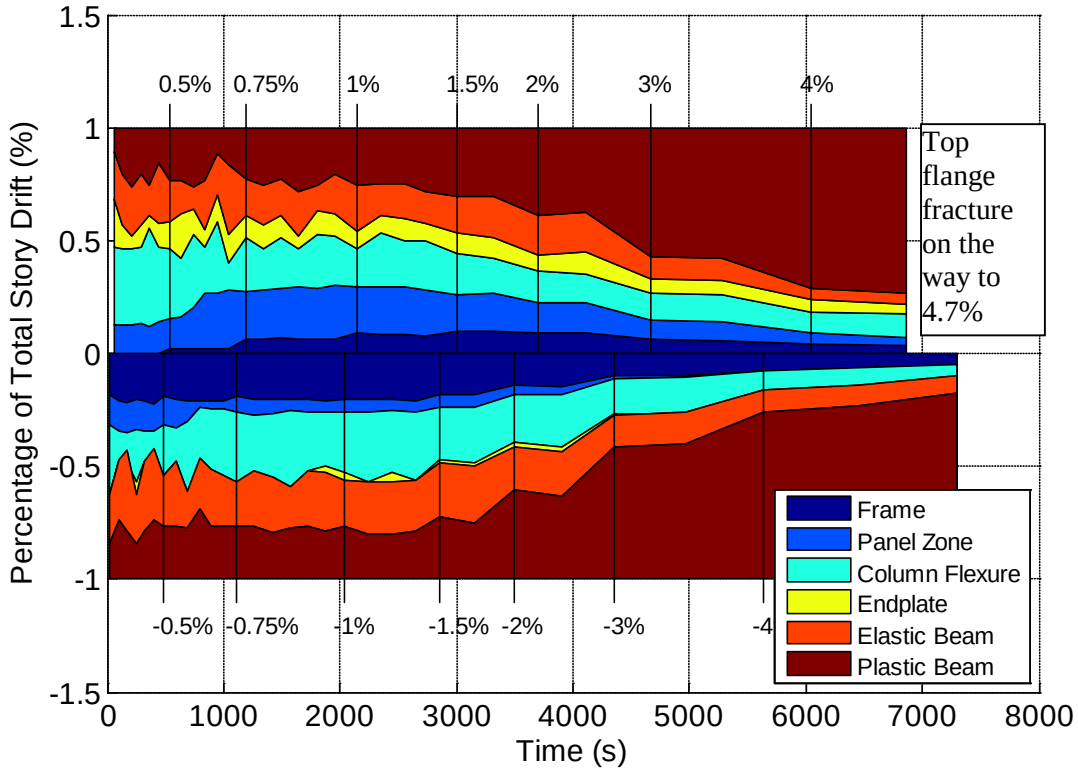

Figure 4.8 – Relative Story Drift Contributions for a Representative W36x150 with RBS (Specimen 9)

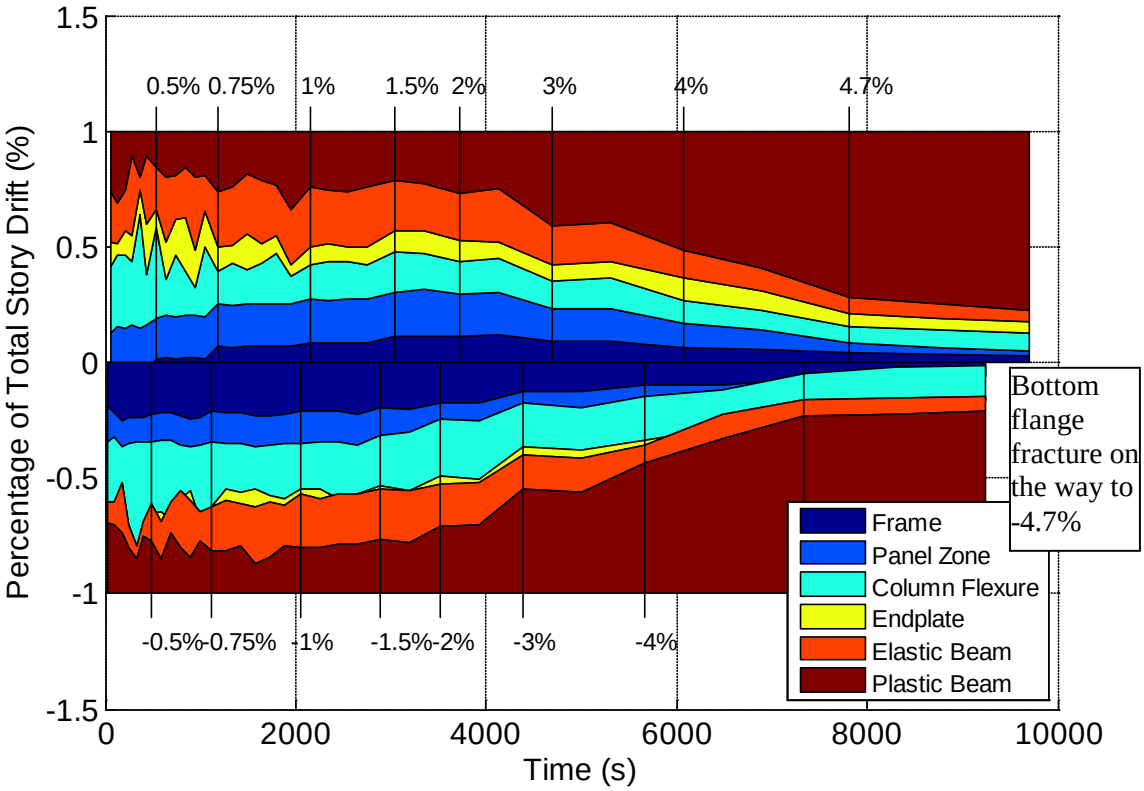

Figure 4.9 – Relative Story Drift Contributions for a Representative W36x150 without RBS (Specimen 12)

Several conceptual observations can be made about the four beam types through comparison of the relative contribution percentage plots. All W24x62 Specimens (1-6) showed a greater contribution from beam elasticity than the W36x150 Specimens (7-12). It is also apparent from the plots that the W36x150 specimens cause larger deformations in the column-related components such as the frame, panel zone and column flexure than the W24x62 specimens. This is expected as both the W36x150 specimens have a greater moment capacity and will only begin yielding once more flexible system components have displaced or deformed due to the applied moment by the actuator.

Table 4.1 summarizes the contribution of the plastic hinge region to the total story drift during the 4% story drift cycles. The testing direction was changed after Specimen 5 to go up first to encourage fractures in the top flange where they could be better viewed. As a result, the story drift values in Table 4.1 are negative for Specimens 1-5 and positive for Specimens 6-12. Another anomaly is noted in that the contribution of beam plasticity for Specimen 10 is noticeably less than that of comparable specimens. This is due to recurring slip between the top of the test column and the column reaction frame. Additional connection reinforcement was made for subsequent tests.

It is apparent from Table 4.1 that plastic deformation of RBS specimens contributes a significantly greater percentage of the total story drift than do non-RBS sections of the same beam type. This is expected due to the weaker moment capacity of the RBS sections which leads to smaller elastic deformation components.

AISC 341-10 Commentary K2.3a (AISC 2010a) states that 75% of the total system story drift should occur in the plastic hinge region of the beam during the qualification cycle. Typical measurement of story drift due to plastic hinge deformations made in tests found in the literature include the rotation of the beam relative to the column. In the story drift decomposition presented in this chapter, both the story drift contributions attributed to the plastic hinge and the end plate would contribute to the plastic hinge and connection deformation. The contribution of these two components to the total story drift is tabulated in Table 4.1 for the qualification cycle and the subsequent cycle labeled as the final 4% cycle amplitude.

Table 4.1 shows that five of the specimens did not produce plastic hinge deformations that accounted for 3% story drift during the qualification cycle. Two of the specimens did not produce

3% story drift associated with the plastic hinge by the end of the 4% story drift cycles. However, the qualification requirement is interpreted to mean that the qualifying cycle should occur when the plastic hinge is contributing 3% story drift. For most specimens, this occurred during the 4% cycles. Although this was not the case for Specimens 6 and 10, these specimens achieved more than 3% story drift due to plastic hinge rotation in the first 4.7% drift cycle and they sustained the required $0.80M_p$ during this cycle. In this way, all specimens satisfied the qualification criteria of sustaining 80% of their nominal plastic moment capacity during one full cycle in which the beam plastic hinge contributed at least 3% story drift.

Table 4.1: Portion of Total Story Drift Due to Beam Plastic Hinge and End Plate Connection

Beam Type	**Test**	**At Qualification (Second 4% Amplitude)**				**Final 4% Amplitude**			
		Total Story Drift (%)		**Beam Plasticity With Endplate (%)**		**Total Story Drift (%)**		**Beam Plasticity With Endplate (%)**	
		Calc.	Actual	Beam Plasticity	Percent of Actual Total	Calc.	Actual	Beam Plasticity	Percent of Actual Total
W24x62 RBS	Test 1	-4.28	-4.00	-3.58	**90%**	-4.29	-4.00	-3.68	**92%**
	Test 2	-4.31	-4.00	-3.81	**95%**	-4.30	-4.00	-3.81	**95%**
	Test 5	-4.29	-4.00	-3.60	**90%**	-4.30	-4.00	-3.66	**92%**
W24x62 Non-RBS	Test 3	-4.23	-4.00	-2.88	**72%**	-4.26	-4.00	-3.27	**82%**
	Test 4	-4.23	-4.00	-2.84	**71%**	-4.26	-4.00	-3.25	**81%**
	Test 6	4.21	4.00	2.56	**64%**	4.23	4.00	2.86	**72%**
W36x150 RBS	Test 7	4.42	4.00	3.25	**81%**	4.44	4.00	3.38	**85%**
	Test 8	4.49	4.00	3.33	**83%**	4.53	4.00	3.44	**86%**
	Test 9	4.58	3.99	3.50	**88%**	4.62	3.99	3.58	**90%**
W36x150 Non-RBS	Test 10	4.30	4.00	2.21	**55%**	4.37	4.00	2.64	**66%**
	Test 11	4.39	4.00	3.09	**77%**	4.45	4.00	3.29	**82%**
	Test 12	4.34	4.00	2.68	**67%**	4.39	4.00	2.99	**75%**

CHAPTER 5 DISCUSSION OF RESULTS

5.1 Discussion of Fracture

Several general observations are made regarding the fracture behavior of the twelve specimens. Table 5.1 provides a summary of the fractures and shows that all six RBS specimens experienced some degree of fracture during 4.7% story drift cycling with Specimen 1 experiencing a ductile flange tear and the other five RBS specimens experiencing brittle fractures along an entire flange width and a portion of the web. The only non-RBS specimen to experience a fracture was Specimen 12 which contained a grid of PAF over both flanges and the web.

Table 5.1 – General Observations of the Twelve Specimens

Specimen Number	Specimen Description	Cycle at Significant Fracture	Fracture Location
1	W24x62 with RBS but No Fasteners	2nd Cycle at 4.7% Story Drift	Bottom Flange Near Center of RBS (Ductile tear, half the flange width, stopped at web)
2	W24x62 with RBS and PAF at 12	2nd Cycle at 4.7% Story Drift	Through PAF at Center of RBS on Top Flange
3	W24x62 without RBS or Fasteners	N/A	Test Stopped After Two Cycles at 4.7% No Fracture
4	W24x62 without RBS and PAF at 12	N/A	Test Stopped After Two Cycles at 4.7% No Fracture
5	W24x62 with RBS and Puddle Welds at 12 in.	3rd Cycle at 4.7% Story Drift	Bottom Flange, Away from Puddle Welds, Near Center of RBS
6	W24x62 without RBS and Grid of PAF	N/A	Test Stopped After Five Cycles at 4.7% No Fracture
7	W36x150 with RBS and No Fasteners	5th Cycle at 4.7% Story Drift	Top Flange at Center of RBS, Initial Fracture Partial Depth then Opened
8	W36x150 with RBS and Puddle Welds at 12	2nd Cycle at 4.7% Story Drift	Bottom Flange at Tip of End-Plate Stiffener, Not at Puddle Welds
9	W36x150 with RBS and Grid of PAF	1st Cycle at 4.7% Story Drift	Top Flange Near Center of RBS Through Two PAF
10	W36x150 without RBS and No Fasteners	N/A	Test Stopped After Five Cycles at 4.7% No Fracture
11	W36x150 without RBS and PAF at 12	N/A	Test Stopped After Five Cycles at 4.7% No Fracture
12	W36x150 without RBS and Grid of PAF	During 4th Cycle at 4.7% Story Drift	Bottom Flange Through Multiple PAF and Into a PAF Located on the Web

For the W24x62 beam specimens with RBS, the fractures occurred during the 2nd or 3rd cycle at 4.7% story drift regardless of whether there were PAF, puddle welds, or no fasteners included in the protected zone. The W36x150 RBS specimen with no fasteners fractured during

the 5th cycle at 4.7% story drift whereas the specimens with a grid of PAF and puddle welds fractured in the 2nd and 1st cycles at 4.7% story drift respectively. However the fracture in the specimen with puddle welds (Specimen 8) was not related to the puddle welds, but instead occurred at the junction of the stiffener and flange. This implies some inherent variability in the cycle at which fracture occurs. Specimen 12 which included a grid of PAF fractured during the 4th cycle at 4.7% story drift whereas the other non-RBS specimens (Specimens 10 and 11) did not experience fracture through the 5th cycle at 4.7% story drift even though Specimen 11 included PAF at 12 in. spacing.

Although the W24x62 specimens suggest no difference, the results for the W36x150 specimens that included a grid of fasteners not representative of common construction practices suggest that one or more PAF applied in critical locations such as the inside of a local buckle may lead to fracture during an earlier cycle in the displacement protocol. The potential for fracture is supported by the small tears that formed at PAF in critical locations after a large number of inelastic strain cycles. It is noted, however, that fracture occurred well after SMRF qualification had been satisfied, the difference in the cycle number at fracture was small, and that the two W36x150 specimens that fractured included a grid of PAF that represent an extreme condition, not indicative of construction practice. Since the sample size is small and the difference in the cycle number at fracture is small, it was not possible to evaluate the difference in a statistically significant manner.

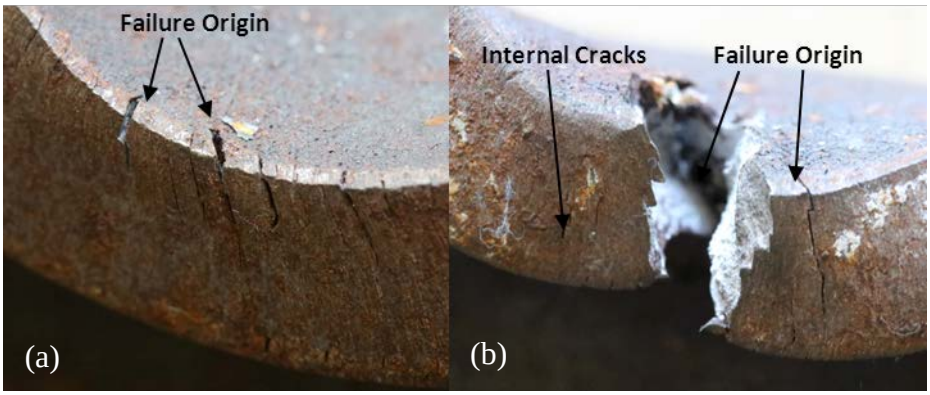

Figure 5.1 – Crack initiation at two different locations on both sides of the bottom flange. Crack and fracture initiation (a) and crack initiation at other side of the flange (b)

For the W24x62 beam specimens, multiple failure origins at different sides and locations were observed at the flange tip for all of the failed specimens (Specimen 1, 2, and 5) but only one of them controlled the fracture propagation for the fractured specimens. Some examples of the crack initiation and fracture origin for the W24x62 specimens are shown in Figure 5.1. For Specimens 2 and 5, it was noted that the specimens went through a ductile overload before the brittle failure. This can be clearly seen from the failed surface texture and striations as shown in Figure 5.2.

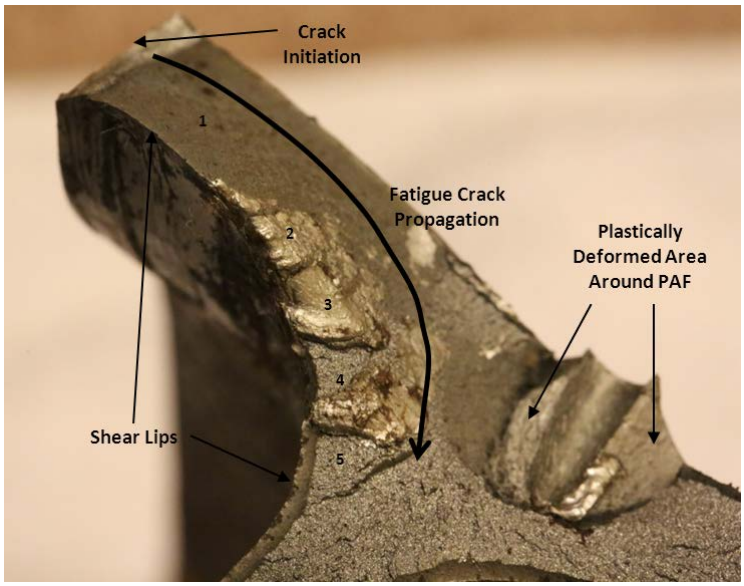

Figure 5.2 – Striation locations and fatigue crack propagation

While for the W36x150 beam specimens, the crack initiation and fracture origin were observed at the surface of the flange near the tip of the flange, as shown in Figure 5.3, typically at one side only. This was most clearly observed in Specimen 7. Specimens 9 and 12 failure origins were similar to Specimen 7, the difference being that a PAF is located at the failure origin at the surface of the flange. The only specimen which showed a different fracture pattern was Specimen 8 in which fracture initiated at the toe of the flange stiffener. This fracture occurred due to high stress triaxiality at the stiffener toe.

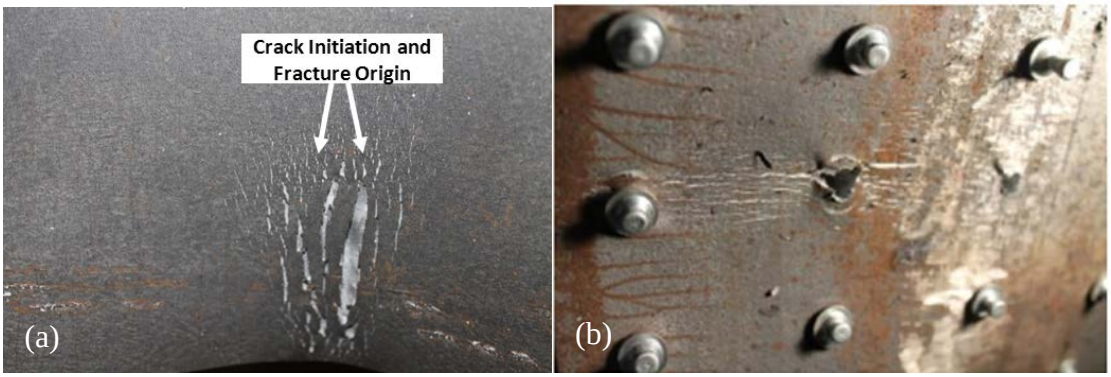

Figure 5.3 – Crack Initiation and Failure Origin at the Flange Surface Before Fracture Occurrence for Specimen 7 (a) and Specimen 12 (b)

5.2 Comparison of Cyclic Load-Deformation Behavior

Figure 5.4 shows an overlay of the load-deformation response for all three W24x62 RBS specimens. Figure 5.5 shows the moment envelope from the same test data. Envelope plots show the maximum moments at each new story drift amplitude and provide a simplified visual reference of the load-deformation behavior at peak moments. As shown in Figure 5.4 and Figure 5.5, the inclusion of fasteners or puddle welds had a negligible effect on the load-deformation behavior of the specimens as all three performed in a nearly identical manner.

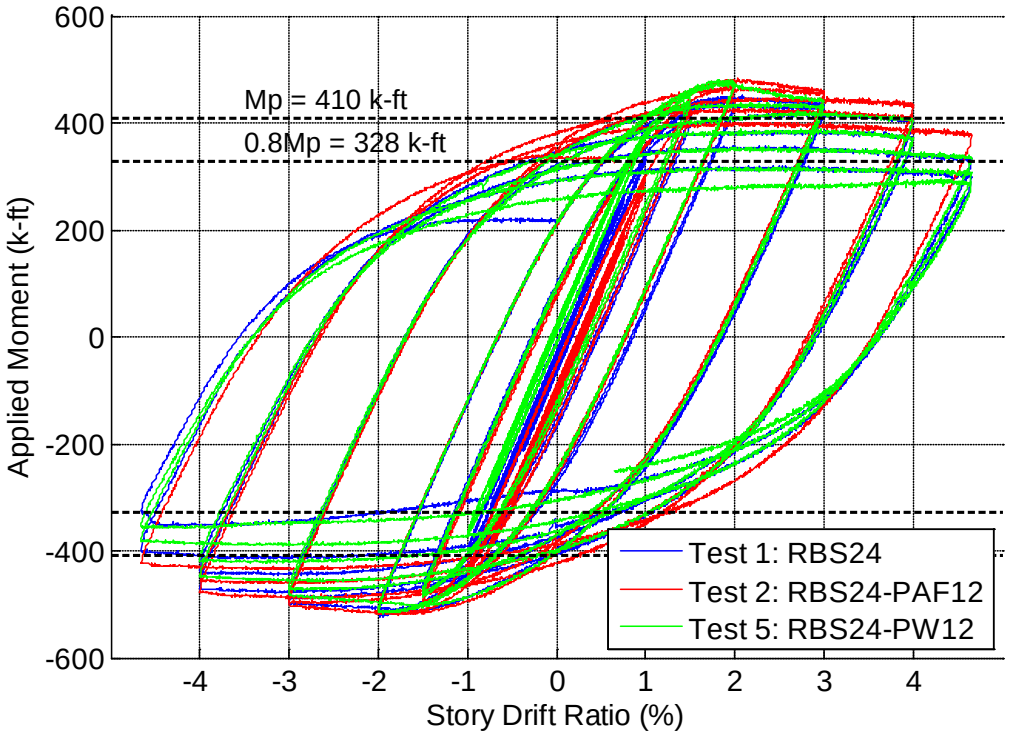

Figure 5.4 – Hysteresis Comparison of W24x62 RBS Specimens

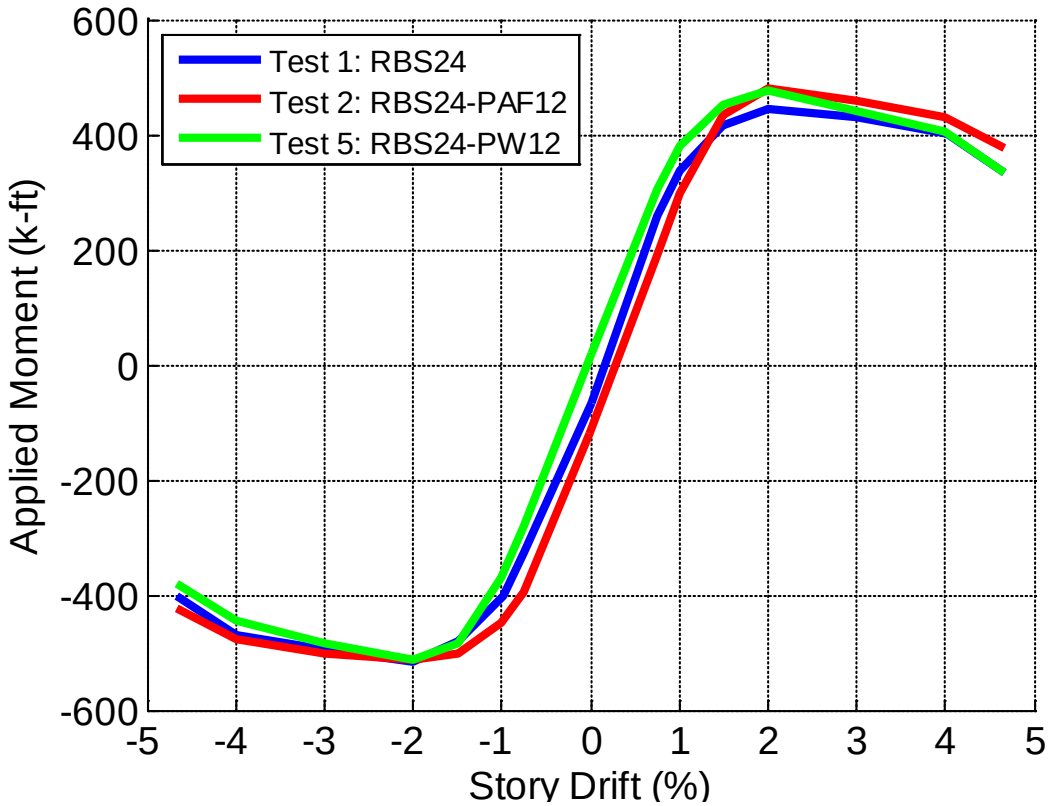

Figure 5.5 – Envelope Comparison of W24x62 RBS Specimens

Figure 5.6 shows an overlay of the load-deformation behavior of all three W24x62 specimens with no RBS. Figure 5.7 shows the cyclic envelope from the same test data. As shown in Figure 5.6, the inclusion of fasteners did not seem to have a significant effect on the load-deformation behavior of the specimen as all three performed in a similar manner. Specimen 6 included a grid of PAFs. The specimen exhibited a moment-drift response similar to the other specimens and was subjected to five cycles at 4.7% story drift without fracture. During the final several cycles, tears were forming at the PAF locations but were propagating so slowly that they did not significantly affect the moment-rotation behavior.

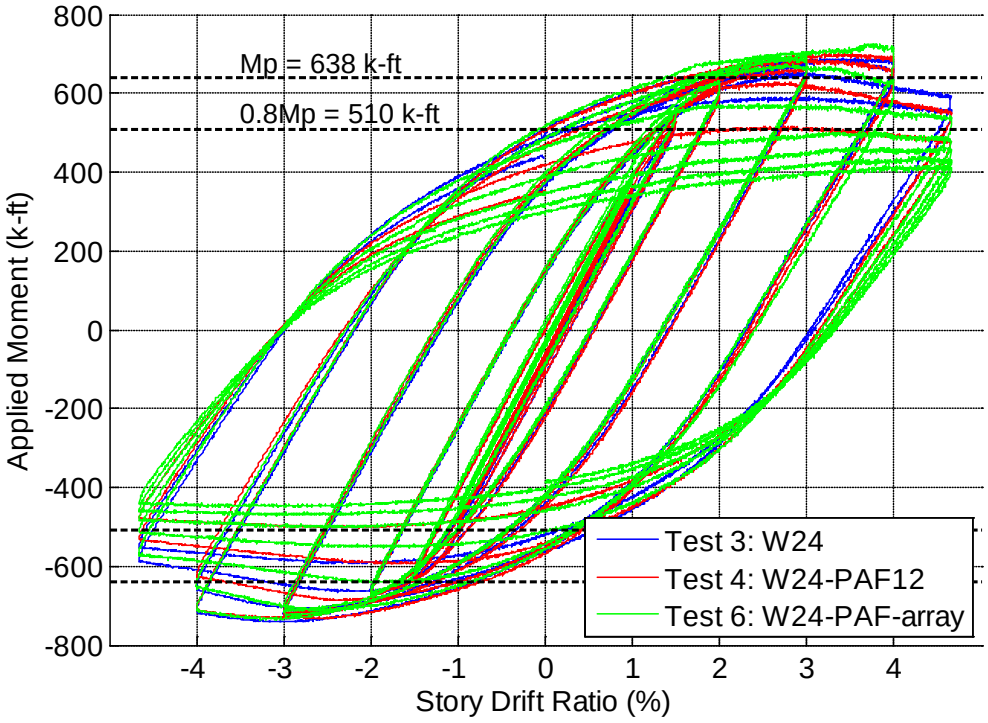

Figure 5.6 – Hysteresis Comparison of W24x62 Non-RBS Specimens

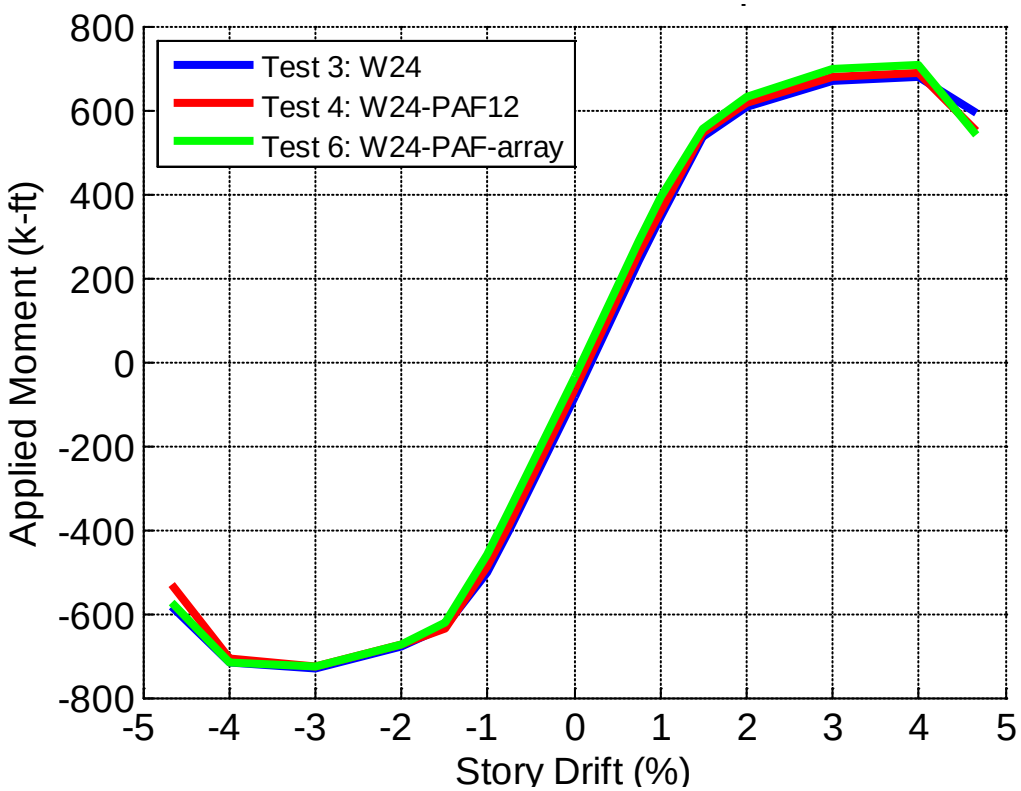

Figure 5.7 – Envelope Comparison of W24x62 Non-RBS Specimens

Figure 5.8 shows an overlay of the load-deformation behavior of all three W36x150 RBS specimens. Figure 5.9 shows the moment-drift envelope from the same test data. Again, it is shown in Figure 5.8, that the inclusion of fasteners or puddle welds did not seem to have a significant effect on the moment-rotation behavior of the specimen prior to fracture as all three performed in a similar manner through the first cycle of 4.7% story drift.

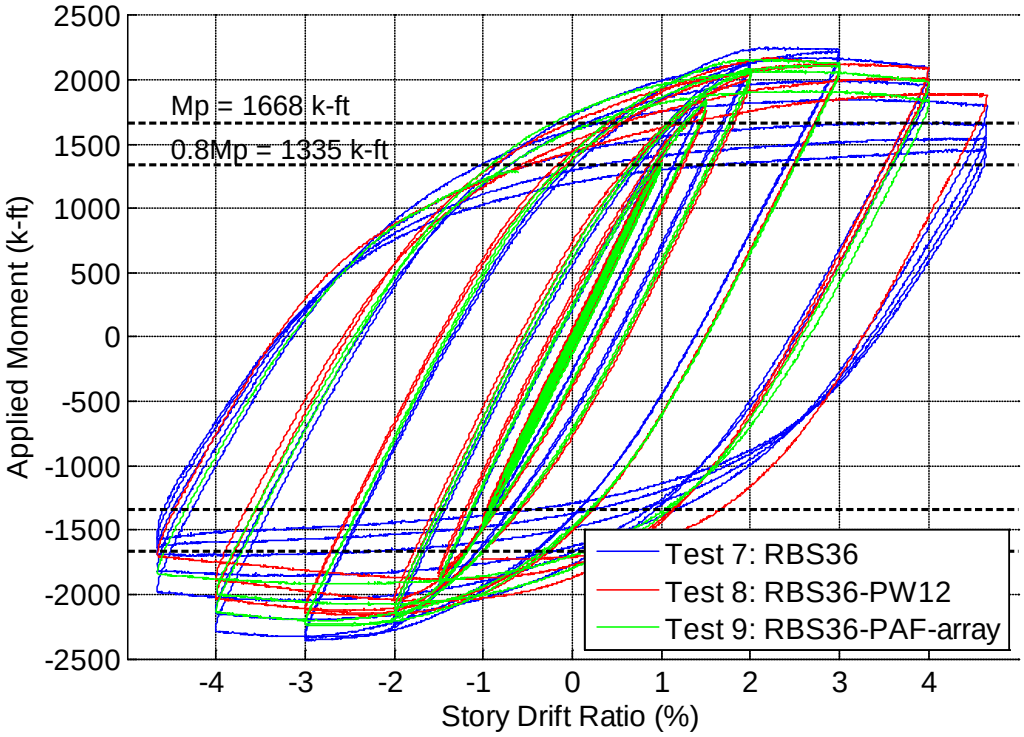

Figure 5.8 – Hysteresis Comparison of W36x150 RBS Specimens

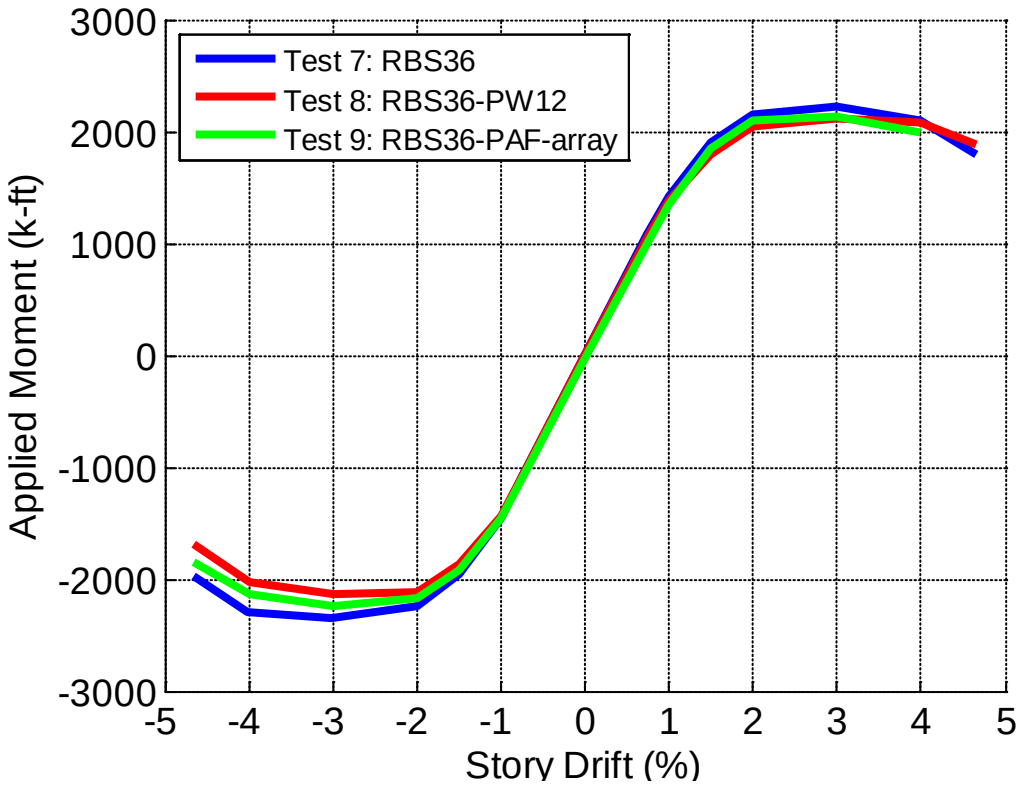

Figure 5.9 – Envelope Comparison of W36x150 RBS Specimens

Figure 5.10 shows an overlay of the load-deformation behavior of all three W36x150 non-RBS specimens. Figure 5.11 shows the moment envelope from the same test data. Similar to the previous plots, Figure 5.10 shows that the inclusion of fasteners did not have a significant effect on the moment-drift behavior of the specimen as all three showed a similar hysteresis behavior up to the point of fractures.

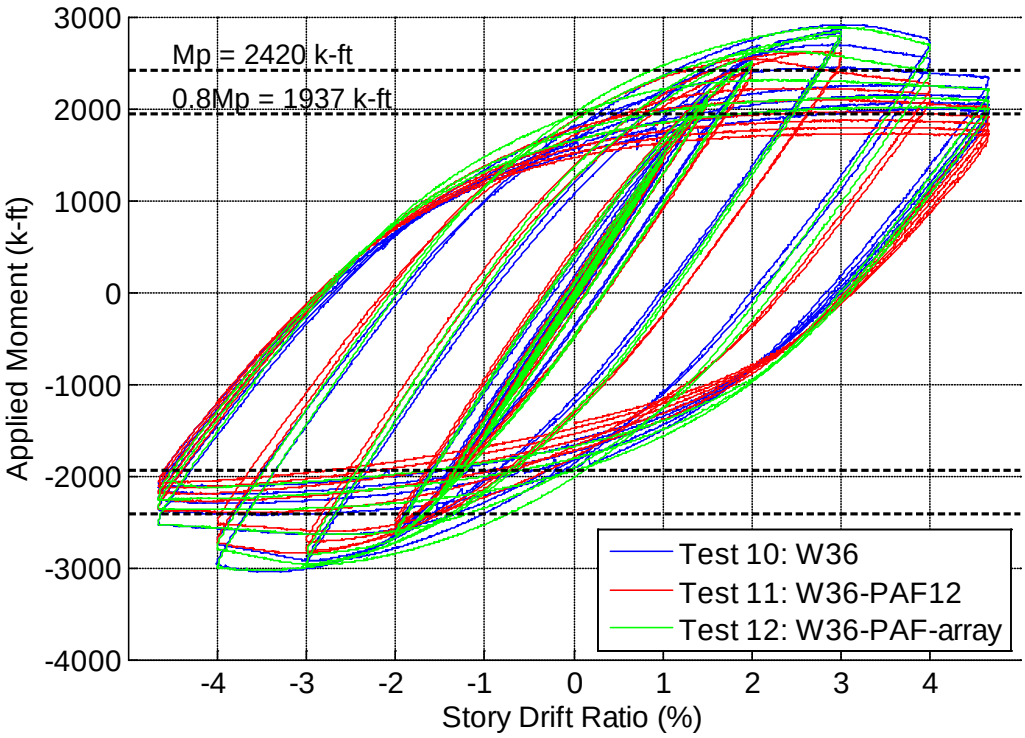

Figure 5.10 – Hysteresis Comparison of W36x150 Non-RBS Specimens

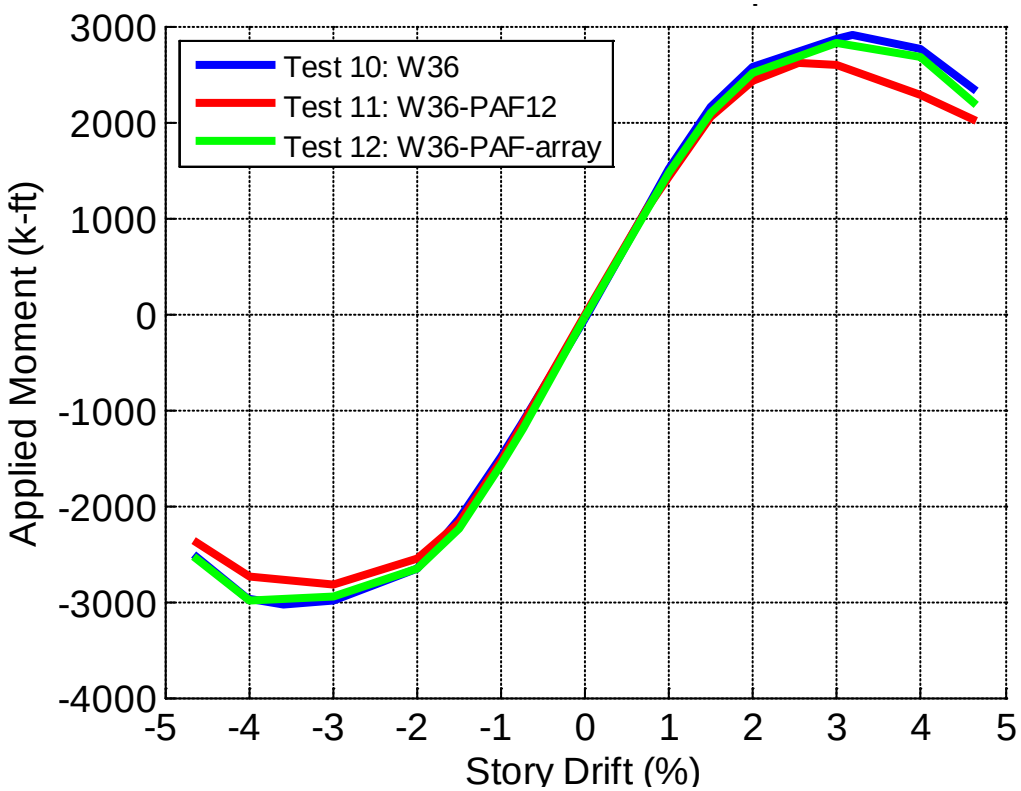

Figure 5.11 – Envelope Comparison of W36x150 Non-RBS Specimens

5.2 Test Specimen Strength Analysis

This section provides a summary of the moment capacity of all test specimens. All moment capacities in this section are reported as the applied moment at the face of the column. Figure 5.12 shows a reference image for the values quantified in subsequent tables. Table 5.2 presents a summary of the moment capacities of all test specimens at both positive and negative 4% story drift during the first cycle at this displacement level. It is clear from Table 5.2 that all specimens satisfied qualification requirements by maintaining greater than 80% of their nominal plastic moment capacity during the first cycle of 4% story drift.

It is noted that the first five specimens (Specimens 1-5) were tested such that for any given cycle the beams were deflected downward (positive story drift) first. All remaining tests were reversed so that beams were deflected upward before being deflected down. The change was made after it was observed that the flanges that were more likely to fracture were those that experienced

compression first. It was desirable to switch the displacement direction so that it was more likely to fracture in the top flange where it was easier to observe and document crack propagation.

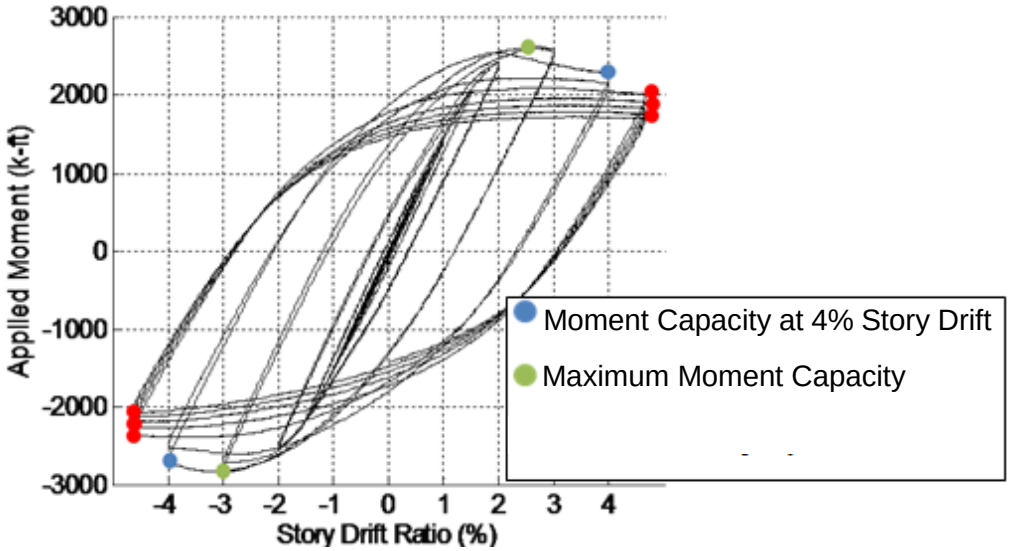

Figure 5.12 – Moment Capacity Reference Image

Table 5.2 – Qualification Cycle - Moment Capacity

Beam Type	.8Mp	Test	First Qualification Amplitude		Second Qualification Amplitude	
			Story Drift	Moment (k-ft)	Story Drift	Moment (k-ft)
W24x62 with RBS	328 k-ft	Test 1	4 %	402	- 4 %	-471
		Test 2	4 %	432	- 4 %	-476
		Test 5	4 %	404	- 4 %	-446
W24x62 with BUEEP	510 k-ft	Test 3	4 %	681	- 4 %	-718
		Test 4	4 %	688	- 4 %	-709
		Test 6	- 4 %	-715	4 %	709
W36x150 with RBS	1335 k-ft	Test 7	- 4 %	-2287	4 %	2091
		Test 8	- 4 %	-2033	4 %	2082
		Test 9	- 4 %	-2141	4 %	1990
W36x150 with BSEEP	1937 k-ft	Test 10	- 4 %	-2966	4 %	2754
		Test 11	- 4 %	-2733	4 %	2280
		Test 12	- 4 %	-2984	4 %	2683

Table 5.3 tabulates the maximum moment capacity experienced at any time during the test with corresponding story drift. The values are tabulated for both positive (downward deflection) and negative (upward deflection) moments. It also provides an average of these values for each of the four specimen types. Nominal moment capacities are listed for each beam type and an additional predicted moment capacity using the measured yield stress of 53 ksi is provided.

The results tabulated in Table 5.3 demonstrate, as expected, that all specimens experienced significant plastic hinging and developed quite a bit of strain hardening. Furthermore, there was negligible difference in the peak moment capacities of specimens with and without fasteners or puddle welds.

Table 5.3 – Maximum Moment Capacity

Beam Type	Nominal Mp Fy=50ksi	Predicted Mp Fy=53ksi	Test	Maximum Positive Moment Capacity			Maximum Negative Moment Capacity		
				Story Drift	Moment (k-ft)	Average (k-ft)	Story Drift	Moment (k-ft)	Average (k-ft)
W24x62 with RBS	410 k-ft	435 k-ft	Test 1	2.1 %	452	471	-1.9 %	-524	-520
			Test 2	2.0 %	482		-1.8 %	-520	
			Test 5	1.8 %	480		-1.9 %	-517	
W24x62 with BUEEP	638 k-ft	676 k-ft	Test 3	3.6 %	690	706	-3.0 %	-743	-737
			Test 4	3.4 %	701		-2.5 %	-733	
			Test 6	3.8 %	726		-3.0 %	-736	
W36x150 with RBS	1668 k-ft	1768 k-ft	Test 7	2.3 %	2252	2195	-2.9 %	-2357	-2257
			Test 8	2.2 %	2171		-2.3 %	-2167	
			Test 9	2.0 %	2161		-3.0 %	-2246	
W36x150 with BSEEP	2420 k-ft	2565 k-ft	Test 10	3.0 %	2916	2809	-3.4 %	-3047	-2974
			Test 11	2.7 %	2625		-3.1 %	-2844	
			Test 12	2.9 %	2886		-3.5 %	-3030	

5.3 Strength Degradation

As given in Equation (5.1, a strength degradation ratio, η, was defined for a given story drift amplitude, i, as the ratio of the moment at the second peak displacement, M_{cycle2}, to the moment at the first peak displacement, M_{cycle1}. Despite its designation as a strength reduction ratio, values greater than 100% are possible and indicate an increase in moment capacity due to strain hardening. Figure 5.13 through Figure 5.16 shows the strength degradation ratio plotted for each of the four specimen types starting with the 1% story drift cycles. It is noted that additional strength degradation beyond the first two 4.7% story drift cycles are not reflected in these plots.

$$\eta = \left[\frac{M_{Cycle2}}{M_{Cycle1}}\right]_i * 100\% \tag{5.1}$$

As shown in Figure 5.13 and Figure 5.15, local buckling in the RBS specimens contributes to strength degradation in a more gradual way as compared to the Non-RBS specimens (Figure 5.14 and Figure 5.16) which experience an abrupt change in strength degradation behavior from 3% story drift to 4% story drift. Most specimens (RBS and Non-RBS) did not experience a significant reduction in moment capacity over repeated cycles until the 4% story drift cycles. During both 4% and 4.7% cycles, most specimens showed a strength reduction of 90-95% from the first to the second peak displacement. Regardless of specimen type, the inclusion of PAF and puddle welds do not have any observable effect on strength degradation.

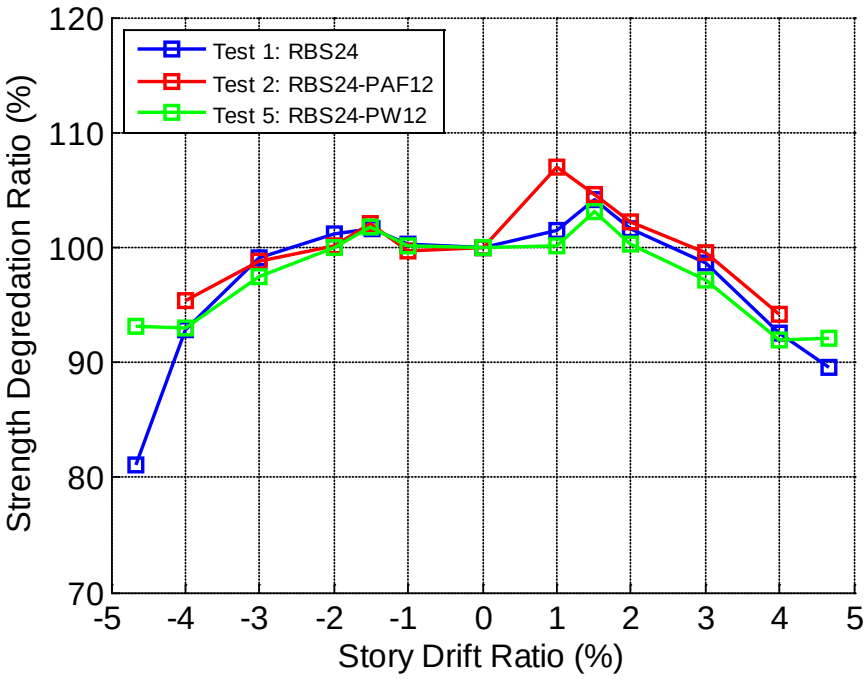

Figure 5.13 – Strength Degradation Comparison of W24x62 RBS Specimens

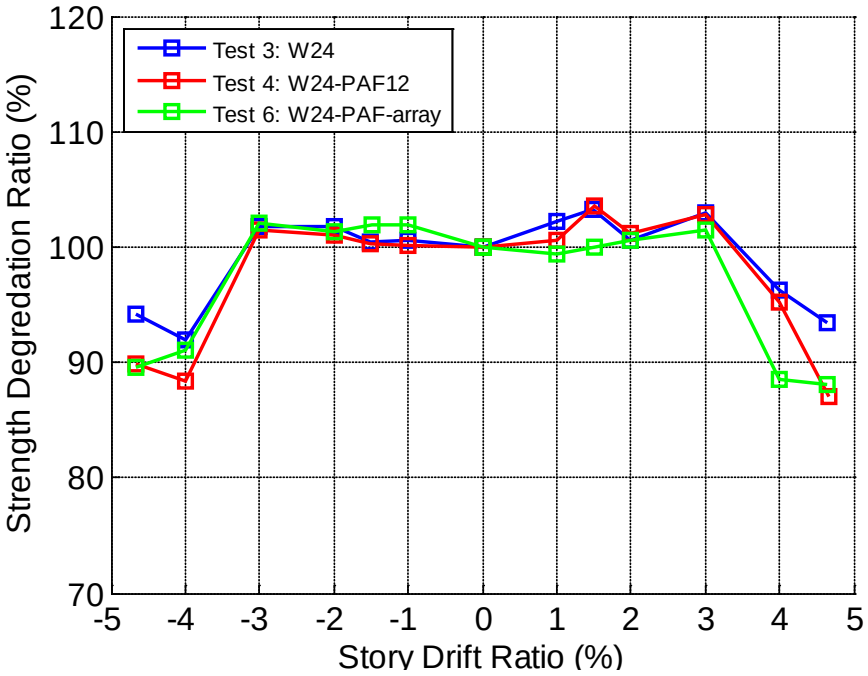

Figure 5.14 – Strength Degradation Comparison of W24x62 BUEEP Specimens

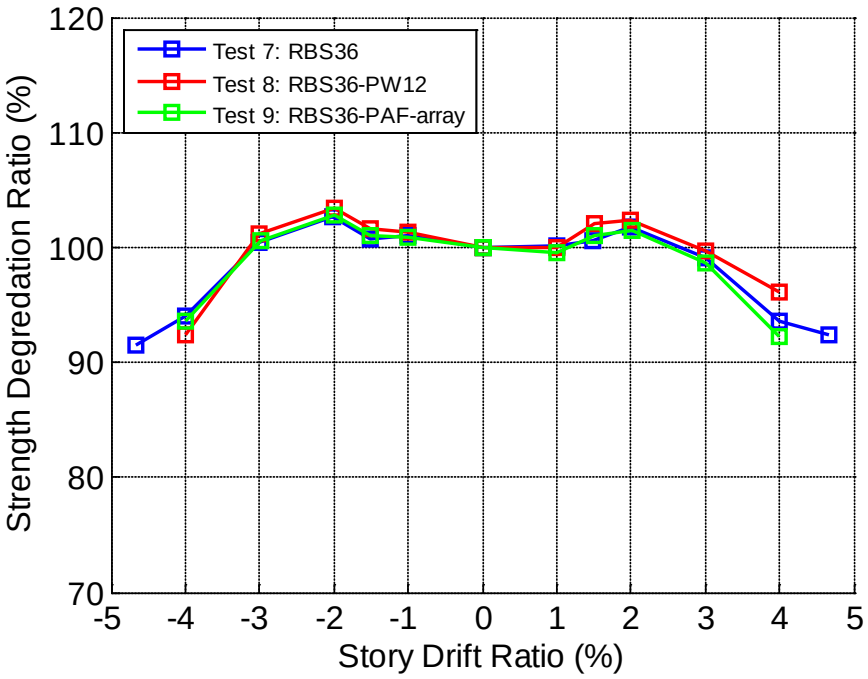

Figure 5.15 – Strength Degradation Comparison of W36x150 RBS Specimens

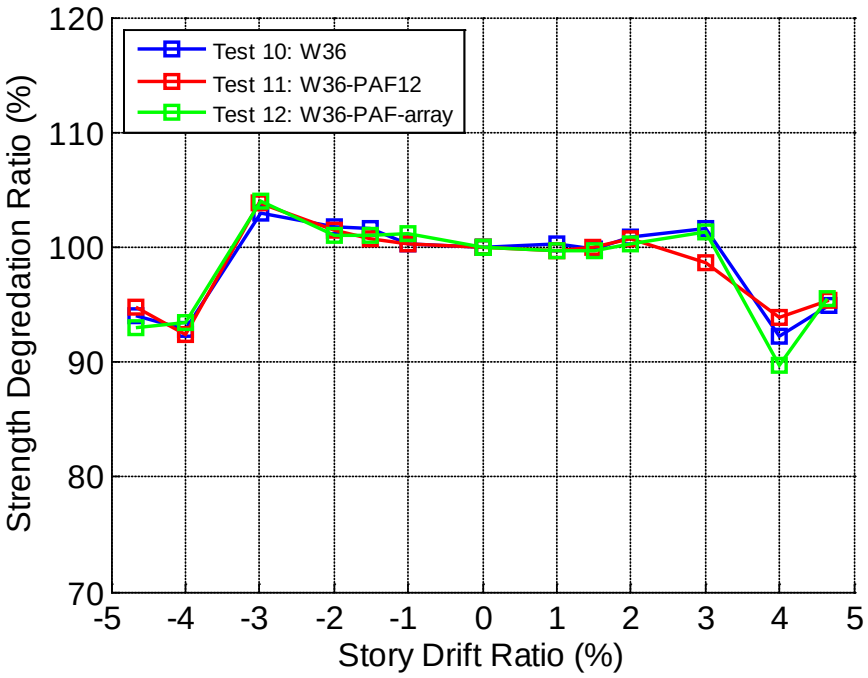

Figure 5.16 – Strength Degradation Comparison of W36x150 BSEEP Specimens

5.4 Energy Dissipation

Dissipated energy was calculated as the numerical integration of the cyclic moment versus story drift curve. Figure 5.17 through Figure 5.20 show the evolution of energy dissipation for each of the four specimen types. Markers on individual lines indicate the instances of peak rotation magnitudes (both positive and negative peaks) starting at 1% story drift. Peaks prior to 1% story drift cycles are not shown as the plastic deformation is negligible prior to 1%. Figure 5.17 through Figure 5.20 show that the inclusion of PAF and puddle welds have no observable effect on energy dissipated by the beam-to-column moment connection.

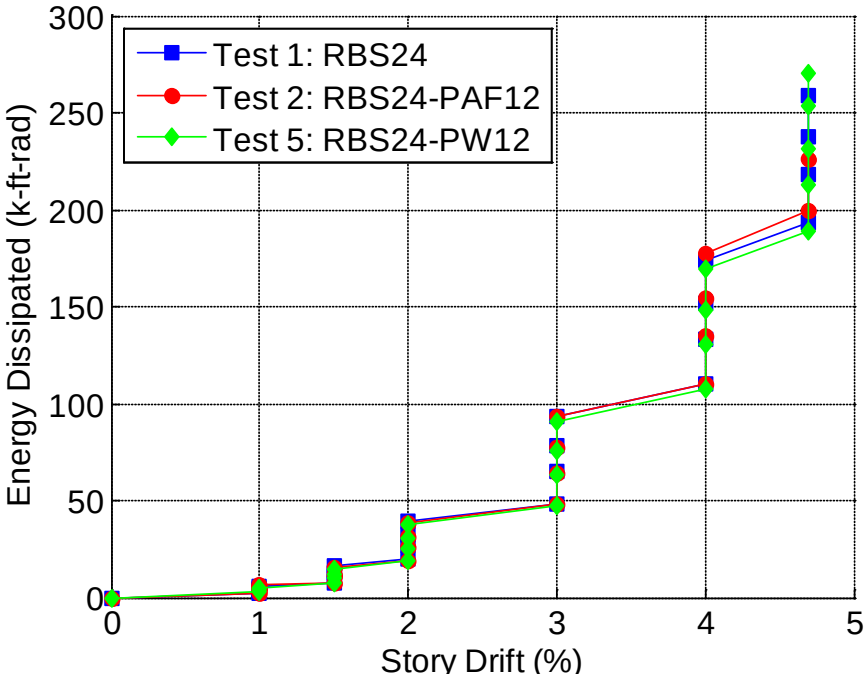

Figure 5.17 – Energy Dissipation Comparison of W24x62 RBS Specimens

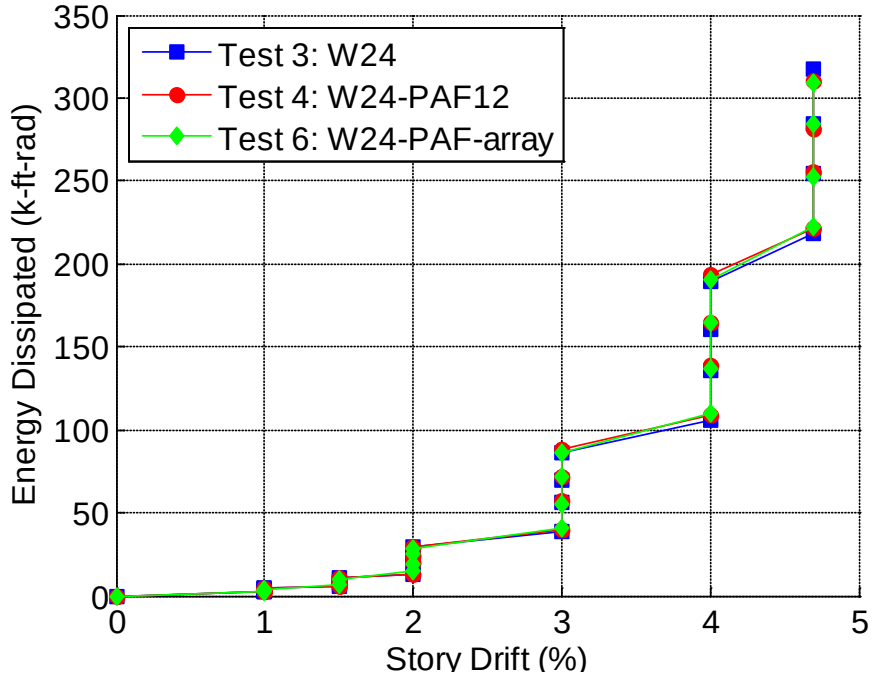

Figure 5.18 – Energy Dissipation Comparison of W24x62 Non-RBS Specimens

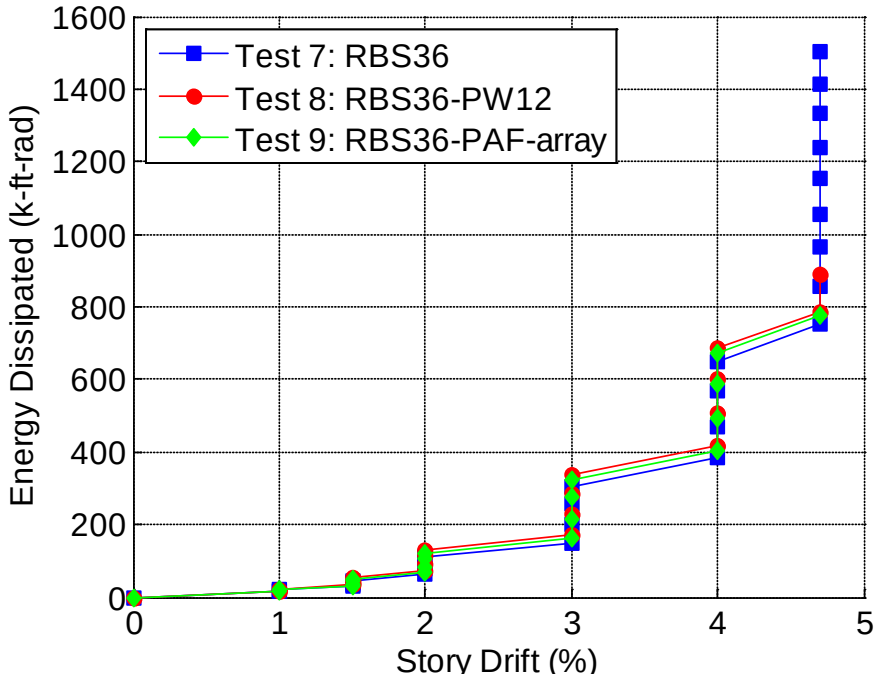

Figure 5.19 – Energy Dissipation Comparison of W36x150 RBS Specimens

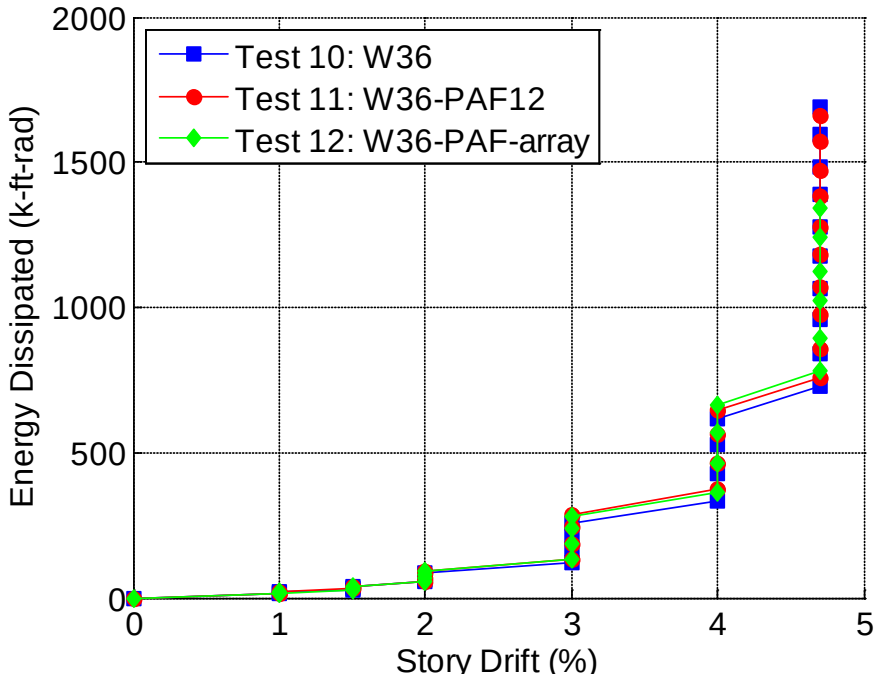

Figure 5.20 – Energy Dissipation Comparison of W36x150 Non-RBS Specimens

5.5 Strain Distribution Comparison

Strain gages were located along lines and attached to the top and bottom surfaces of the beam top flange of all twelve specimens at consistent locations. The motivation behind these lines of strain gages is to provide strain profiles at the location of the fasteners. Comparison of strain profiles between tests is conducted to assess strain concentrations that might occur due to the presence of PAFs or puddle welds.

The effect of fasteners and puddle welds on the measured strain gradient across the flange was negligible for the W24 and W36. This was observed during the first six tests of the W24 specimens. After finding that the effect of fasteners on the strain gradient across the flange was small, only two strain gage lines were used for the W36 specimens instead of three strain gage lines which were used for the W24 specimens.

Progression of strain during a test is shown in Figure 5.21 and Figure 5.22 for a W24 and W36 specimen. It can be clearly noticed the strain increasing as the story drift increases in a consistent trend while cycling elastically. After that the strain line starts deforming in a non-

consistent behavior which represents the profile of the top flange local buckling. For Specimen 3, strain line 1 shows higher strain than strain line 2. For this non-RBS W24 specimen there is a higher potential for a fracture to occur in the region of strain line 1 which is located few inches from the connection. Also, the strain gradient is more uniform farther away from the column connection, as shown in Figure 5.21, since strain line 1 is closer to the column connection followed by line 2 and line 3 respectively. For Specimen 12, strain line 2 experiences larger strains than strain line 1. For this non-RBS W36 specimen, it showed a different behavior from Specimen 3. Furthermore, the strains are significantly larger in the W36 section than the W24 section. This is expected since the distance from the extreme fiber to the neutral axis is larger. The extreme fibers in the W36 are therefore subjected to larger inelastic strain demands. This may be another reason that the surface cracks formed on the W36 flanges.

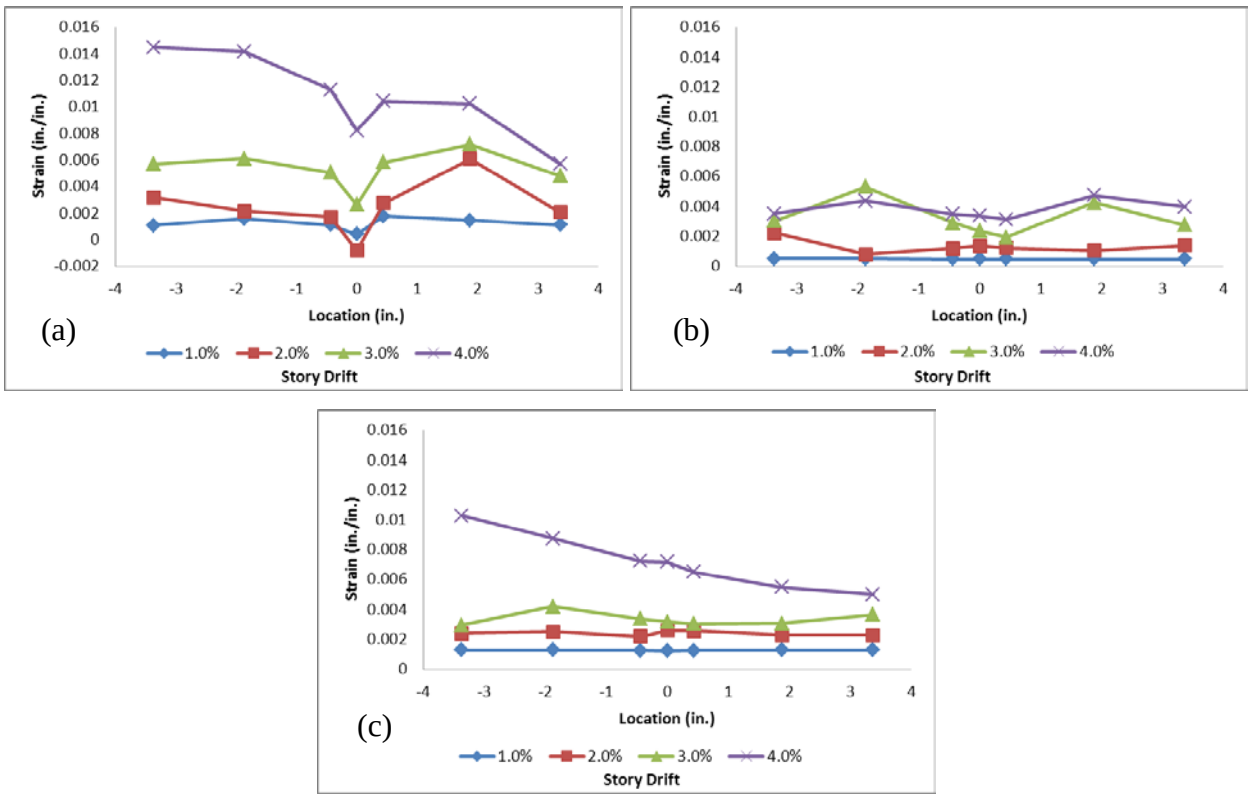

Figure 5.21 – Top Flange Strain Gradient for Specimen 3 (W24x62 without RBS or Fasteners) (a) Line 1, (b) Line 2, and (c) Line 3

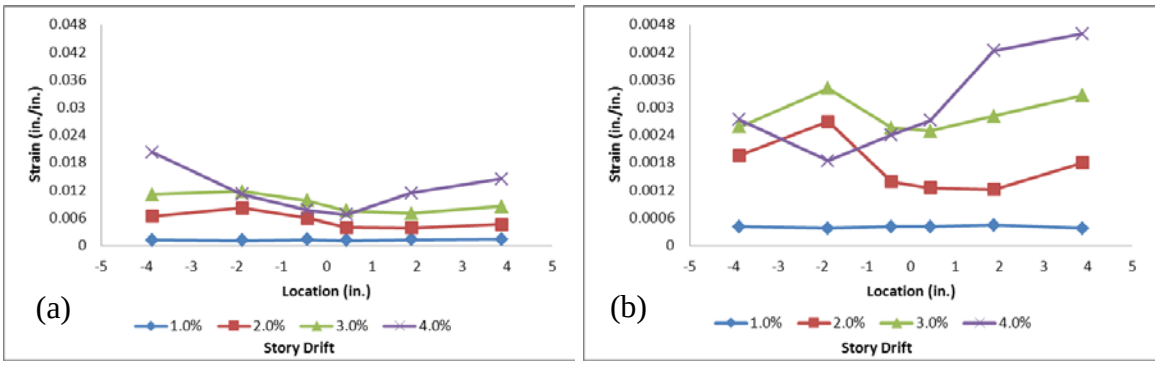

Figure 5.22 – Specimen 12 (W36x150 with No RBS and Grid of PAFs) Top Flange Strain Data (a) Line 1, and (b) Line 2

When comparing strain distributions with and without fasteners, as shown in Figure 5.23, all specimens had similar behavior during the elastic cycles. Specimen 10, 11 and 12 are W36 non-RBS sections. Specimen 10 contains no fasteners, Specimen 11 contains PAF spaced at 12 in., and Specimen 12 contains a grid of PAF. For Specimen 11 and 12, no strain gages were mounted at the center of the flange of strain line 2 since a PAF was located in this location. The data points were connected linearly between the existing closest strain gages which show a continuous strain gradient through the fasteners for Specimen 11 and 12. During the inelastic cycles, each specimen had a unique strain profile as local buckling developed. However, the inelastic strains were not found to concentrate in the vicinity of PAF or puddle welds.

In general, strain gages can be unreliable during large inelastic strain cycles. At large strains, gages are prone to delaminating from the steel and loss of electrical continuity leading to loss of signal. All of the strain gradient plots for the twelve specimens are included in Appendix D. Similar trends can be seen for all twelve specimens.

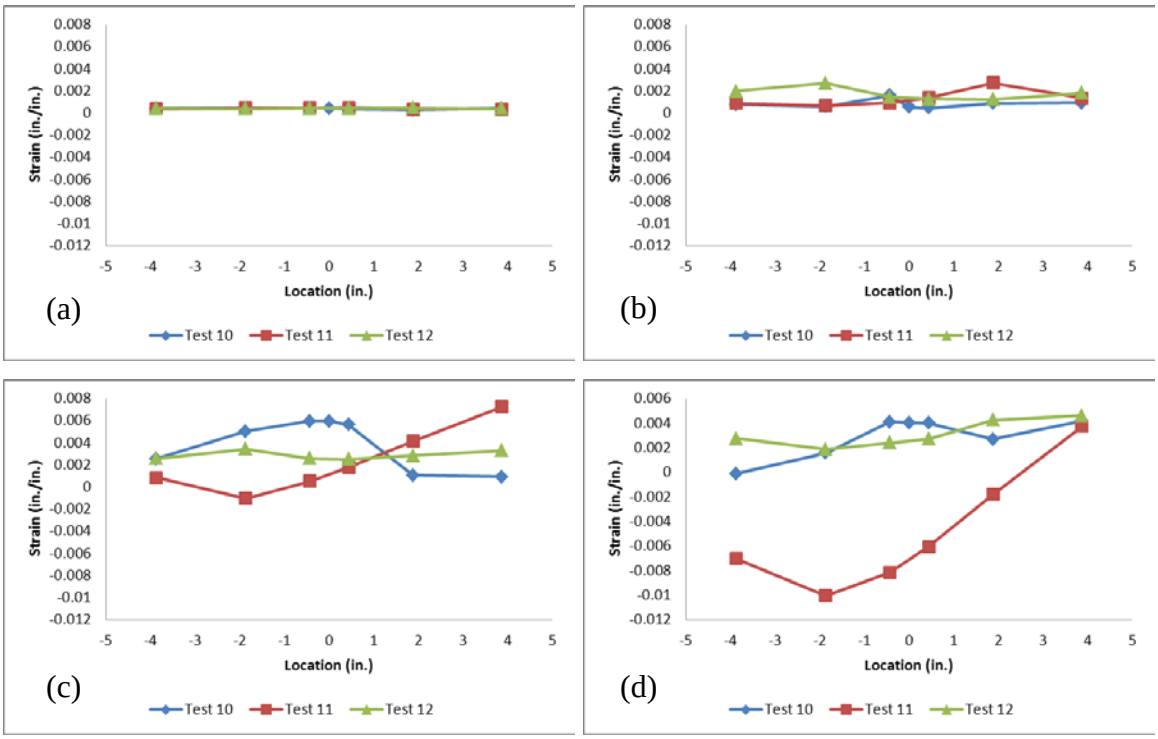

Figure 5.23 – W36x150 (Specimen 10, 11 and 12) Top Flange Strain Data Line 2 at (a) 1% Story Drift, and (b) 2% Story Drift, (c) 3% Story Drift, and (d) 4% Story Drift

5.6 Ongoing Research

A complimentary experimental program is underway to investigate the low cycle fatigue resistance of steel flange material including PAF, welds, defect repairs such as those specified in AWS D1.8, and other artifacts. The objective of this second phase of testing is to use the framework of existing low cycle fatigue models to characterize the supply of low cycle fatigue resistance for steel plates including artifacts. Then, using the same low cycle fatigue model framework, the low cycle fatigue demands will be estimated based on stress and strain histories at various critical locations in finite element models of typical moment connections subjected to the AISC qualification cyclic loading protocol. By comparing the supply of low cycle fatigue fracture resistance determined from the tests to demands computed by the finite element models, the potential for fracture to occur in a full-scale moment connection prior to the qualification criteria will be assessed. This experimental program will also provide fundamental data regarding the effect of artifacts on the low cycle fatigue resistance of structural steel plates.

CHAPTER 6 SUMMARY AND CONCLUSIONS

Twelve full-scale beam-to-column moment connection tests were conducted with a range of variables to investigate the effect of powder actuated fasteners and puddle welds on the seismic behavior of moment frames. Variations in the test specimens included control specimens with no fasteners, PAF at 12 in. spacing representing typical deck attachment, puddle welds at 12 in. spacing, and PAF in a dense grid over the protected zone with 1 in. spacing to any edge. Sections tested included W24x62 and W36x150 beams with flange thicknesses of 0.59 in. and 0.94 in. respectively. Reduced beam section (RBS) connections and non-RBS connections were considered representative of the range of currently prequalified moment connection types.

The progression of limit states for RBS specimens included significant yielding in the extreme fibers at the reduced section, spread of plasticity, and then local buckling of the flanges and out-of-plane buckling of the web. Flange local buckling was concentrated in the RBS length. For W24x62 RBS specimens, cracks typically initiated at the flange tips on the inside face of local buckles. For W36x150 RBS specimens, cracks initiated on the flange surface, again at the inside face of local buckles. Fracture originating from these cracks, propagated through the entire flange in all six RBS specimens. In one specimen (Specimen 8), cracking at the toe of the flange stiffener, which was observed for all of the W36x150 specimens, led to the ultimate brittle fracture.

Specimens with no RBS showed slight differences in the progression of limit states. In the absence of a reduced section, initial yielding occurred in the extreme fibers closer to the end of the beam, followed by a spread in plasticity. Local buckling of the flanges occurred over a slightly longer length of flange than for RBS specimens and was accompanied by out-of-plane web buckling. Cracks again occurred on the inside face of local buckles, but in general they were less prominent than for RBS specimens. The only fracture for specimens without an RBS (Specimen 12) occurred in a similar manner to the fractures of W36x150 RBS specimens. In that specimen, propagation of a crack that formed at the flange surface of a local buckle around a PAF developed into a full flange fracture.

All twelve specimens satisfied the SMRF qualification criteria in ANSI / AISC 341-10 Chapter K and thus would be considered adequate for use in a special moment resisting frame.

Story drift decomposition of test data indicates that every test successfully underwent at least 3% story drift due to the beam plastic hinge deformation while still maintaining a moment capacity above the 80% nominal plastic moment limit. While most tests achieved this during the cycles at 4% story drift, two specimens satisfied this criteria during the first cycle of 4.7% story drift.

The behavior of the twelve specimens were quantitatively compared using several different approaches. The cyclic-load deformation behavior and cyclic envelopes were compared for specimens with no fasteners, puddle welds, and PAF. It was found that the fasteners had no effect on the hysteretic behavior or envelope prior to fracture. Furthermore the achieved moment capacities during the qualification cycle and maximum moment capacities were unaffected by the inclusion of the puddle welds and PAF. The effect of puddle welds and PAF on strength degradation and energy dissipation were similarly found to be negligible prior to fracture even in the specimens with dense grid of PAF.

Although the W24x62 specimens suggest no difference in the cycle number when fracture occurs, the results for the W36x150 specimens that included a grid of fasteners suggest that one or more PAF applied in critical locations such as the inside of a local buckle may lead to fracture during an earlier cycle in the displacement protocol. It is noted, however, that fracture occurred well after SMRF qualification had been satisfied, the difference in the cycle number at fracture was small, and that the two W36x150 specimens that fractured included a grid of PAF that represent an extreme condition not typical of construction practice. Since the sample size is small and the difference in the cycle number at fracture is small, it was not possible to evaluate the difference in a statistically significant manner.

Three test specimens included a grid of PAF representing an extreme condition not typical of construction practice (Specimens 6, 9, and 12). All three of these specimens produced hysteretic response, cyclic load-deformation envelope, strength degradation, and energy dissipation similar to specimens with no fasteners through the SMRF qualification cycles. Since all of the specimens including these three specimens with a grid of PAF satisfied the qualification criteria, it is expected that SMRF beams in configurations such as the ones tested in this study, with PAF applied in the protected zone with 1 in. spacing to edges or welds, would satisfy SMRF qualification criteria and thus be expected to produce ductile SMRF seismic performance.

REFERENCES

AISC (2010a). (2010). *ANSI/AISC 341-10 Seismic Provisions for Structural Steel Buildings.* Publishes by AISC.

AISC (2010b). (n.d.). *ANSI/AISC 358-10 Prequalified Connections for Special and Intermediate Steel Moment Frames for Seismic Applications, and supplement No. 1 (2010).* Published by AISC.

ASTM A370-07a. (2007). *A370-07a Standard Test Methods and Definitions for Mechanical Testing of Steel Products.* ASTM.

ASTM A6/A6M-12. (2012). *A6/A6M-12 Standard Specification for General Requirements for Rolled Structural Steel Bars, Plates, Shapes, and Sheet Piling.*

Chen, S.-J. and Chao, Y.C. (2001). "Effect of Composite Action on Seismic Performance of Steel Moment Connections with Reduced Beam Sections". *Journal of Constructional Steel Research,* Vol. 57, pp. 417-434.

Civjan, S.A., Engelhardt, M.D., and Gross, J.L. (2000). "Retrofit of Pre-Northridge Moment-Resisting Connections". *ASCE Journal of Structural Engineering,* Vol. 126, No. 4, pp. 445-452.

Engelhardt, M. D., Fry, G. T., Jones, S., Venti, M., and Holliday, S. (2000). *SAC/BD-00/17 Behavior and Design of Radius Cut Reduced Beam Section Connections.* SAC Joint Venture, Sacramento, Calif.

Hajjar, J.F., Leon, R.T., Gustafson, M.A., and Shield, C.K. (1998). "Seismic Response of Composite Moment-Resisting Connections. II: Behavior". *ASCE Journal of Structural Engineering,* Vol. 124, No. 8, pp. 877-885.

Hamburger, R.O., Krawinkler, H., Malley, J.O., and Adan, S.M. (2009). *NEHRP Seismic Design Technical Brief No. 2 Seismic Design of Steel Special Moment Frames: A Guide for Practicing Engineers.* Published by the National Institute of Standards and Technology (NIST), Report No. NIST GCR 09-917-3.

Lee, M., Kobayashi, G., and Tagawa, Y. (2012). “Comparative Study on Effect of Powder Actuated Nail and Stud Welding on Steel Member". *15 World Conference of Earthquake Engineering, Lisbon 2012.*

Leon, R.T., Hajjar, J.F., and Gustafson, M.A. (1998). "Seismic Response of Composite Moment-Resisting Connections. I: Performance". *ASCE Journal of Structural Engineering*, Vol. 124, No. 8, pp. 868-876.

Niessner, M. and Seeger, T. (1999). "Fatigue Strength of Structural Steel with Powder Actuated Fasteners According to Eurocode 3". *Stahlbau*, Vol. 68, pp. 941-948.

Ricles, J. M., Fisher, J. W., Lu, L. -W., & Kaufmann, E. J. (2002). "Development of Improved Welded Moment Connections for Earthquake-Resistant Design". *Journal of Constructional Steel Research, Vol. 58*, 565-604.

Timoshenko, S. (1955). *Strength of Materials.* Huntington, New York: Robert E. Krieger Publishing Co.

Toellner, B. W. (2013). *"Evaluation of the Effect of Defects on the Seismic Behavior of Steel Moment Connections".* Master’s Thesis, Virginia Polytechnic and State University, Blacksburg, Virginia.

Tremblay, R. and Filiatrault, A. (1997). "Seismic Performance of Steel Moment Resisting Frames Retrofitted with a Locally Reduced Beam Section Connection". *Canadian Journal of Civil Engineering*, Vol. 24, pp. 78-89.

Uang, C.-M., Yu, Q.-S., Noel, S., and Gross, J. (2000b). "Cyclic Testing of Steel Moment Connections Rehabilitated with RBS or Welded Haunch". *ASCE Journal of Structural Engineering*, Vol. 126, No. 1, pp. 57-68.

Watkins, C. (2013). *"Effects of Powder Actuated Fasteners in the Protected Zone of Steel Moment Frames".*

APPENDIX A ADDITIONAL TEST SETUP DETAILS

In order to execute full-scale tests for beams with varying geometric configurations and moment capacities, a robust test setup was required. The test setup consisted of three main frames, see

Figure A.1, all designed to resist the MTS 201.70T actuator's maximum tensile force, 220 kips. All frames, members, and connections were designed for the actuator load applied to cantilever beams at 17 ft from the centerline of the column and should therefore be assessed for any other application. The MTS 201.70T actuator consisted of a three stage servovalve, axial load cell, MTS 249.51N swivel heads at each end, and was capable of a 20 in. stroke. Figure A.2 and Figure A.3 show the setup for each size specimen.

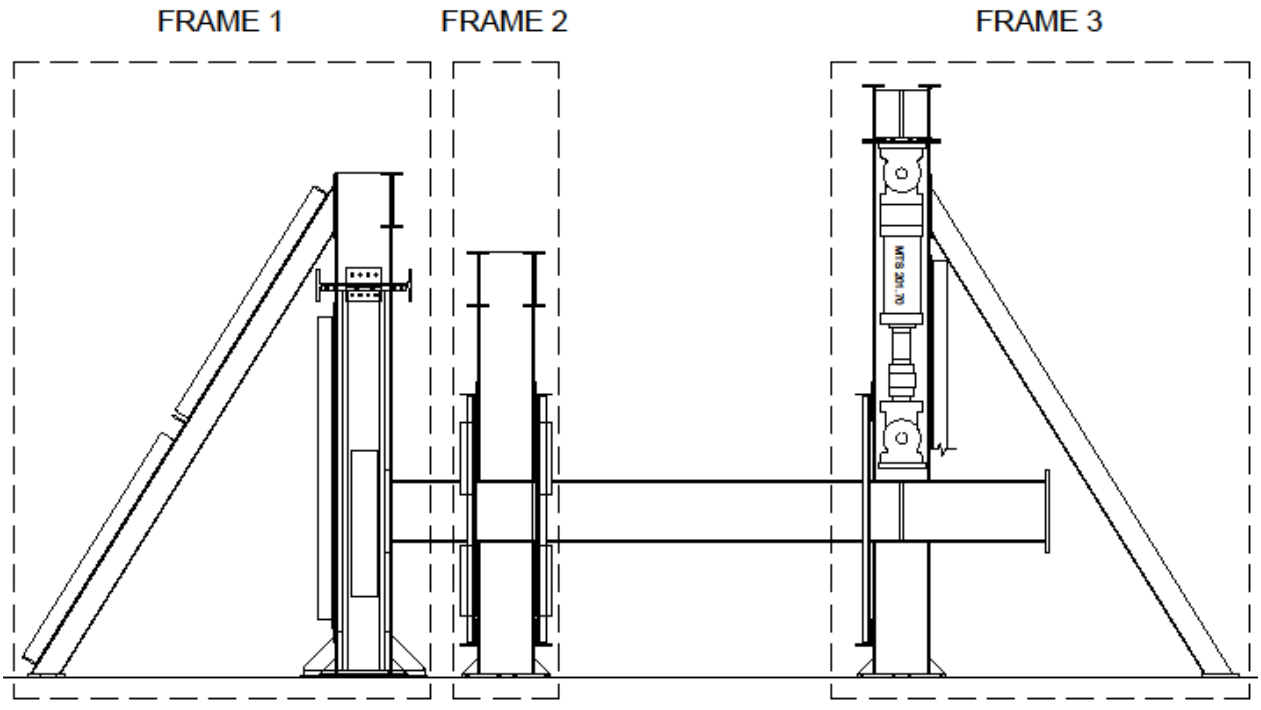

Figure A.1. Test Setup Frames

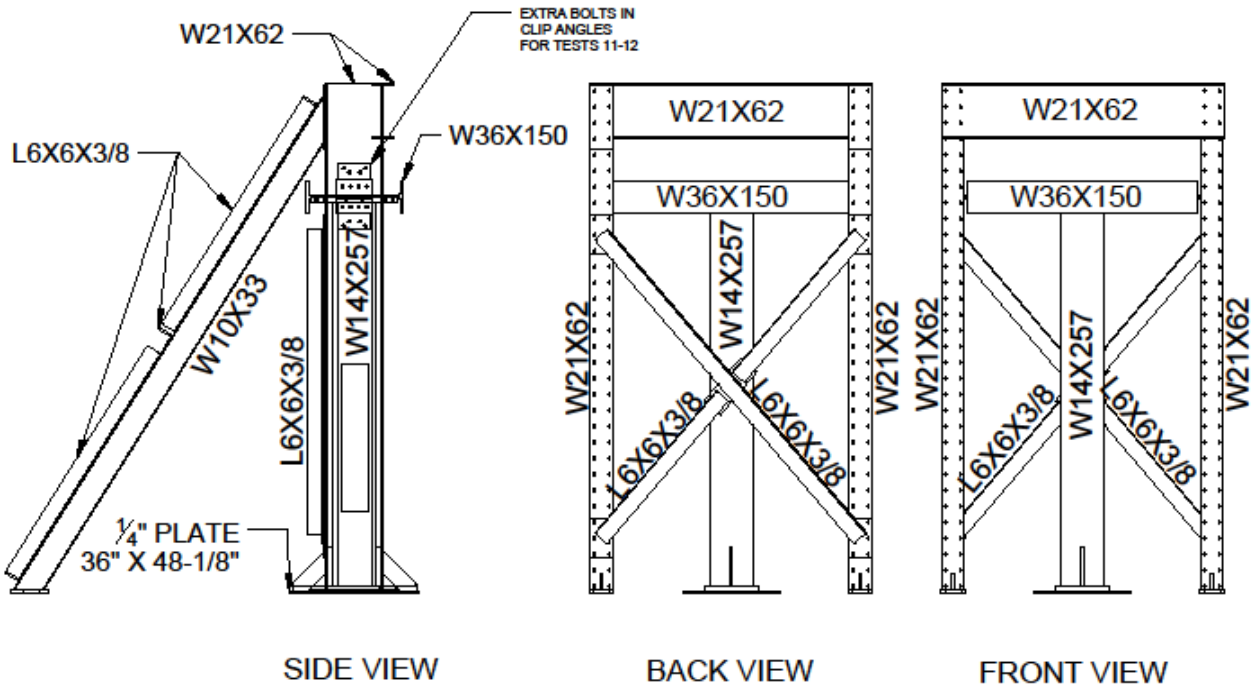

Figure A.2. Frame 1, Column Frame, Member Shapes

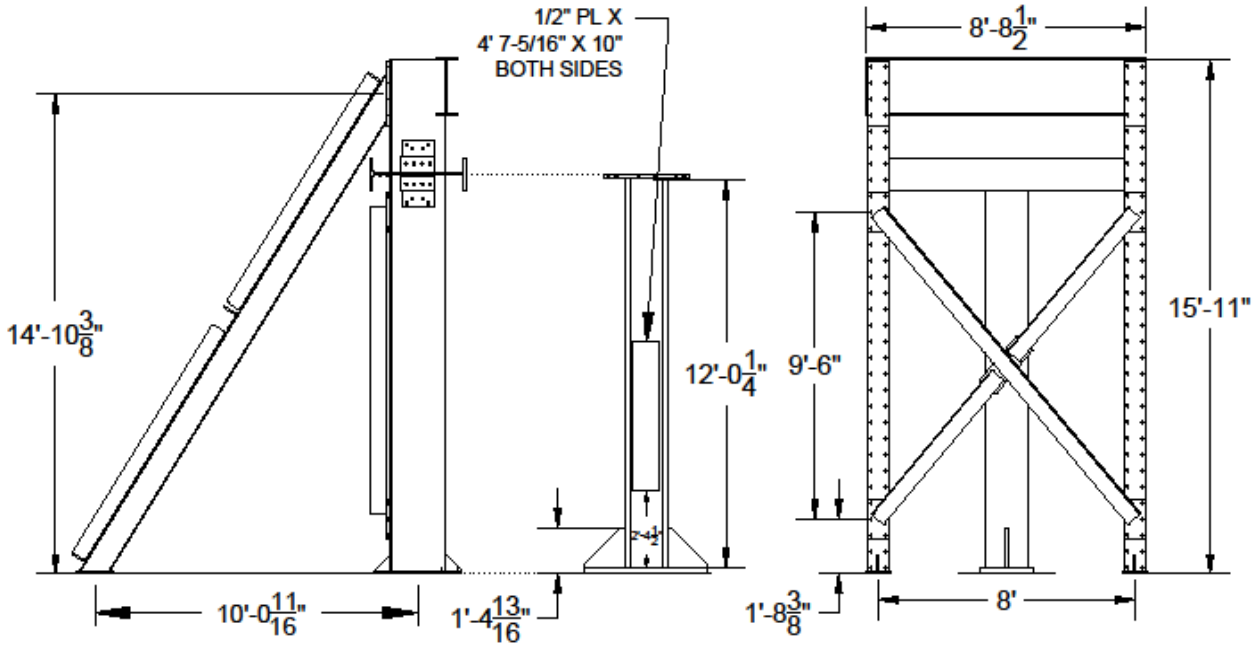

Figure A.3. Frame 1, Column Frame, Key Dimensions

The lateral brace frame, labeled as Frame 2 in Figure A.4, provided lateral restraint to the beam test specimens preventing them from lateral-torsional buckling out of plane. The location of the frame differs for each size beam because of varying moment capacities, differences in lengths of protected zones, and maximum allowable un-braced lengths. The specific locations were 4 ft – 6 in. and 5 ft – 6 in. from center of the column to center of the lateral brace frame for all W24x62 and all W36x150 specimens respectively.

There were no lateral buckling issues witnessed during the twelve tests. Approximate locations of laterally bracing for the first six specimens were 33 in., 58.5 in., and 183 in. from the column face. The second six tests had lateral bracing at locations approximately 45 in., 70.5 in., and 183 in. from the column face.

The lateral bracing was intended to act as a semi rigid and low friction surface preventing movement out of the plane of the beam specimen and column but not to impinge on the vertical motion of the specimen. Notice the width of the opening between the channels is greater than the flange widths of both specimen sizes. This allowed room for the use of Teflon like material and/or automobile grease between the bracing and specimen surfaces to reduce friction forces. For the W24x62 specimens, HSS shims were clamped to the flanges of the channels to narrow the opening to an appropriate width.

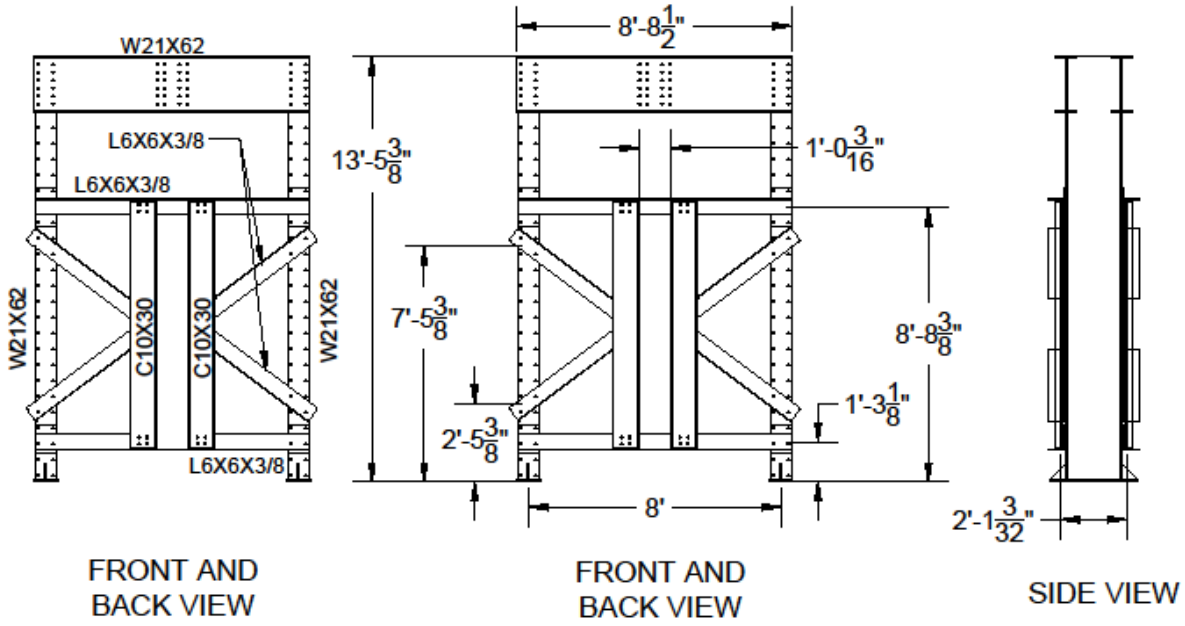

Figure A.4. Frame 2, Lateral Brace Frame, Members and Key Dimensions

The actuator frame, labeled as Frame 3, provided support to the actuator. The frame was designed for the maximum actuator compressive load of 330 kips. As previously mentioned, one side of the actuator frame incorporated the same lateral bracing system to supply restraint to the specimens near the location of the applied load. Members and significant dimensions for the actuator frame are shown in Figure A.5. The frame was supported from rotating about its base by two large diagonals that connected to the top of the frame and into the strong floor about 10 ft from the center of the frame. Also, lateral cross bracing was supplied to brace the frames exterior columns in weak axis bending. The diagonal braces and lateral cross bracing were designed to resist five percent of the maximum actuator load.

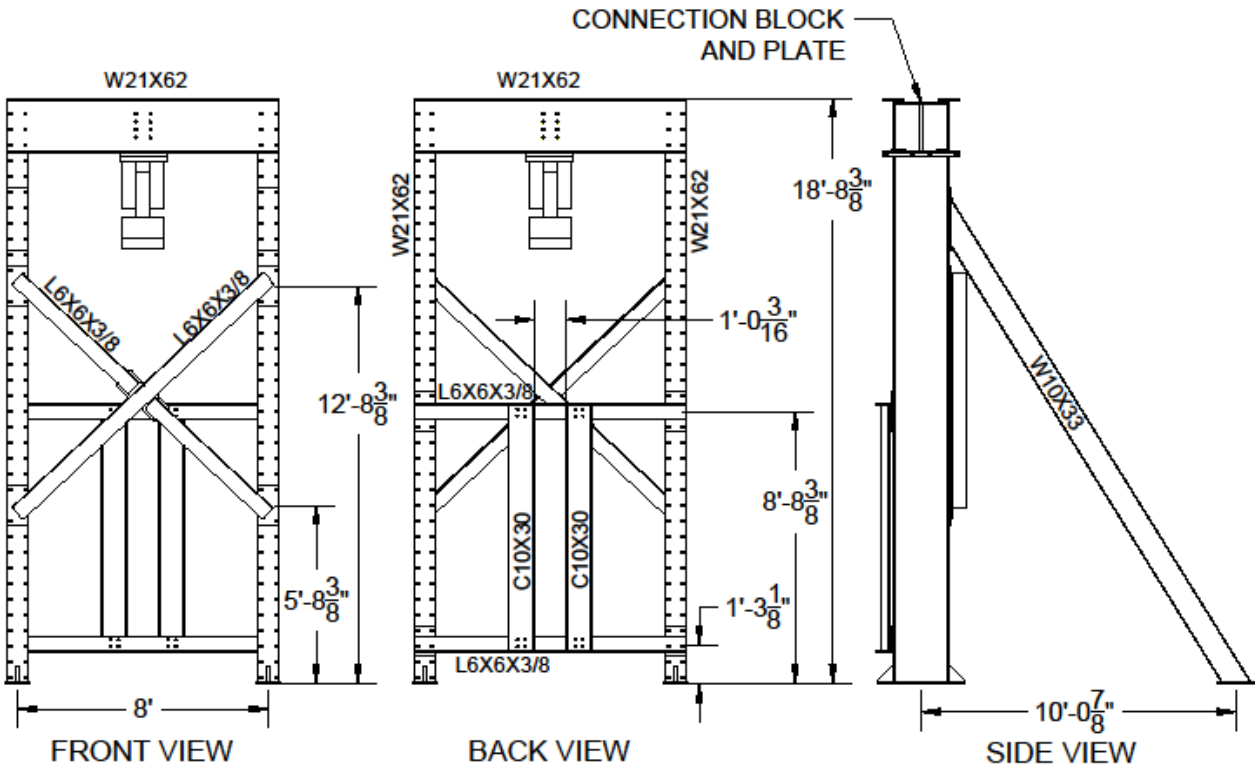

Figure A.5. Frame 3, Actuator Frame, Members and Key Dimensions

APPENDIX B STORY DRIFT DECOMPOSITION PROCEDURE

In order to quantify the contribution of each component to the total story drift, instrumentation attached to that component is used to determine its deformation. This is accomplished using geometry of the test setup, locations of each end of instrumentation, and recorded data from instrumentation. This appendix includes a series of diagrams and accompanying equations summarizing the procedure to decompose the total story drift into components. All diagrams represent configurations assuming an upward deflection of the beam. It should be noted that all diagrams are schematic and are not drawn to scale.

B.1 Flexibility of the Reaction Frame

The column reaction frame is designed to be stiff and elastic during testing. The string potentiometer mounted to the top of the reaction column (Figure B.1) provides a measurement of any drift of the column relative to the bottom of the column. A horizontal LVDT placed along the floor captures any motion of the base of the column. Data from this LVDT indicated a negligible amount of motion at the column base for all tests. This allows the column to be considered fixed against translation at the base and heavily restrained but still capable of motion at the top. The system story drift represented by the column reaction frame drift is shown in Figure B.1.

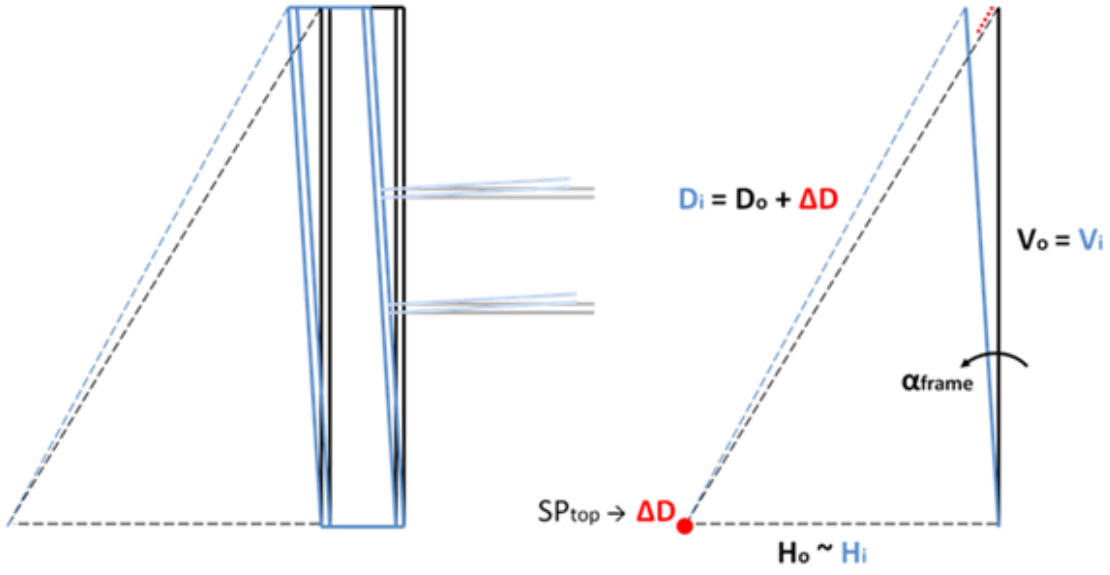

Figure B.1: Frame Drift - Story Drift Component

Equation B.1 utilizes the law of cosines to relate the angle of reaction frame drift, α_{frame}, to known system geometries and string potentiometer data of the motion of the top of the column. Equation B.1 is written in the typical form of the law of cosines, in which α_{frame} can be solved explicitly as in Equation B.2. H_0 and V_0 are the initial horizontal and vertical separations between the string potentiometer base and the top of the column, respectively. D_i is the length spanned by the string potentiometer from its base to the top of the column, which varies as the column reaction frame moves. The current diagonal length, D_i is equal to the original length, D_o, plus the change in length measured using the string potentiometer, ΔD.

$$D_i^2 = H_0^2 + V_0^2 - 2H_0V_0\cos\left(\frac{\pi}{2} - \alpha_{frame}\right) \tag{B.1}$$

$$\alpha_{frame} = \frac{\pi}{2} - \text{acos}\left(\frac{H_0^2 + V_0^2 - D_i^2}{2H_0V_0}\right) \tag{B.2}$$

B.2 Shear Deformation of the Panel Zone

Shear deformation of the column panel zone is measured using a pair of LVDTs oriented diagonally in an 'X' configuration such that they span the intersection of beam flange and column flange centerlines. The LVDTs, each mounted to one column flange, measure displacement against perpendicular reaction surfaces mounted to the opposite column flange. Shear deformation of the panel zone is assumed to behave exclusively as horizontal shearing due to beam flange forces as shown in Figure B.2. Any vertical shear is accounted for by the calculation of column flexure.

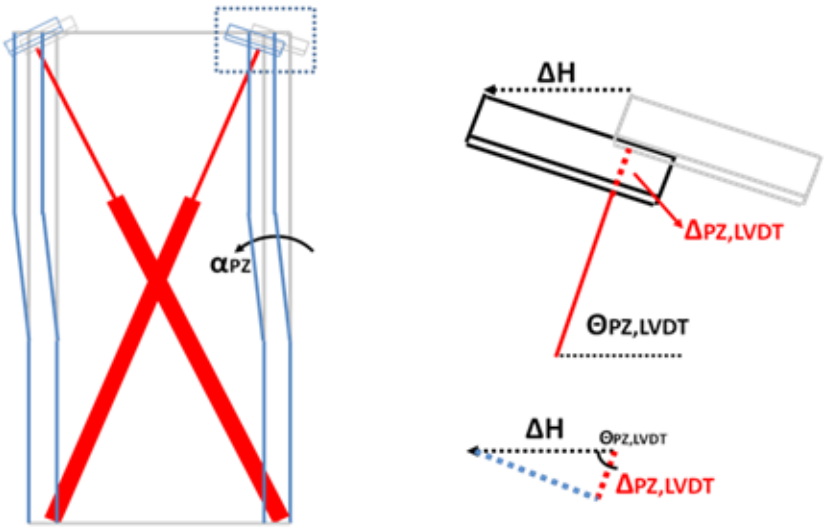

Figure B.2: Panel Zone Shear - Story Drift Component

The average change in length recorded by the LVDTs, $\Delta_{PZ,AVG}$, can be converted into an equivalent horizontal component, Δ_H, by Equation 3.5 which uses the angle of the panel zone LVDTs, $\theta_{PZ,LVDT}$. The LVDTs were mounted such that they approximately spanned the opposite corners of a rectangle formed by the beam and column flange depth centerlines. While the precise angle may have varied slightly between tests, $\theta_{PZ,LVDT}$ was estimated by nominal beam and column geometries as given in Equation B.4 where d_B and d_C are the depths of the beam and column, respectively, and t_{fB} and t_{fC} are the flange thicknesses of the beam and column, respectively. As the panel zone undergoes shear deformation, one LVDT extends and the other shortens. This difference of signs is reflected by the difference in signs in Equation B.3 where $\Delta_{PZ,LVDT1}$ and $\Delta_{PZ,LVDT2}$ are the diagonal LVDT extensions. The resulting horizontal deflection due to shear is then related to the accompanying panel zone drift ratio, α_{PZ}, as given in Equation B.6 by the vertical span of the LVDTs, $d_B - t_{fB}$.

$$\Delta_{PZ,AVG} = \frac{\Delta_{PZ,LVDT1} - \Delta_{PZ,LVDT2}}{2} \tag{B.3}$$

$$\theta_{PZ,LVDT} = atan\left(\frac{d_B - t_{fB}}{d_c - t_{fc}}\right) \tag{B.4}$$

$$\Delta_H = \frac{\Delta_{PZ,AVG}}{\cos(\theta_{PZ,LVDT})} \quad \text{(B.5)}$$

$$\alpha_{PZ} = \frac{\Delta_H}{d_B - t_{fB}} \quad \text{(B.6)}$$

B.3 Flexural deformation of the column

In addition to global motion of the column due to reaction frame flexibility and panel zone deformation, flexibility of the test column itself accounts for a portion of the system story drift. Figure B.3 shows the general deformed shape of the column due to column flexibility. Two methods are possible for quantifying the angular rotation of the panel zone, $\alpha_{col,rot}$. The primary method, given in Equation B.7, uses an inclinometer, θ_{inc1}, placed at the center of the panel zone in line with the beam centerline. As an alternate method, given in Equation B.8, two fixed, horizontal LVDTs along the back side of the column can provide this angular rotation. The LVDTs are spaced vertically at a separation approximately equal to the beam depth. The specific separation spacing, d_{sep}, is driven by clearance constraints due to the presence of cross bracing behind the column. The LVDTs measure displacements $\Delta_{COL,LVDT1}$ and $\Delta_{COL,LVDT2}$, providing the means to quantify the angle of the column. It is important to note that the column rotation angle depicted by Figure B.3 and Equations B.7 and B.8 incorporates contributions by the reaction frame drift and panel zone shear deformations already derived. Therefore, in order to quantify the drift ratio due exclusively to column flexibility, the aforementioned reaction frame and panel zone values must be removed. This is shown in Equation B.9. This operation also allows for the calculation of column flexure to include any deformations due to panel zone flexure and column shear.

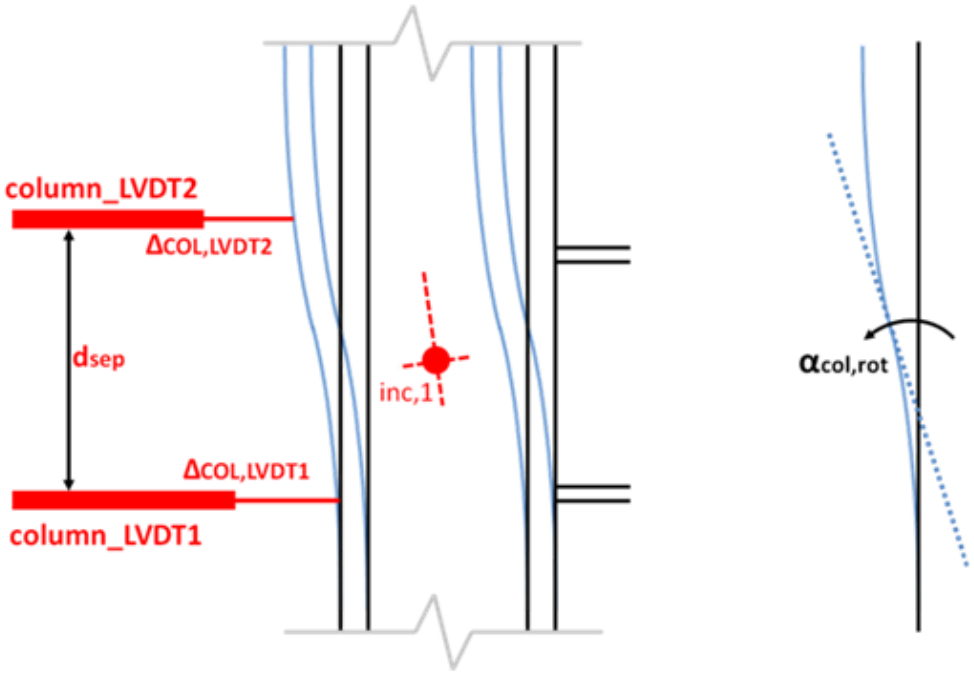

Figure B.3: Column Flexure - Story Drift Component

$$\alpha_{col,rot,1} = \tan(\theta_{inc,1}) \tag{B.7}$$

$$\alpha_{col,rot,2} = \frac{\Delta_{COL,LVDT1} - \Delta_{COL,LVDT2}}{d_{sep}} \tag{B.8}$$

$$\alpha_{col,flex} = \alpha_{col,rot} - \alpha_{frame} - \alpha_{PZ} \tag{B.9}$$

While the bottom LVDT is in line with each beam type bottom flange, due to spatial restrictions of the test setup, the top LVDT was located at a consistent location above the beam top flange line. Since flexure is assumed to be greatest at the centerline of the beam, it is expected that the LVDT resulting column rotation angle will be less than the actual rotation angle. Since the column inclinometer is placed in the center of the column panel zone, it is expected that the angle recorded by the inclinometer will better represent the actual rotation of the column.

B.4 Prying of the endplate connection

All bolts connecting the beam endplate to the column face were pretensioned in order to minimize relative motion between the adjoining surfaces. It is possible to estimate the relative motion due to prying, $\alpha_{endplate}$, by considering the difference in measured angle between two local inclinometers as given in Equation B.10. One is located in the middle of the panel zone, θ_{inc1}, and one is located at the beam mid-depth and two inches from the endplate, θ_{inc2}, as shown in Figure B.4.

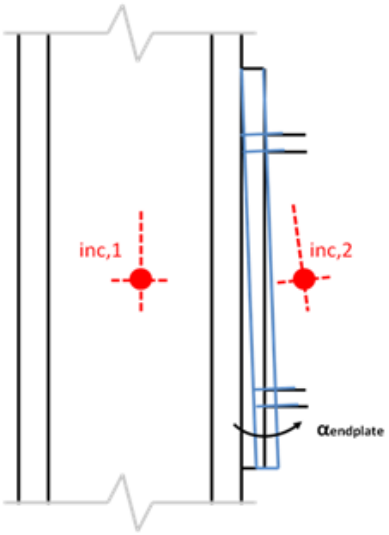

Figure B.4: Endplate Prying - Story Drift Component

$$\alpha_{endplate} = \tan(\theta_{inc,1} - \theta_{inc,2}) \quad \text{(B.10)}$$

B.5 Elastic deformation of the beam

The applied force by the actuator causes elastic flexural and shear deformation in the beam. Although the entire length of the beam experiences elastic deformation, it is difficult to decompose the deformation of the plastic hinge region into elastic and plastic parts. An inclinometer located on the web at the beam mid-depth beyond the protected zone, however, allows the contribution of elastic beam displacement outside the plastic hinge region to be determined. Total deflection of

the beam free end can be considered a summation of the vertical deflection of the beam at the inclinometer location (Equation B.11 or B.12), and the deflection of the remaining length of beam beyond the beam inclinometer. The rise of the beam inclinometer, $\delta_{inc,rise}$, as given by Equation B.11 for Specimens 1-6, is calculated using the recorded angular rotations of the column and beam inclinometers, $\theta_{inc,1}$ and $\theta_{inc,3}$ respectively, and the distance between them, L_1. Specimens 7-12 utilized a string potentiometer to directly measure this rise of the inclinometer (Equation B.12). From Equation B.13, the angle reported by the beam inclinometer, $\theta_{inc,3}$, allows for a deflection calculation, δ_{rigid}, using an ideal assumption that the length of beam beyond this inclinometer, L_2, remains rigid as it deflects. Summing these two deflections results in an extrapolated deflection of the beam at the location of the actuator assuming the remaining beam length does not undergo any rotation. As given in Equation B.14, any difference between this summed deflection and the reported input drift value of the vertical string potentiometer controlling the test, δ_{tot}, is due to elastic deflection of the length of beam beyond the inclinometer, $\delta_{el,beam,1}$. This is demonstrated in Figure B.5.

The theoretical elastic deflection, $\delta_{el,beam,2}$, of the beam length, L_2, is computed using the sum of contributions due to flexure and shear from an applied actuator load, P. This is shown in Equation B.16. Additional material properties include moment of inertia, I, modulus of elasticity, E, shear modulus of elasticity, G, section area, A, and a shape factor, α. The shape factor, α, is dependent on additional properties of web thickness, t, flange width, b, beam depth, d, and clear distance between flanges, d_1 as shown in Equation B.15. The contribution of beam deformation due to shear was provided by Timoshenko (1955). Calculation of the beam elastic deformation drift component, $\alpha_{elastic,beam}$, is given by Equation B.17.

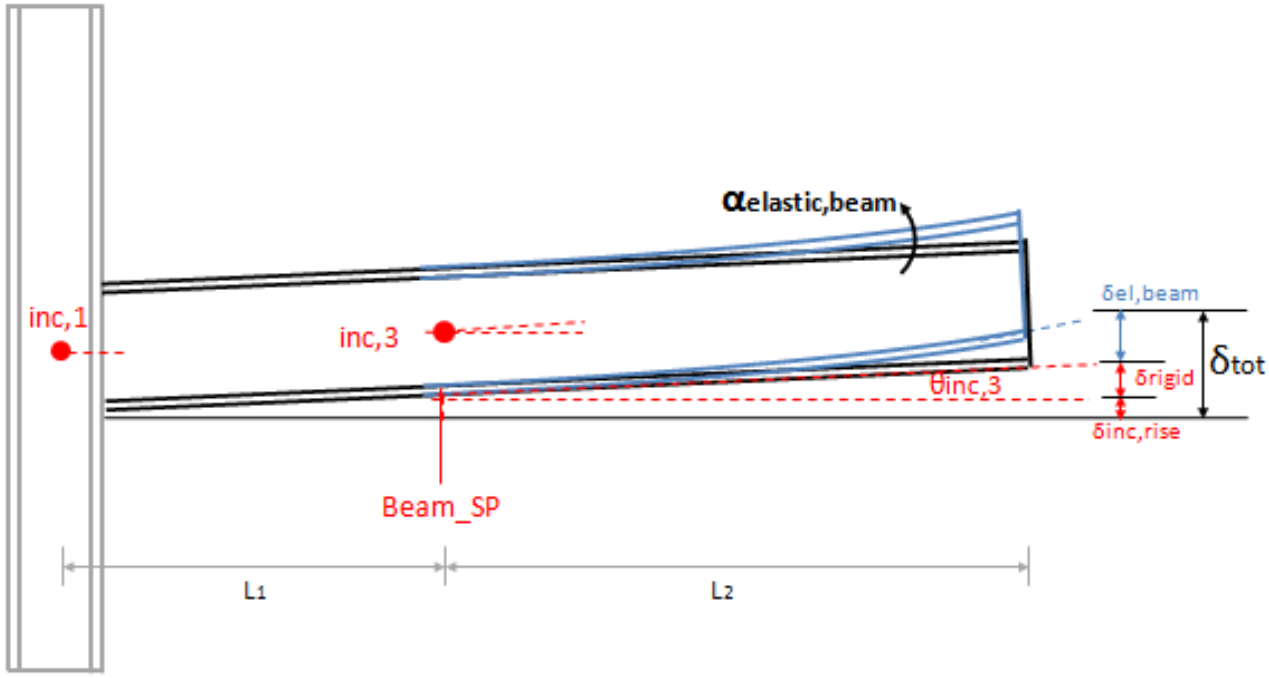

Figure B.5: Beam Elasticity- Story Drift Component

$$\delta_{inc,rise} = \tan\left(\frac{\theta_{inc,1}+\theta_{inc,3}}{2}\right) \times L_1 \quad \text{(Specimens 1-6)} \tag{B.11}$$

$$\delta_{inc,rise} = \Delta_{beam\_SP} \quad \text{(Specimens 7-12)} \tag{B.12}$$

$$\delta_{rigid} = \tan(\theta_{inc,3}) \times L_2 \tag{B.13}$$

$$\delta_{el,beam,1} = \delta_{tot} - \delta_{inc,rise} - \delta_{rigid} \tag{B.14}$$

$$\alpha = \frac{A}{8It}(bd^2 - bd_1^2 + td_1^2) \tag{B.15}$$

$$\delta_{el,beam,2} = \frac{PL_2^3}{3EI} + \frac{PL_2\alpha}{AG} \quad \text{(B.16)}$$

$$\alpha_{elastic,beam} = \frac{\delta_{el,beam}}{17\ ft} \quad \text{(B.17)}$$

B.6 Plastic deformation of the beam

Story drift due to plastic deformation of the beam is represented by the rotation occurring in the protected zone region. The hinging was highly irregular based on the particular buckling and failure mode that the beam underwent. Two methods are possible for quantifying the angular rotation of the plastic hinge. As in column flexure, the primary method, given as $\alpha_{plastic,beam,1}$ in Equation B.18, is the comparison of recorded angles between two inclinometers, $\theta_{inc,2}$ and $\theta_{inc,3}$, mounted to the beam on either side of the protected zone. The alternate method used for data validation is given in Equation B.19, based on two LVDTs (linear potentiometers for Specimens 4-12) located above and below the beam flange that measure the distance between the endplate and the end of the protected zone as shown in Figure B.6. It is noted that this alternate method originally called for LVDTs as shown in Figure 2.11. Excessive out-of-plane deformation of the top flange prompted the decision to use linear potentiometers for Specimens 4-12 because they allowed direct attachment at both ends. With this in mind, any further reference to the two LVDTs used to measure beam plastic hinge rotation actually corresponds to linear potentiometers for Specimens 4-12. The difference between LVDT deflection values, $\Delta_{BEAM,LVDT1}$ and $\Delta_{BEAM,LVDT2}$, divided by the vertical distance between LVDTs, *d'*, approximates the angular deflection of the protected zone, $\alpha_{plastic,beam,2}$. It is noted that this plastic deformation component inherently includes any beam elasticity in the protected zone. Practical instrumentation limitations make it infeasible to distinguish these two different components. Therefore, for purposes of simplification, an assumption is made that elasticity along this relatively short length of beam is small compared to the significant plastic hinging.

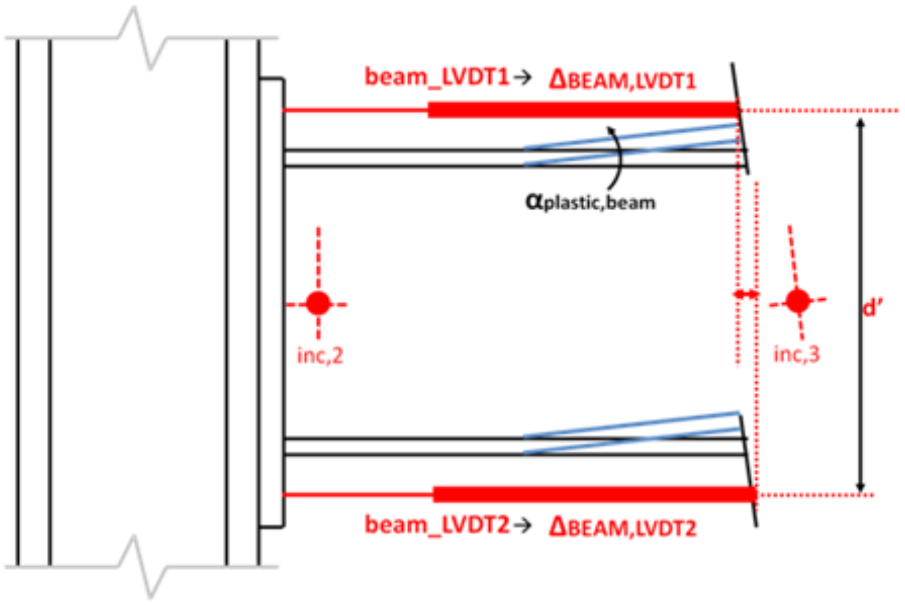

Figure B.6: Beam Plasticity- Story Drift Component

$$\alpha_{plastic,beam,1} = \tan(\theta_{inc,2} - \theta_{inc,3}) \tag{B.18}$$

$$\alpha_{plastic,beam,2} = \frac{\Delta_{BEAM,LVDT1} - \Delta_{BEAM,LVDT2}}{d'} \tag{B.19}$$

B.7 Total story drift

The summation of the six story drift components discussed above represents the total story drift, α_{total}, of the system. Equation B.20 represents this summation. The actual total story drift applied to the system by the actuator is measured by the vertical string potentiometer. Comparison of the actual total story drift and the story drift component summation will provide an indication of the adequacy of the story drift algorithms in accounting for all motion of the system.

$$\alpha_{total} = \alpha_{frame} + \alpha_{PZ} + \alpha_{col,rot} + \alpha_{endplate} + \alpha_{elastic,beam} + \alpha_{plastic,beam} \tag{B.20}$$

B.8 Data Validation

Several system components used two redundant instrumentation methods to quantify story drift contribution. Multiple measurements for the same quantity provide the means to validate the accuracy of the data. Figure B.7 shows a comparison of both instrumentation methods for measuring the column rotation. The figure shows data from Specimen 2 as an example of the general comparison of the two methods. The column inclinometer records a greater column rotational deformation than that of the LVDTs. This supports the supposition made in the story drift decomposition discussion section that since the LVDTs are spaced farther apart vertically than the beam depth, they will likely imply a lesser rotation angle than actually exists. Inclinometer data is plotted using Equation B.7. LVDT data is plotted using Equation B.8.

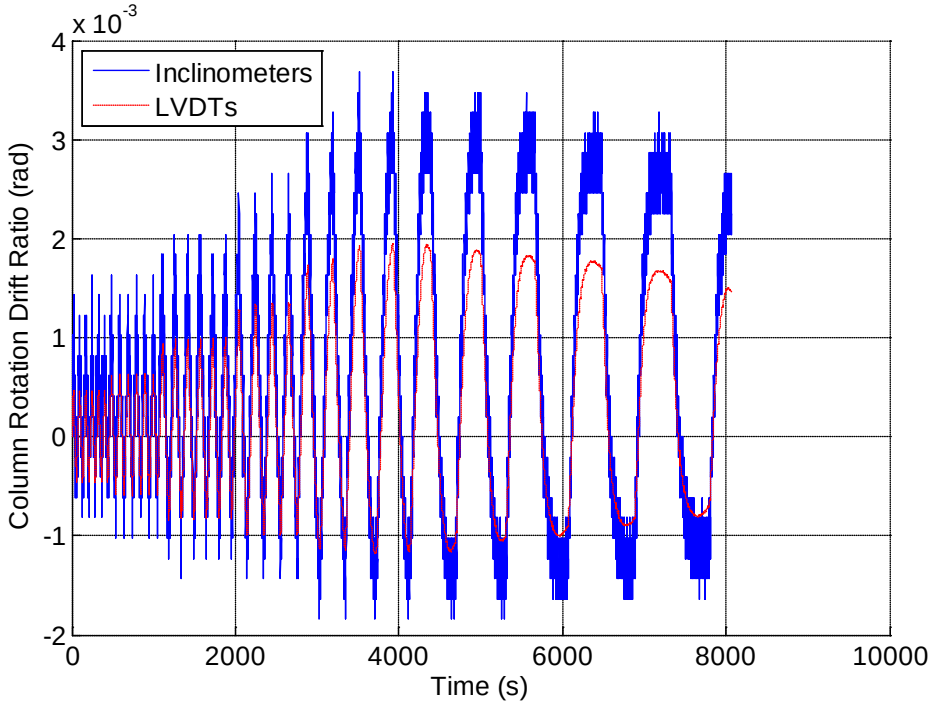

Figure B.7: Column Rotation - Instrumentation Comparison from Specimen 2

Figure B.8 shows a strong correlation between the beam plasticity story drift component calculated using inclinometer measurements and LVDT measurements. As in column flexure, the test data shown in Figure B.7 is from Specimen 2 and represents the general trend exhibited by all tests. The last few cycles show a greater drift measurement from the inclinometers than that of the

LVDTs. This trend is typical of the W24x62 specimens and can be explained by the fact that for these tests, the outer inclinometer is located several inches longitudinally beyond the point at which the LVDTs are mounted. This enables the inclinometer to account for the small degree of additional beam elasticity beyond the LVDT. Comparison data from the W36x150 tests show a near identical story drift profile between the two methods.

It is noted that the two methods are measuring slightly different motions of the plastic hinge region of the beam. Since the inclinometers are mounted to the beam web, it is possible that in some cases, their rotation measurements may be influenced slightly by out of plane motion of the beam due to buckling and local deformations near the endplate. Likewise, the LVDT deflection measurements used in the second method for calculating beam plasticity story drift are susceptible to error due to the local buckling of the flanges. Most tests that proceeded into numerous cycles at 4.7% story drift saw such significant buckling of the flanges that the LVDTs spanning the plastic hinge fell from the contact points at which they were initially adhered for most of the test. Inclinometers stayed adhered to the web better and, therefore, provided data further into the tests. For this reason, inclinometer data is used in the story drift decomposition for all tests. The inclinometer data is also preferred because of the presence of a shared inclinometer between beam plasticity calculations and the beam elasticity along the undeformed length of beam already discussed. This continuity provides for a more accurate account of elasticity along the entire length of the beam. Inclinometer data is plotted using Equation B.16. LVDT data is plotted using Equation B.17.

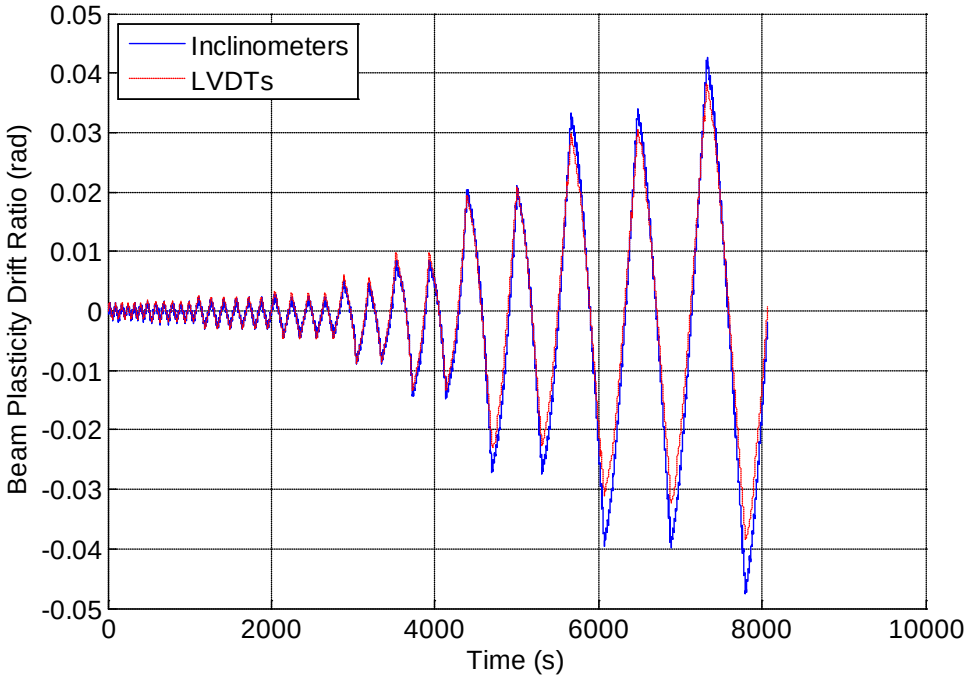

Figure B.8: Beam Plasticity - Instrumentation Comparison from Specimen 2

Figure B.9 shows a typical comparison of the measured and theoretical elastic deflection of the beam using data from Specimen 7. Measured deflection is computed using Equation B.14. Theoretical deflection is calculated using Equation B.16. Noise in the inclinometer data results in false data spikes seen in the early part of the test. Later cycles show a reasonable correlation between theoretical and measured beam elastic deflections.

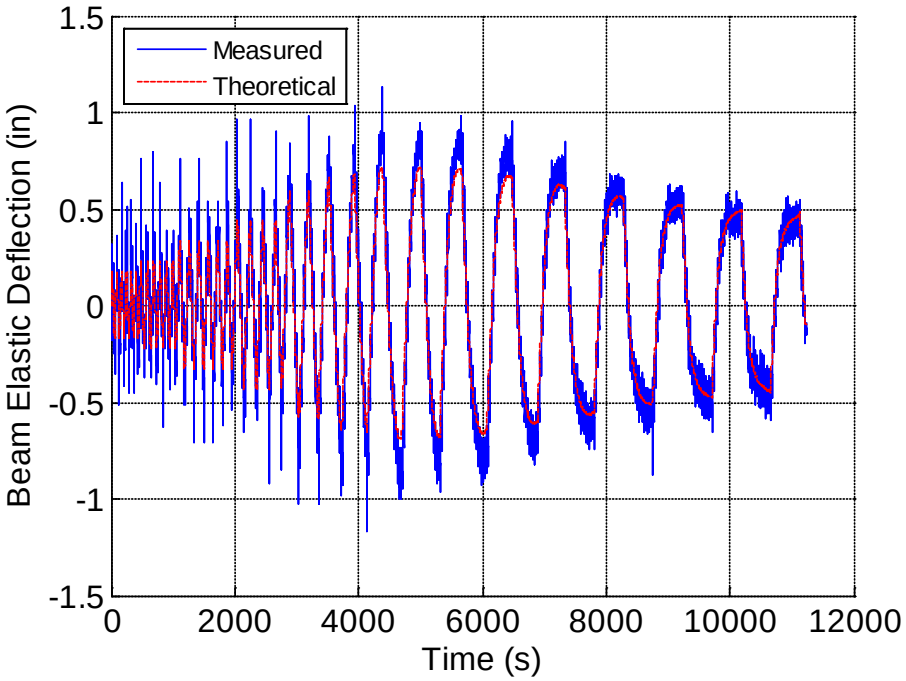

Figure B.9: Beam Elasticity - Comparison of Measured and Theoretical Deflection

APPENDIX C STORY DRIFT DECOMPOSITION

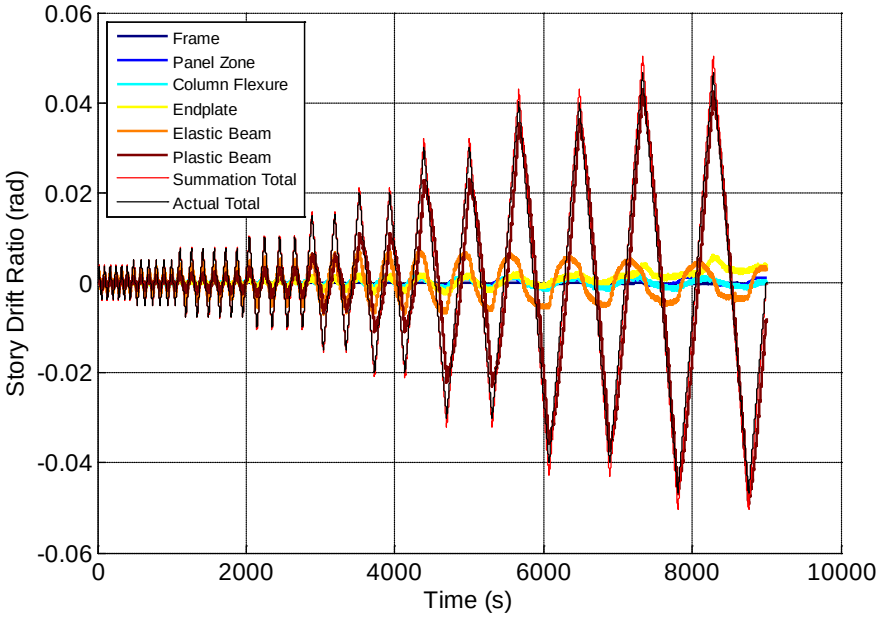

Figure C.1 – Specimen 1 Story Drift Decomposition Line Plot

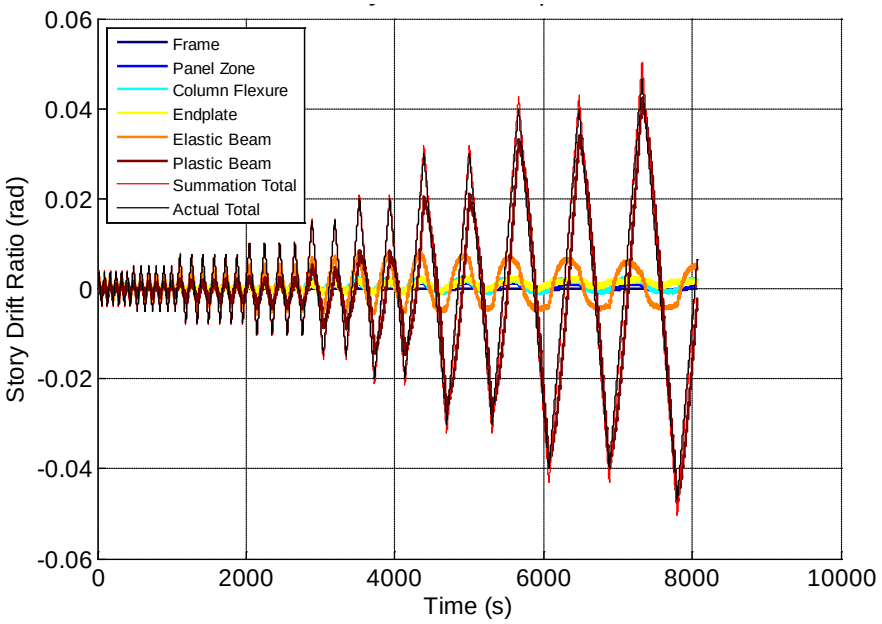

Figure C.2 – Specimen 2 Story Drift Decomposition Line Plot

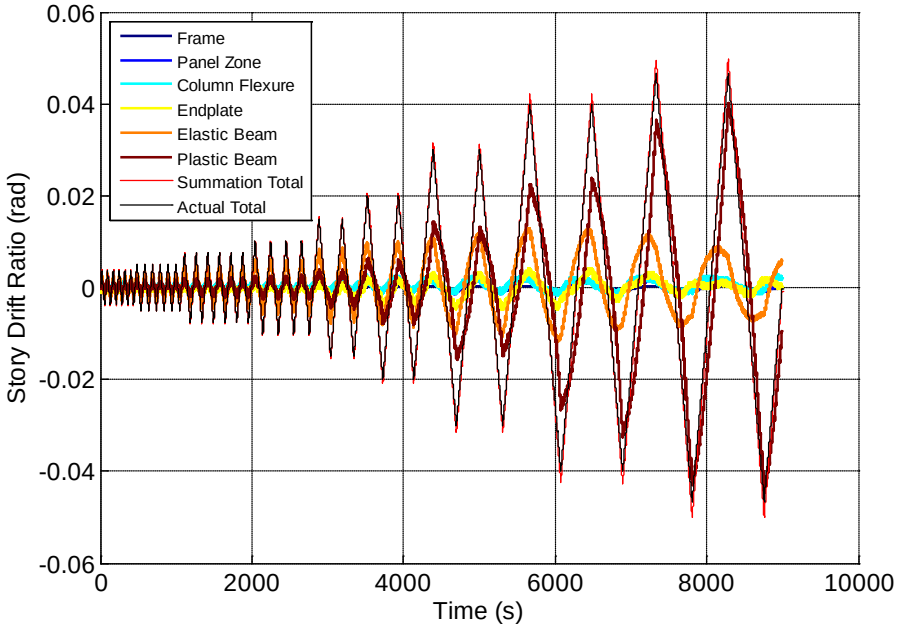

Figure C.3 – Specimen 3 Story Drift Decomposition Line Plot

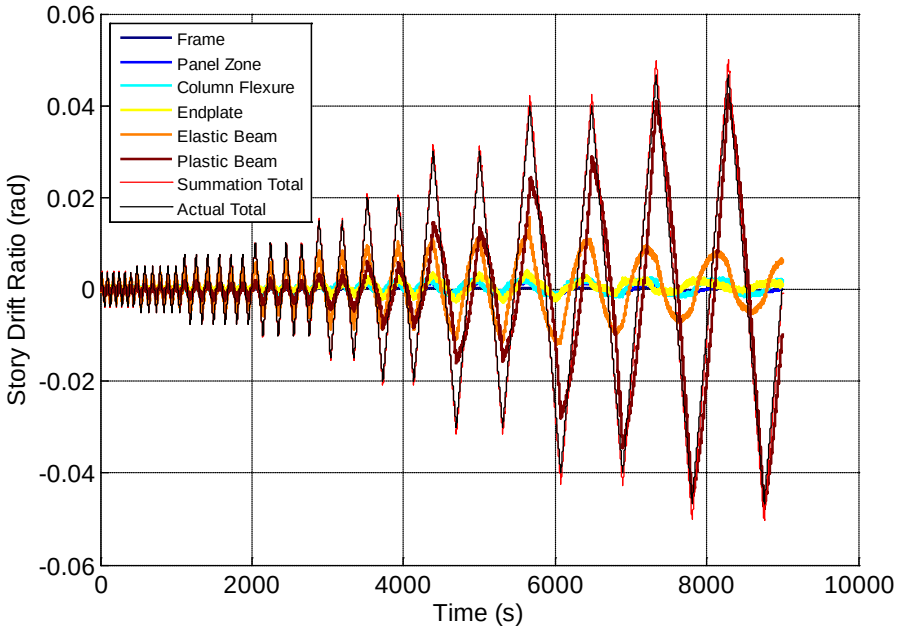

Figure C.4 – Specimen 4 Story Drift Decomposition Line Plot

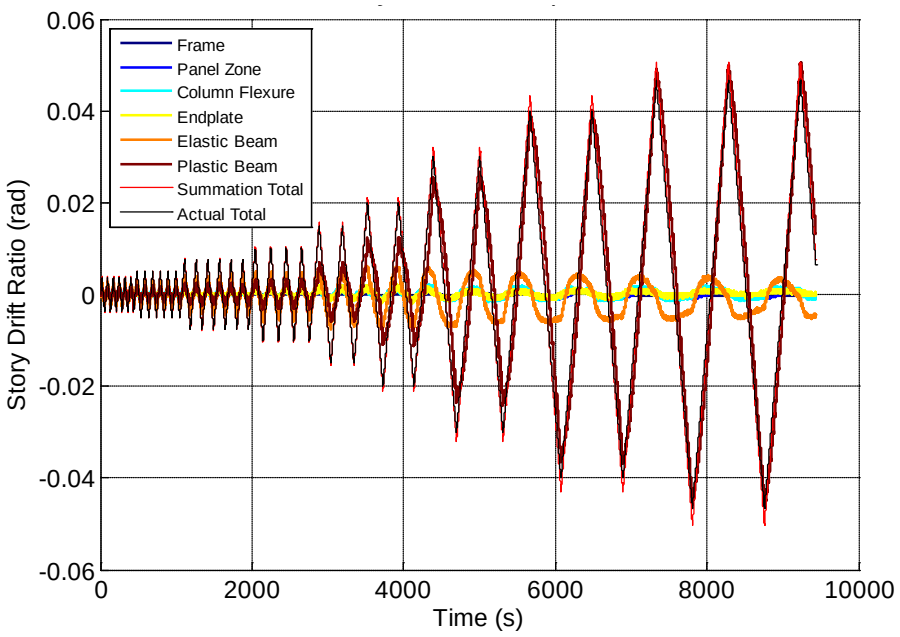

Figure C.5 – Specimen 5 Story Drift Decomposition Line Plot

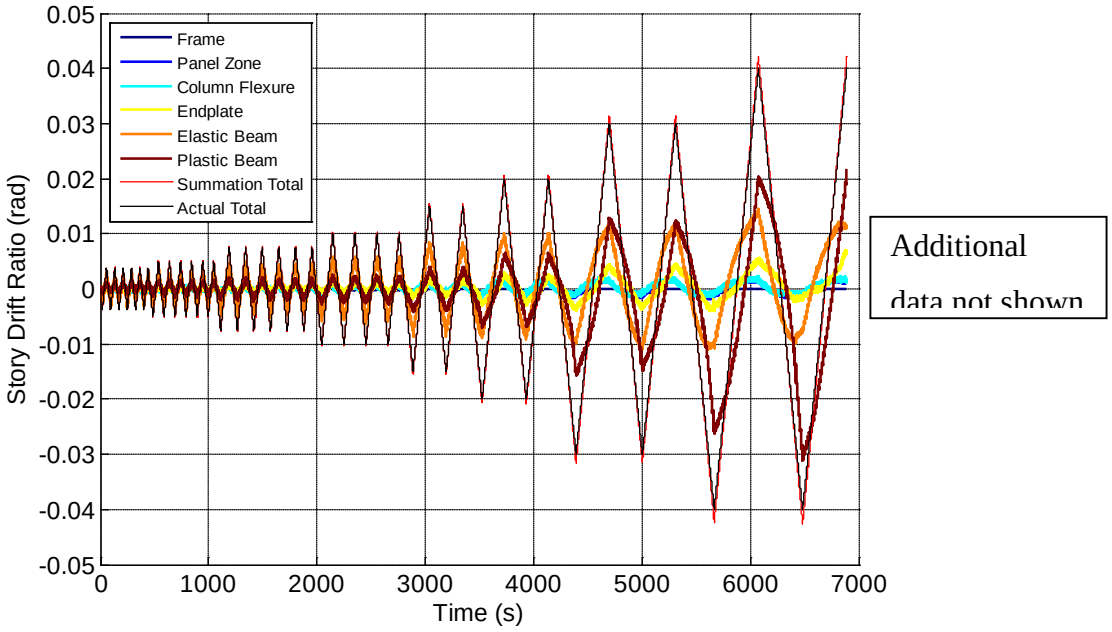

Figure C.6 – Specimen 6 Story Drift Decomposition Line Plot

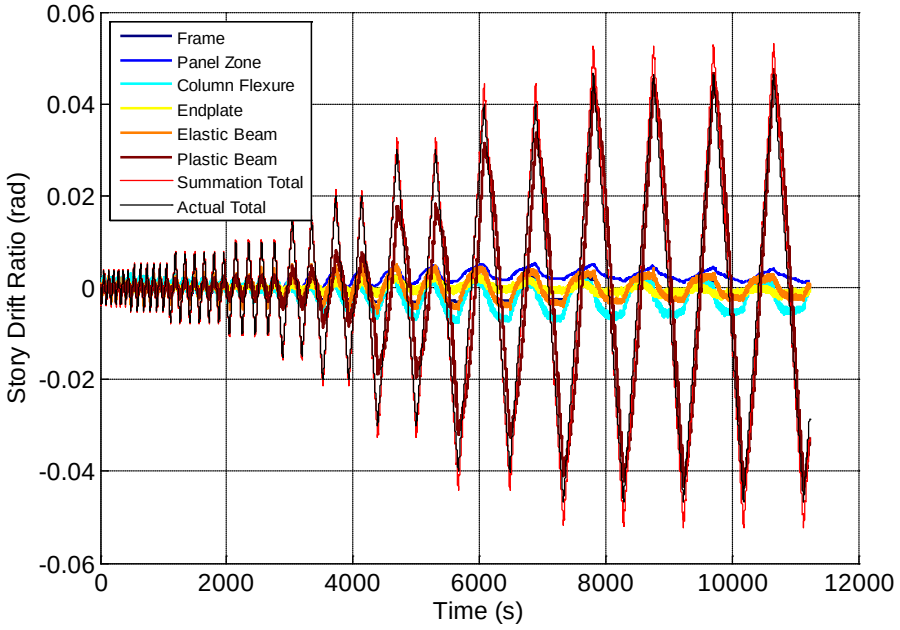

Figure C.7 – Specimen 7 Story Drift Decomposition Line Plot

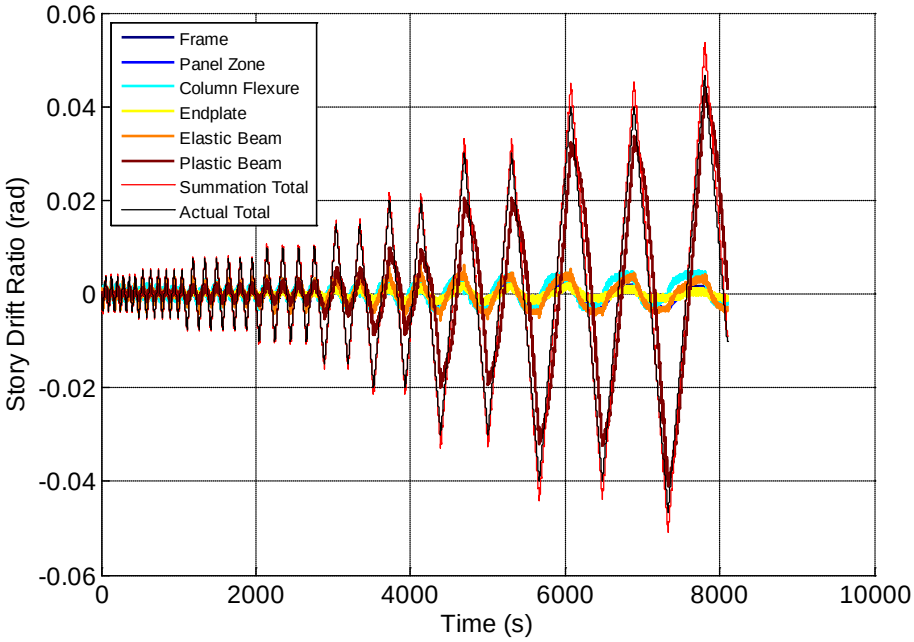

Figure C.8 – Specimen 8 Story Drift Decomposition Line Plot

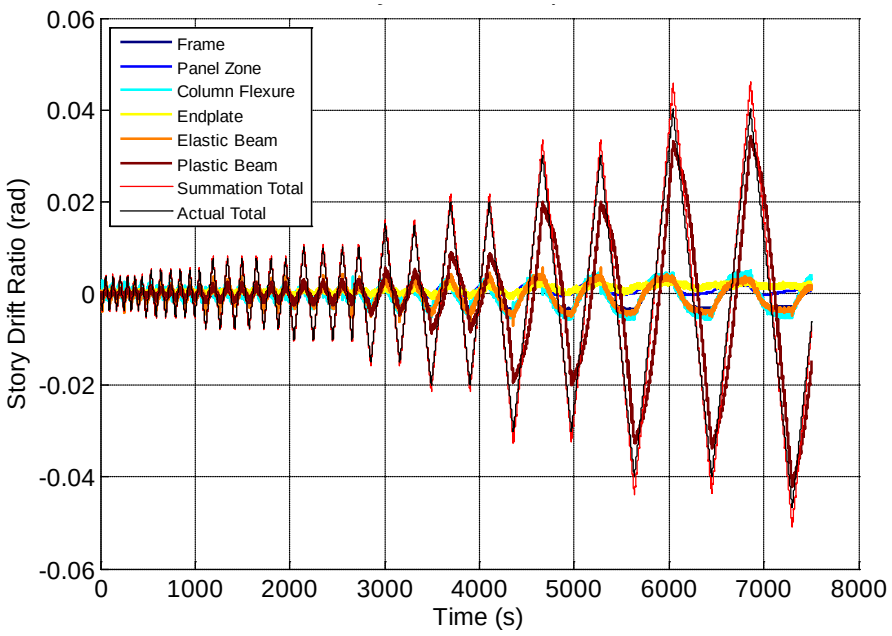

Figure C.9 – Specimen 9 Story Drift Decomposition Line Plot

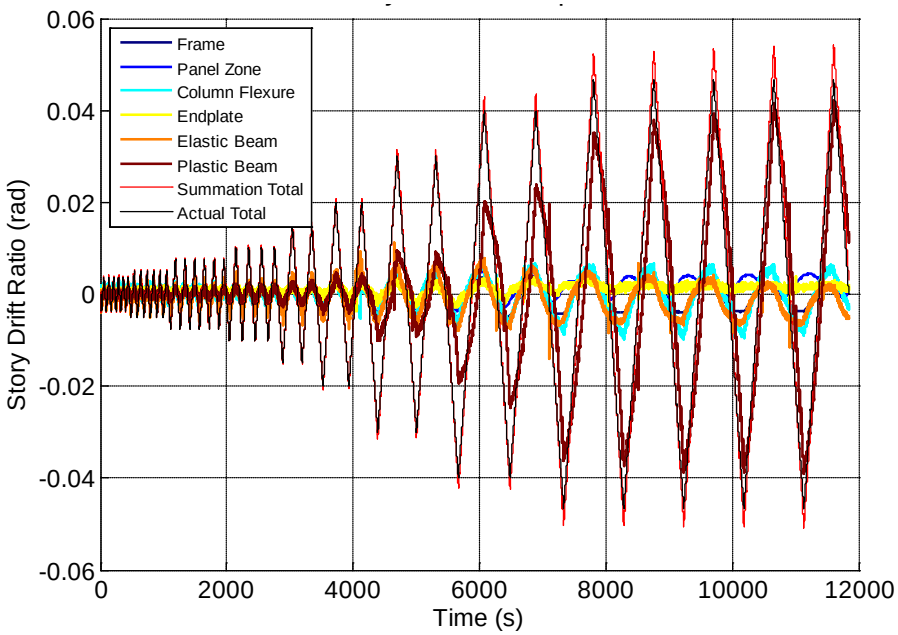

Figure C.10 – Specimen 10 Story Drift Decomposition Line Plot

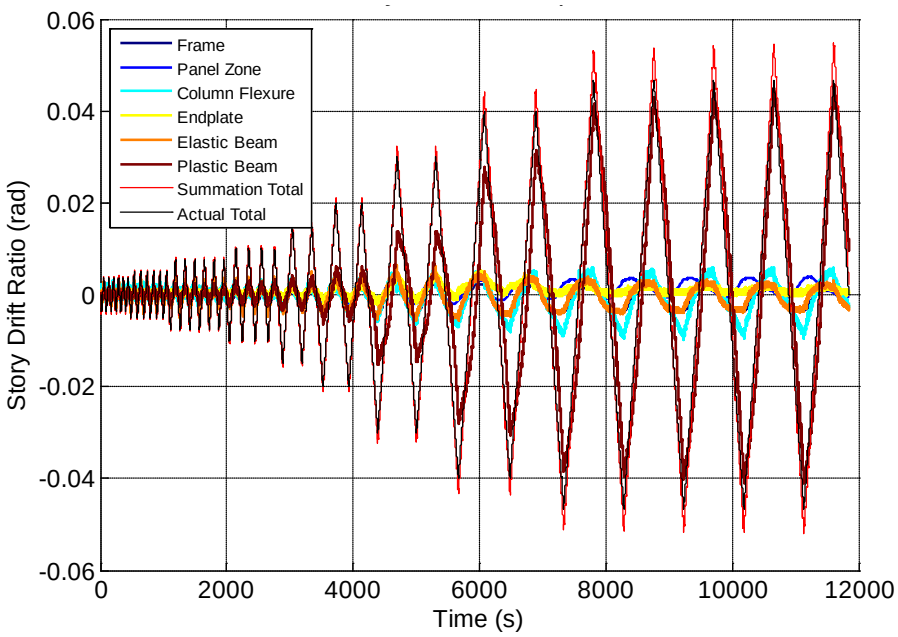

Figure C.11 – Specimen 11 Story Drift Decomposition Line Plot

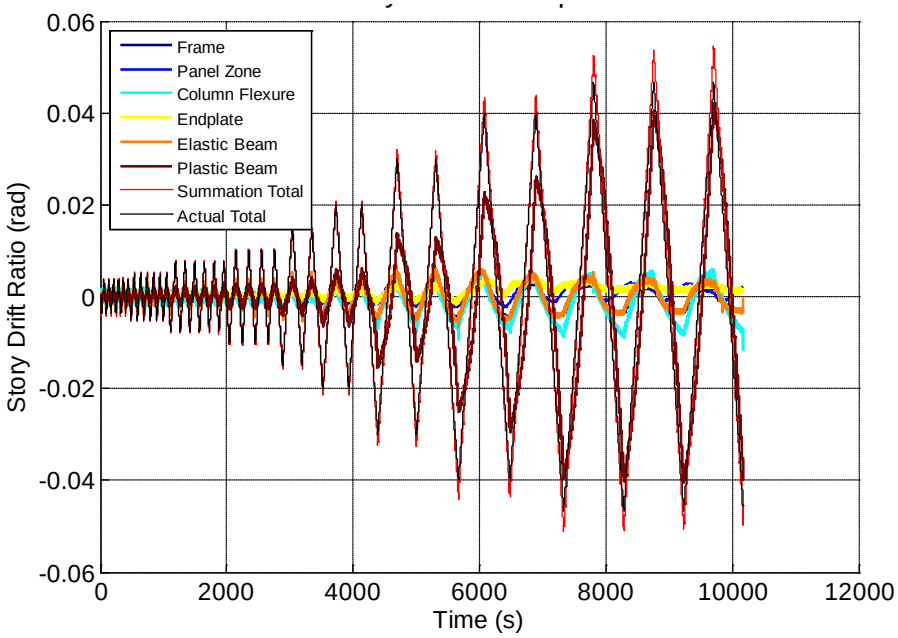

Figure C.12 – Specimen 12 Story Drift Decomposition Line Plot

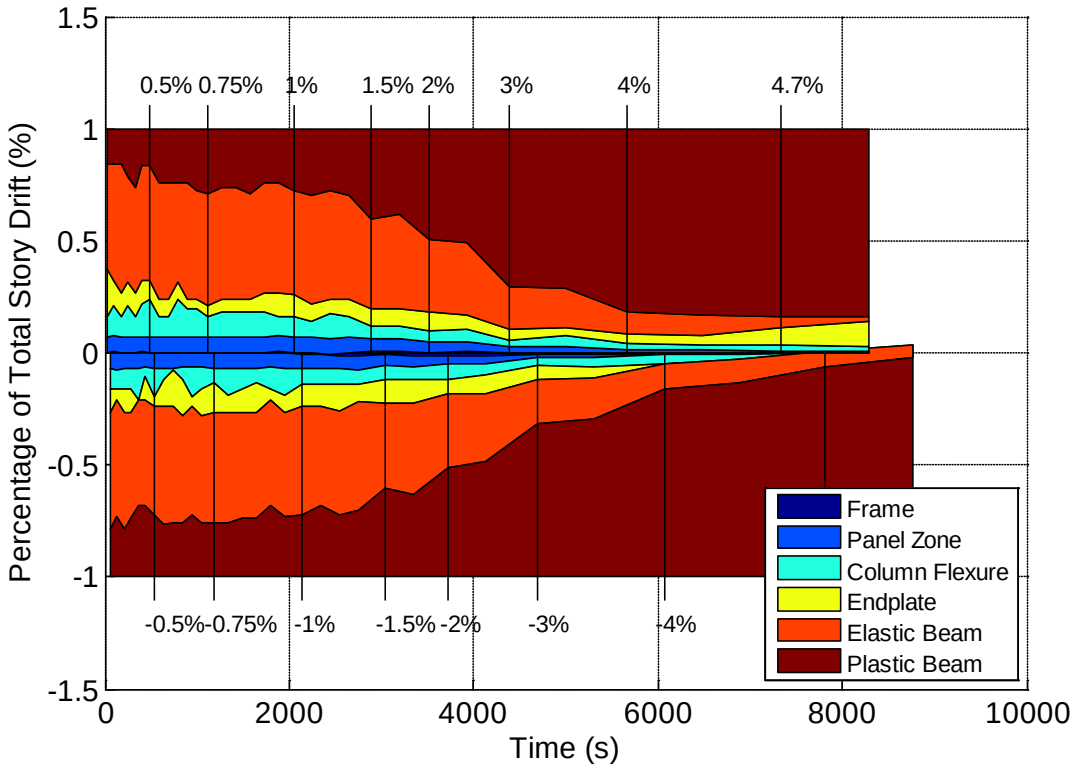

Figure C.13 – Specimen 1 Story Drift Percentage Contributions

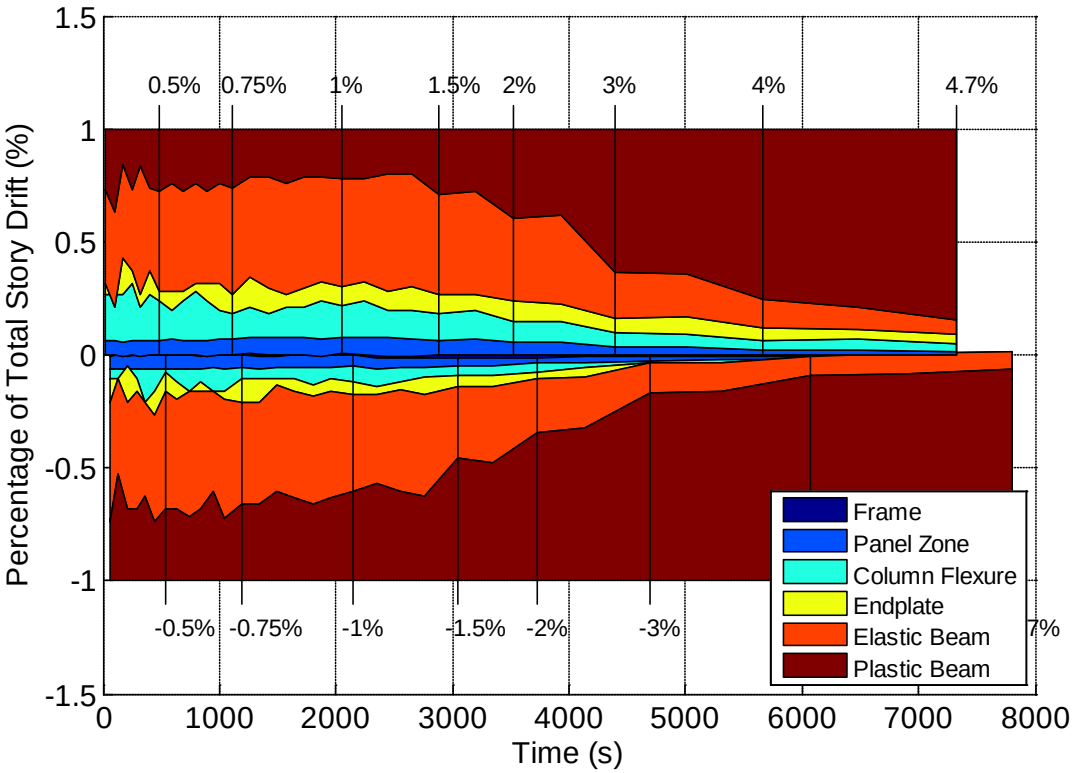

Figure C.14 – Specimen 2 Story Drift Percentage Contributions

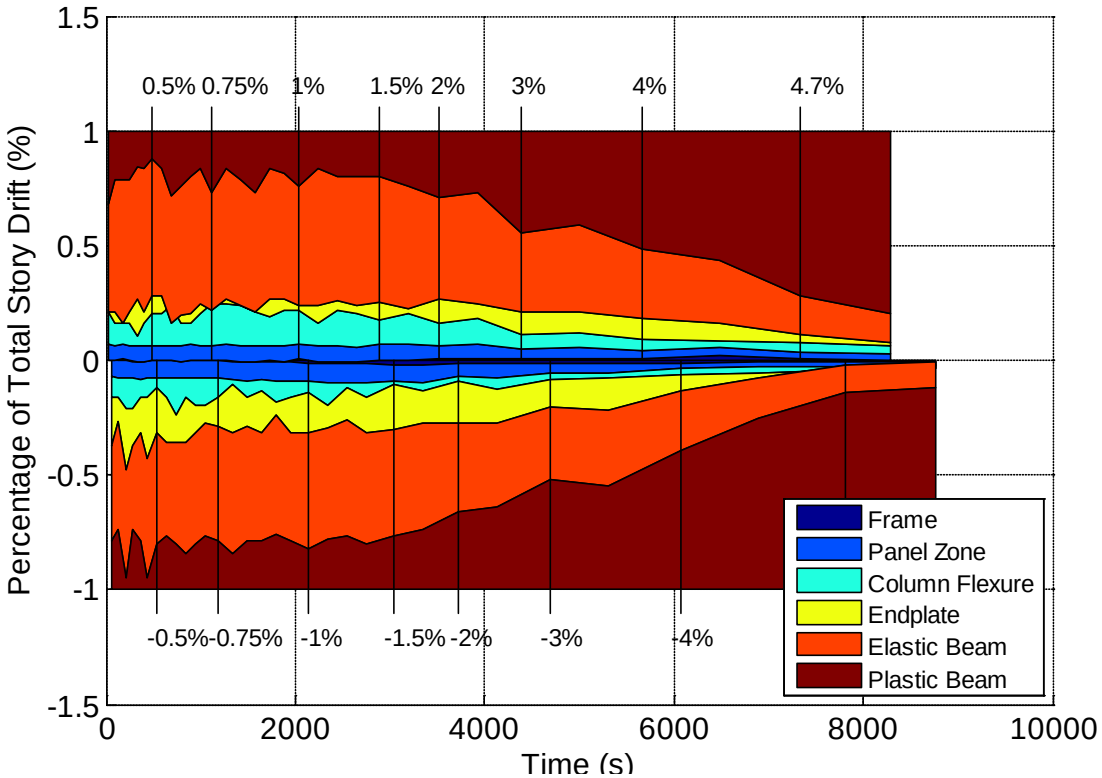

Figure C.15 – Specimen 3 Story Drift Percentage Contributions

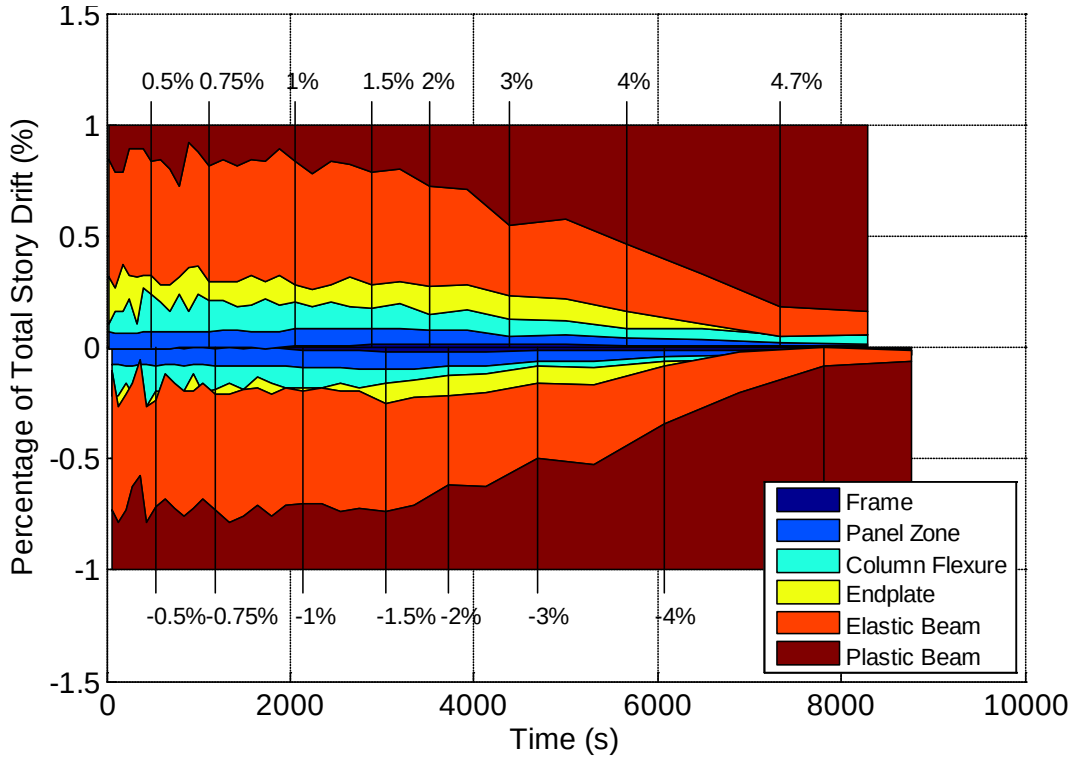

Figure C.16 – Specimen 4 Story Drift Percentage Contributions

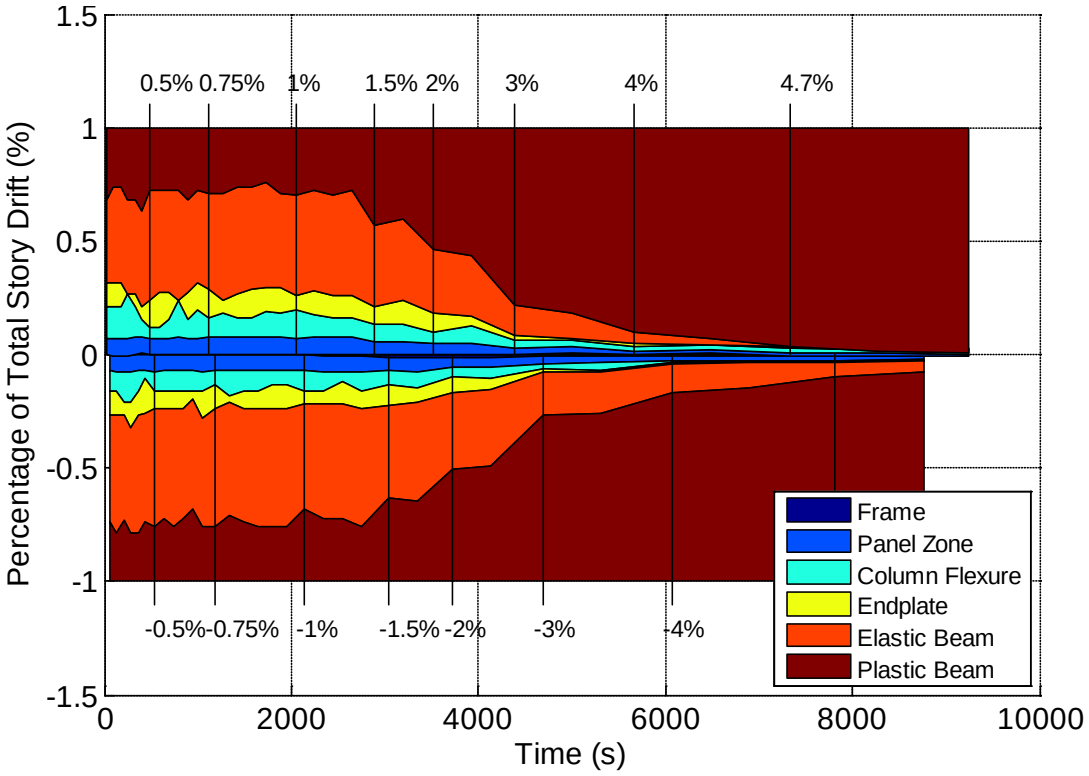

Figure C.17 – Specimen 5 Story Drift Percentage Contributions

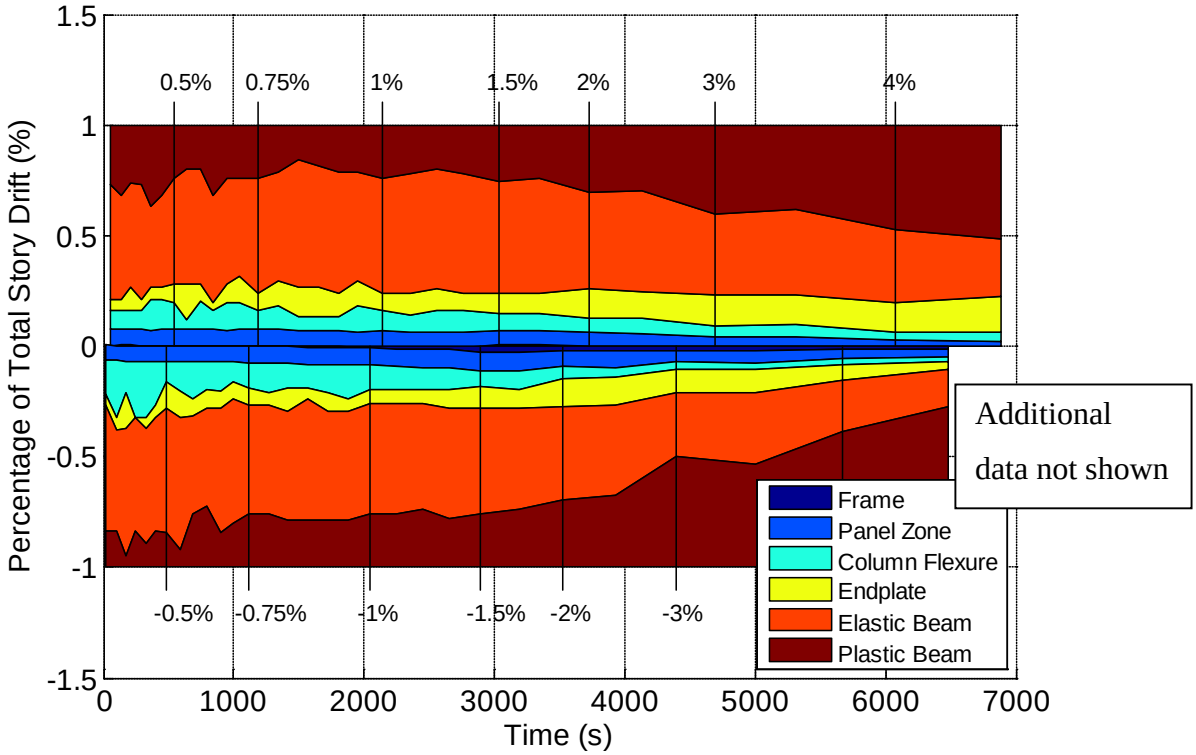

Figure C.18 – Specimen 6 Story Drift Percentage Contributions

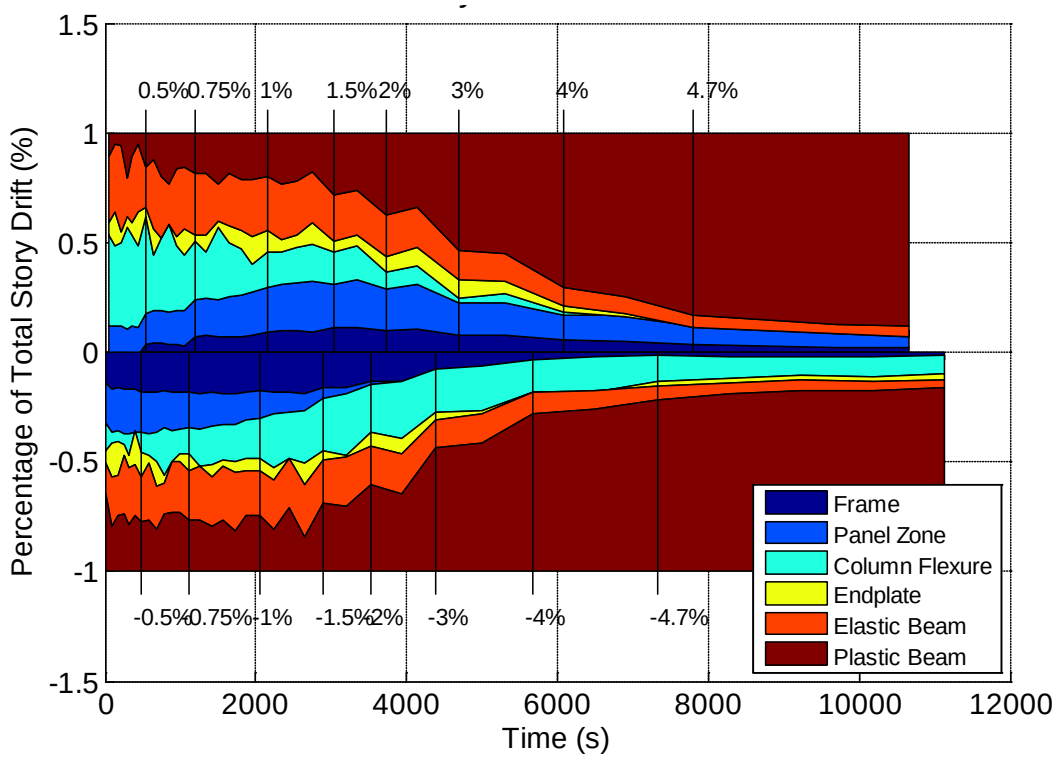

Figure C.19 – Specimen 7 Story Drift Percentage Contributions

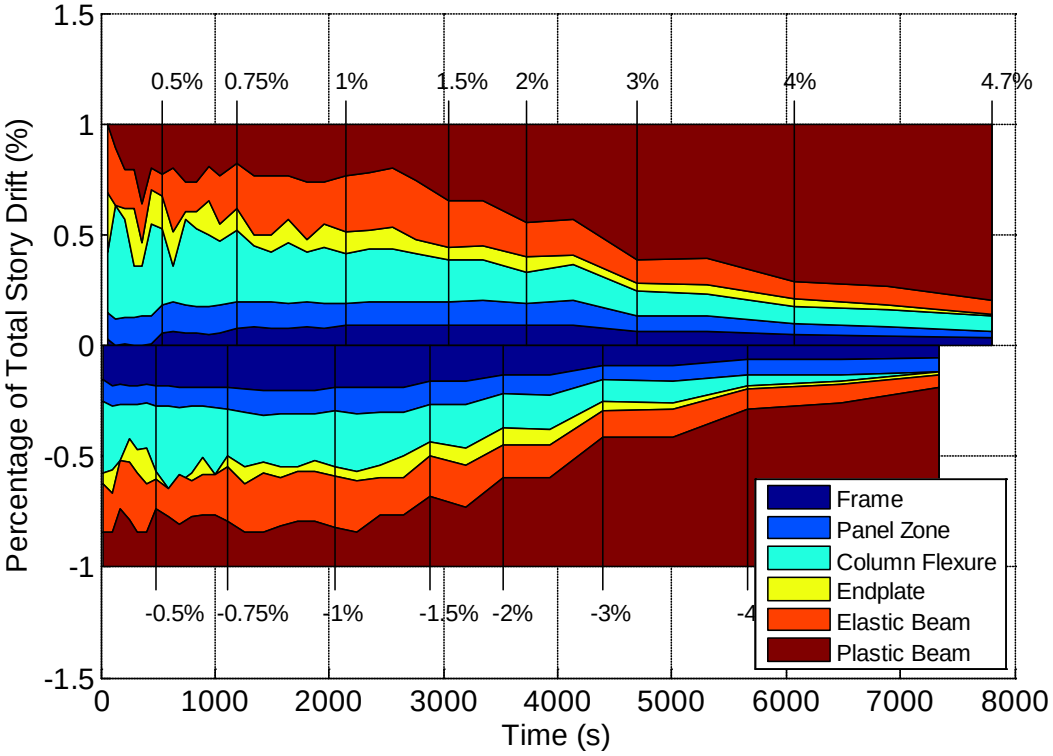

Figure C.20 – Specimen 8 Story Drift Percentage Contributions

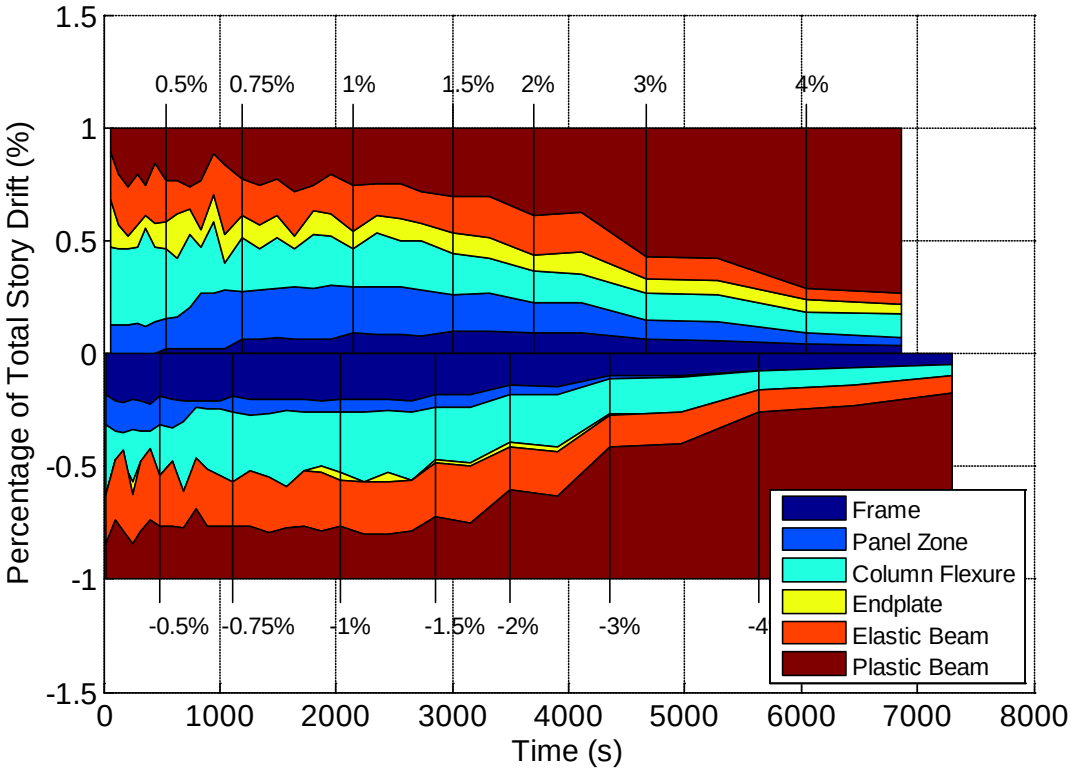

Figure C.21 – Specimen 9 Story Drift Percentage Contributions

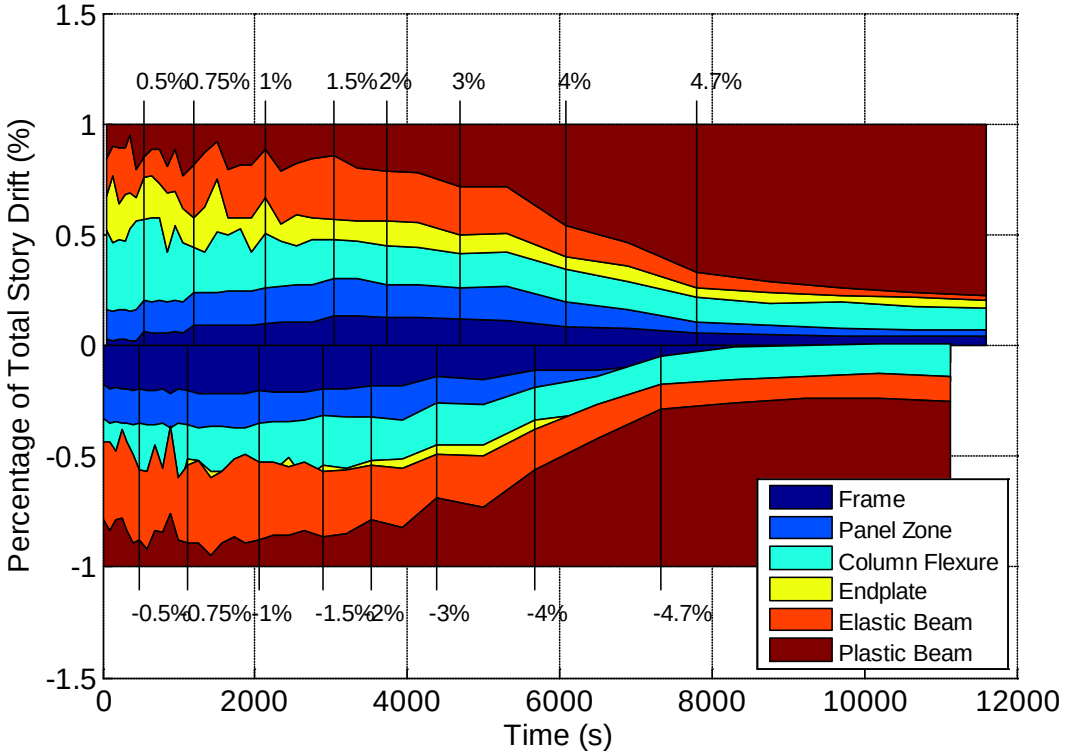

Figure C.22 – Specimen 10 Story Drift Percentage Contributions

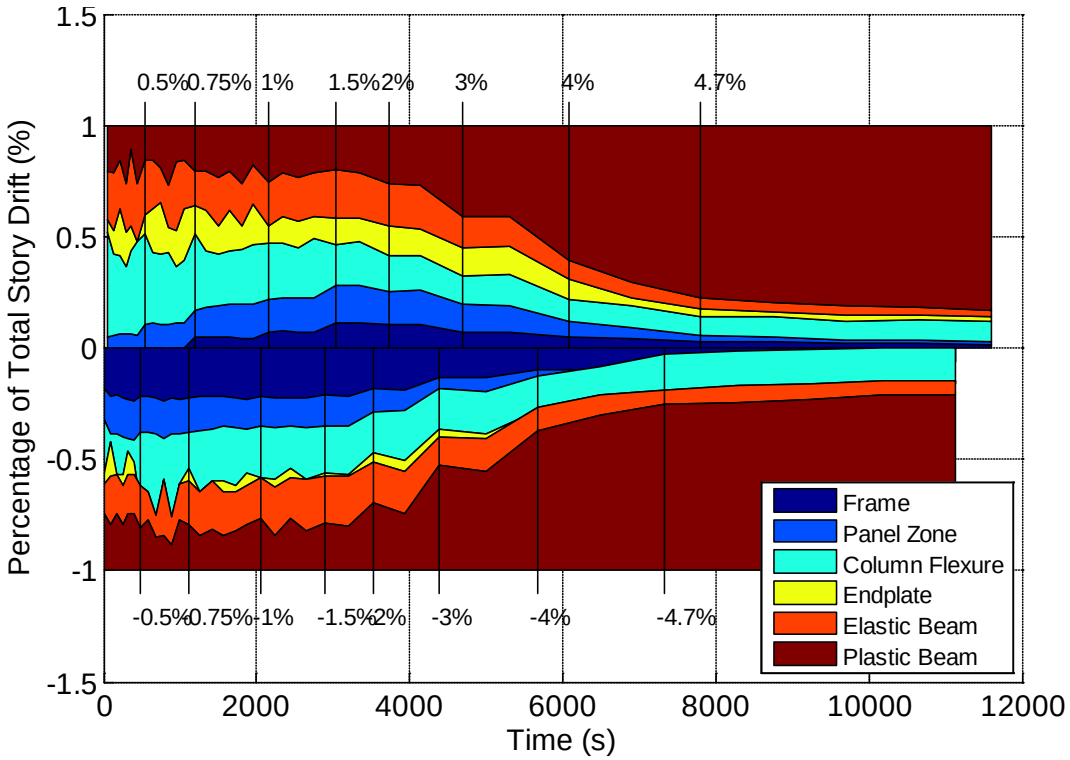

Figure C.23 – Specimen 11 Story Drift Percentage Contributions

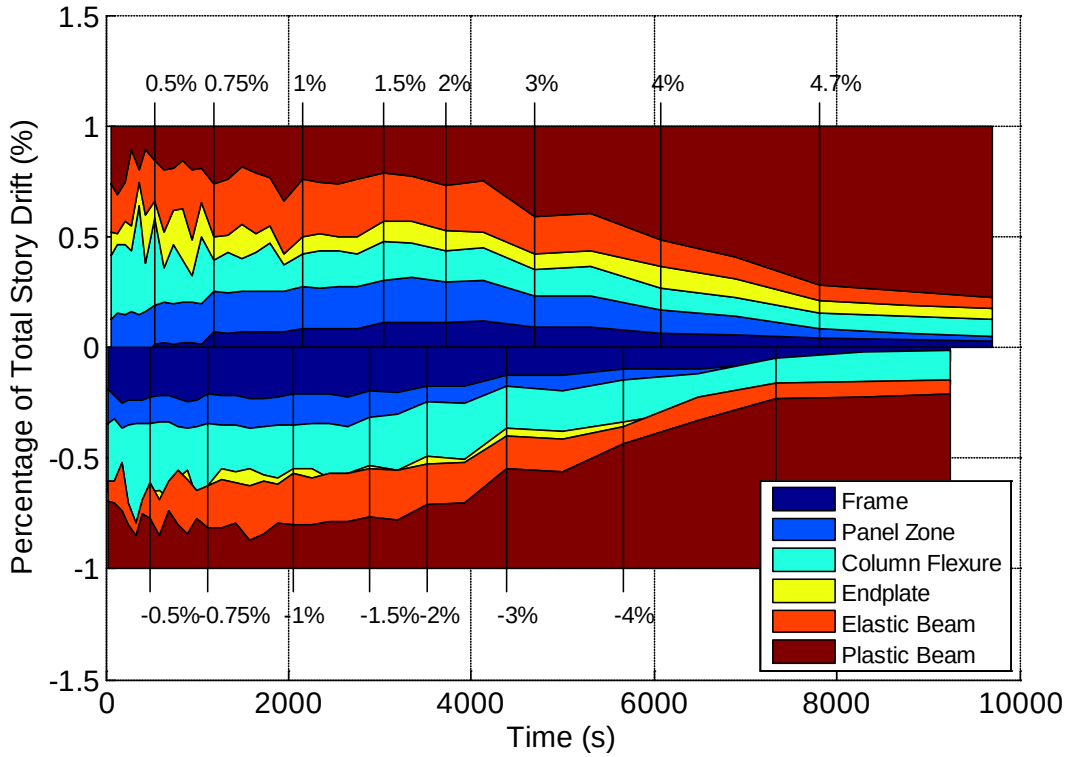

Figure C.24 – Specimen 12 Story Drift Percentage Contributions

APPENDIX D STRAIN GRADIENTS FROM STRAIN GAGES

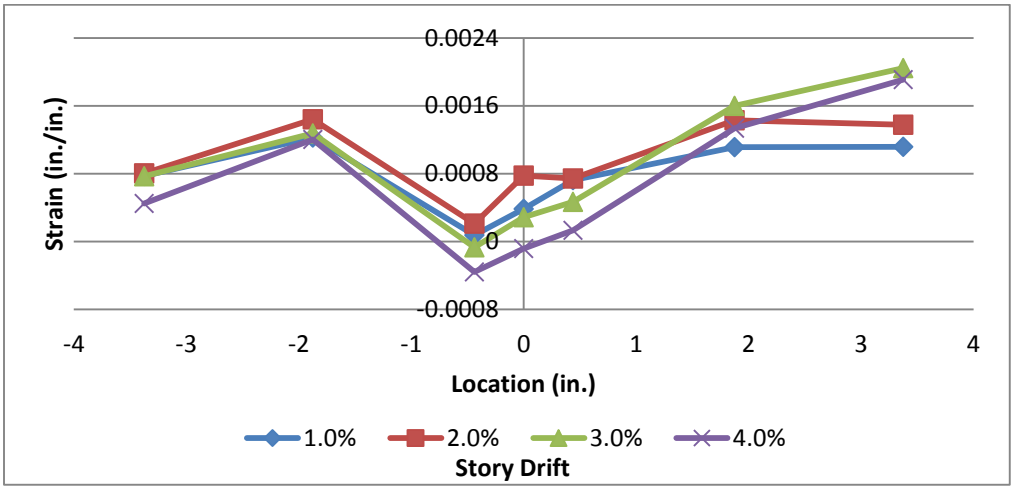

Figure D.1 – Specimen 1 (W24x62 with RBS and No Fasteners) Top Flange Strain Data Line 1

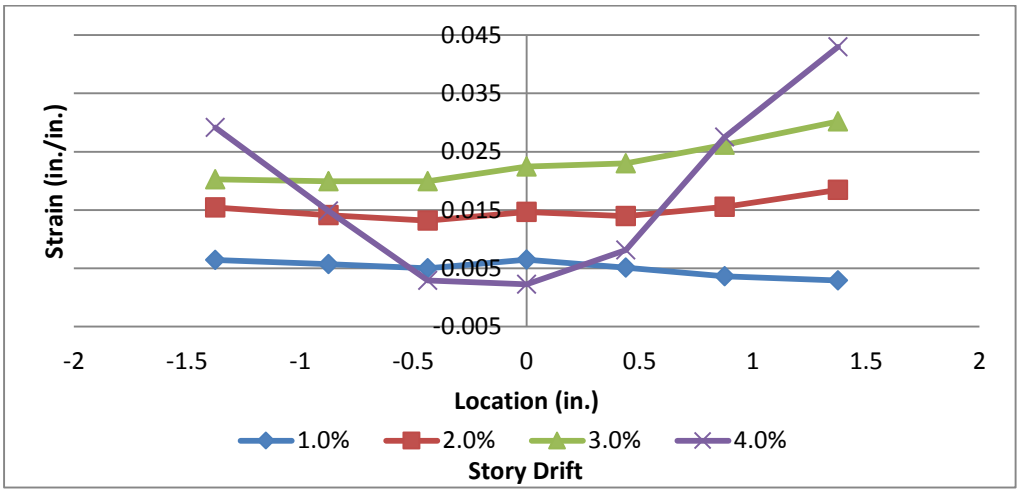

Figure D.2 – Specimen 1 (W24x62 with RBS and No Fasteners) Top Flange Strain Data Line 2

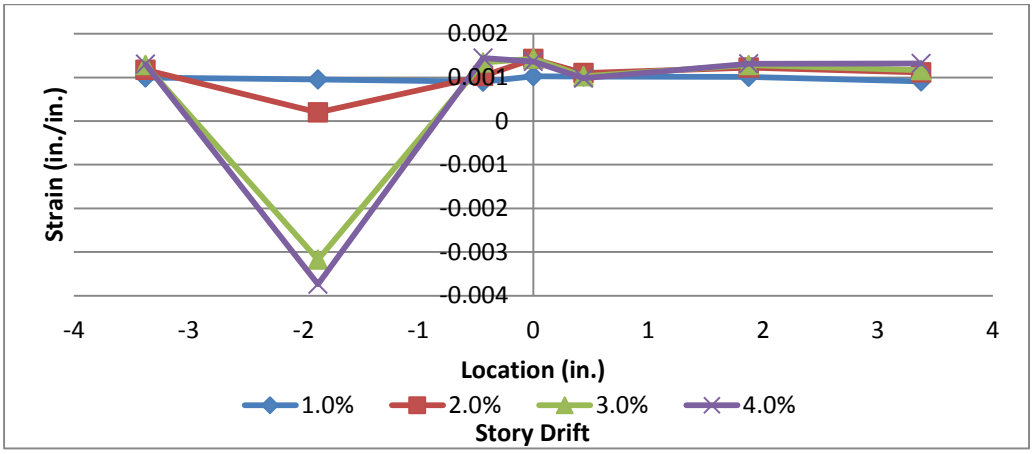

Figure D.3 – Specimen 1 (W24x62 with RBS and No Fasteners) Top Flange Strain Data Line 3

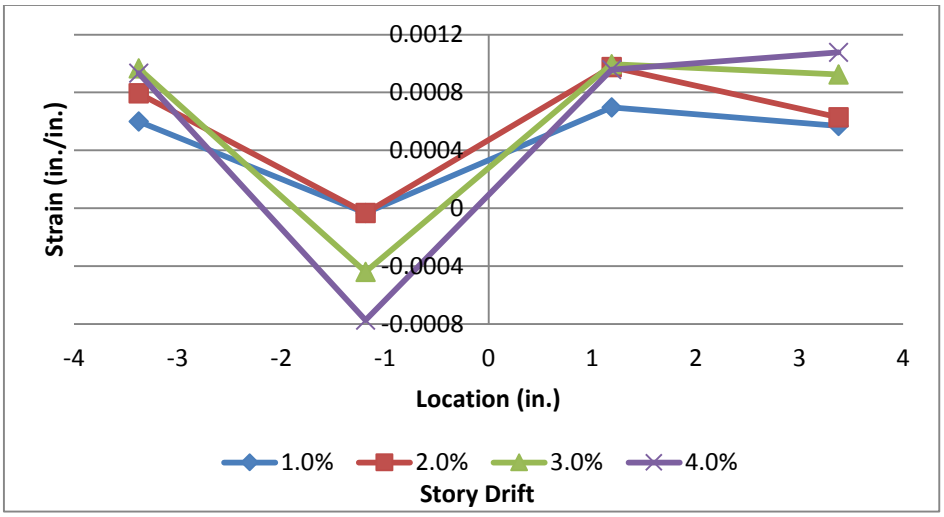

Figure D.4 – Specimen 1 (W24x62 with RBS and No Fasteners) Underside of Top Flange Strain Data Line 1

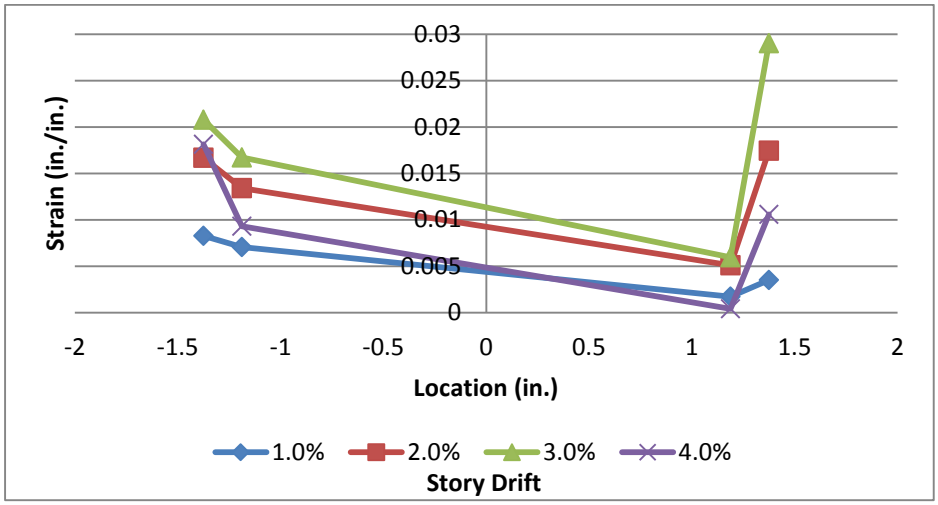

Figure D.5 – Specimen 1 (W24x62 with RBS and No Fasteners) Underside of Top Flange Strain Data Line 2

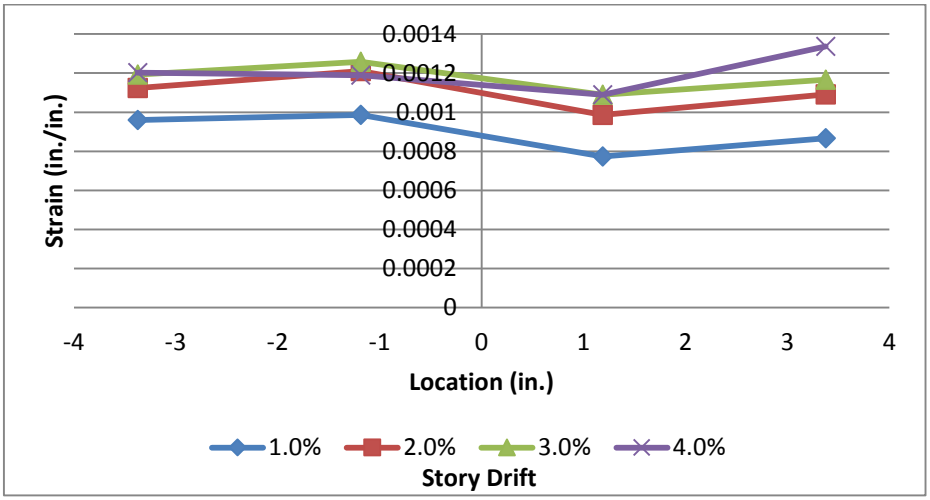

Figure D.6 Specimen 1 (W24x62 with RBS and No Fasteners) Underside of Top Flange Strain Data Line 3

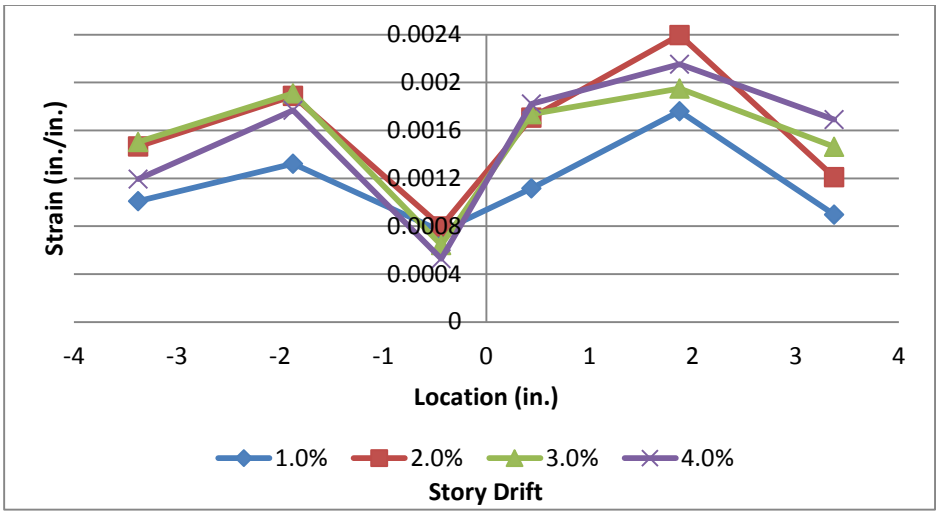

Figure D.7 – Specimen 2 (W24x62 with RBS and PAFs at 12 in.) Top Flange Strain Data Line 1

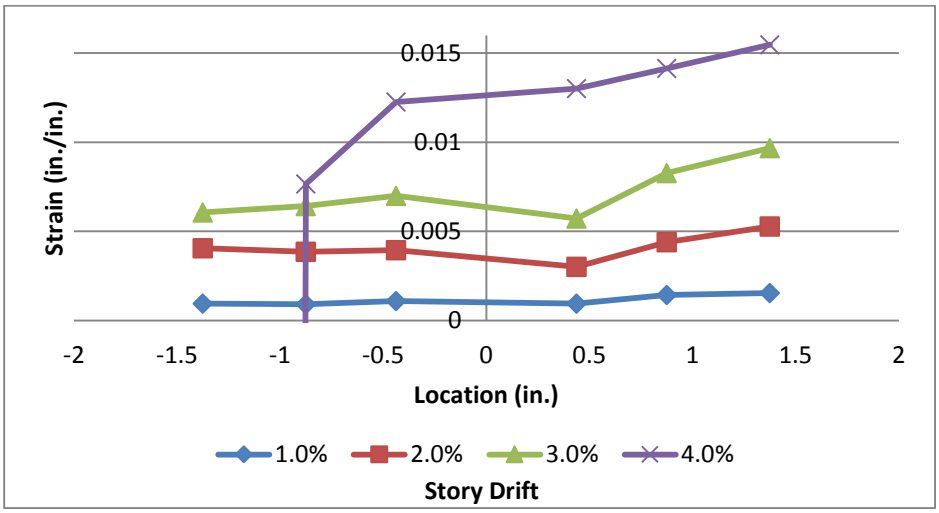

Figure D.8 – Specimen 2 (W24x62 with RBS and PAFs at 12 in.) Top Flange Strain Data Line 2

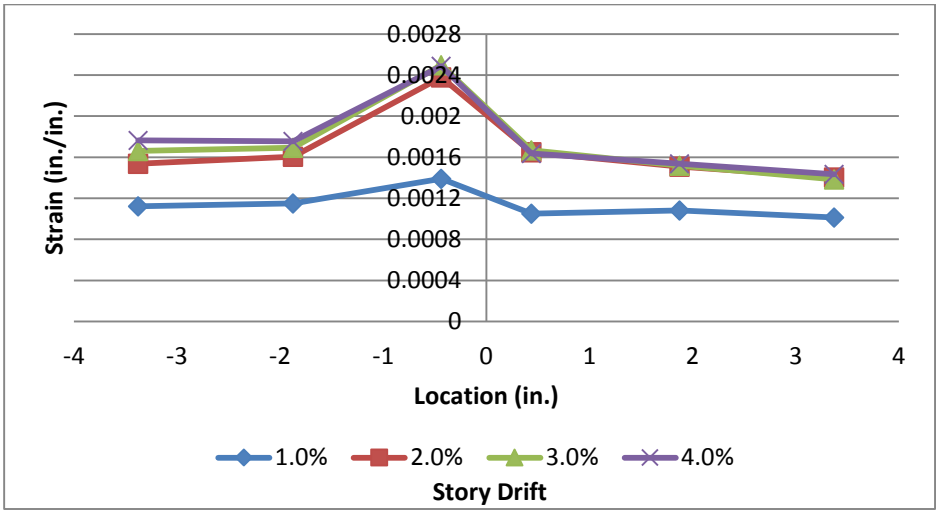

Figure D.9 – Specimen 2 (W24x62 with RBS and PAFs at 12 in.) Top Flange Strain Data Line 3

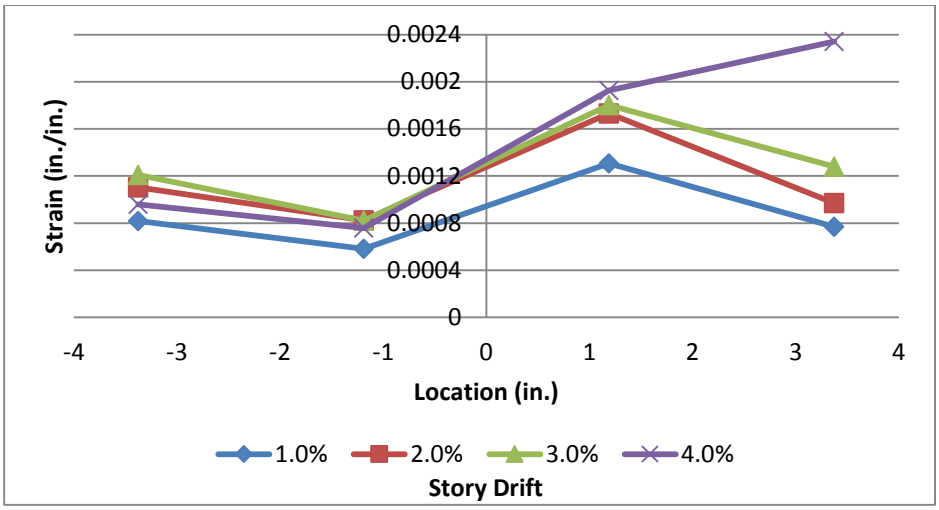

Figure D.10 – Specimen 2 (W24x62 with RBS and PAFs at 12 in.) Underside of Top Flange Strain Data Line 1

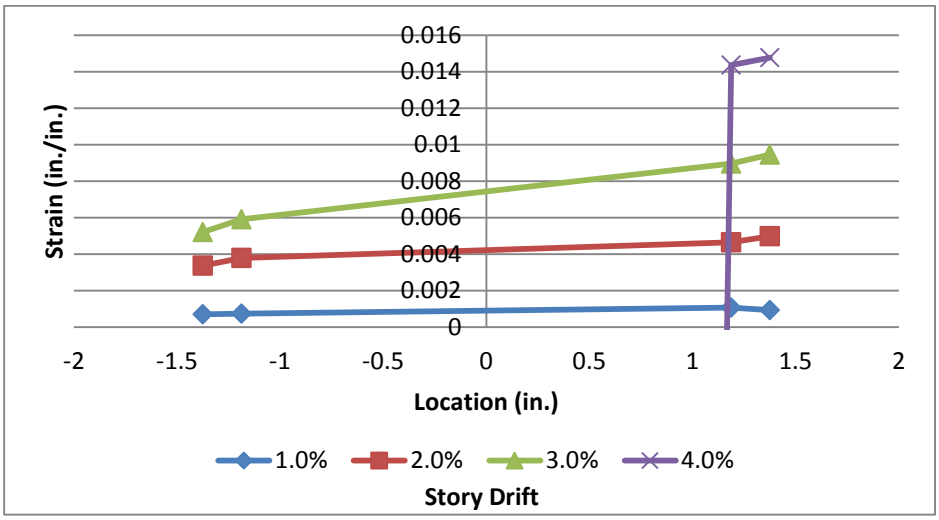

Figure D.11 – Specimen 2 (W24x62 with RBS and PAFs at 12 in.) Underside of Top Flange Strain Data Line 2

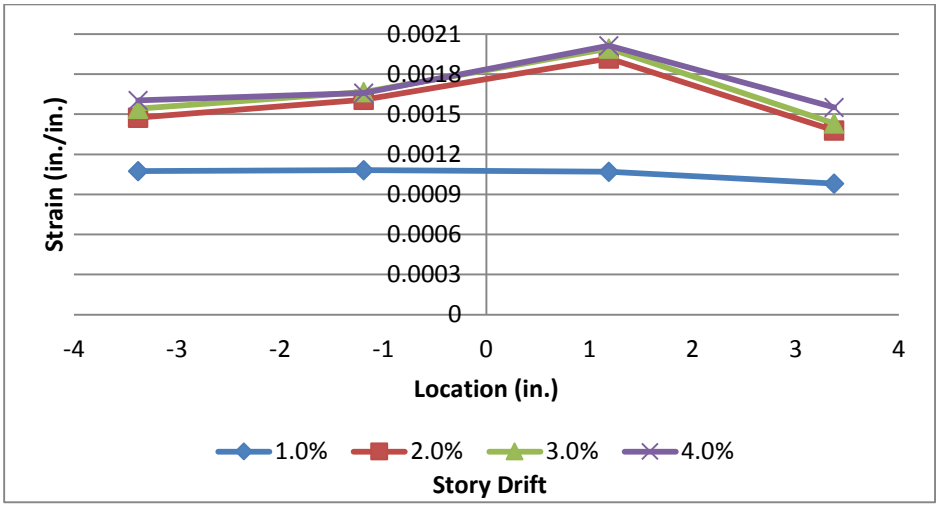

Figure D.12 – Specimen 2 (W24x62 with RBS and PAFs at 12 in.) Underside of Top Flange Strain Data Line 3

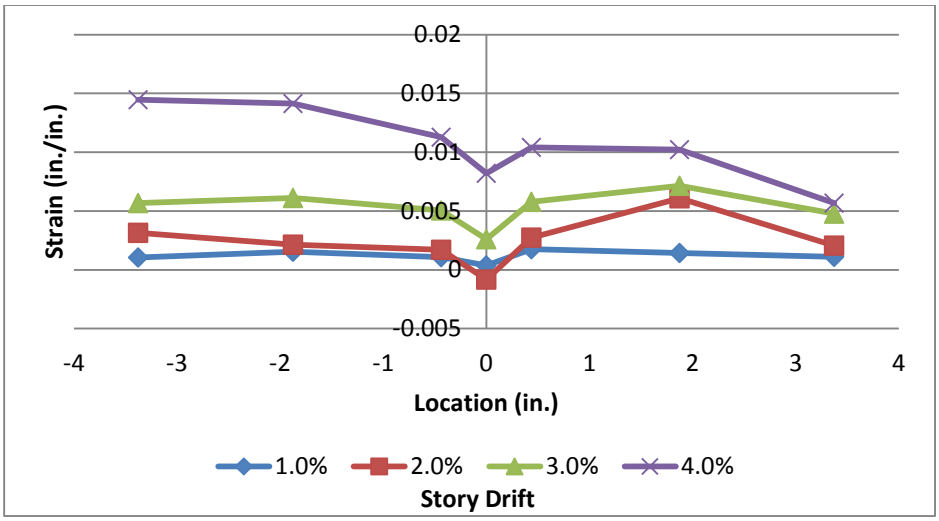

Figure D.13 – Specimen 3 (W24x62 with No RBS and No Fasteners) Top Flange Strain Data Line 1

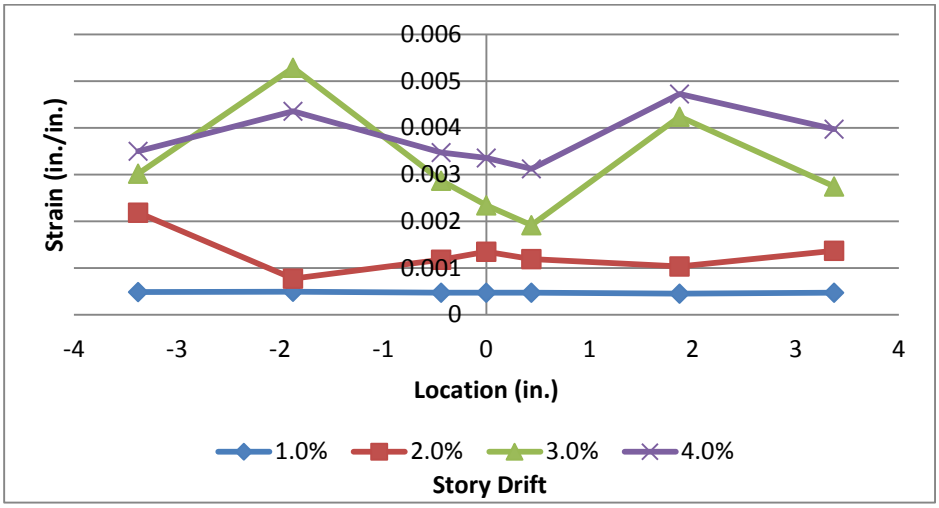

Figure D.14 – Specimen 3 (W24x62 with No RBS and No Fasteners) Top Flange Strain Data Line 2

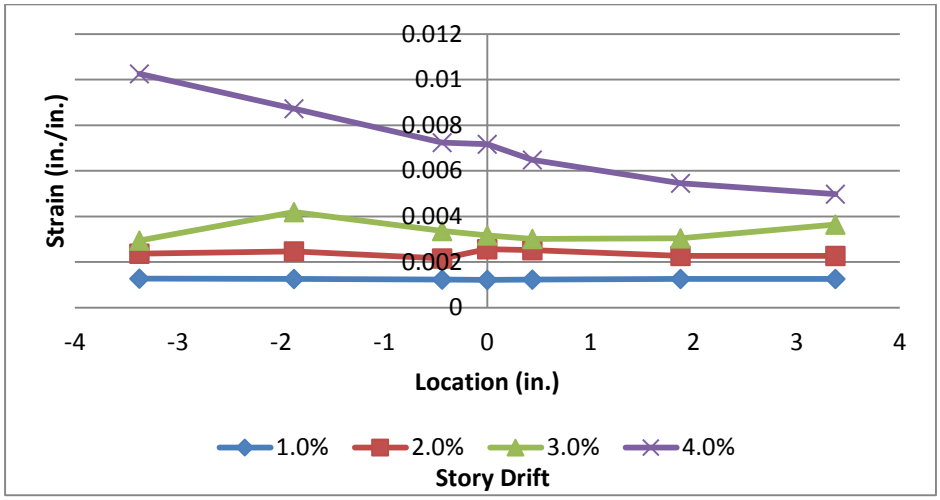

Figure D.15 – Specimen 3 (W24x62 with No RBS and No Fasteners) Top Flange Strain Data Line 3

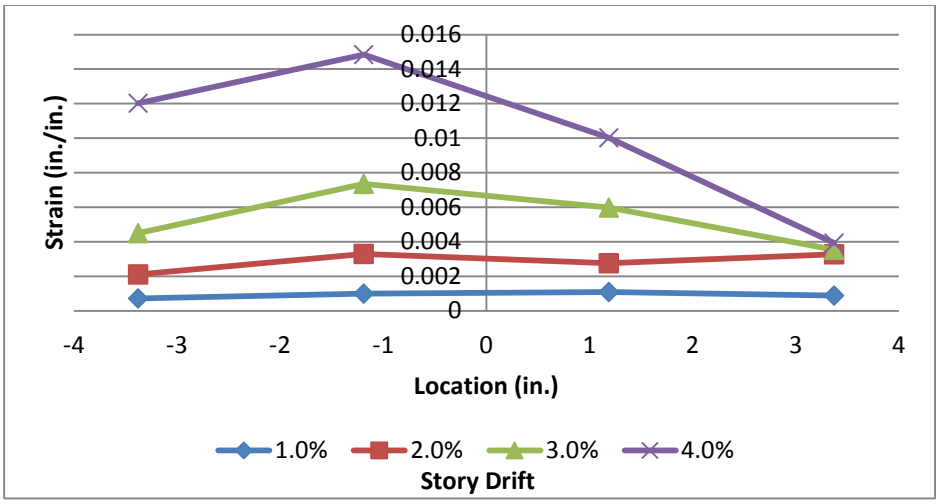

Figure D.16 – Specimen 3 (W24x62 with No RBS and No Fasteners) Underside of Top Flange Strain Data Line 1

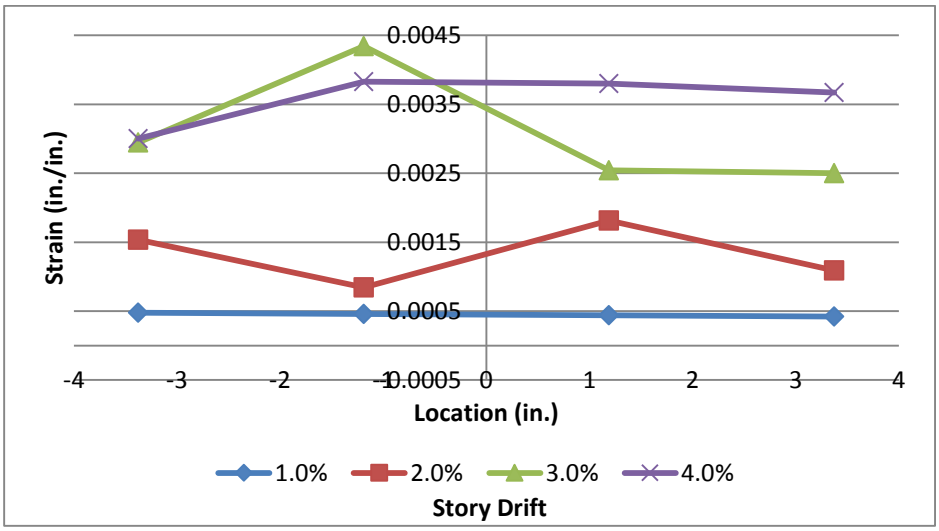

Figure D.17 – Specimen 3 (W24x62 with No RBS and No Fasteners) Underside of Top Flange Strain Data Line 2

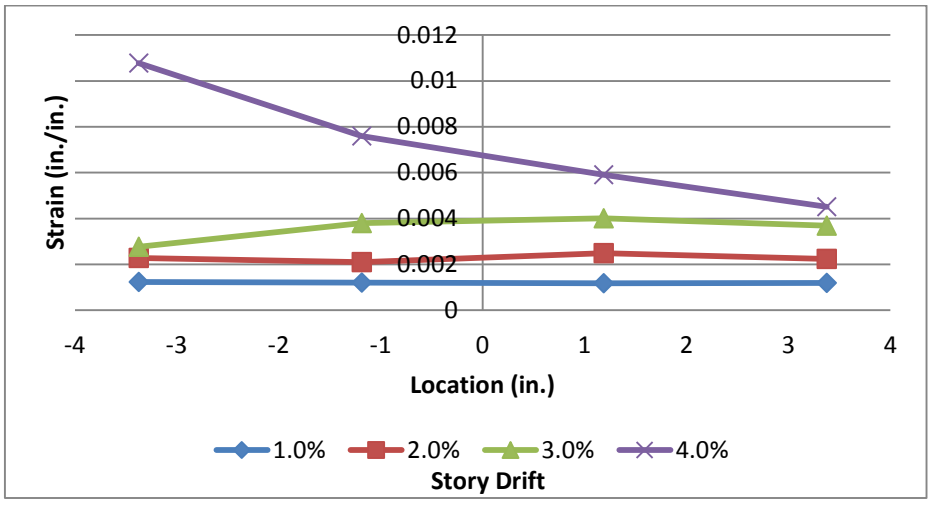

Figure D.18 – Specimen 3 (W24x62 with No RBS and No Fasteners) Underside of Top Flange Strain Data Line 3

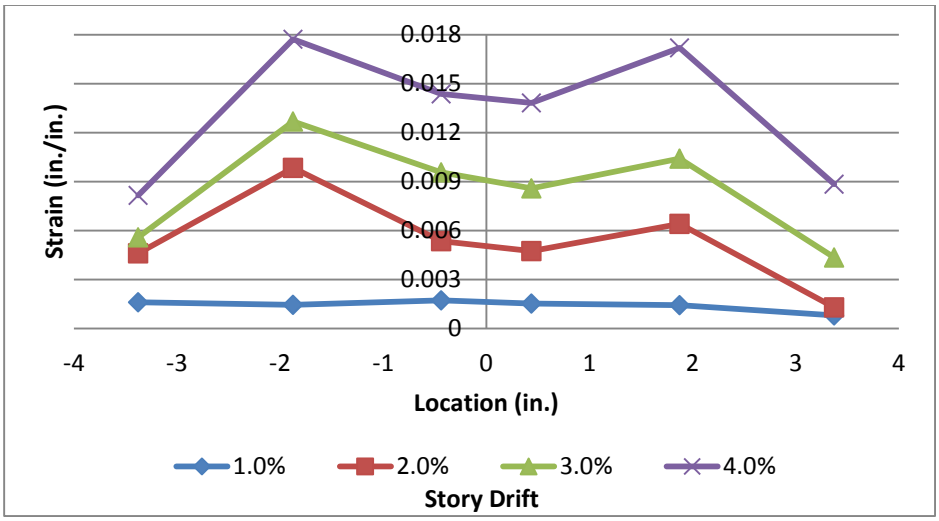

Figure D.19 – Specimen 4 (W24x62 with No RBS and PAFs at 12 in.) Top Flange Strain Data Line 1

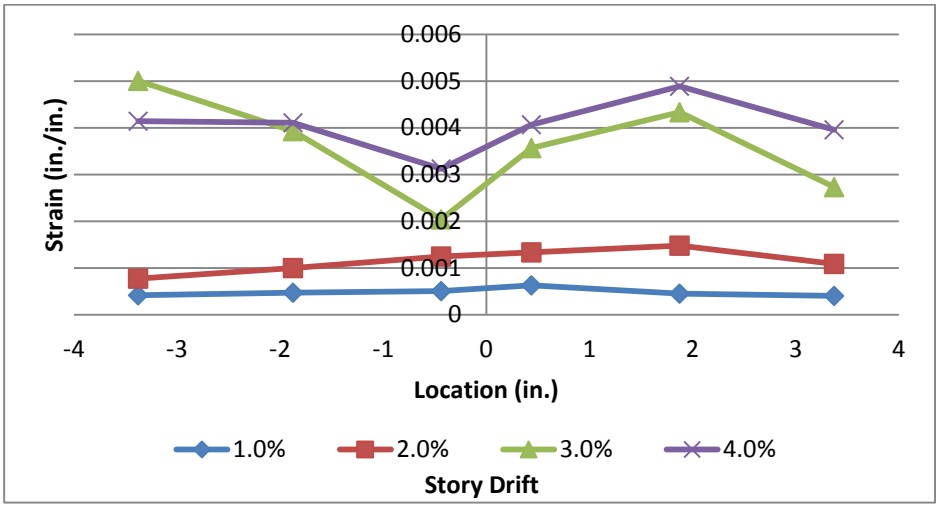

Figure D.20 – Specimen 4 (W24x62 with No RBS and PAFs at 12 in.) Top Flange Strain Data Line 2

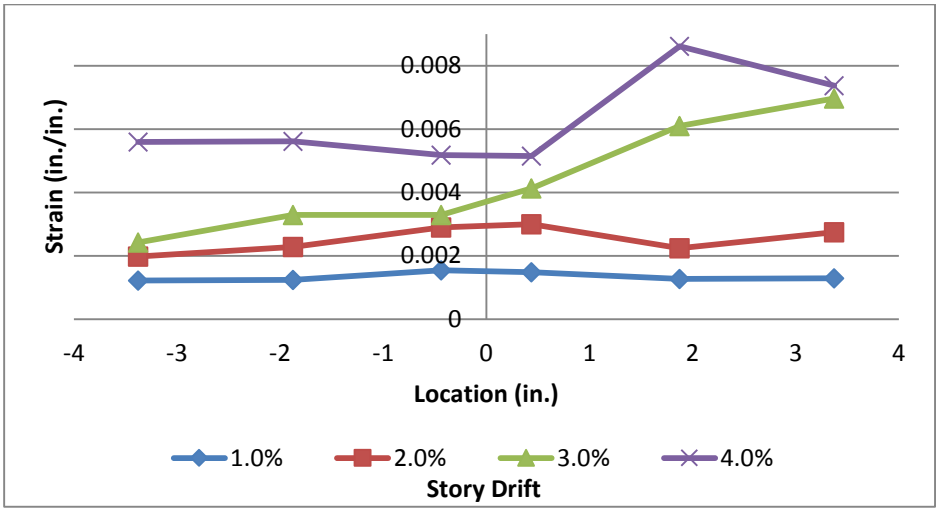

Figure D.21 – Specimen 4 (W24x62 with No RBS and PAFs at 12 in.) Top Flange Strain Data Line 3

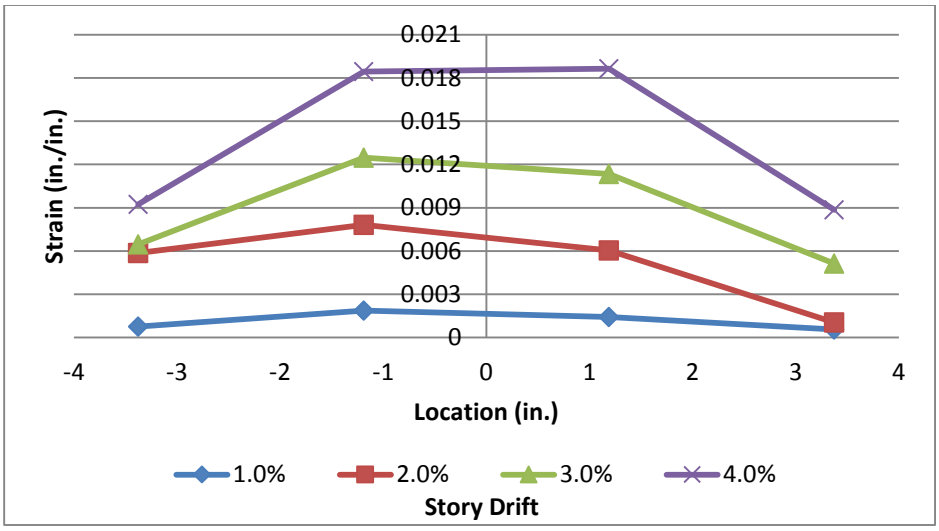

Figure D.22 – Specimen 4 (W24x62 with No RBS and PAFs at 12 in.) Underside of Top Flange Strain Data Line 1

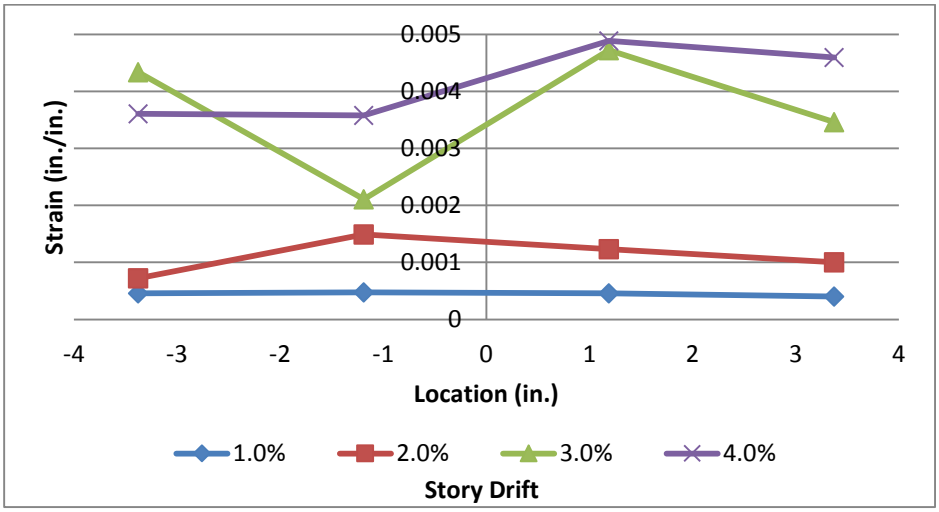

Figure D.23 – Specimen 4 (W24x62 with No RBS and PAFs at 12 in.) Underside of Top Flange Strain Data Line 2

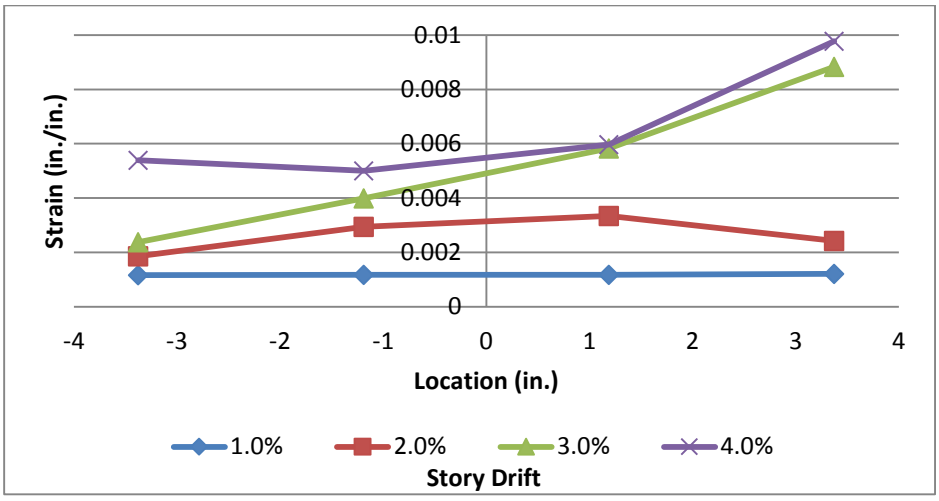

Figure D.24 – Specimen 4 (W24x62 with No RBS and PAFs at 12 in.) Underside of Top Flange Strain Data Line 3

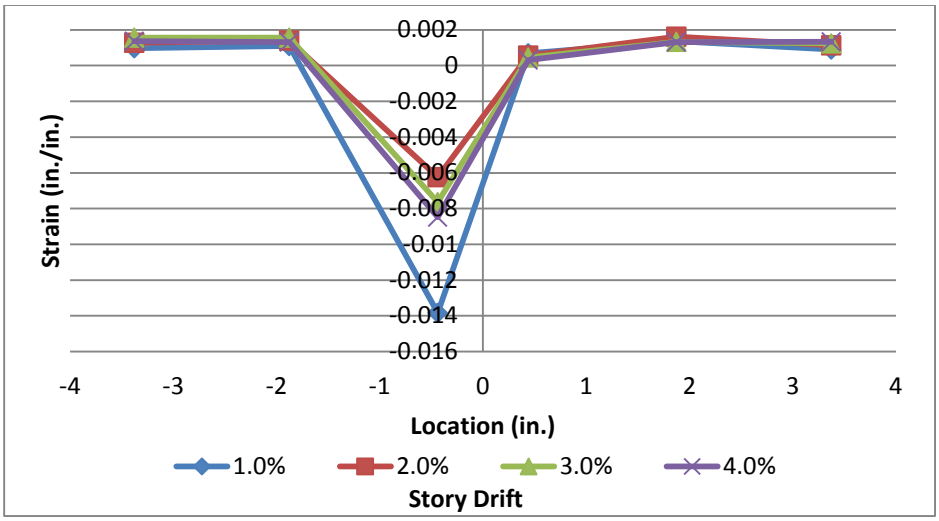

Figure D.25 – Specimen 5 (W24x62 with RBS and Puddle Welds at 12 in.) Top Flange Strain Data Line 1

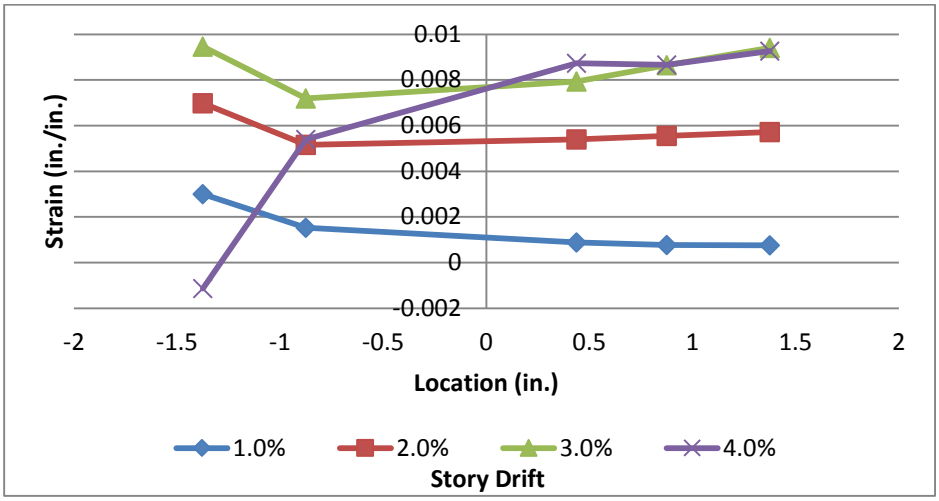

Figure D.26 – Specimen 5 (W24x62 with RBS and Puddle Welds at 12 in.) Top Flange Strain Data Line 2

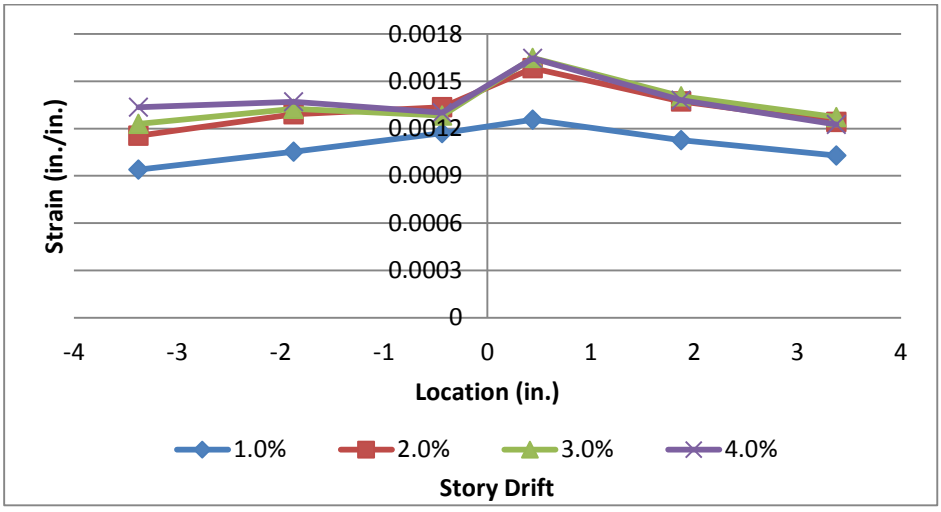

Figure D.27 – Specimen 5 (W24x62 with RBS and Puddle Welds at 12 in.) Top Flange Strain Data Line 3

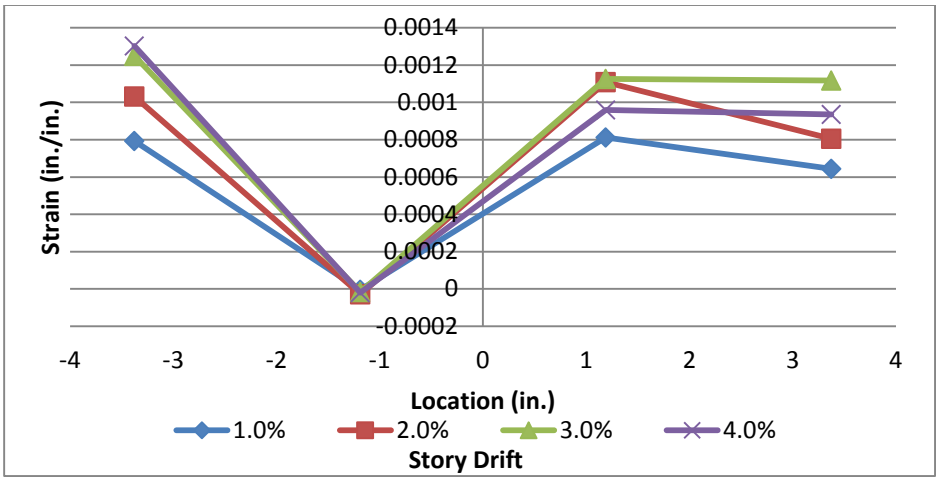

Figure D.28 – Specimen 5 (W24x62 with RBS and Puddle Welds at 12 in.) Underside of Top Flange Strain Data Line 1

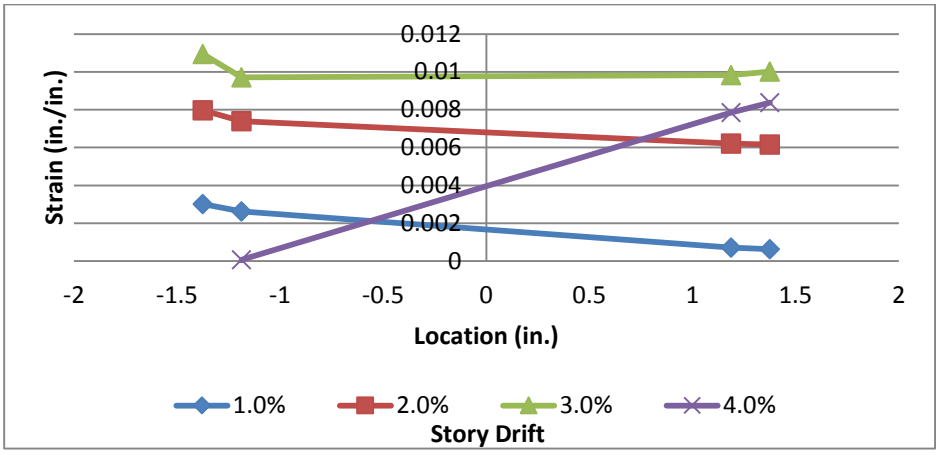

Figure D.29 – Specimen 5 (W24x62 with RBS and Puddle Welds at 12 in.) Underside of Top Flange Strain Data Line 2

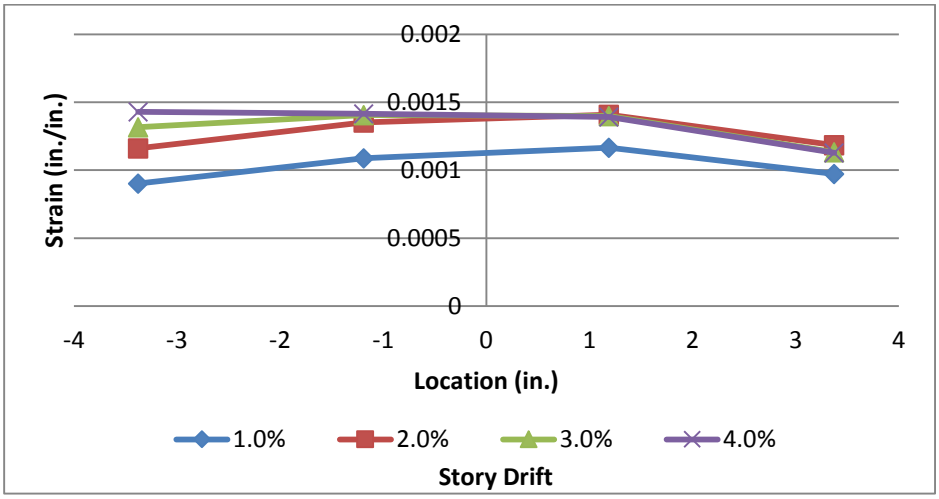

Figure D.30 – Specimen 5 (W24x62 with RBS and Puddle Welds at 12 in.) Underside of Top Flange Strain Data Line 3

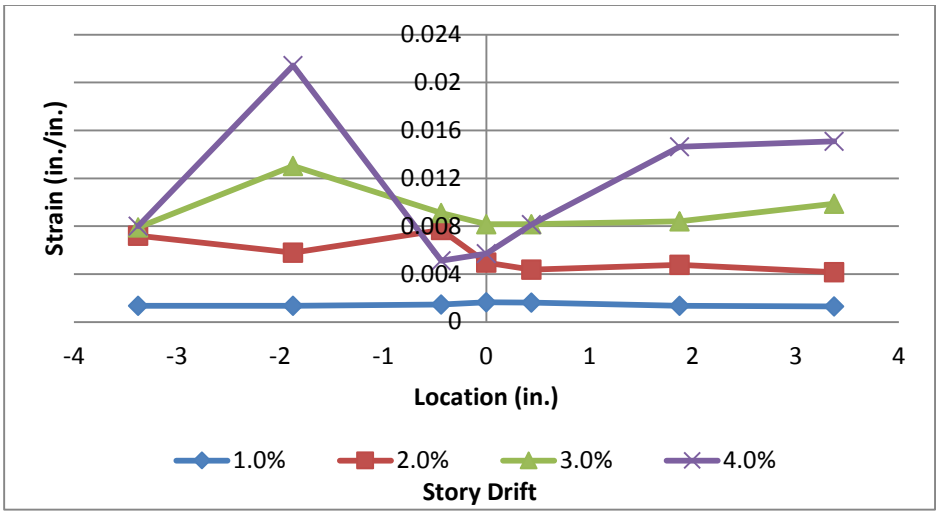

Figure D.31 – Specimen 6 (W24x62 with No RBS and Grid of PAFs) Top Flange Strain Data Line 1

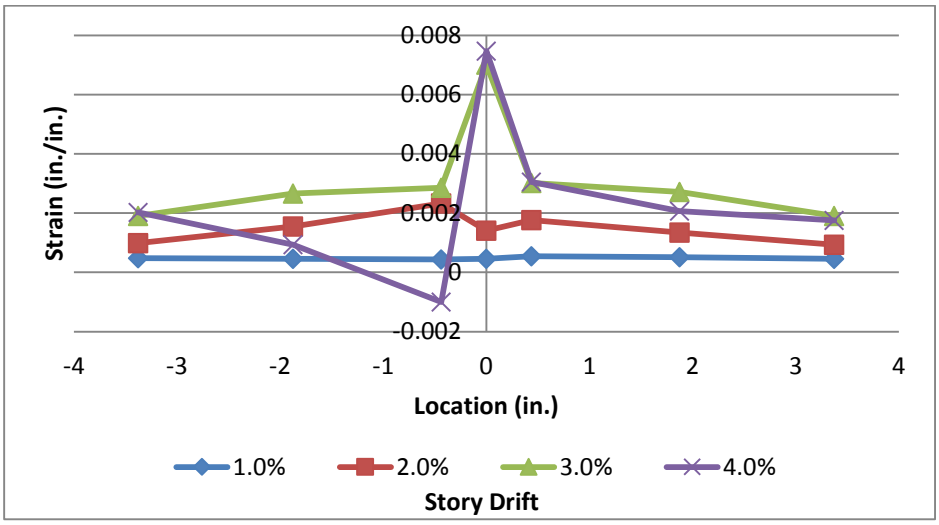

Figure D.32 – Specimen 6 (W24x62 with No RBS and Grid of PAFs) Top Flange Strain Data Line 2

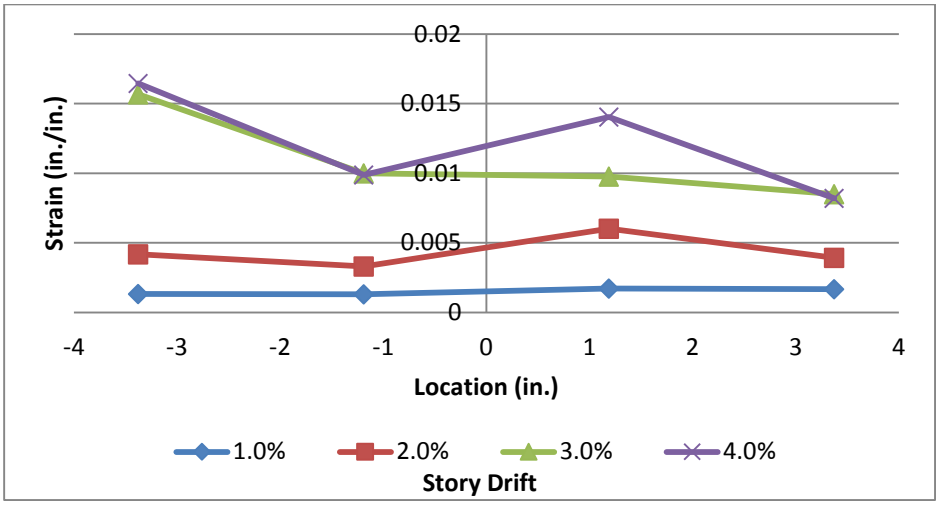

Figure D.33 – Specimen 6 (W24x62 with No RBS and Grid of PAFs) Underside of Top Flange Strain Data Line 1

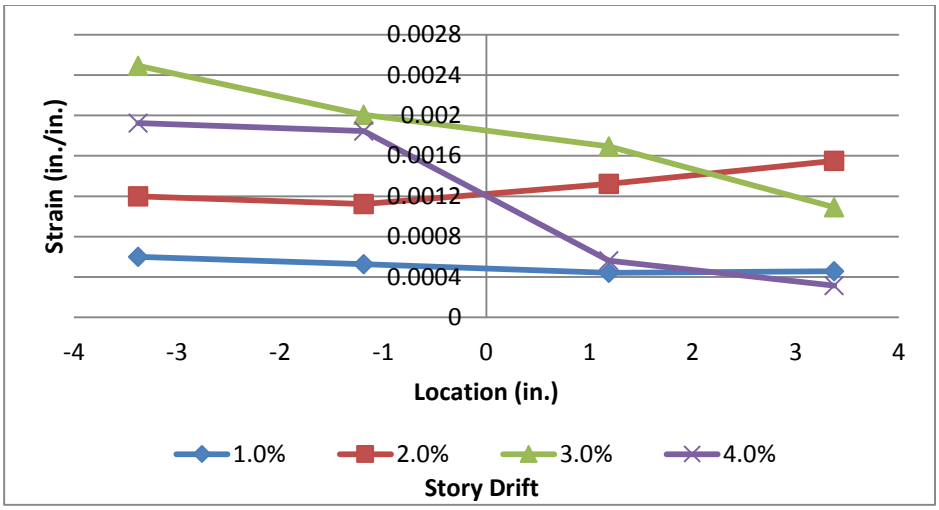

Figure D.34 – Specimen 6 (W24x62 with No RBS and Grid of PAFs) Underside of Top Flange Strain Data Line 2

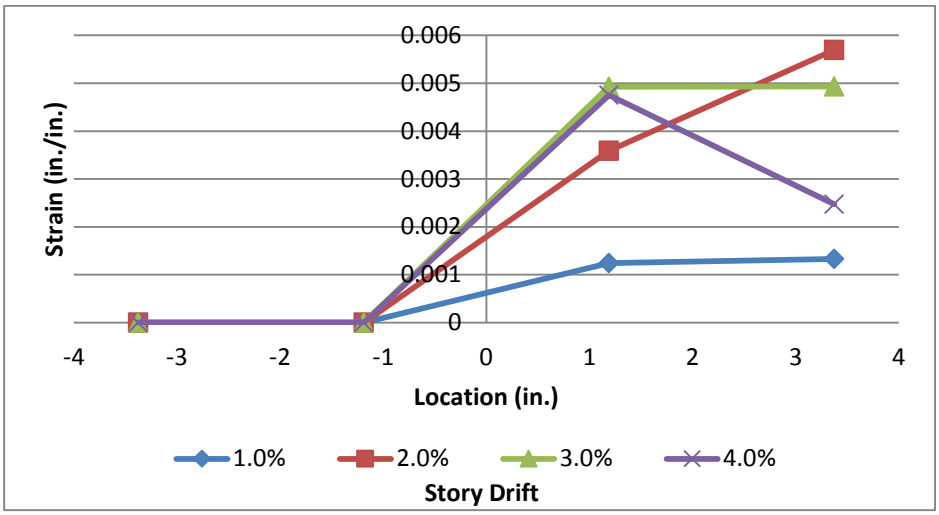

Figure D.35 – Specimen 6 (W24x62 with No RBS and Grid of PAFs) Underside of Top Flange Strain Data Line 3

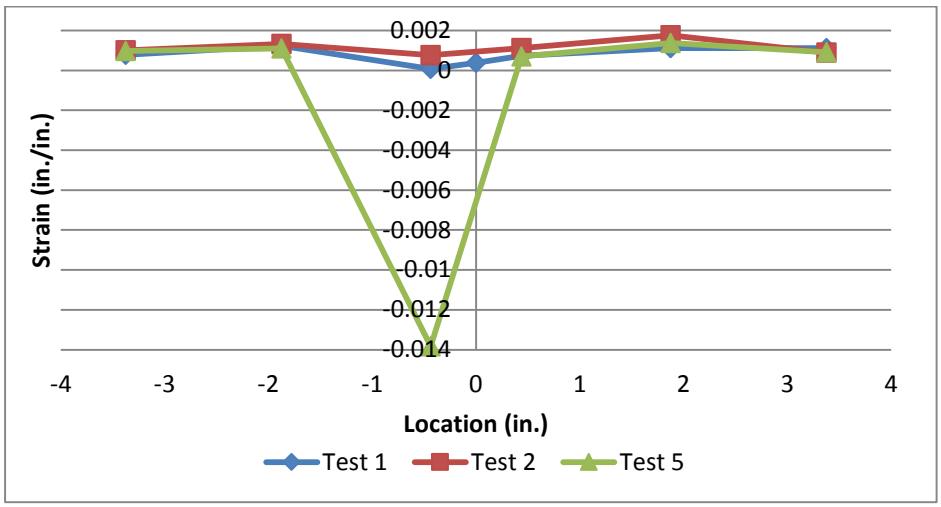

Figure D.36 – RBS24 (Specimen 1, 2 and 5) Top Flange Strain Data Line 1 at 1% Story Drift

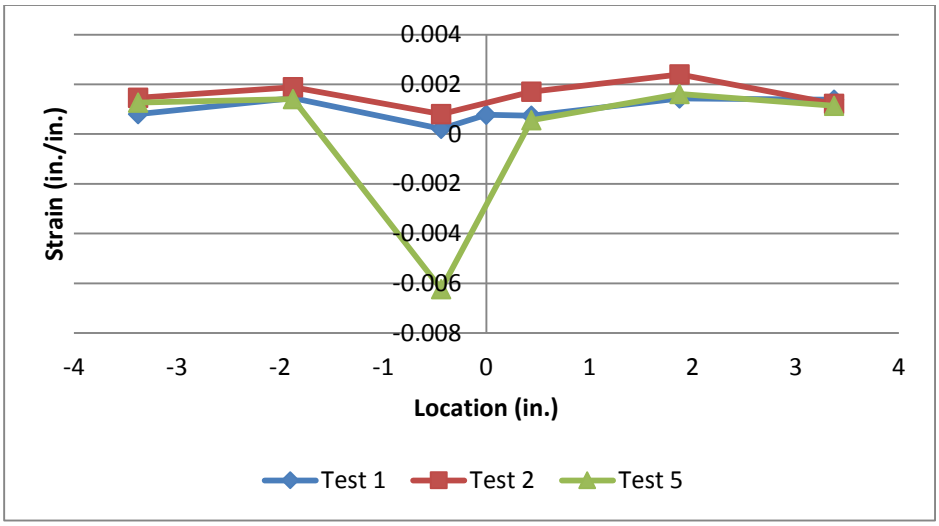

Figure D.37 – RBS24 (Specimen 1, 2 and 5) Top Flange Strain Data Line 1 at 2% Story Drift

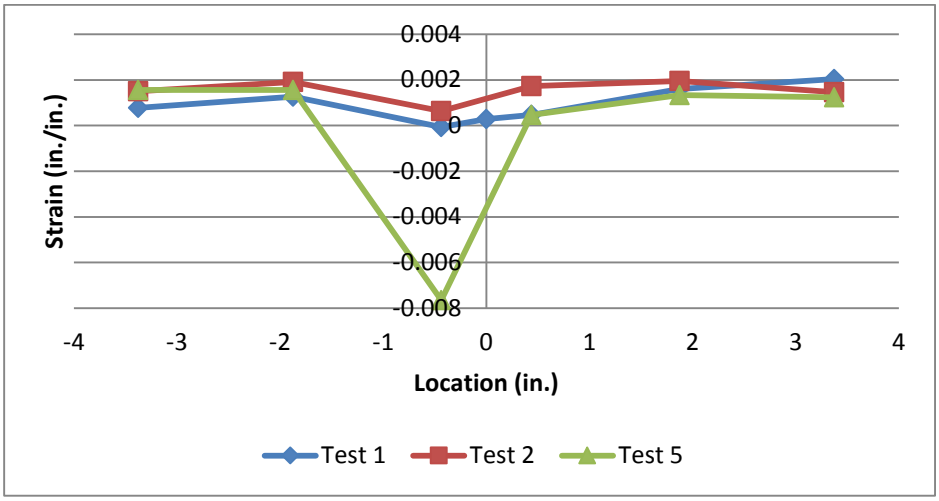

Figure D.38 – RBS24 (Specimen 1, 2 and 5) Top Flange Strain Data Line 1 at 3% Story Drift

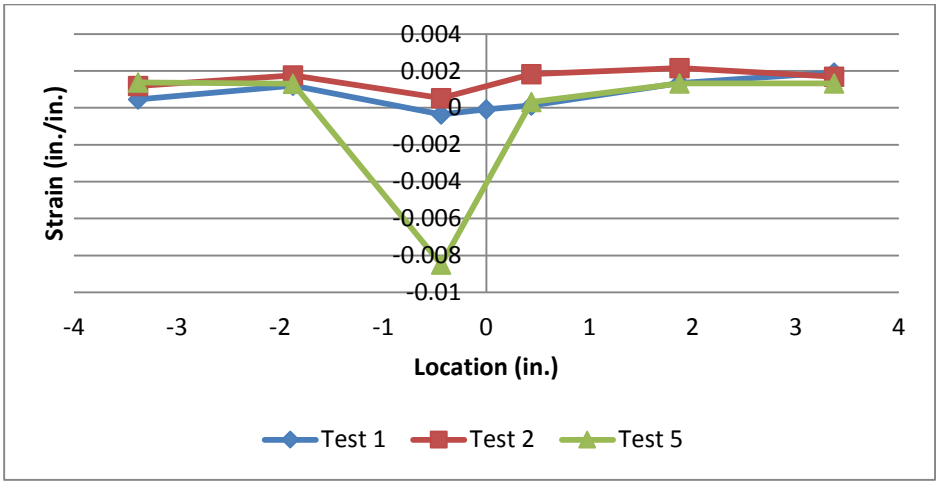

Figure D.39 – RBS24 (Specimen 1, 2 and 5) Top Flange Strain Data Line 1 at 4% Story Drift

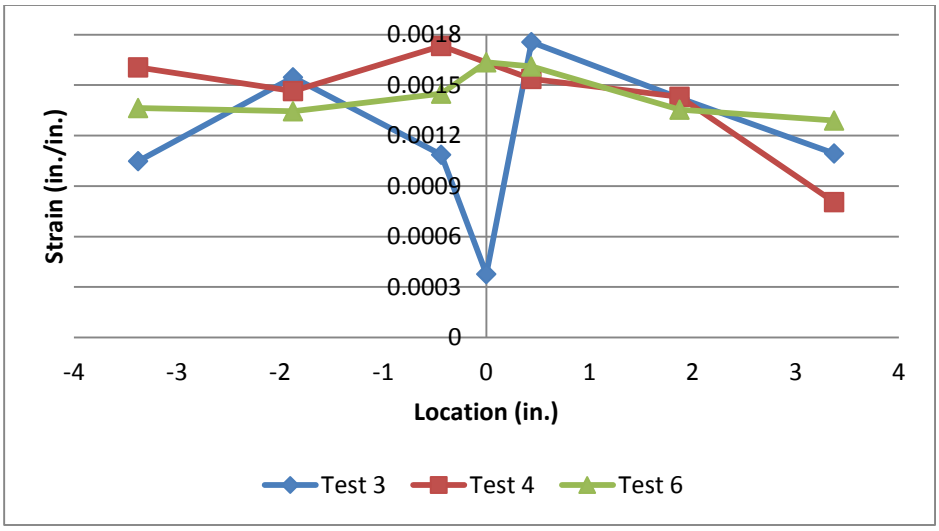

Figure D.40 – W24 (Specimen 3, 4 and 6) Top Flange Strain Data Line 1 at 1% Story Drift

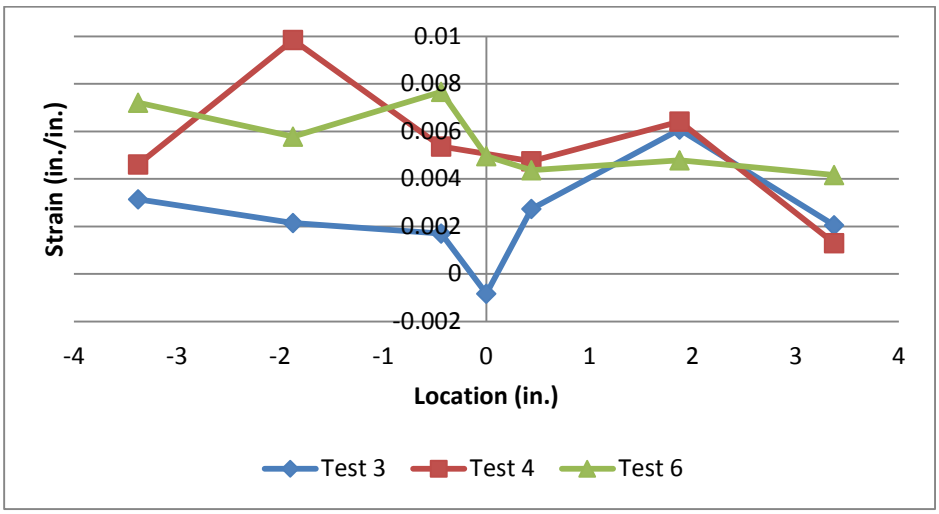

Figure D.41 – W24 (Specimen 3, 4 and 6) Top Flange Strain Data Line 1 at 2% Story Drift

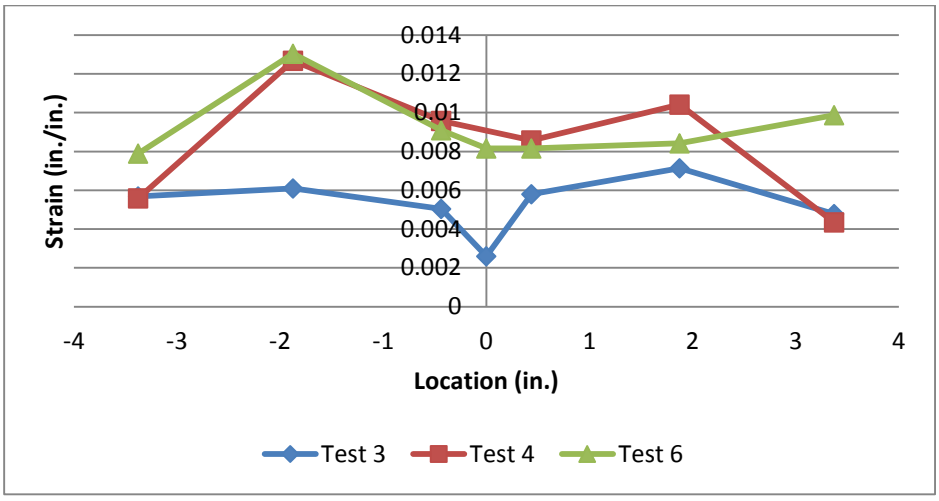

Figure D.42 – W24 (Specimen 3, 4 and 6) Top Flange Strain Data Line 1 at 3% Story Drift

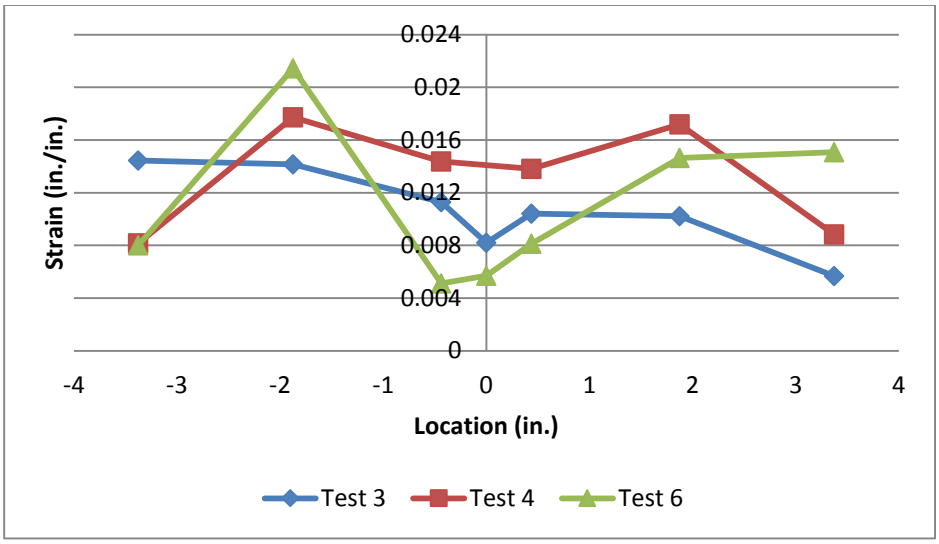

Figure D.43 – W24 (Specimen 3, 4 and 6) Top Flange Strain Data Line 1 at 4% Story Drift

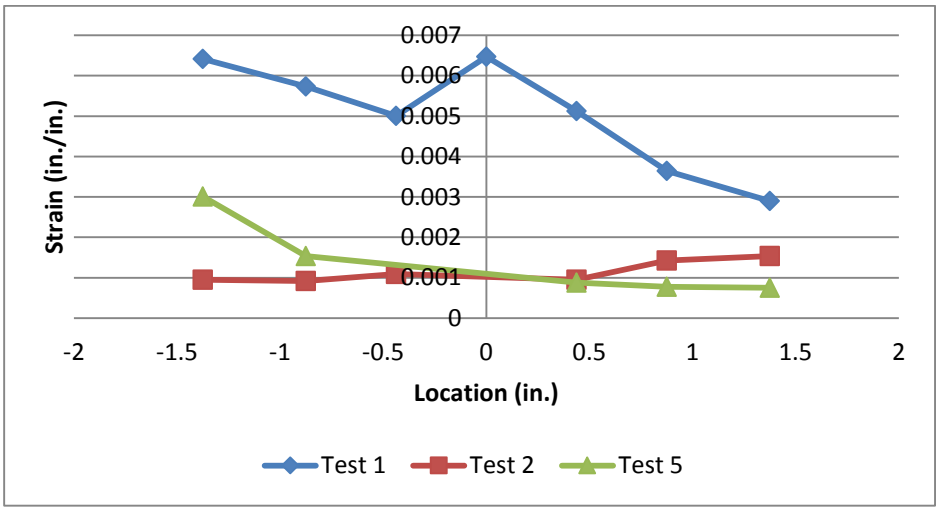

Figure D.44 – RBS24 (Specimen 1, 2 and 5) Top Flange Strain Data Line 2 at 1% Story Drift

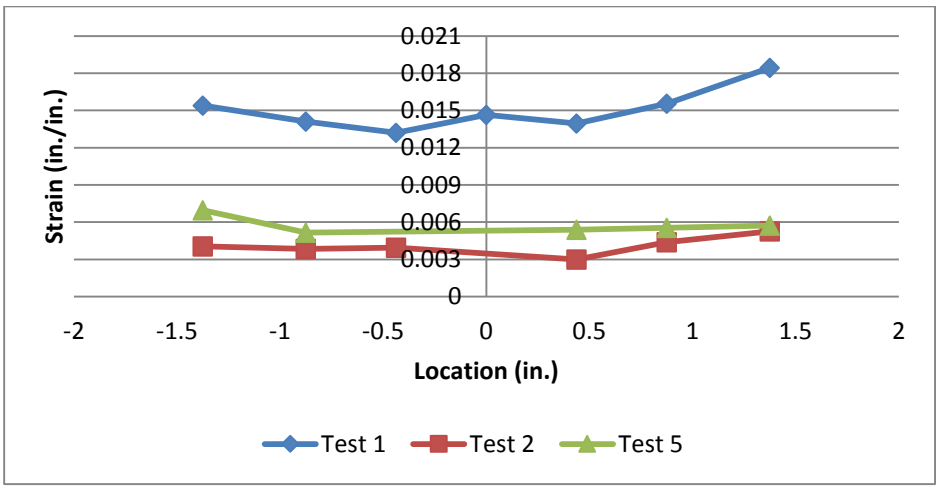

Figure D.45 – RBS24 (Specimen 1, 2 and 5) Top Flange Strain Data Line 2 at 2% Story Drift

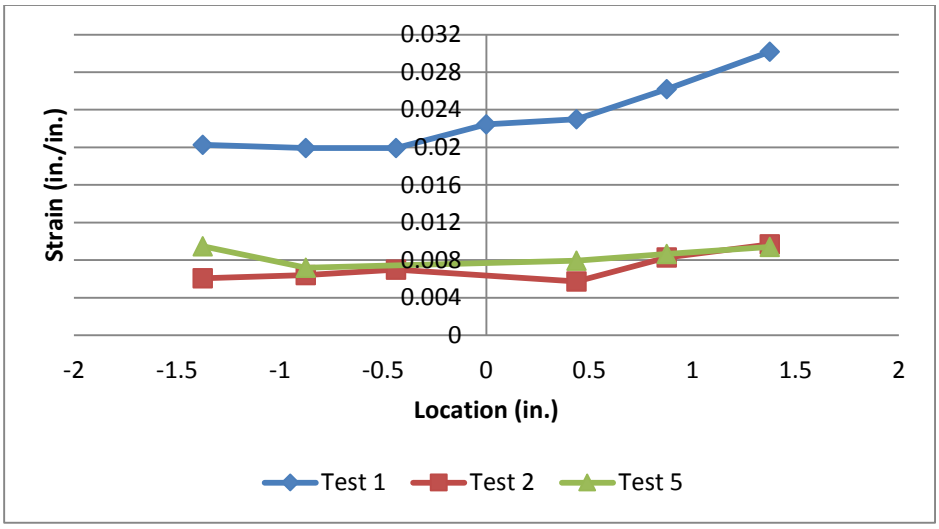

Figure D.46 – RBS24 (Specimen 1, 2 and 5) Top Flange Strain Data Line 2 at 3% Story Drift

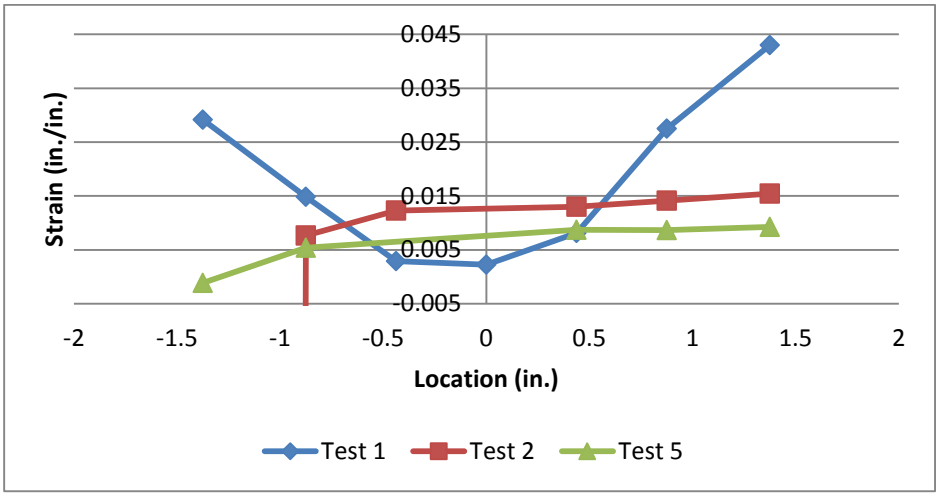

Figure D.47 – RBS24 (Specimen 1, 2 and 5) Top Flange Strain Data Line 2 at 4% Story Drift

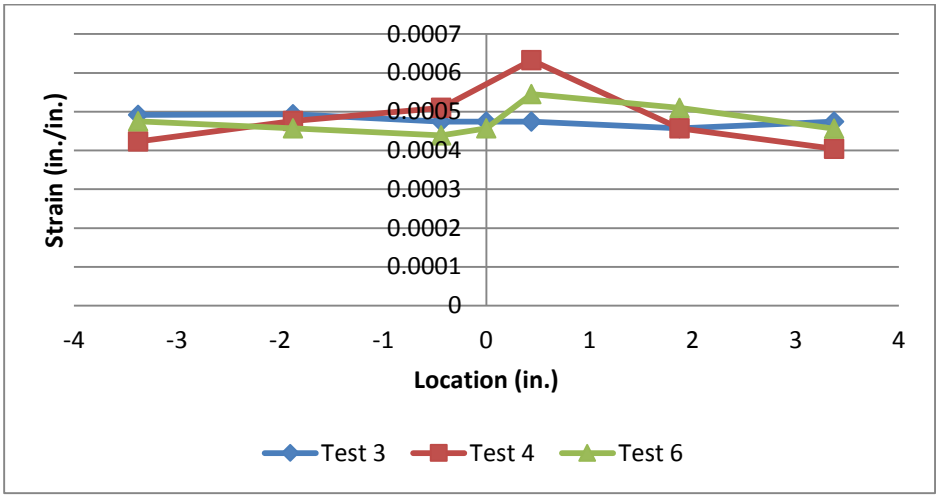

Figure D.48 – W24 (Specimen 3, 4 and 6) Top Flange Strain Data Line 2 at 1% Story Drift

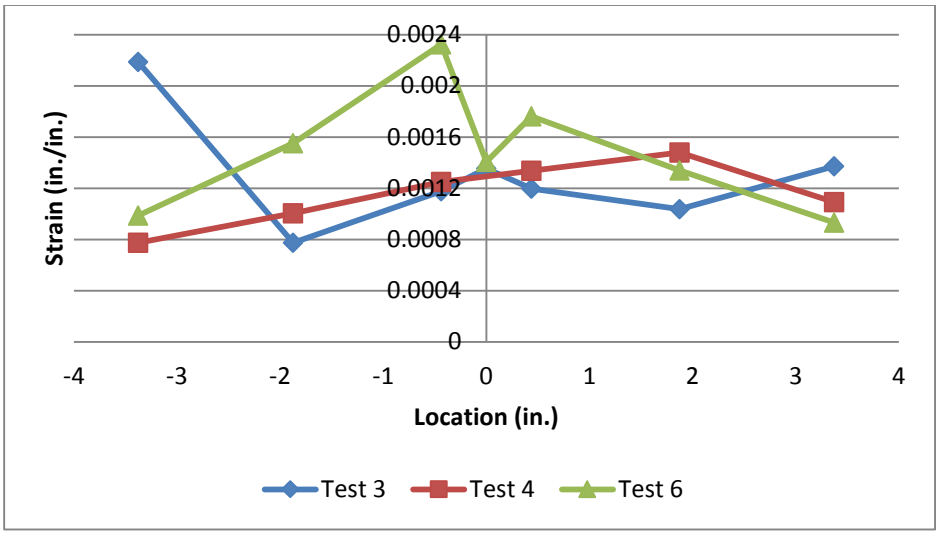

Figure D.49 – W24 (Specimen 3, 4 and 6) Top Flange Strain Data Line 2 at 2% Story Drift

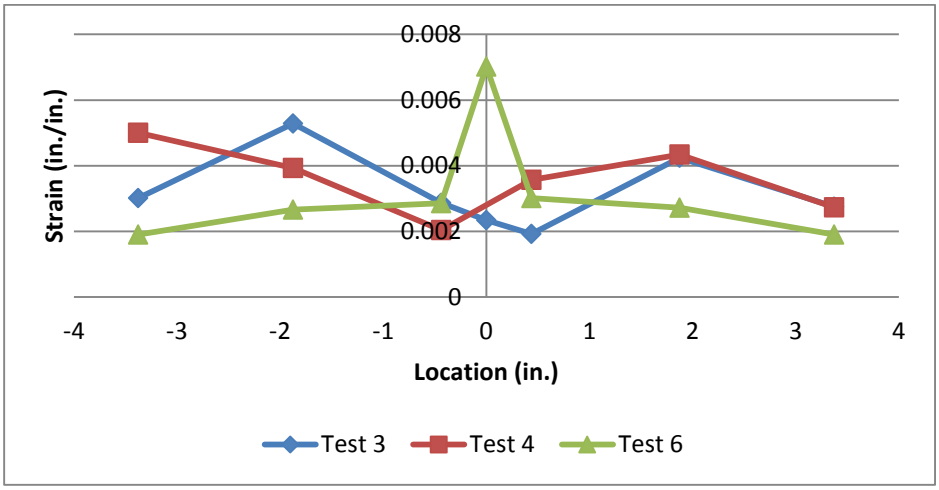

Figure D.50 – W24 (Specimen 3, 4 and 6) Top Flange Strain Data Line 2 at 3% Story Drift

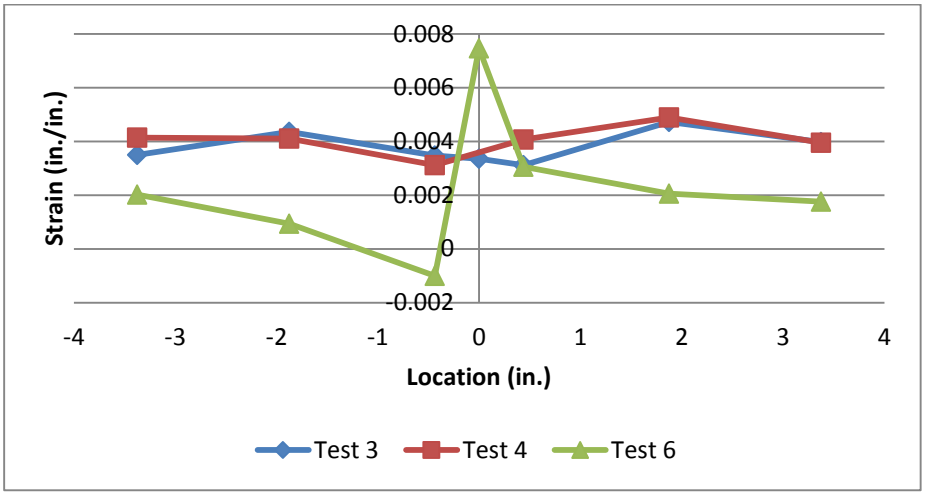

Figure D.51 – W24 (Specimen 3, 4 and 6) Top Flange Strain Data Line 2 at 4% Story Drift

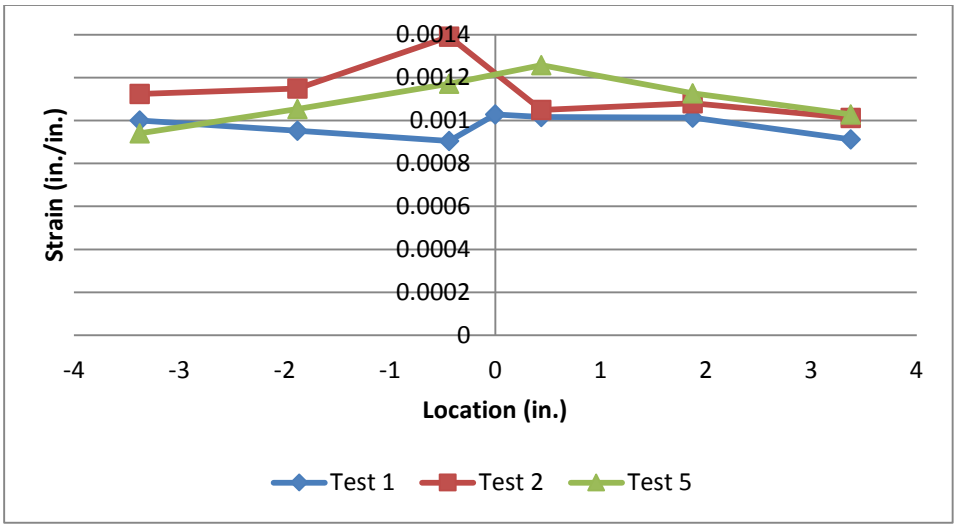

Figure D.52 – RBS24 (Specimen 1, 2 and 5) Top Flange Strain Data Line 3 at 1% Story Drift

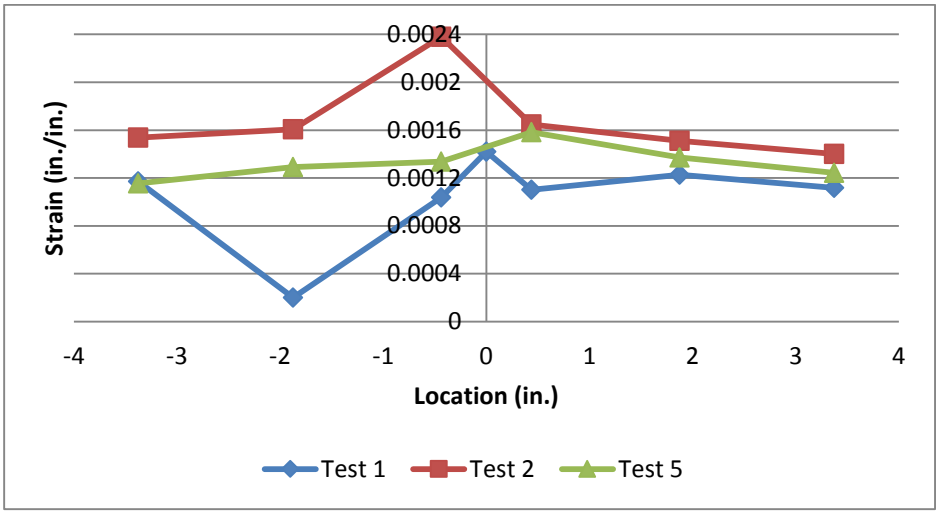

Figure D.53 – RBS24 (Specimen 1, 2 and 5) Top Flange Strain Data Line 3 at 2% Story Drift

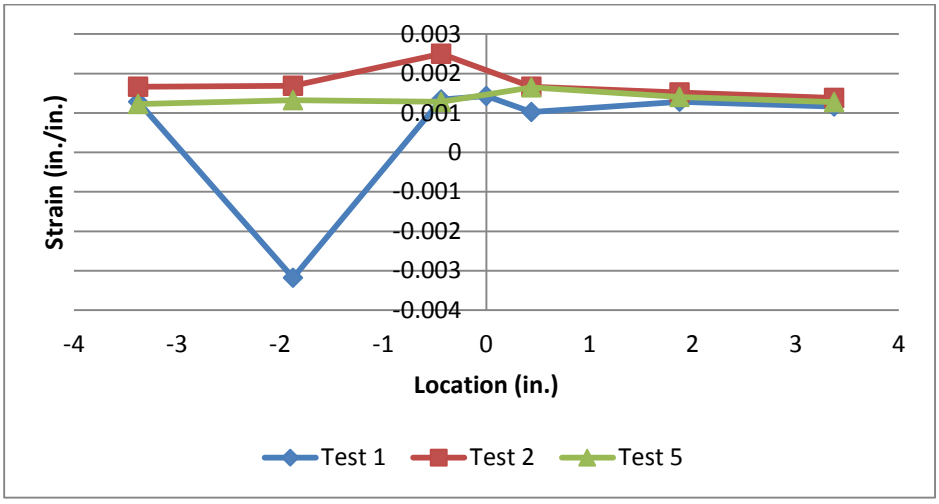

Figure D.54 – RBS24 (Specimen 1, 2 and 5) Top Flange Strain Data Line 3 at 3% Story Drift

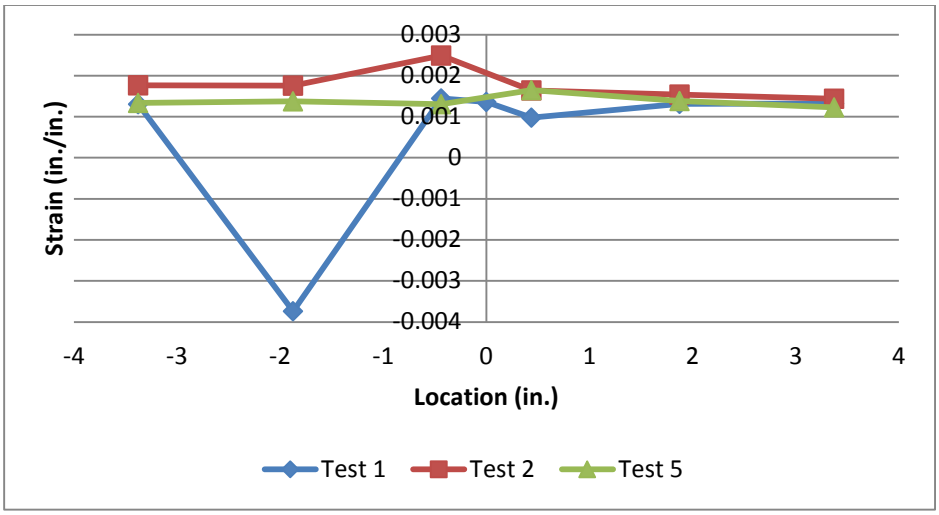

Figure D.55 – RBS24 (Specimen 1, 2 and 5) Top Flange Strain Data Line 3 at 4% Story Drift

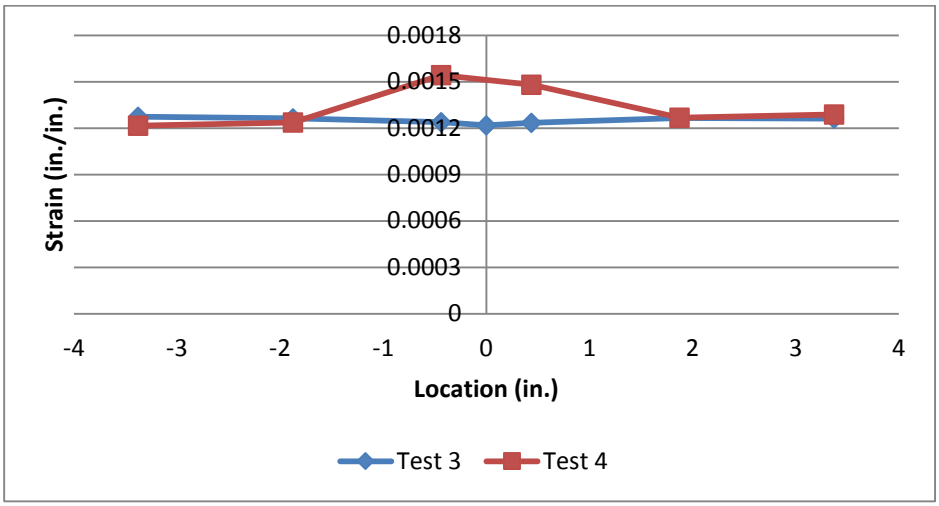

Figure D.56 – W24 (Specimen 3, 4 and 6) Top Flange Strain Data Line 3 at 1% Story Drift

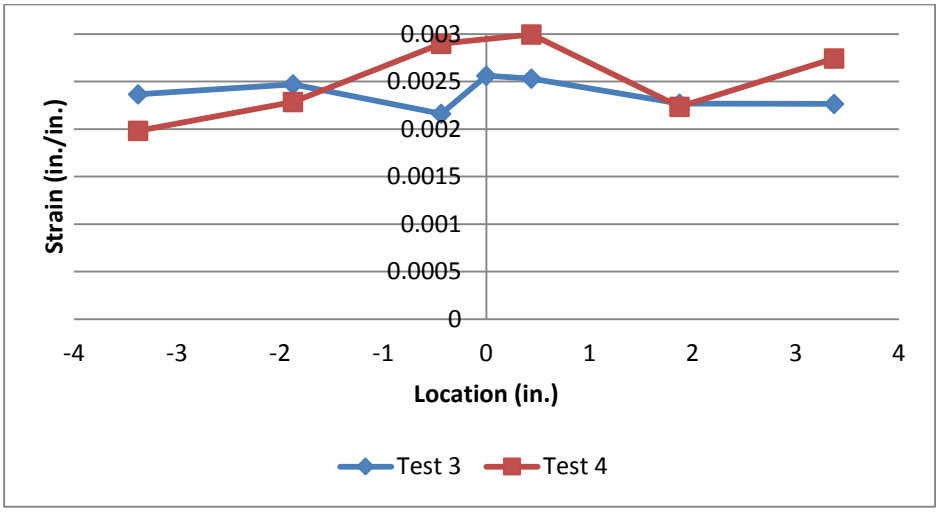

Figure D.57 – W24 (Specimen 3, 4 and 6) Top Flange Strain Data Line 3 at 2% Story Drift

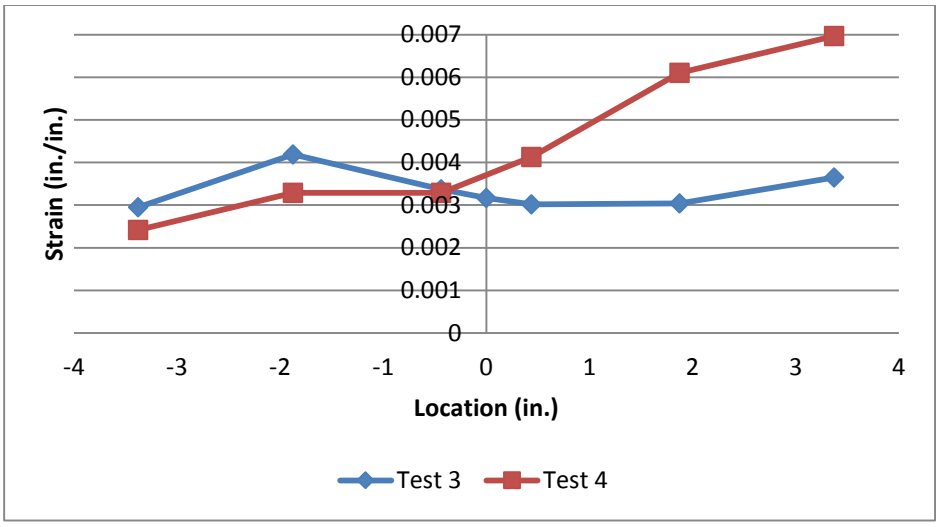

Figure D.58 – W24 (Specimen 3, 4 and 6) Top Flange Strain Data Line 3 at 3% Story Drift

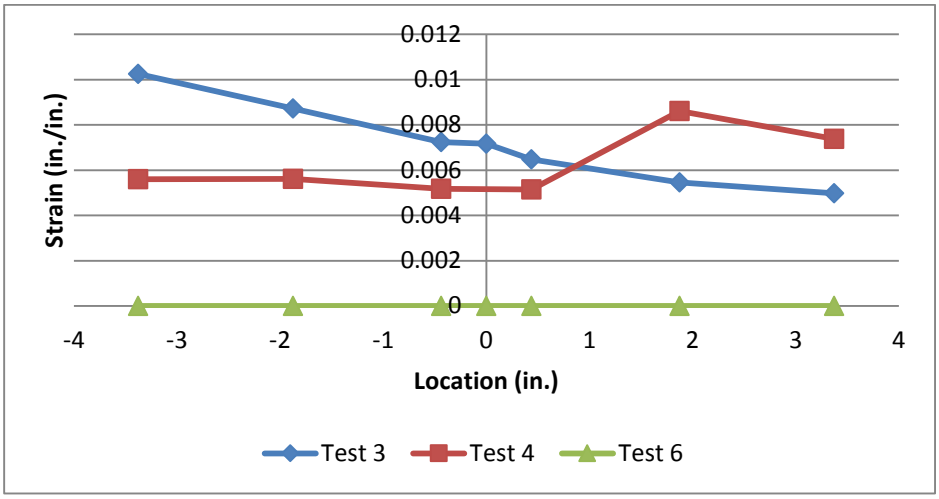

Figure D.59 – W24 (Specimen 3, 4 and 6) Top Flange Strain Data Line 3 at 4% Story Drift

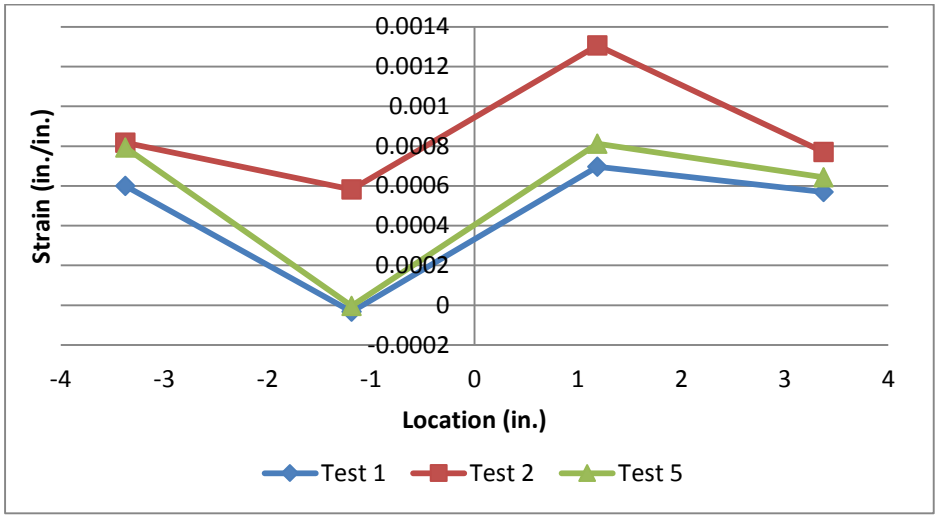

Figure D.60 – RBS24 (Specimen 1, 2 and 5) Underside of Top Flange Strain Data Line 1 at 1% Story Drift

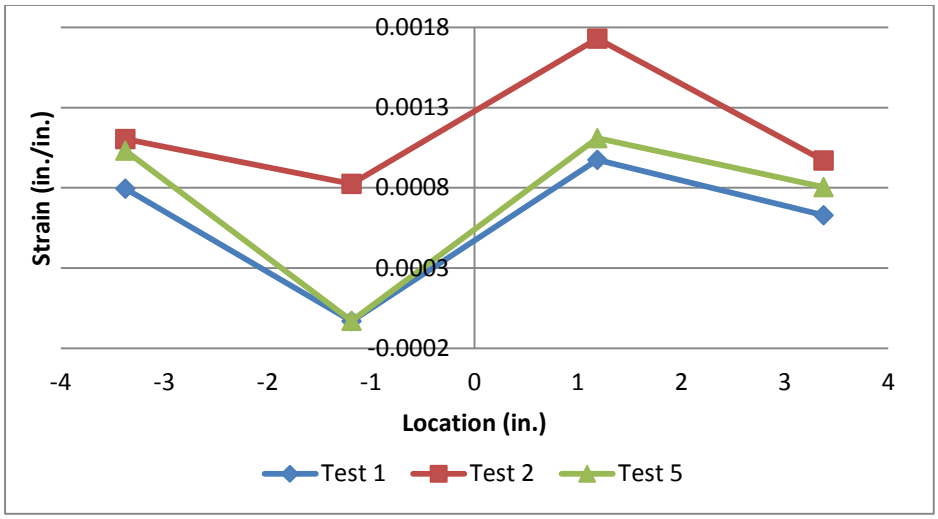

Figure D.61 – RBS24 (Specimen 1, 2 and 5) Underside of Top Flange Strain Data Line 1 at 2% Story Drift

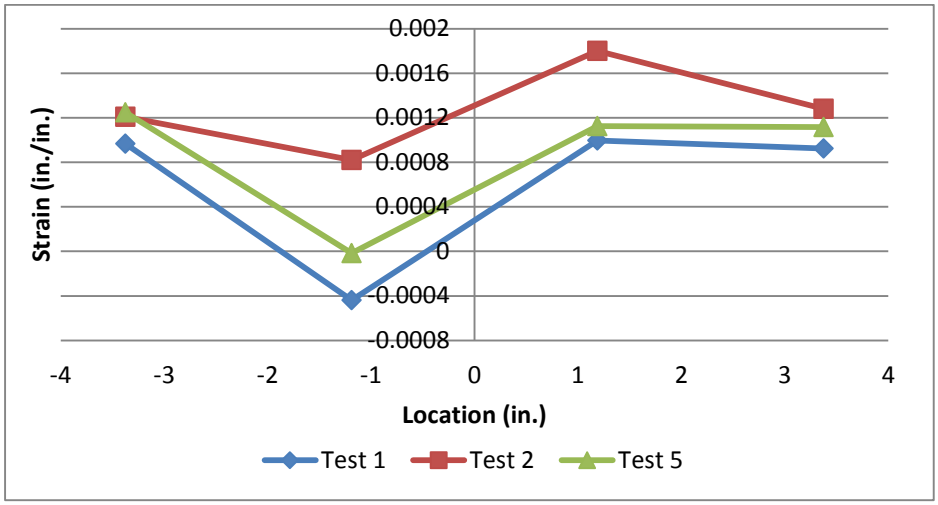

Figure D.62 – RBS24 (Specimen 1, 2 and 5) Underside of Top Flange Strain Data Line 1 at 3% Story Drift

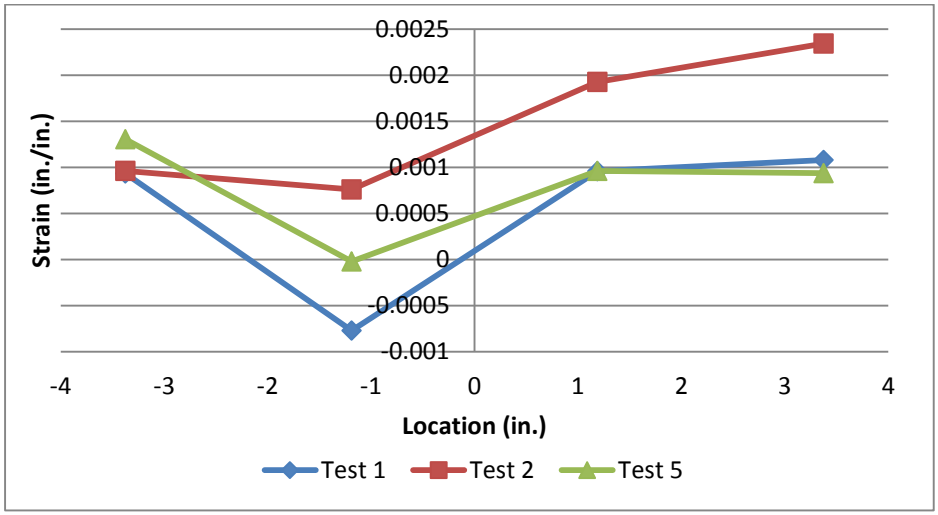

Figure D.63 – RBS24 (Specimen 1, 2 and 5) underside of top flange strain data line 1 at 4% Story Drift

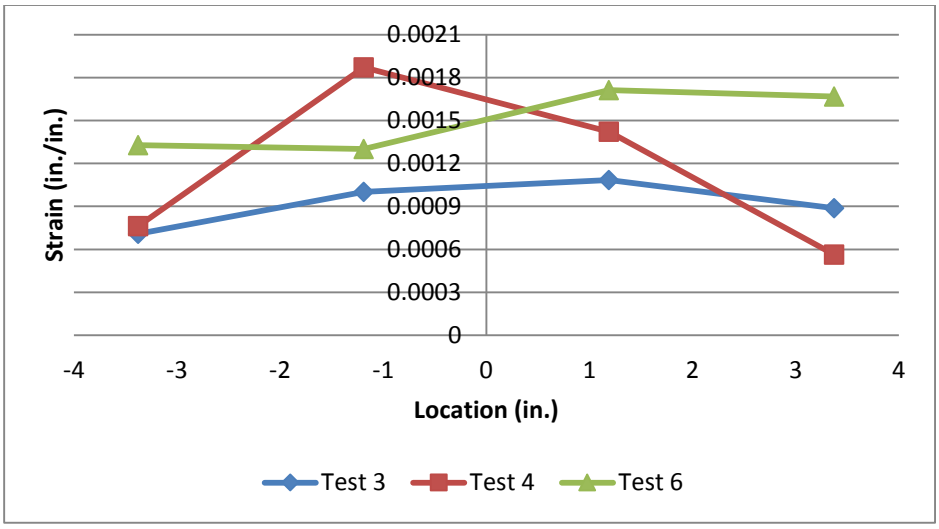

Figure D.64 – W24 (Specimen 3, 4 and 6) underside of top flange strain data line 1 at 1% Story Drift

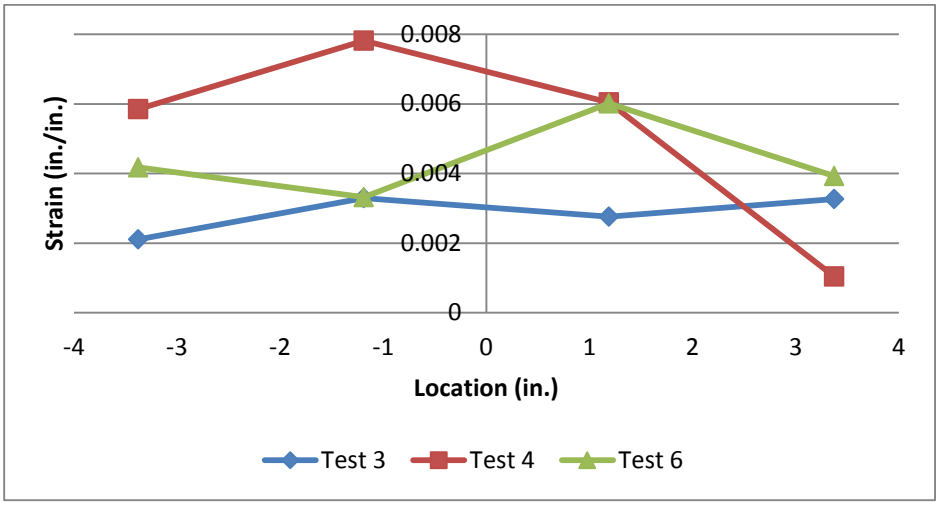

Figure D.65 – W24 (Specimen 3, 4 and 6) Underside of Top Flange Strain Data Line 1 at 2% Story Drift

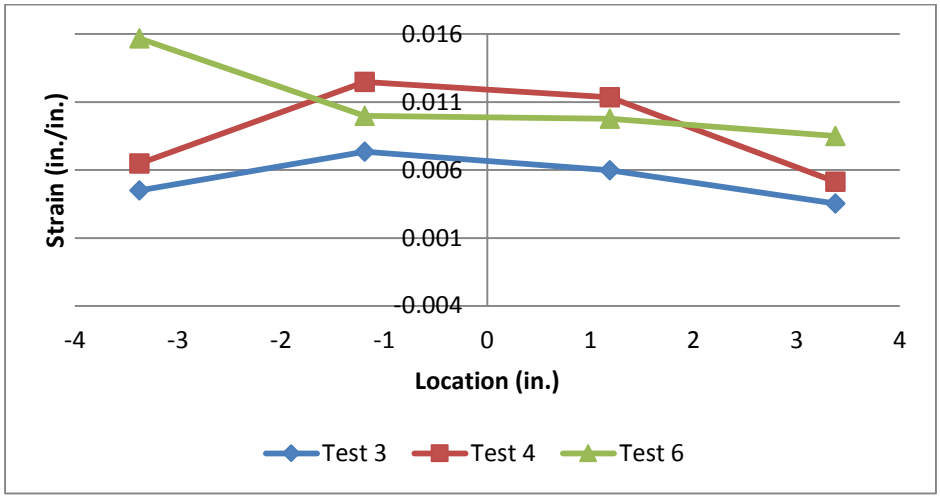

Figure D.66 – W24 (Specimen 3, 4 and 6) Underside of Top Flange Strain Data Line 1 at 3% Story Drift

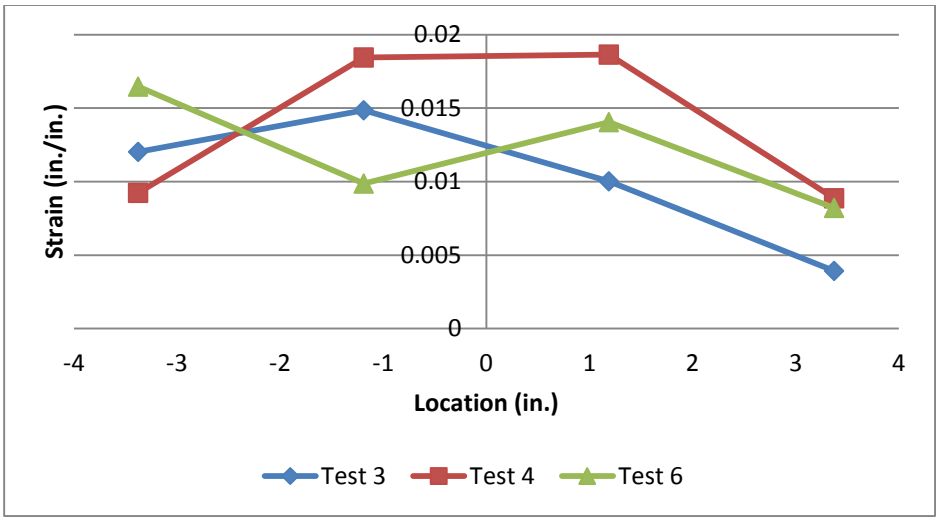

Figure D.67 – W24 (Specimen 3, 4 and 6) Underside of Top Flange Strain Data Line 1 at 4% Story Drift

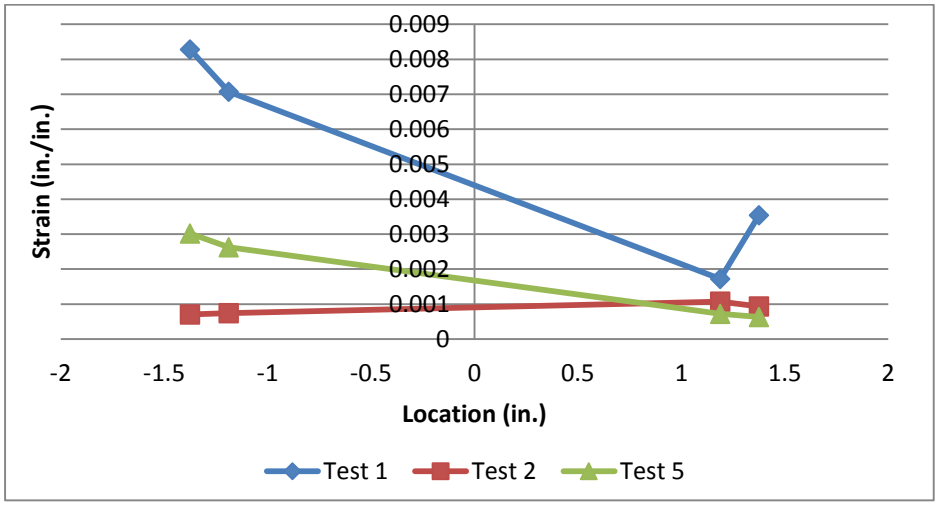

Figure D.68 – RBS24 (Specimen 1, 2 and 5) Underside of Top Flange Strain Data Line 2 at 1% Story Drift

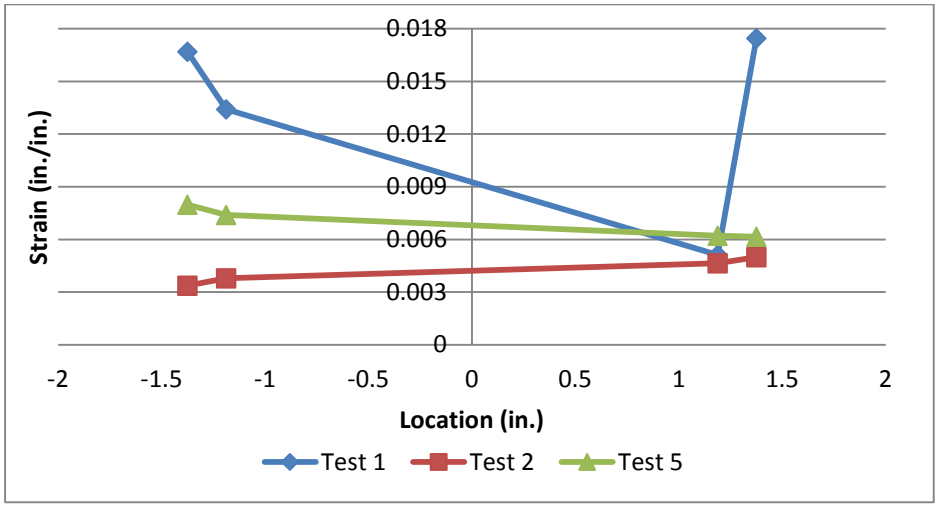

Figure D.69 – RBS24 (Specimen 1, 2 and 5) Underside of Top Flange Strain Data Line 2 at 2% Story Drift

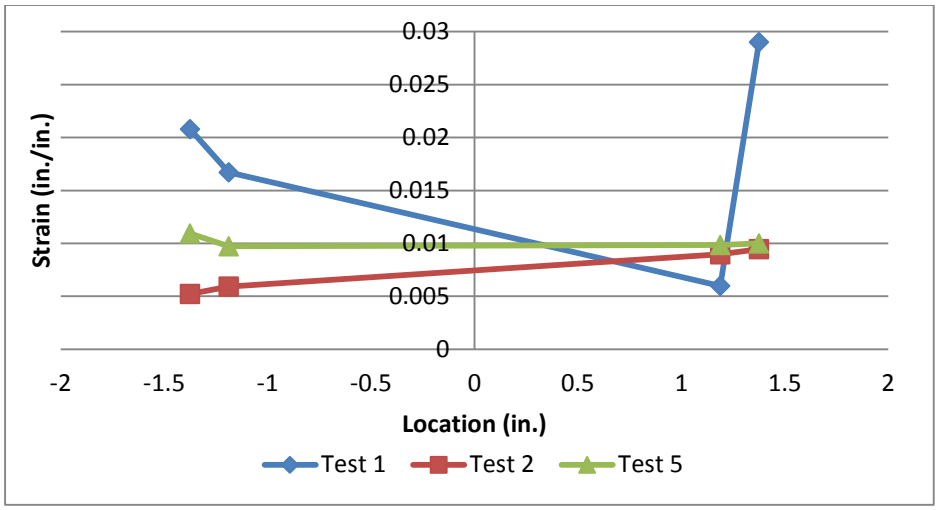

Figure D.70 – RBS24 (Specimen 1, 2 and 5) Underside of Top Flange Strain Data Line 2 at 3% Story Drift

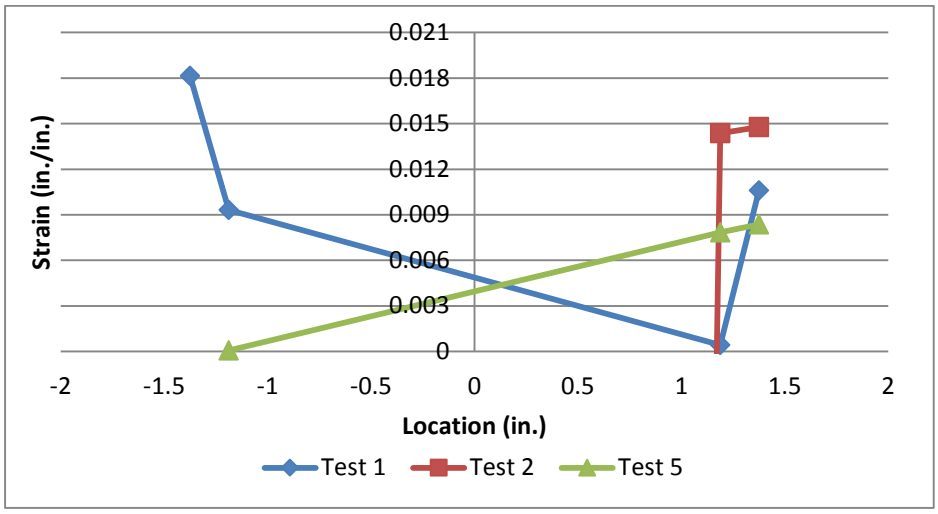

Figure D.71 – RBS24 (Specimen 1, 2 and 5) Underside of Top Flange Strain Data Line 2 at 4% Story Drift

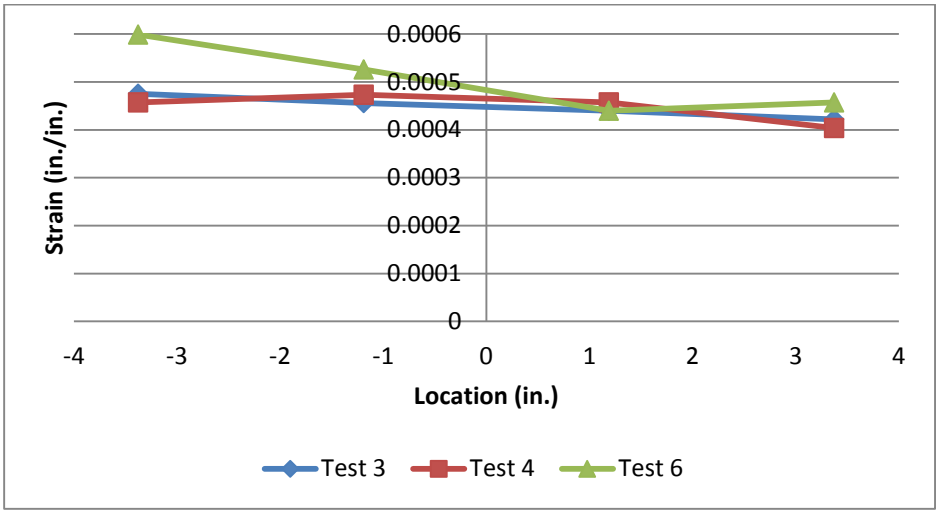

Figure D.72 – W24 (Specimen 3, 4 and 6) Underside of Top Flange Strain Data Line 2 at 1% Story Drift

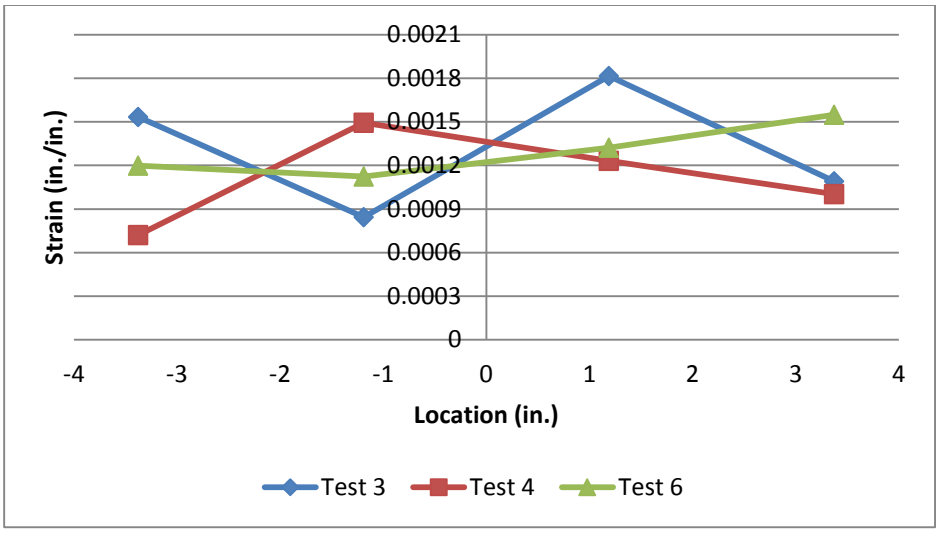

Figure D.73 – W24 (Specimen 3, 4 and 6) Underside of Top Flange Strain Data Line 2 at 2% Story Drift

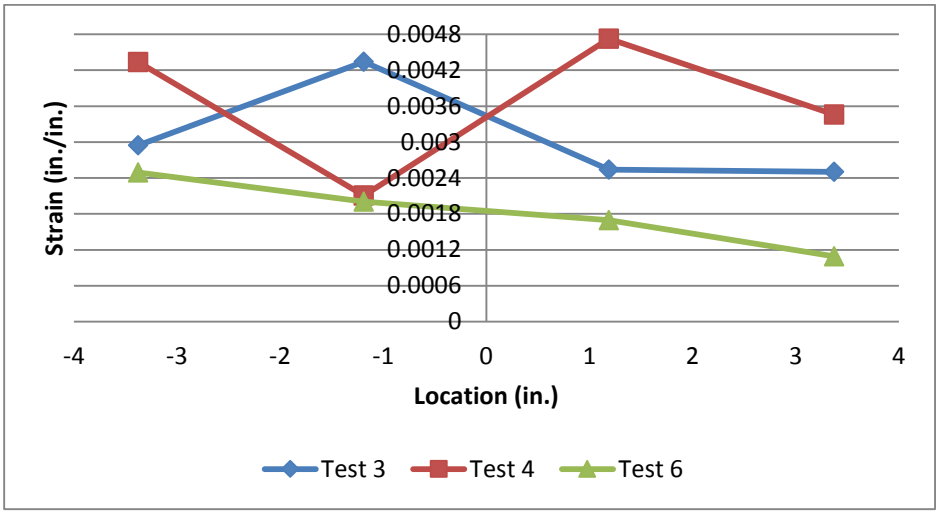

Figure D.74 – W24 (Specimen 3, 4 and 6) Underside of Top Flange Strain Data Line 2 at 3% Story Drift

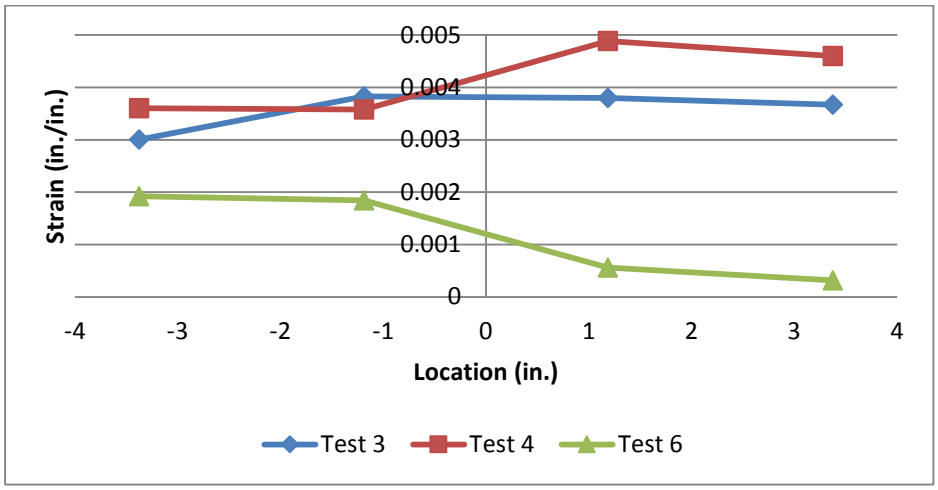

Figure D.75 – W24 (Specimen 3, 4 and 6) Underside of Top Flange Strain Data Line 2 at 4% Story Drift

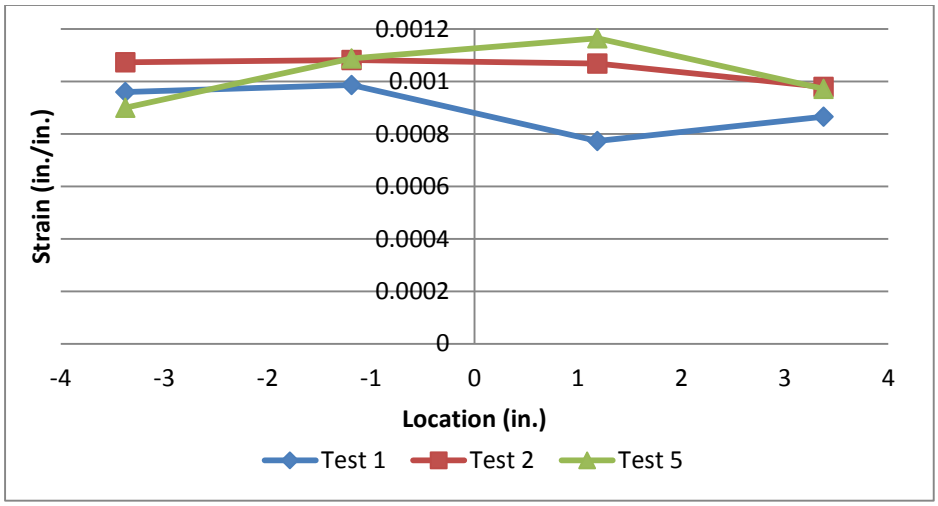

Figure D.76 – RBS24 (Specimen 1, 2 and 5) Underside of Top Flange Strain Data Line 3 at 1% Story Drift

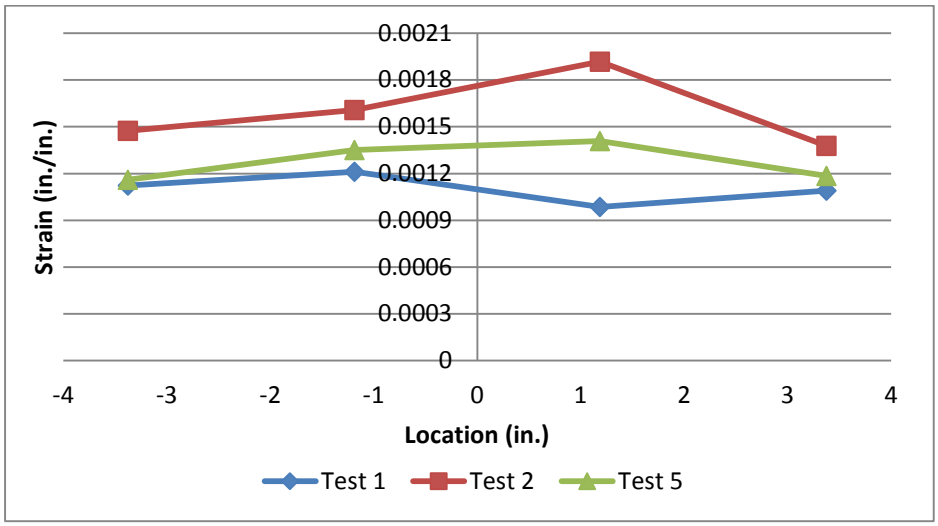

Figure D.77 – RBS24 (Specimen 1, 2 and 5) Underside of Top Flange Strain Data Line 3 at 2% Story Drift

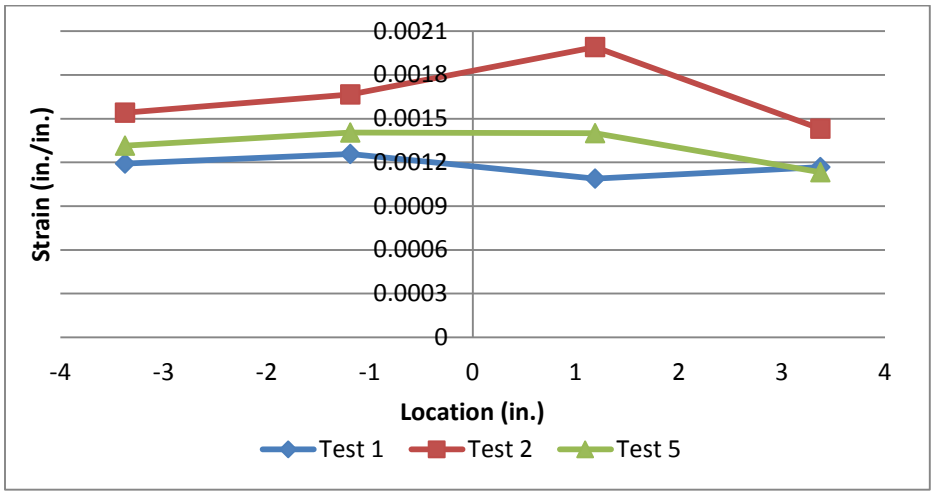

Figure D.78 – RBS24 (Specimen 1, 2 and 5) Underside of Top Flange Strain Data Line 3 at 3% Story Drift

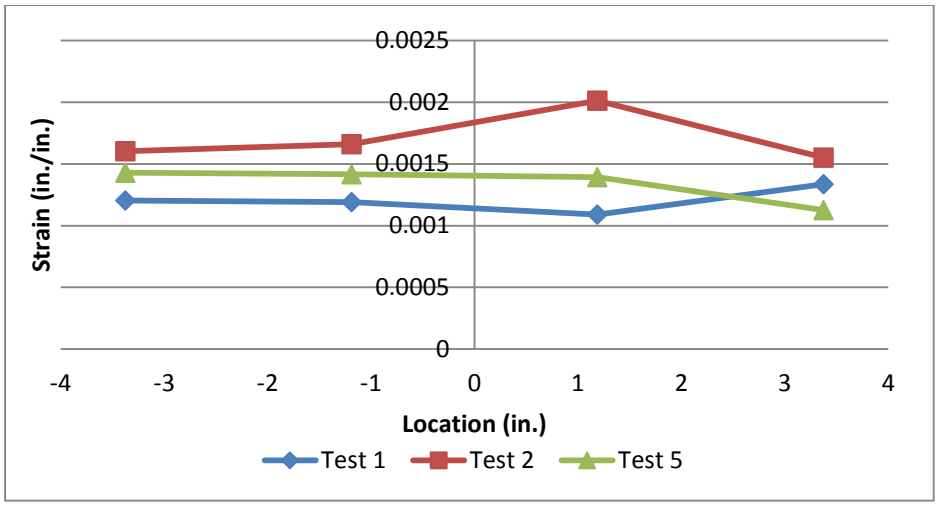

Figure D.79 – RBS24 (Specimen 1, 2 and 5) Underside of Top Flange Strain Data Line 3 at 4% Story Drift

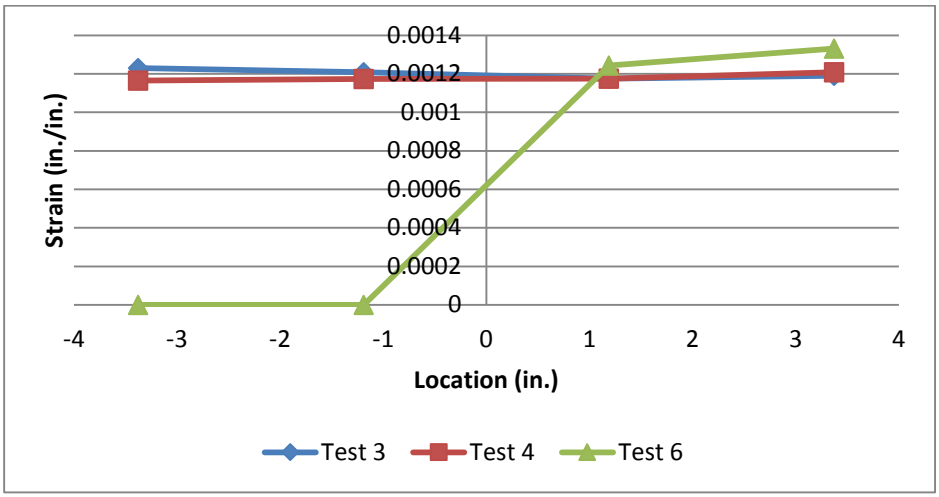

Figure D.80 – W24 (Specimen 3, 4 and 6) Underside of Top Flange Strain Data Line 3 at 1% Story Drift

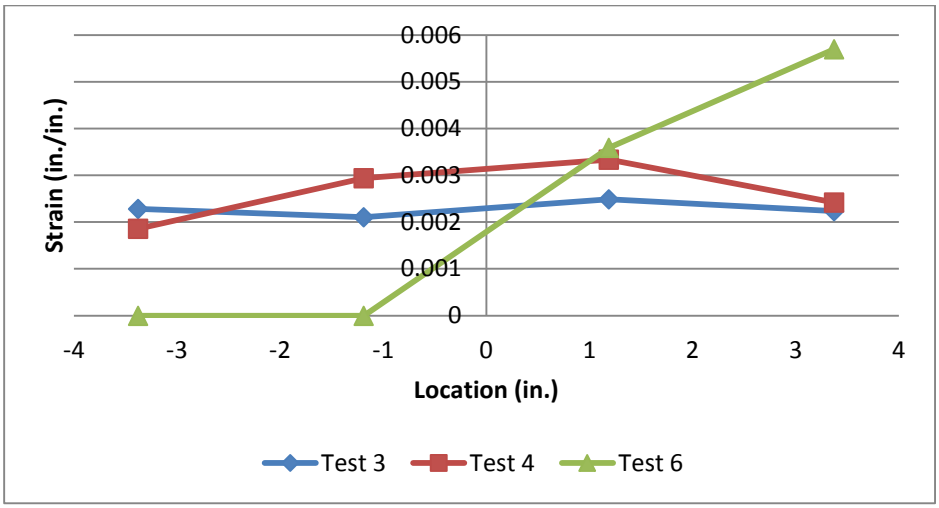

Figure D.81 – W24 (Specimen 3, 4 and 6) Underside of Top Flange Strain Data Line 3 at 2% Story Drift

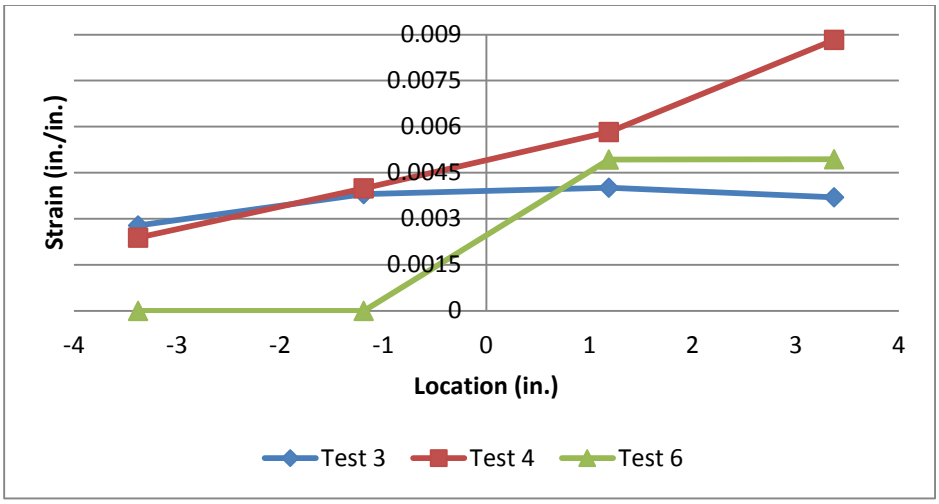

Figure D.82 – W24 (Specimen 3, 4 and 6) Underside of Top Flange Strain Data Line 3 at 3% Story Drift

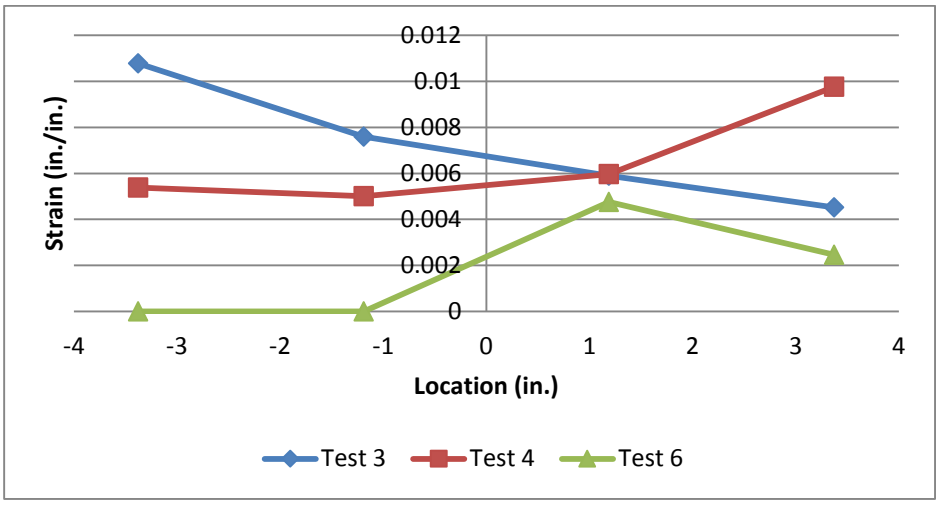

Figure D.83 – W24 (Specimen 3, 4 and 6) Underside of Top Flange Strain Data Line 3 at 4% Story Drift

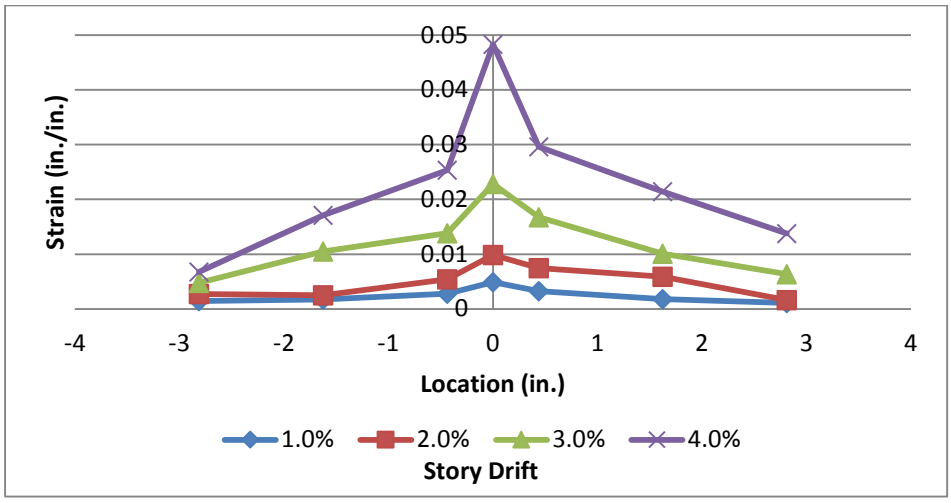

Figure D.84 – Specimen 7 (W36x150 with RBS and No Fasteners) Top Flange Strain Data Line 1

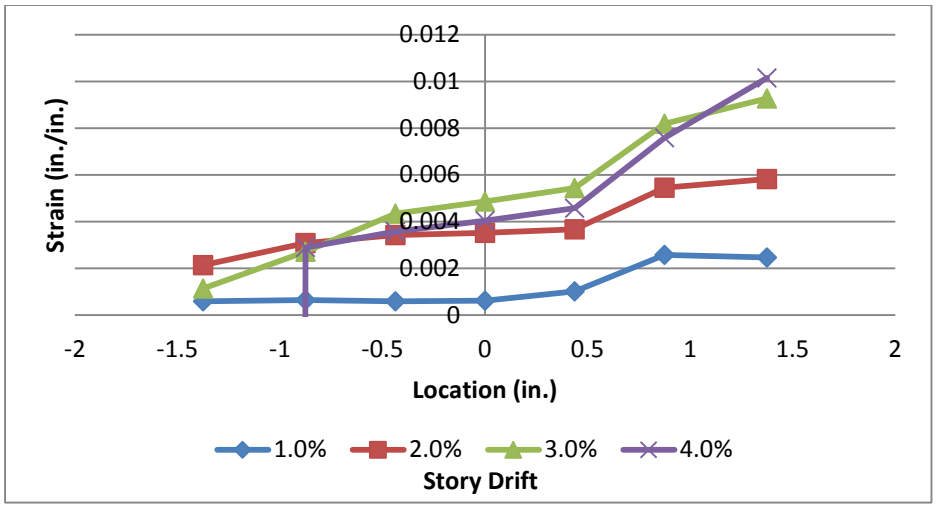

Figure D.85 – Specimen 7 (W36x150 with RBS and No Fasteners) Top Flange Strain Data Line 2

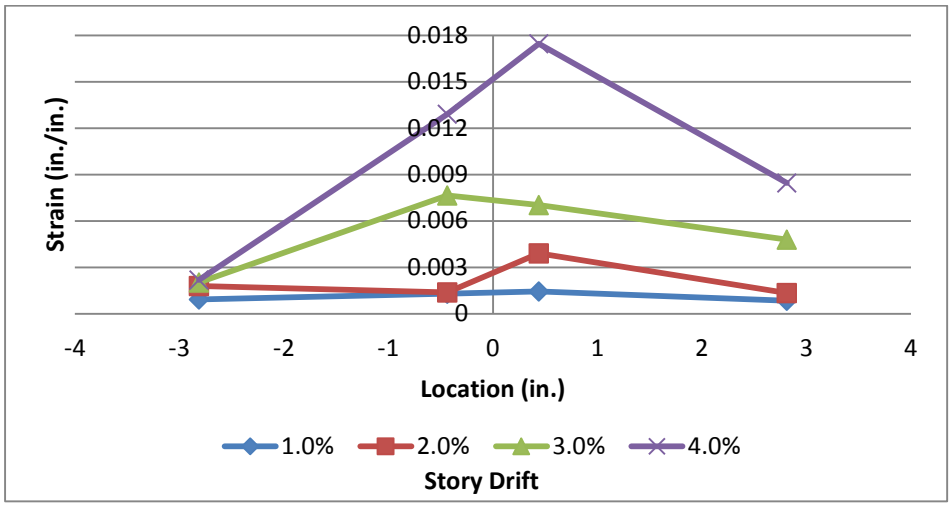

Figure D.86 – Specimen 7 (W36x150 with RBS and No Fasteners) Underside of Top Flange Strain Data Line 1

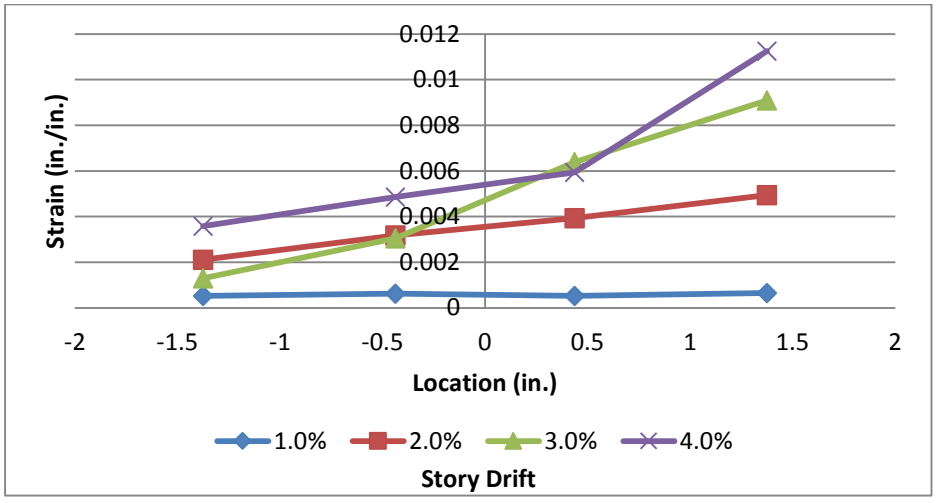

Figure D.87 – Specimen 7 (W36x150 with RBS and No Fasteners) Underside of Top Flange Strain Data Line 2

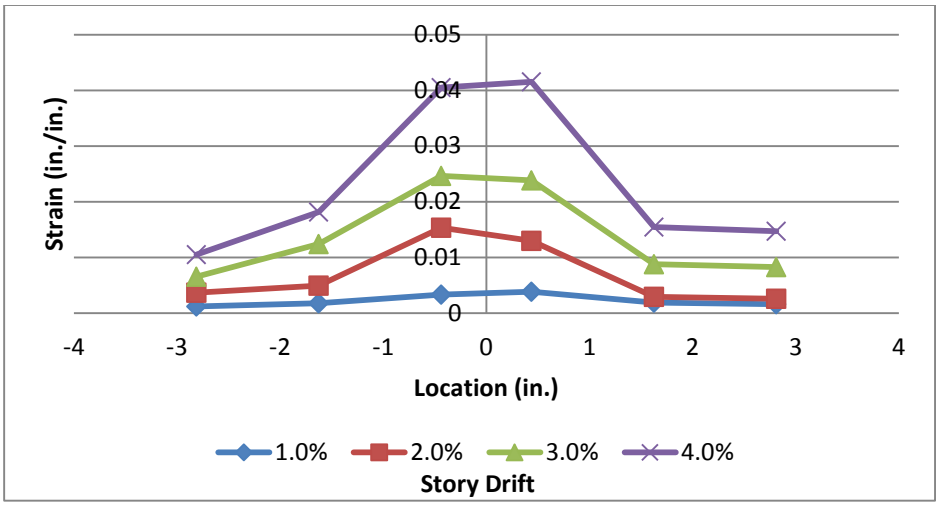

Figure D.88 – Specimen 8 (W36x150 with RBS and Puddle Welds at 12 in.) Top Flange Strain Data Line 1

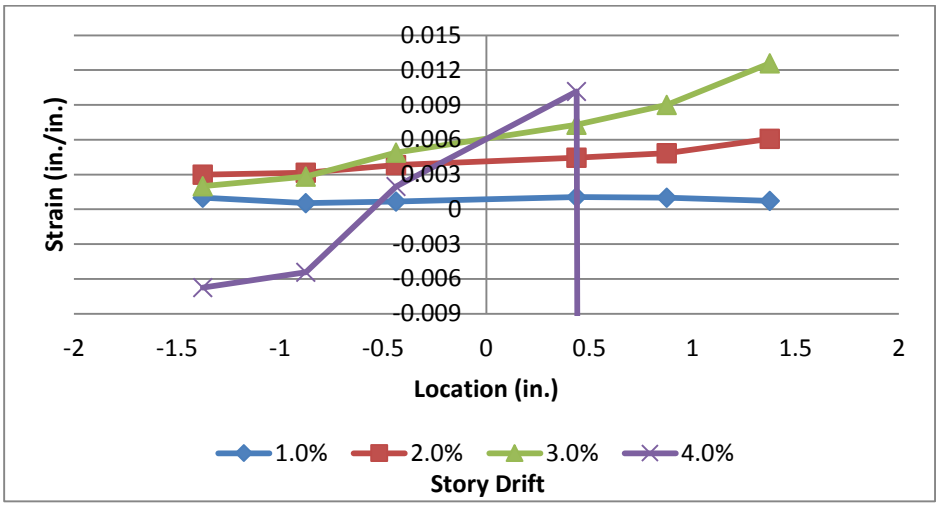

Figure D.89 – Specimen 8 (W36x150 with RBS and Puddle Welds at 12 in.) Top Flange Strain Data Line 2

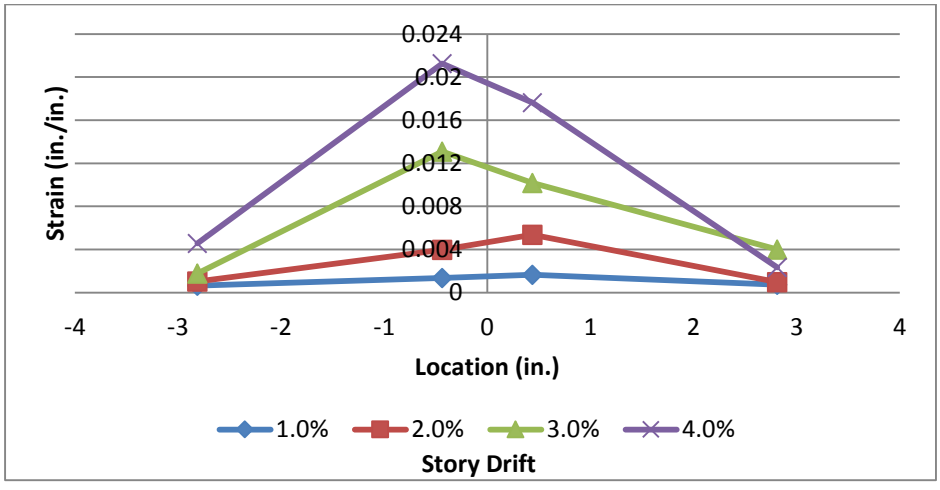

Figure D.90 –Specimen 8(W36x150 with RBS and Puddle Welds at 12 in.) Underside of Top Flange Strain Data Line 1

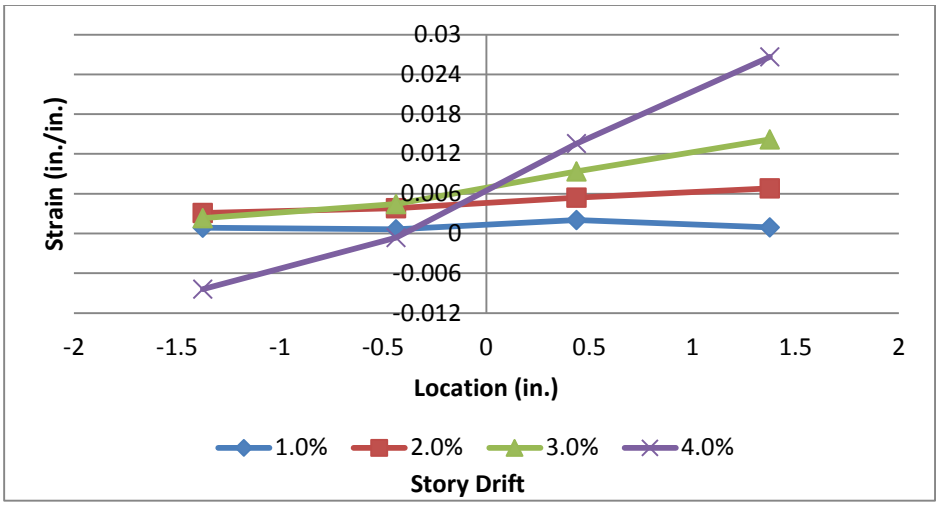

Figure D.91 –Specimen 8(W36x150 with RBS and Puddle Welds at 12 in.) Underside of Top Flange Strain Data Line 2

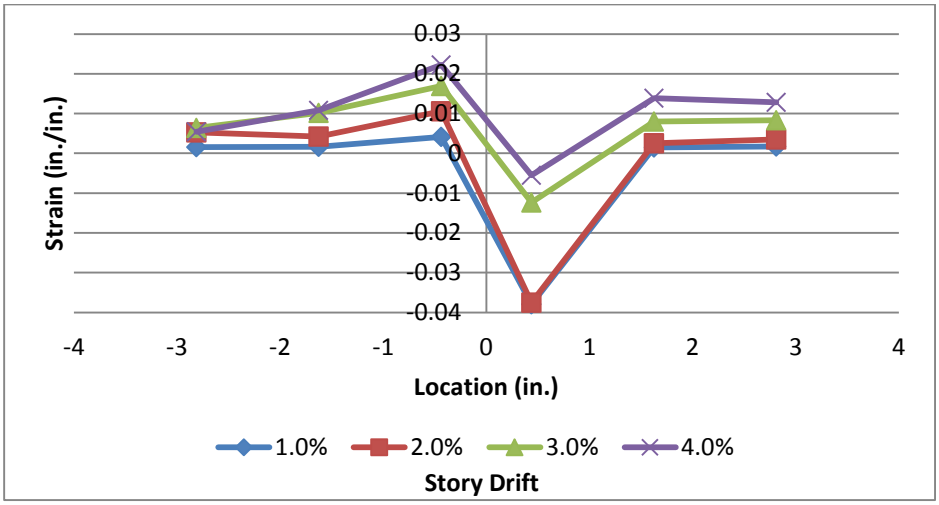

Figure D.92 – Specimen 9 (W36x150 with RBS and Grid of PAFs) Top Flange Strain Data Line 1

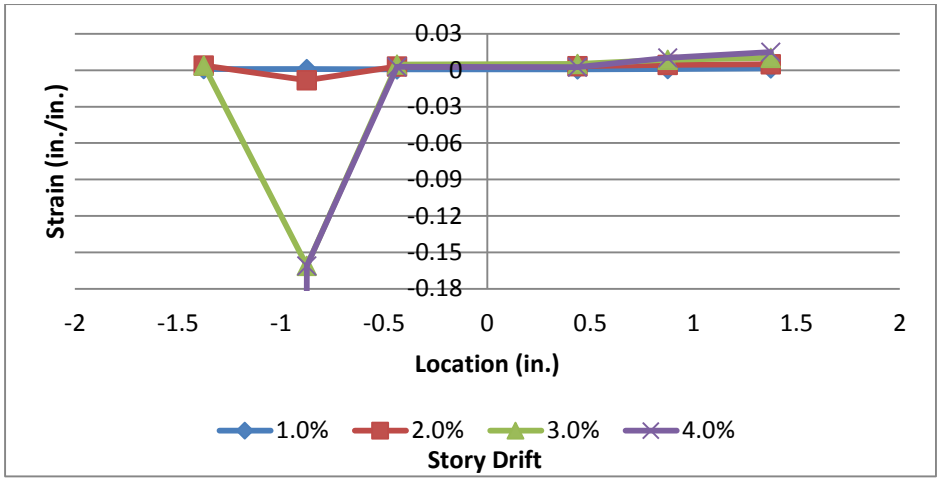

Figure D.93 – Specimen 9 (W36x150 with RBS and Grid of PAFs) Top Flange Strain Data Line 2

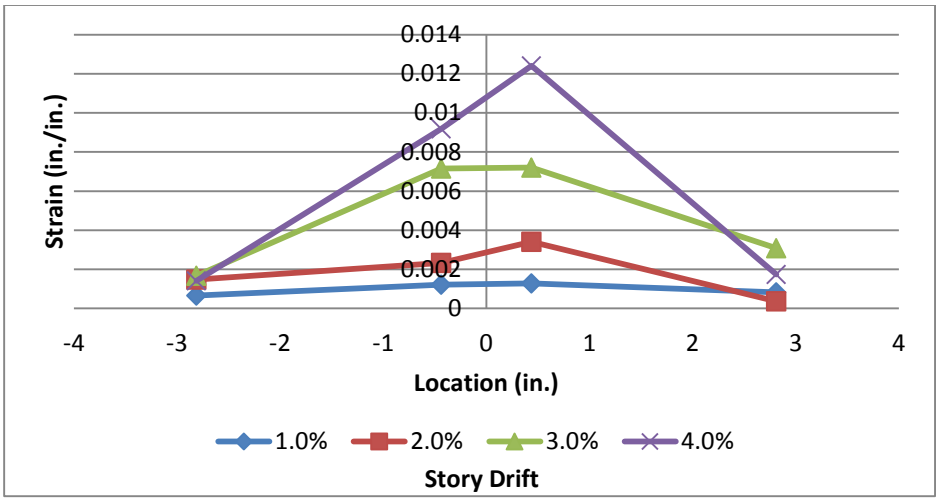

Figure D.94 – Specimen 9 (W36x150 with RBS and Grid of PAFs) Underside of Top Flange Strain Data Line 1

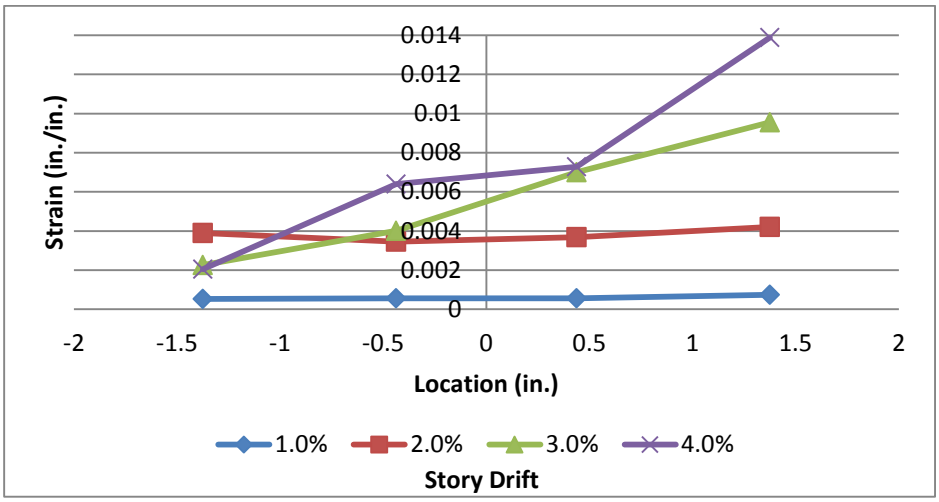

Figure D.95 – Specimen 9 (W36x150 with RBS and Grid of PAFs) Underside of Top Flange Strain Data Line 2

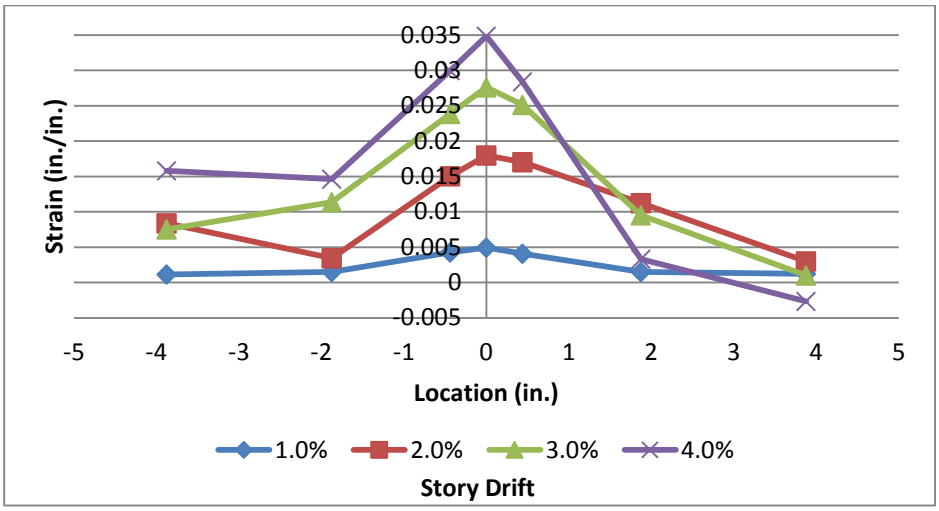

Figure D.96 – Specimen 10 (W36x150 with No RBS and No Fasteners) Top Flange Strain Data Line 1

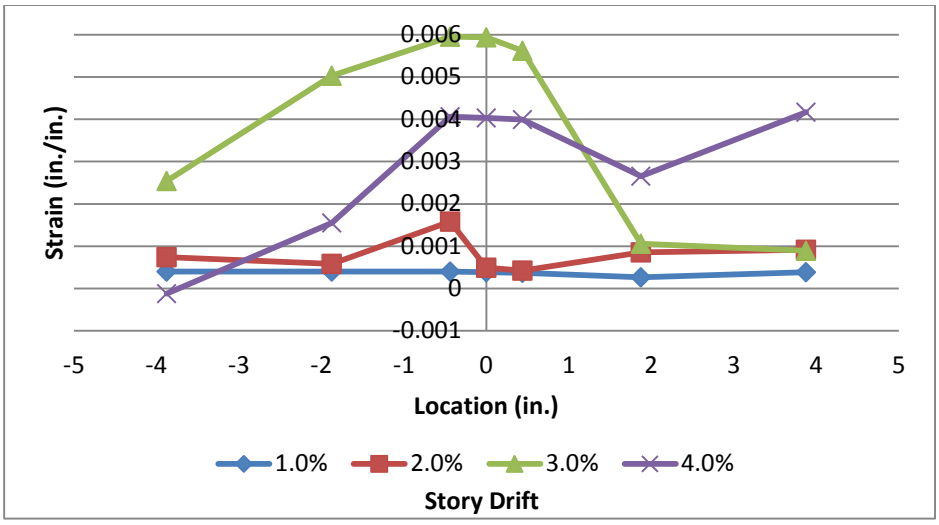

Figure D.97 – Specimen 10 (W36x150 with No RBS and No Fasteners) Top Flange Strain Data Line 2

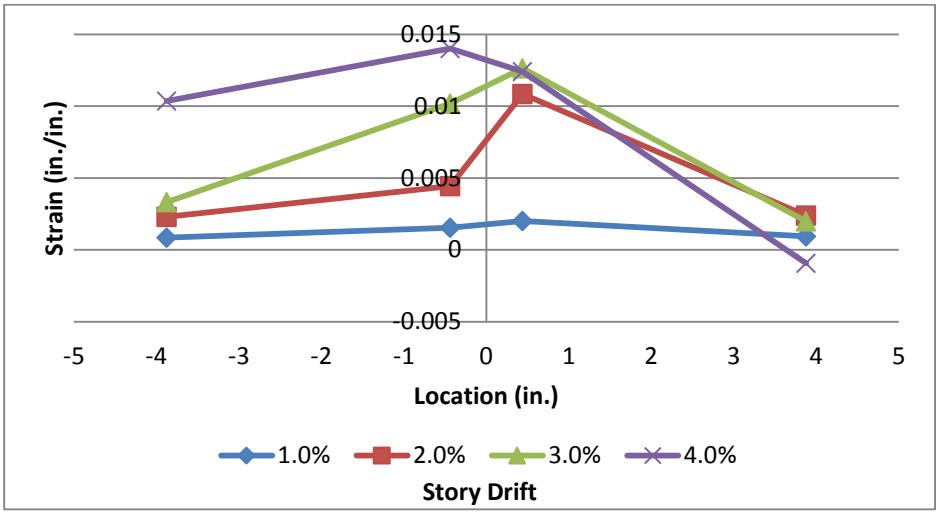

Figure D.98 – Specimen 10 (W36x150 with No RBS and No Fasteners) Underside of Top Flange Strain Data Line 1

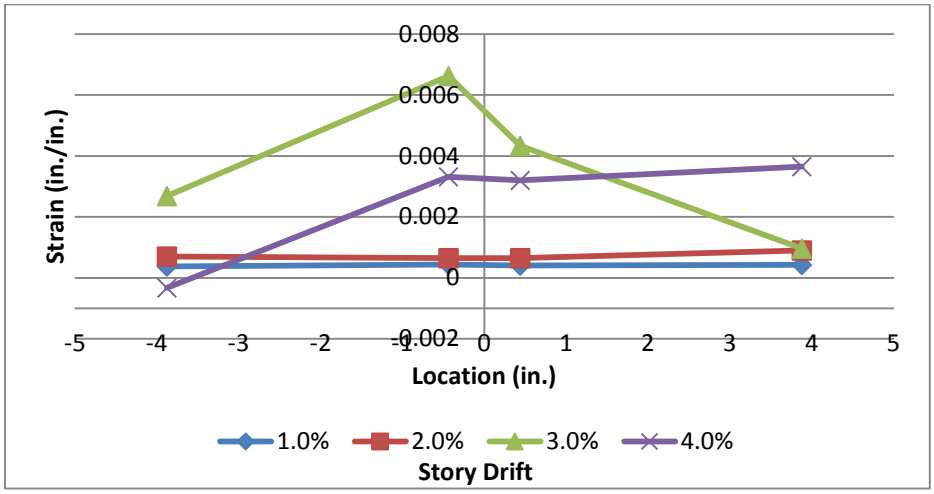

Figure D.99 – Specimen 10 (W36x150 with No RBS and No Fasteners) Underside of Top Flange Strain Data Line 2

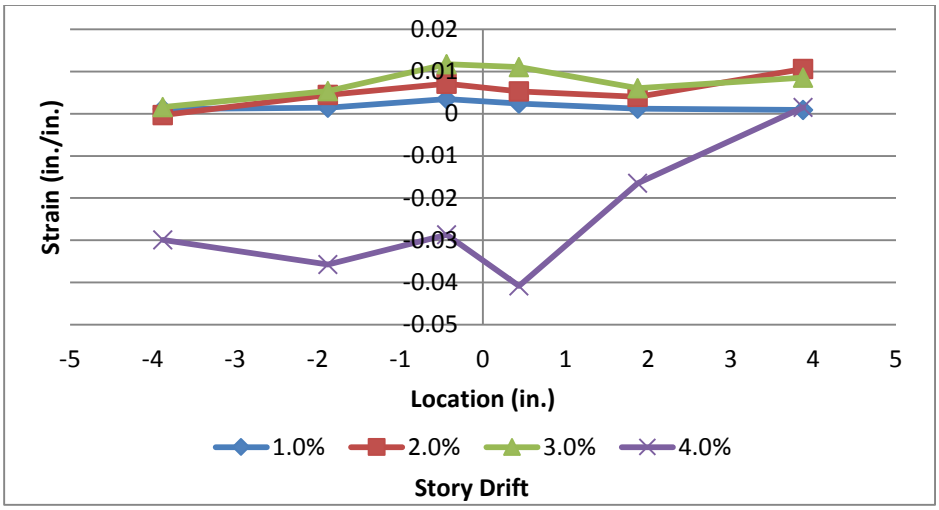

Figure D.100 – Specimen 11 (W36x150 with No RBS and PAFs at 12 in.) Top Flange Strain Data Line 1

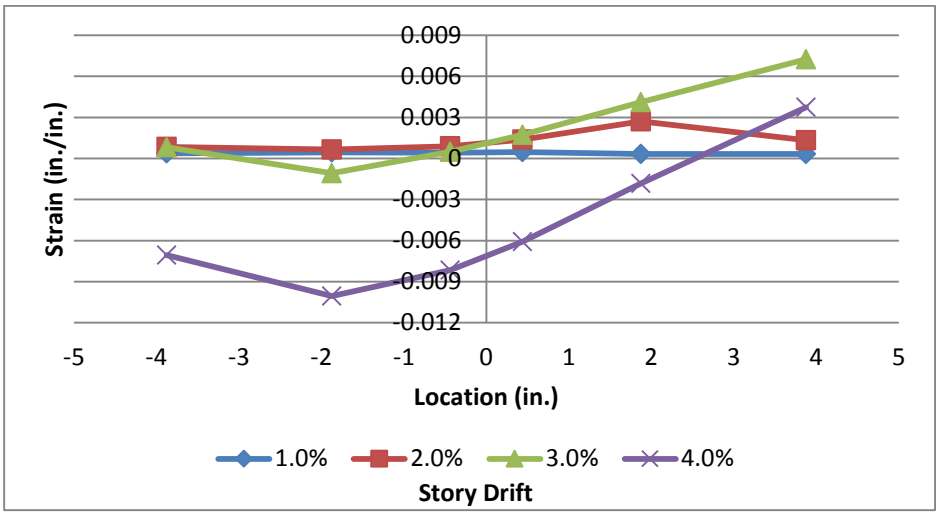

Figure D.101 – Specimen 11 (W36x150 with No RBS and PAFs at 12") Top Flange Strain Data Line 2

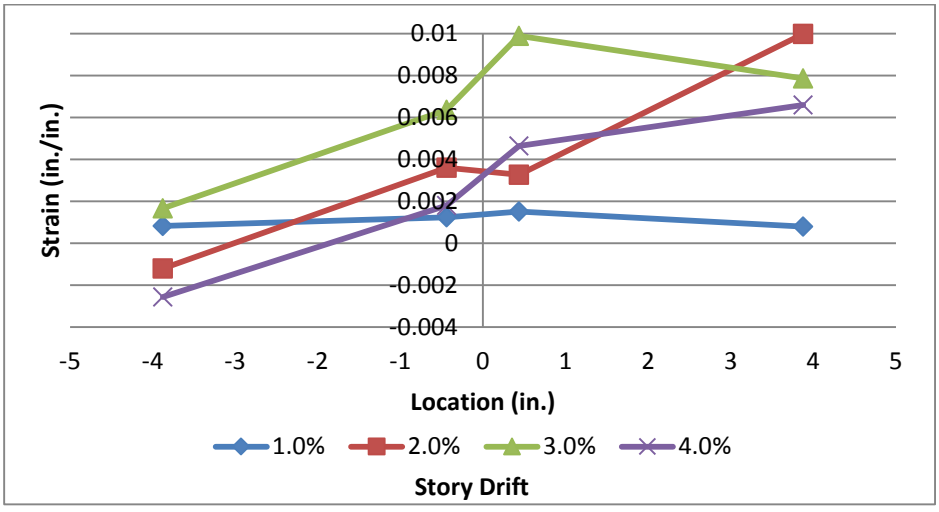

Figure D.102 – Specimen 11 (W36x150 with No RBS and PAFs at 12") Underside of Top Flange Strain Data Line 1

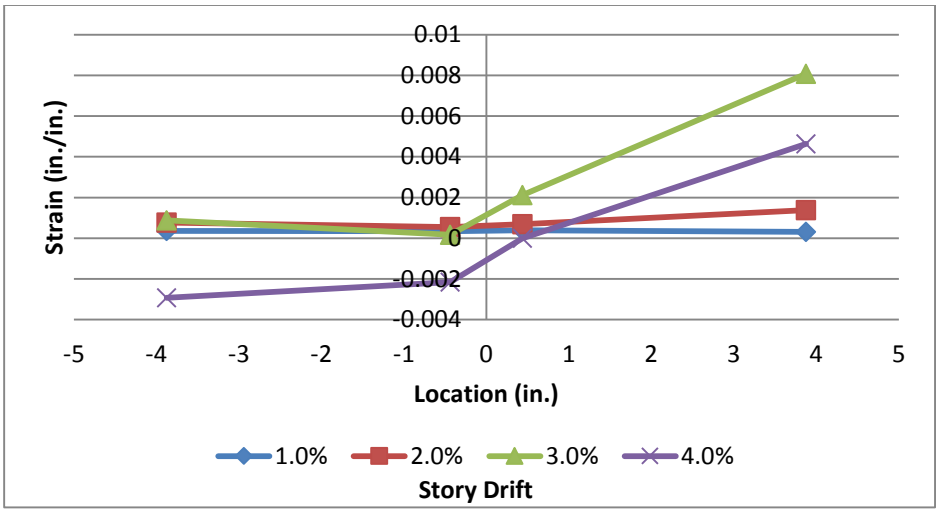

Figure D.103 – Specimen 11 (W36x150 with No RBS and PAFs at 12") Underside of Top Flange Strain Data Line 2

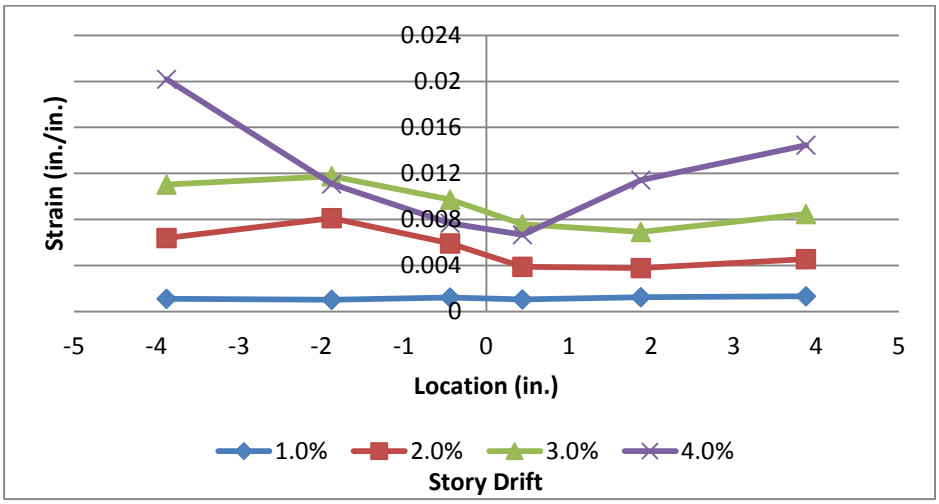

Figure D.104 – Specimen 12 (W36x150 with No RBS and Grid of PAFs) Top Flange Strain Data Line 1

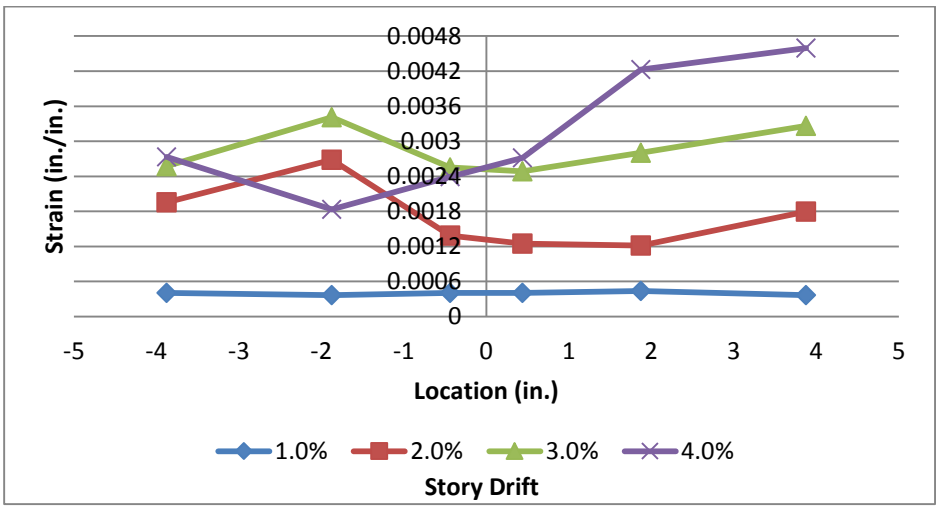

Figure D.105 – Specimen 12 (W36x150 with No RBS and Grid of PAFs) Top Flange Strain Data Line 2

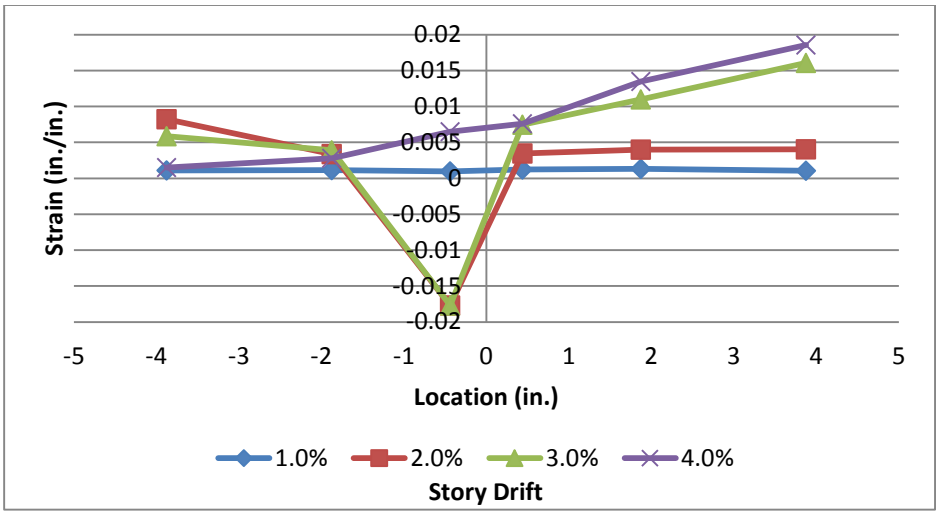

Figure D.106 – Specimen 12 (W36x150 with No RBS and Grid of PAFs) Top Flange Strain Data Line 3

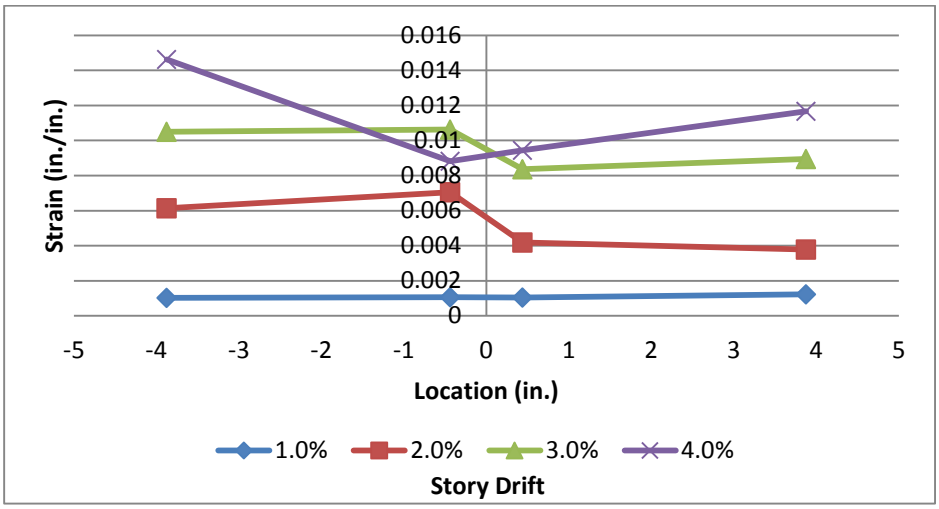

Figure D.107 –Specimen 12(W36x150 with No RBS and Grid of PAFs) Underside of Top Flange Strain Data Line 1

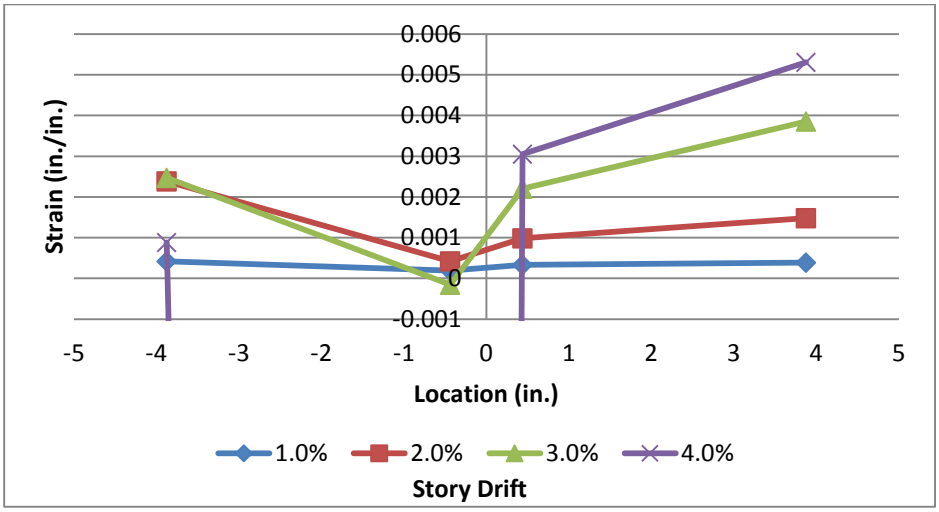

Figure D.108 –Specimen 12(W36x150 with No RBS and Grid of PAFs) Underside of Top Flange Strain Data Line 2

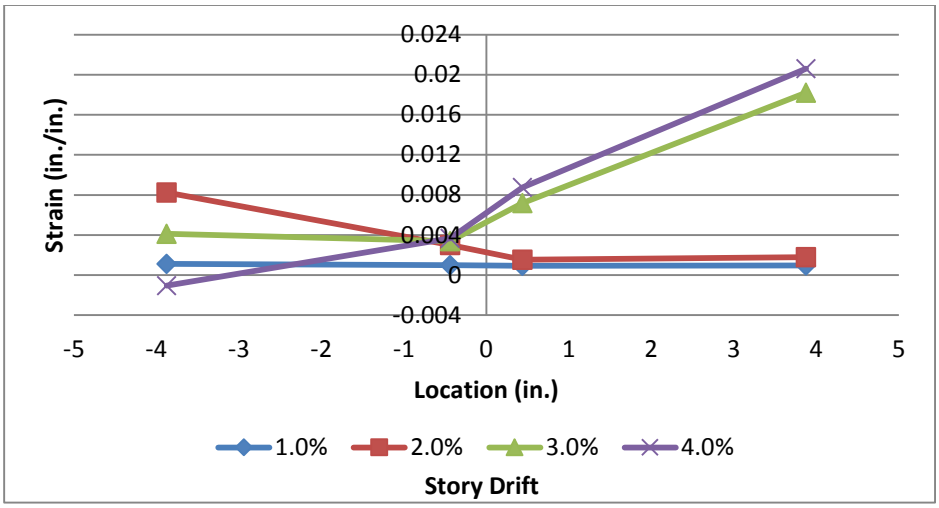

Figure D.109 –Specimen 12(W36x150 with No RBS and Grid of PAFs) Underside of Top Flange Strain Data Line 3

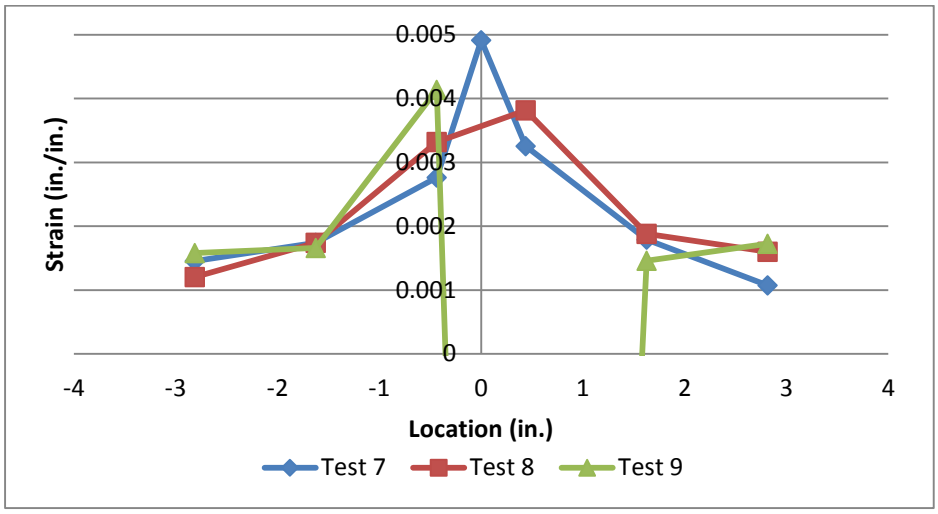

Figure D.110 – RBS36 (Specimen 7, 8 and 9) Top Flange Strain Data Line 1 at 1% Story Drift

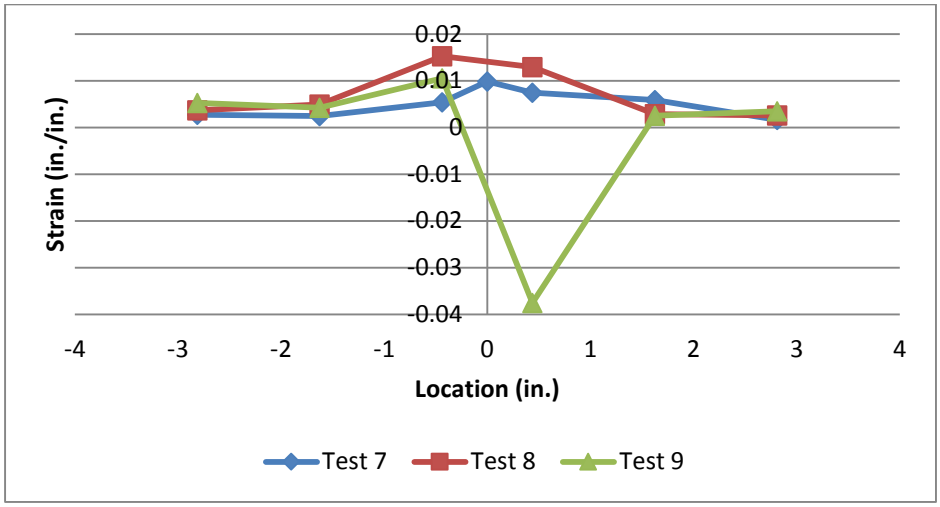

Figure D.111 – RBS36 (Specimen 7, 8 and 9) Top Flange Strain Data Line 1 at 2% Story Drift

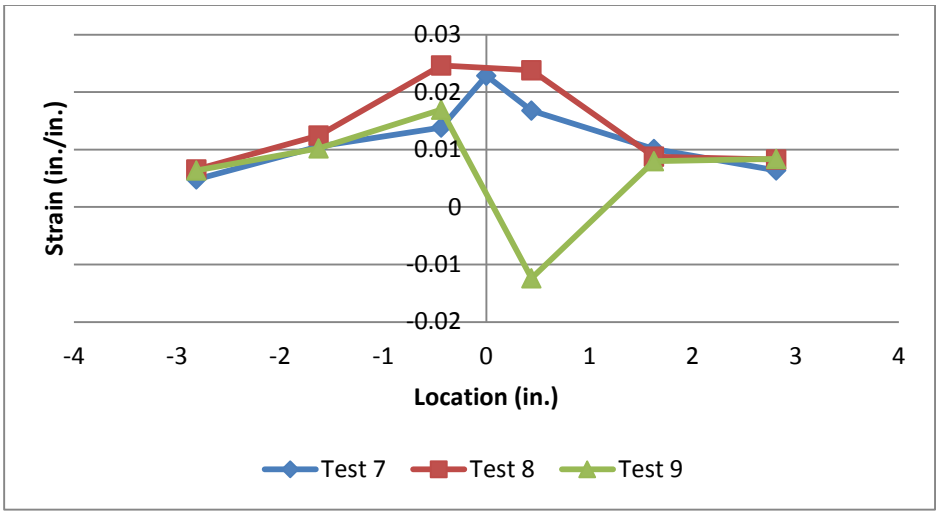

Figure D.112 – RBS36 (Specimen 7, 8 and 9) Top Flange Strain Data Line 1 at 3% Story Drift

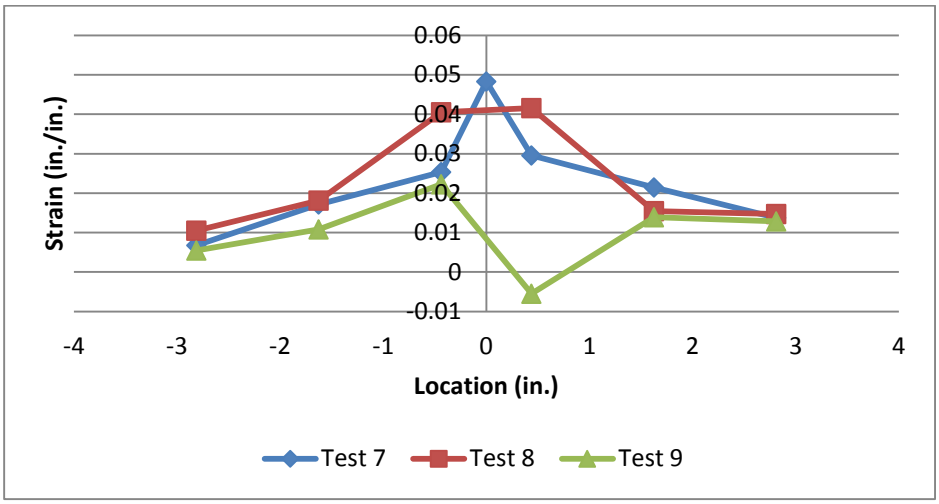

Figure D.113 – RBS36 (Specimen 7, 8 and 9) Top Flange Strain Data Line 1 at 4% Story Drift

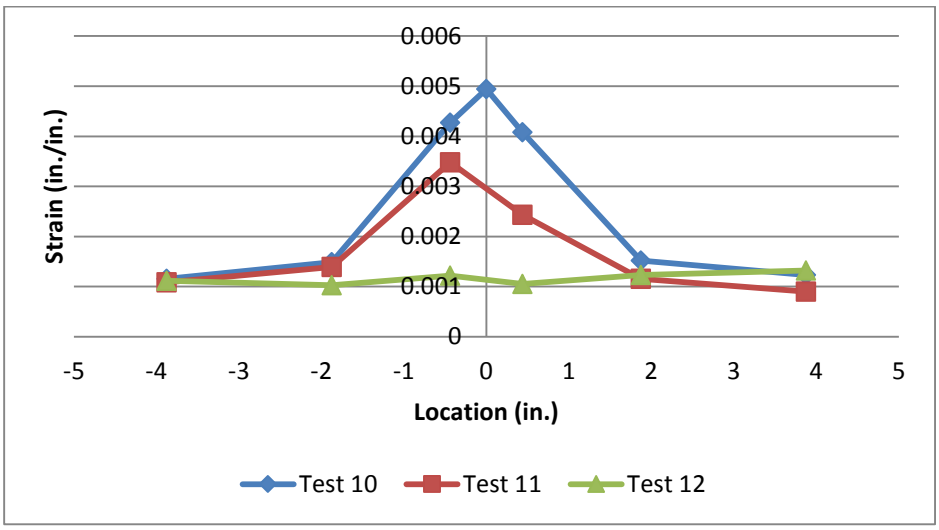

Figure D.114 – W36 (Specimen 10, 11 and 12) Top Flange Strain Data Line 1 at 1% Story Drift

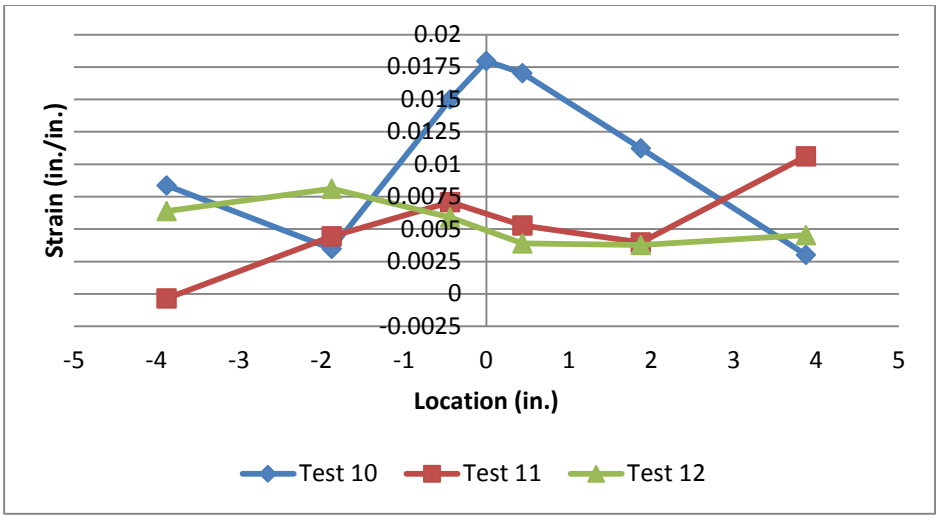

Figure D.115 – W36 (Specimen 10, 11 and 12) Top Flange Strain Data Line 1 at 2% Story Drift

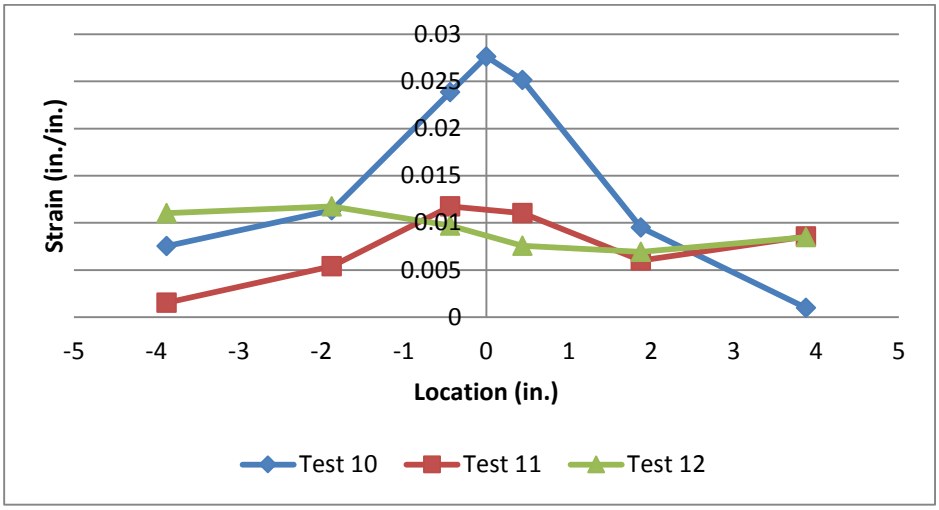

Figure D.116 – W36 (Specimen 10, 11 and 12) Top Flange Strain Data Line 1 at 3% Story Drift

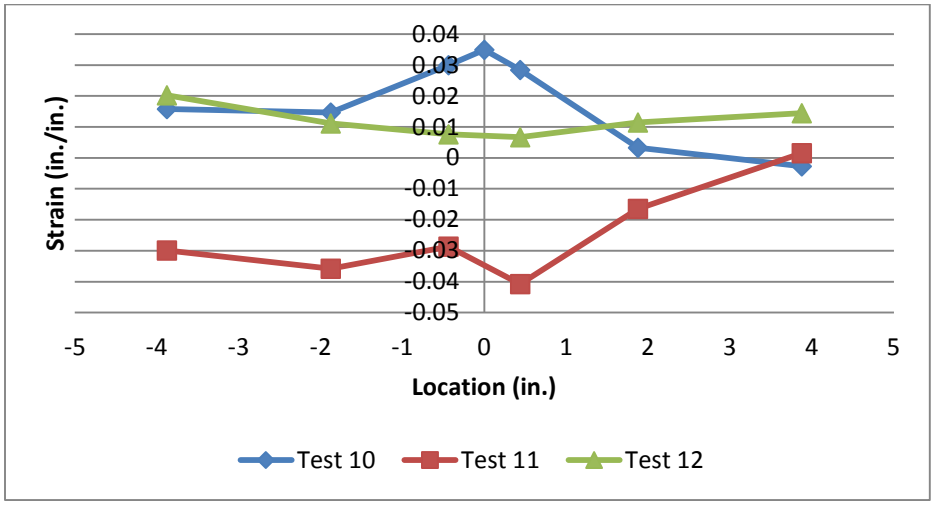

Figure D.117 – W36 (Specimen 10, 11 and 12) Top Flange Strain Data Line 1 at 4% Story Drift

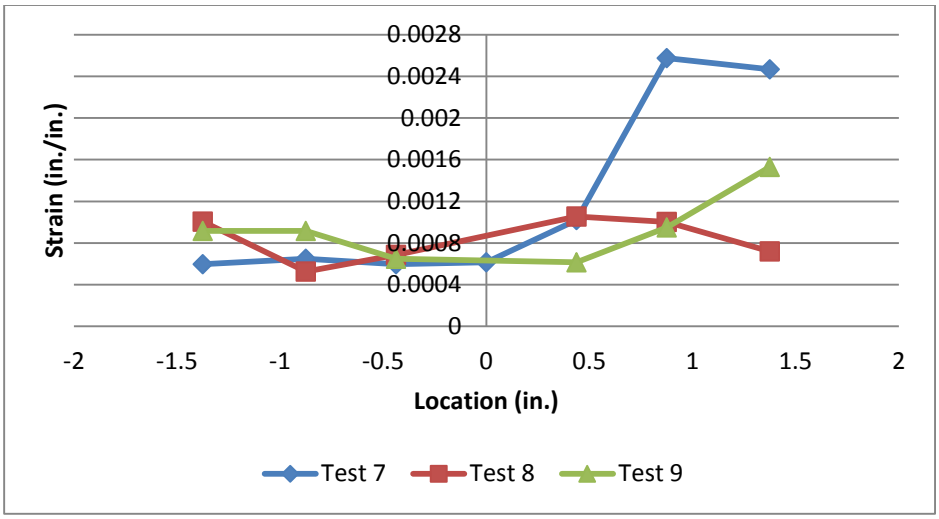

Figure D.118 – RBS36 (Specimen 7, 8 and 9) Top Flange Strain Data Line 2 at 1% Story Drift

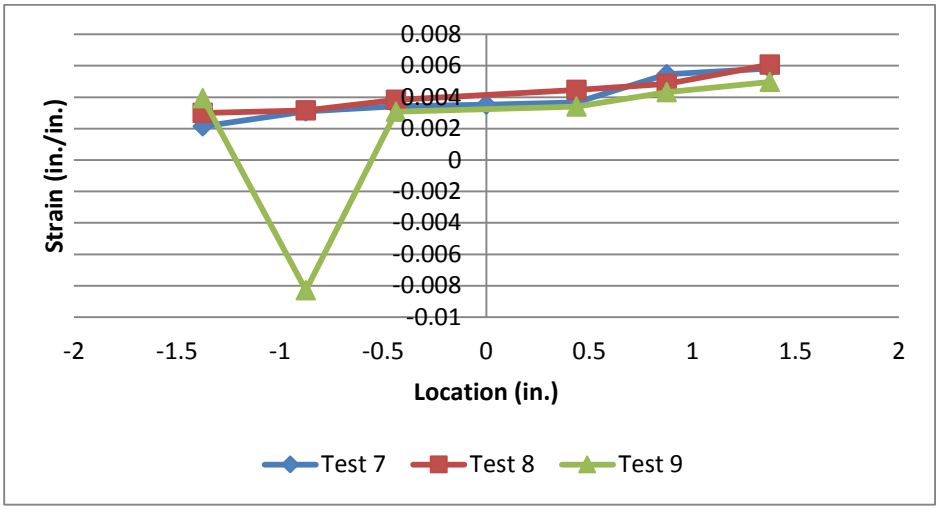

Figure D.119 – RBS36 (Specimen 7, 8 and 9) Top Flange Strain Data Line 2 at 2% Story Drift

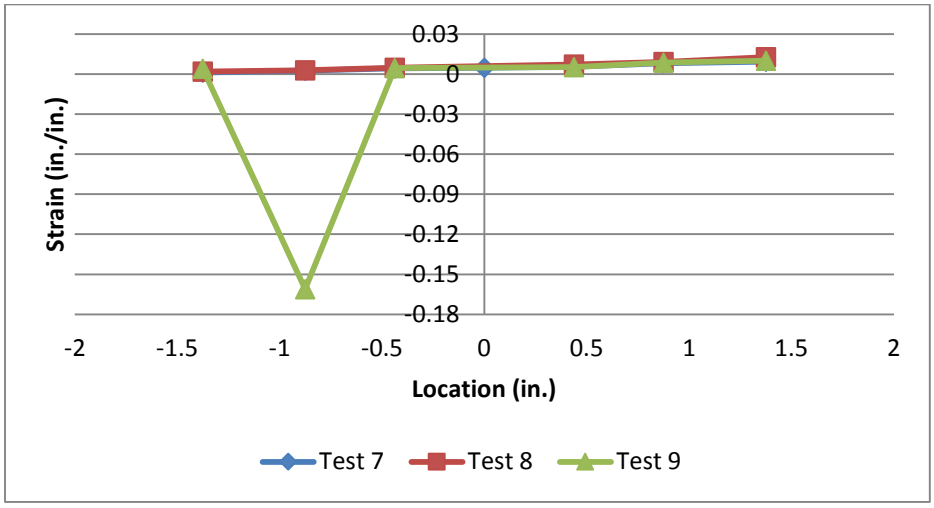

Figure D.120 – RBS36 (Specimen 7, 8 and 9) Top Flange Strain Data Line 2 at 3% Story Drift

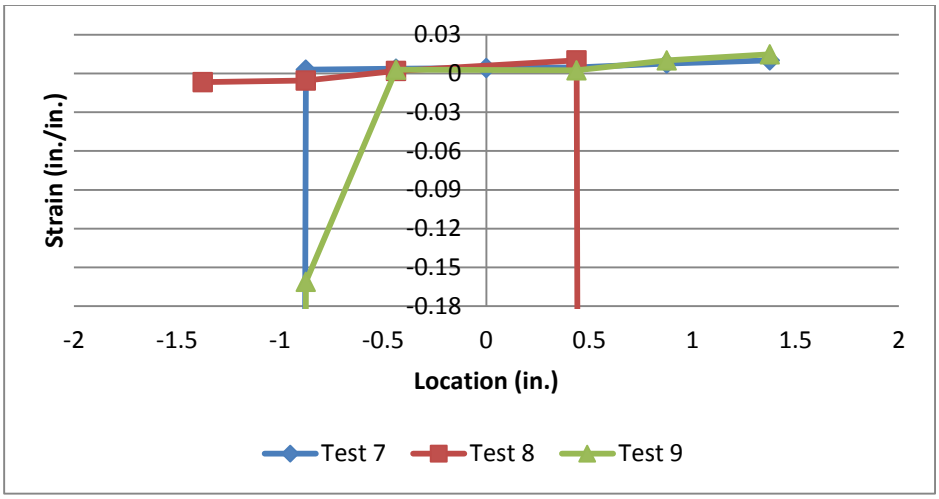

Figure D.121 – RBS36 (Specimen 7, 8 and 9) Top Flange Strain Data Line 2 at 4% Story Drift

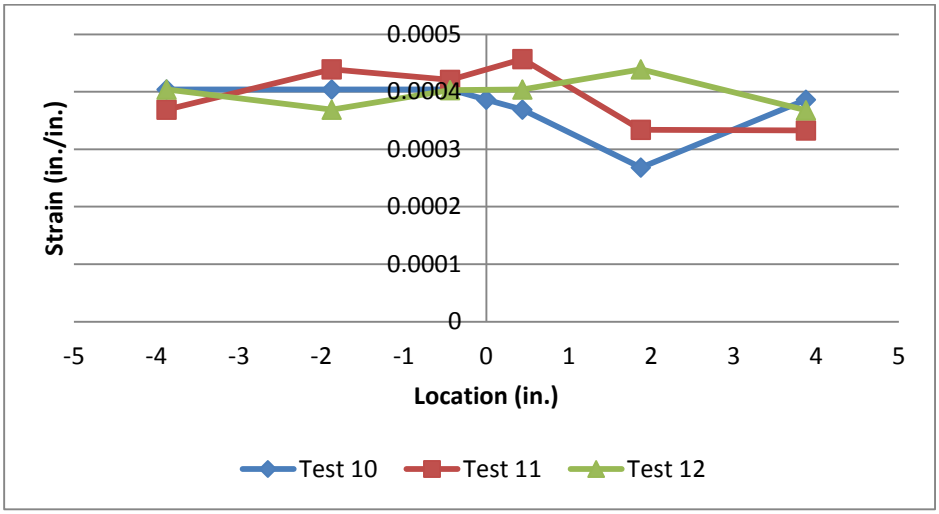

Figure D.122 – W36 (Specimen 10, 11 and 12) Top Flange Strain Data Line 2 at 1% Story Drift

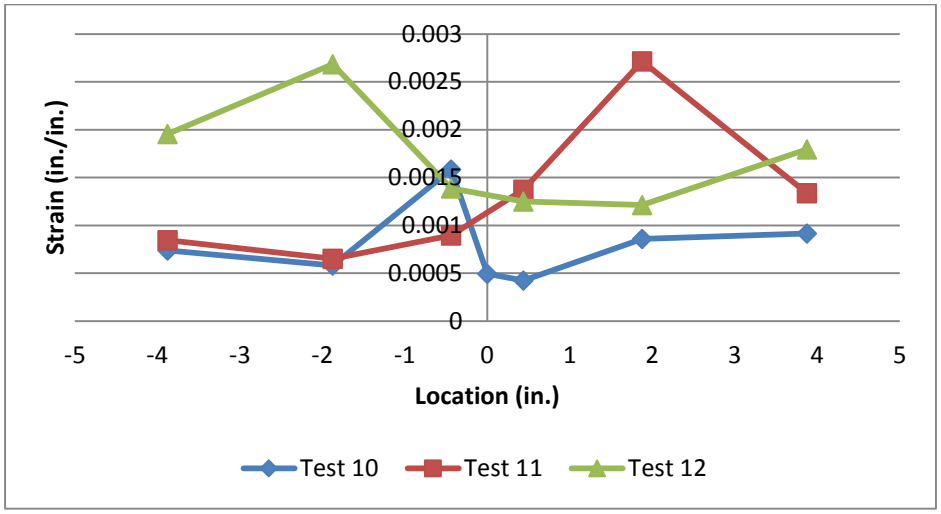

Figure D.123 – W36 (Specimen 10, 11 and 12) Top Flange Strain Data Line 2 at 2% Story Drift

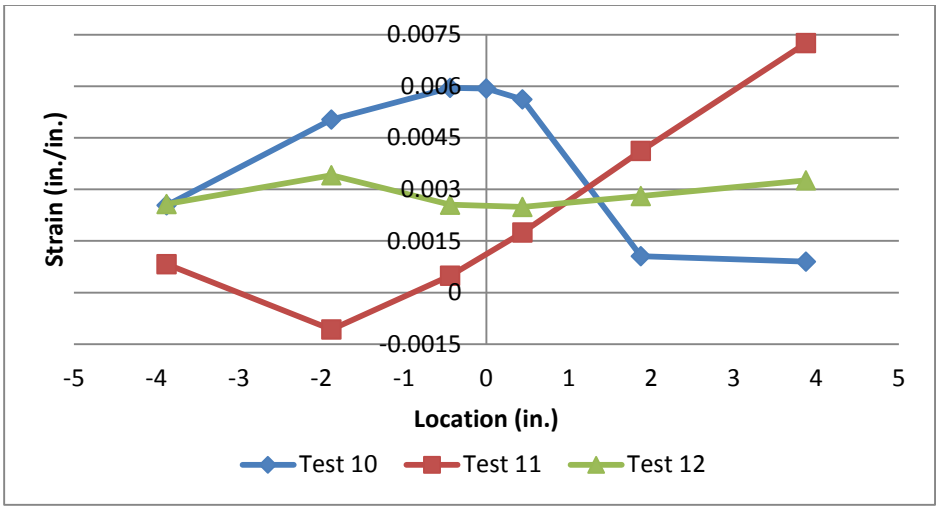

Figure D.124 – W36 (Specimen 10, 11 and 12) Top Flange Strain Data Line 2 at 3% Story Drift

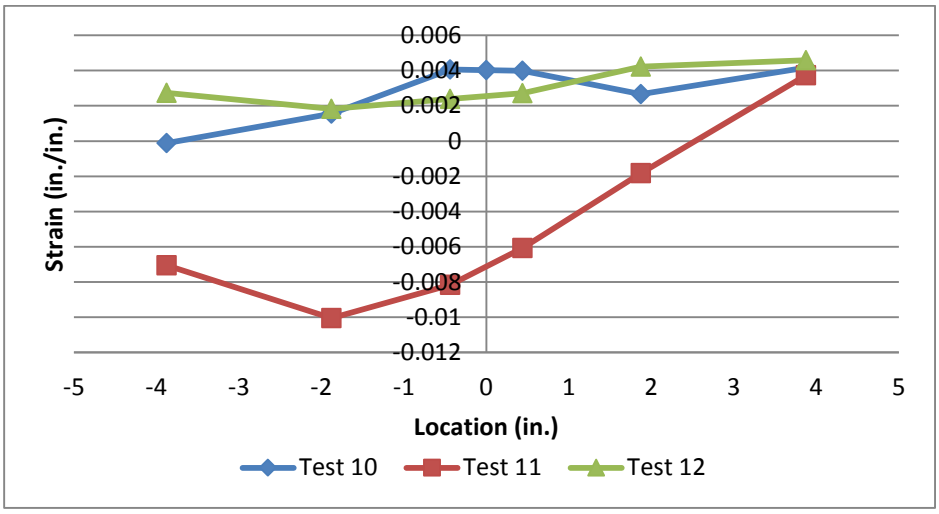

Figure D.125 – W36 (Specimen 10, 11 and 12) Top Flange Strain Data Line 2 at 4% Story Drift

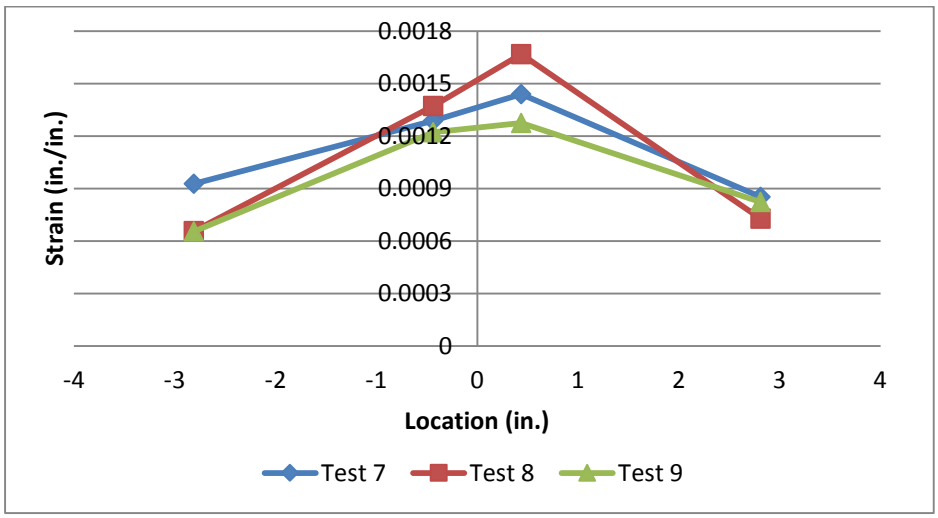

Figure D.126 – RBS36 (Specimen 7, 8 and 9) Underside of Top Flange Strain Data Line 1 at 1% Story Drift

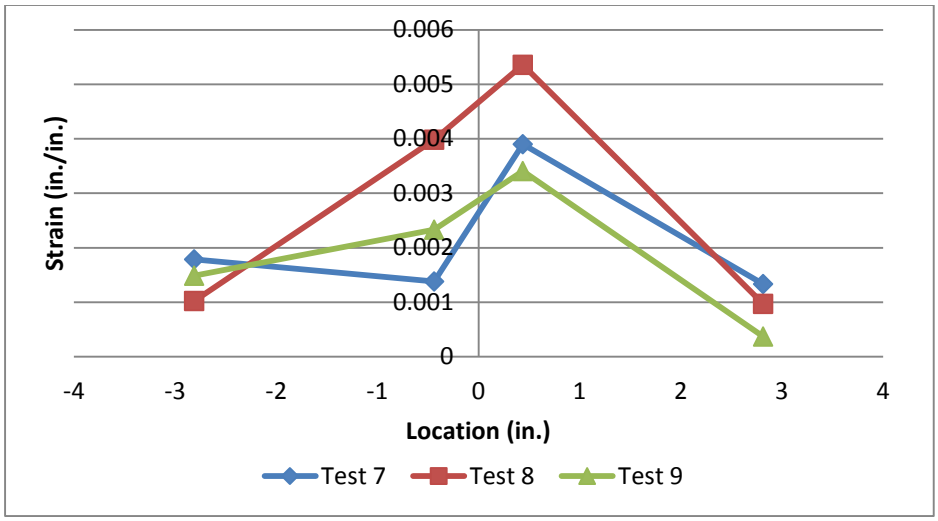

Figure D.127 – RBS36 (Specimen 7, 8 and 9) Underside of Top Flange Strain Data Line 1 at 2% Story Drift

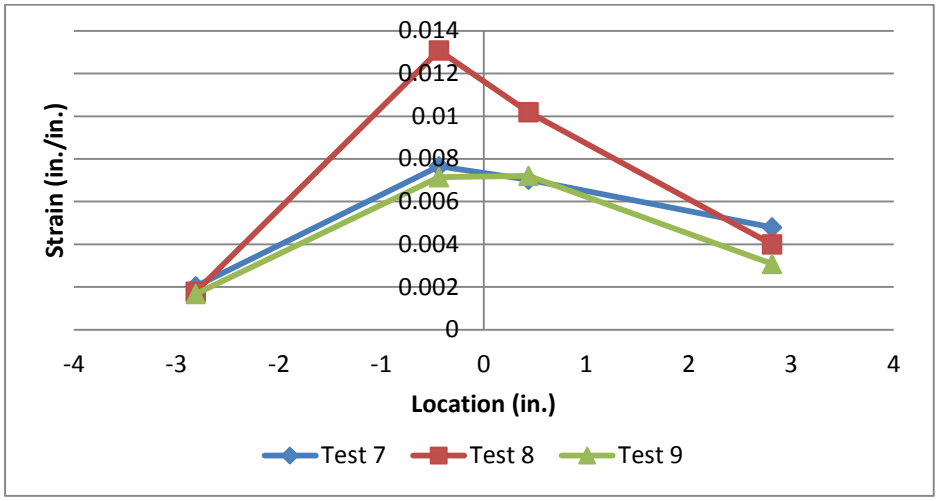

Figure D.128 – RBS36 (Specimen 7, 8 and 9) Underside of Top Flange Strain Data Line 1 at 3% Story Drift

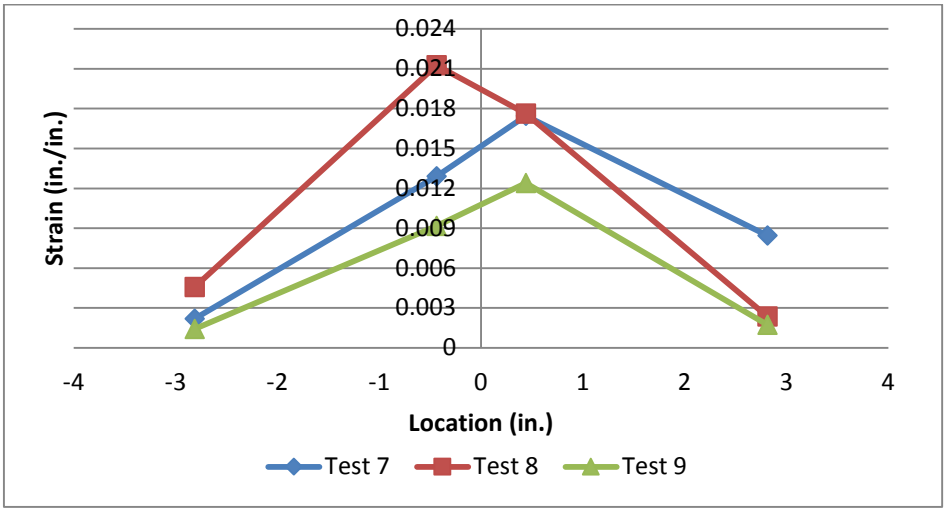

Figure D.129 – RBS36 (Specimen 7, 8 and 9) Underside of Top Flange Strain Data Line 1 at 4% Story Drift

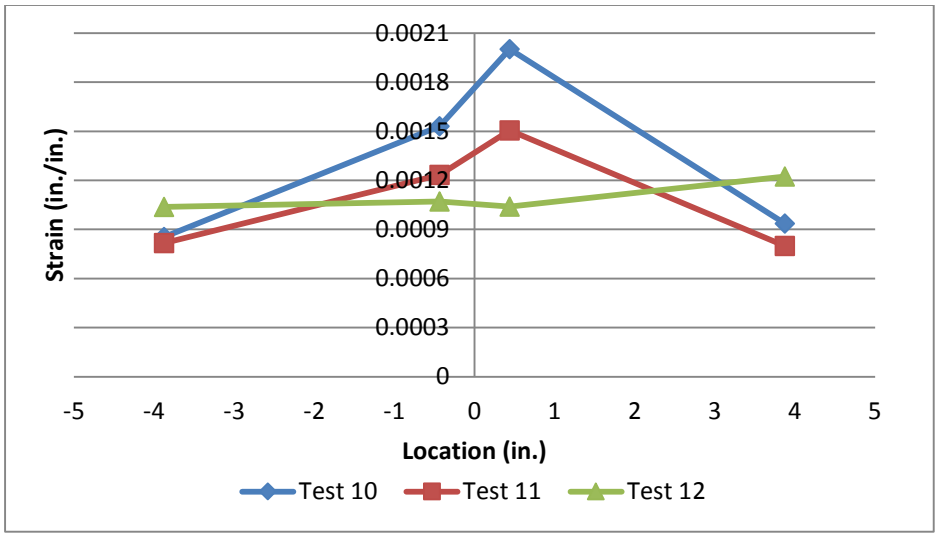

Figure D.130 – W36 (Specimen 10, 11 and 12) Underside of Top Flange Strain Data Line 1 at 1% Story Drift

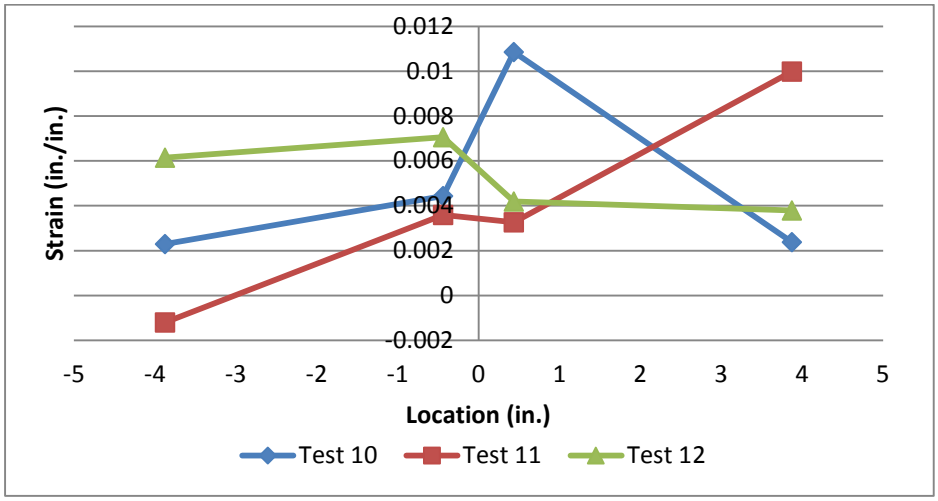

Figure D.131 – W36 (Specimen 10, 11 and 12) Underside of Top Flange Strain Data Line 1 at 2% Story Drift

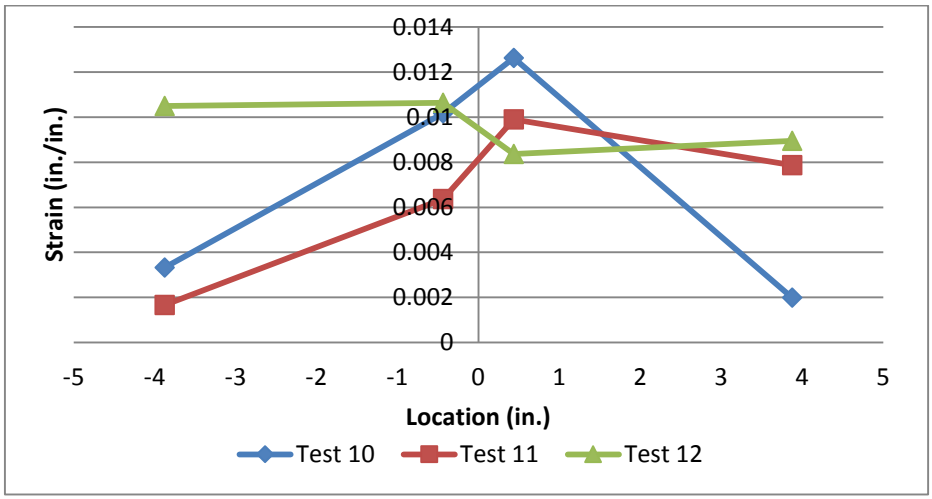

Figure D.132 – W36 (Specimen 10, 11 and 12) Underside of Top Flange Strain Data Line 1 at 3% Story Drift

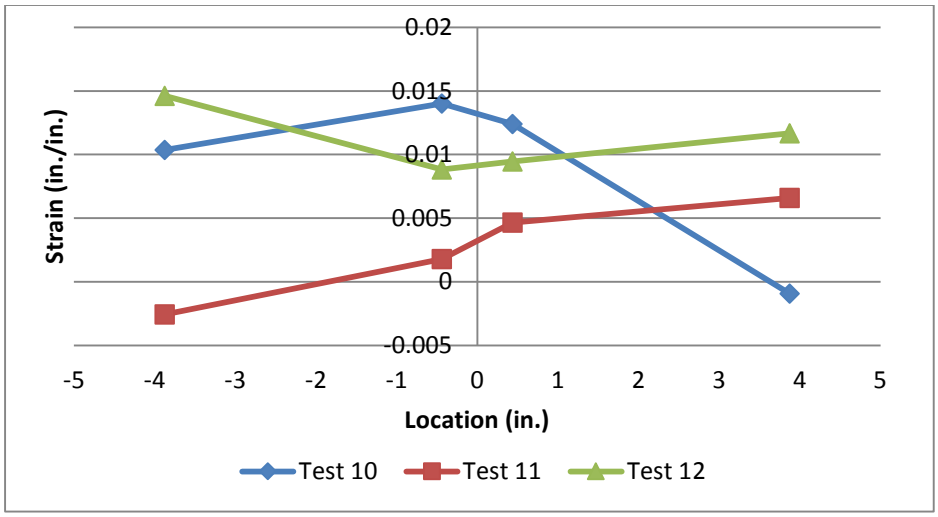

Figure D.133 – W36 (Specimen 10, 11 and 12) Underside of Top Flange Strain Data Line 1 at 4% Story Drift

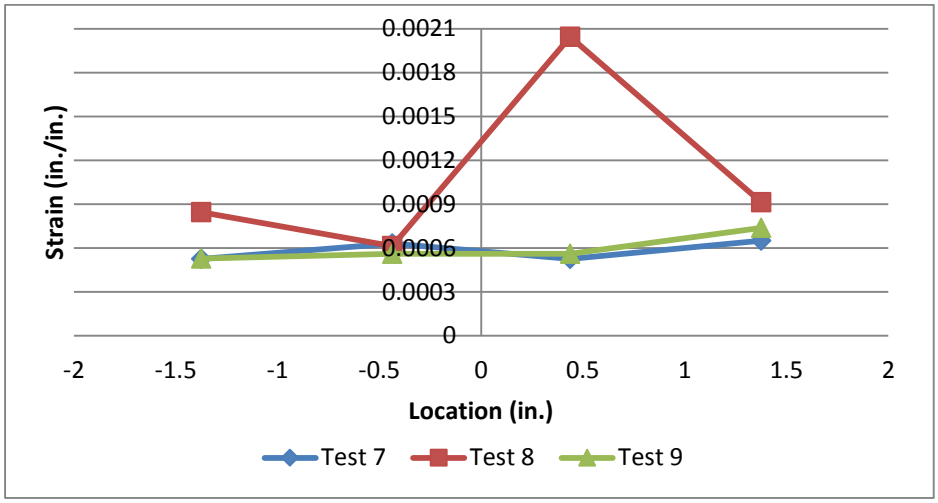

Figure D.134 – RBS36 (Specimen 7, 8 and 9) Underside of Top Flange Strain Data Line 2 at 1% Story Drift

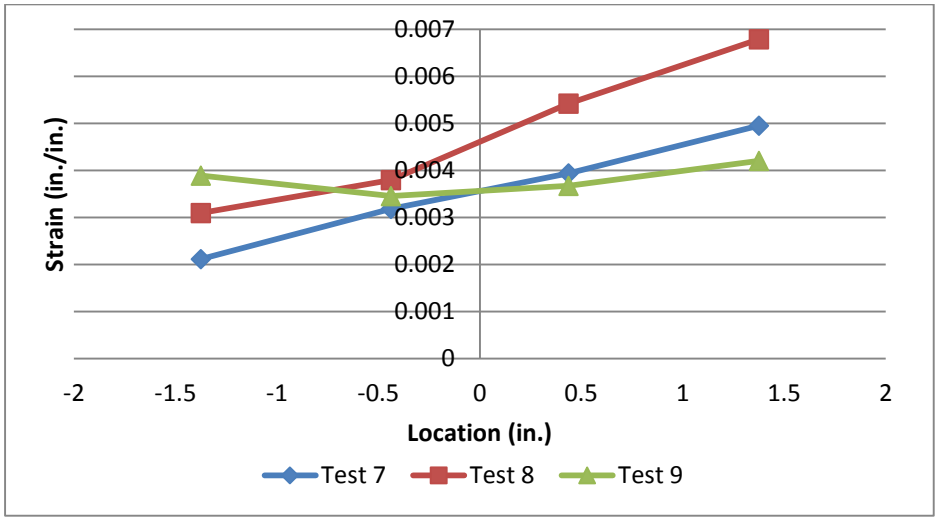

Figure D.135 – RBS36 (Specimen 7, 8 and 9) Underside of Top Flange Strain Data Line 2 at 2% Story Drift

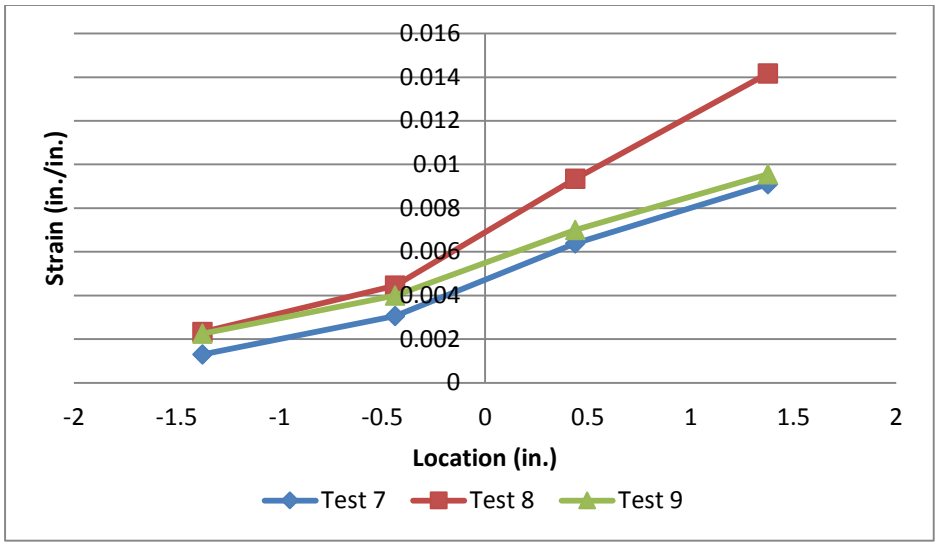

Figure D.136 – RBS36 (Specimen 7, 8 and 9) Underside of Top Flange Strain Data Line 2 at 3% Story Drift

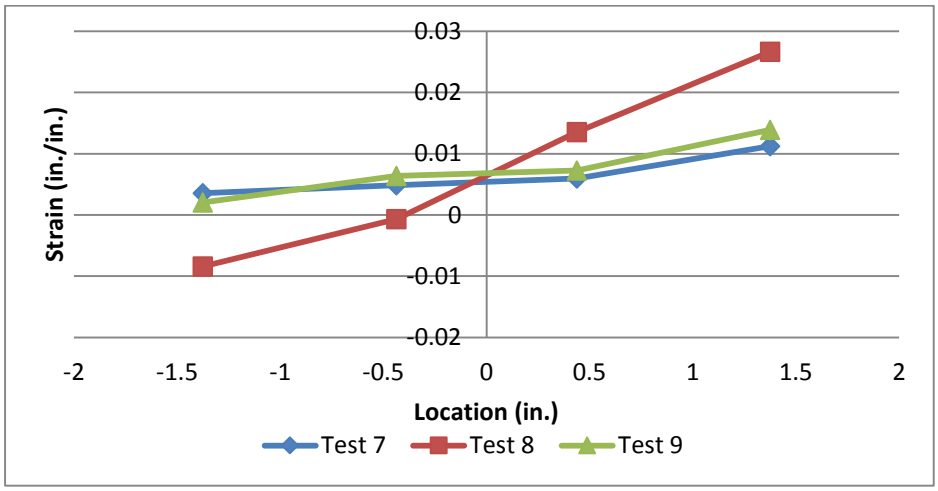

Figure D.137 – RBS36 (Specimen 7, 8 and 9) Underside of Top Flange Strain Data Line 2 at 4% Story Drift

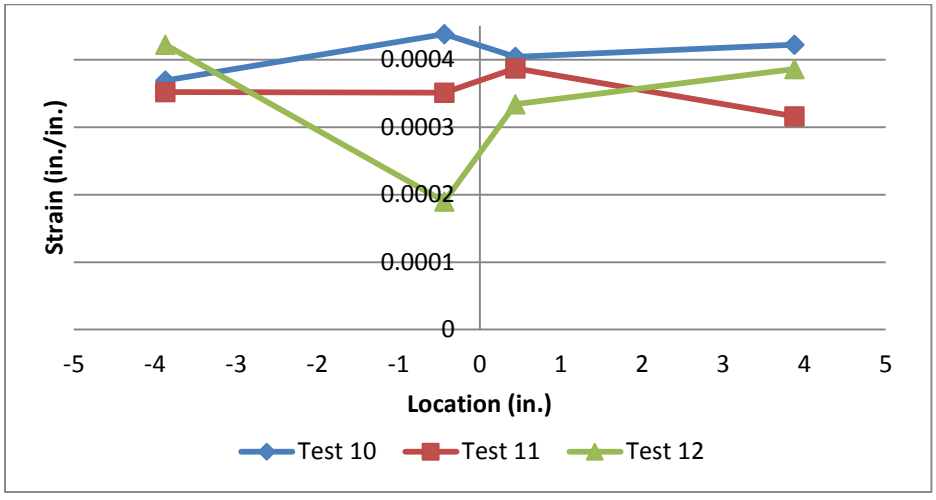

Figure D.138 – W36 (Specimen 10, 11 and 12) Underside of Top Flange Strain Data Line 2 at 1% Story Drift

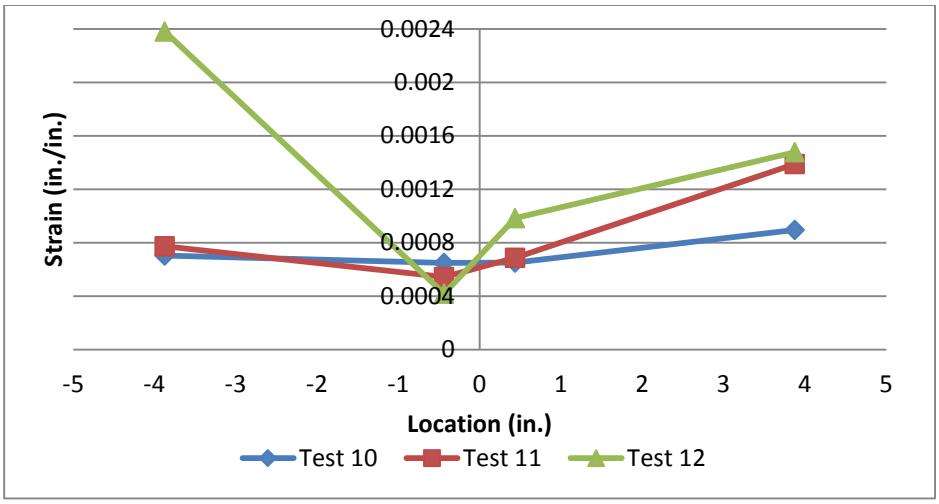

Figure D.139 – W36 (Specimen 10, 11 and 12) Underside of Top Flange Strain Data Line 2 at 2% Story Drift

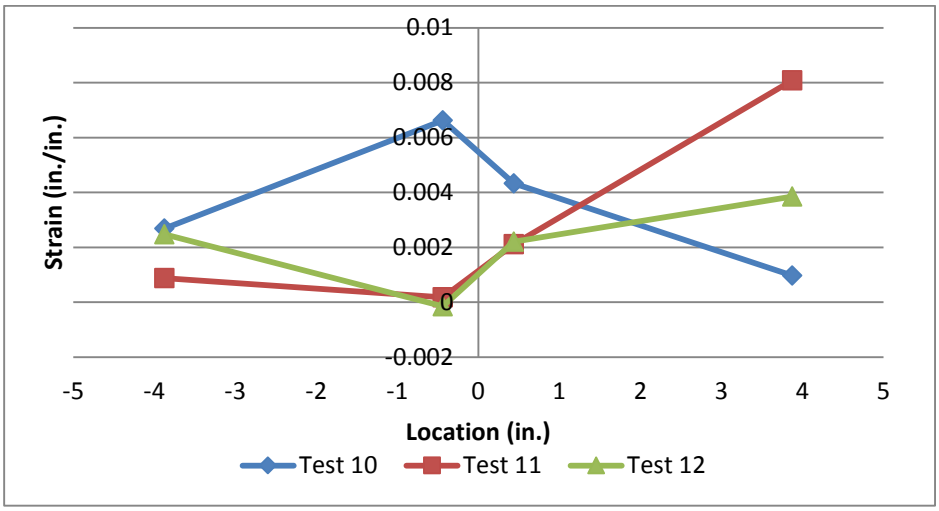

Figure D.140 – W36 (Specimen 10, 11 and 12) Underside of Top Flange Strain Data Line 2 at 3% Story Drift

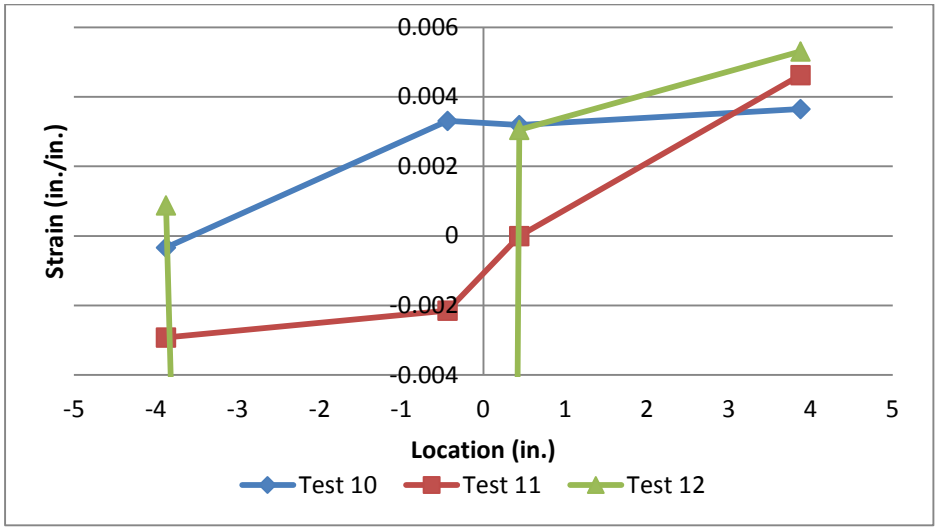

Figure D.141 – W36 (Specimen 10, 11 and 12) Underside of Top Flange Strain Data Line 2 at 4% Story Drift